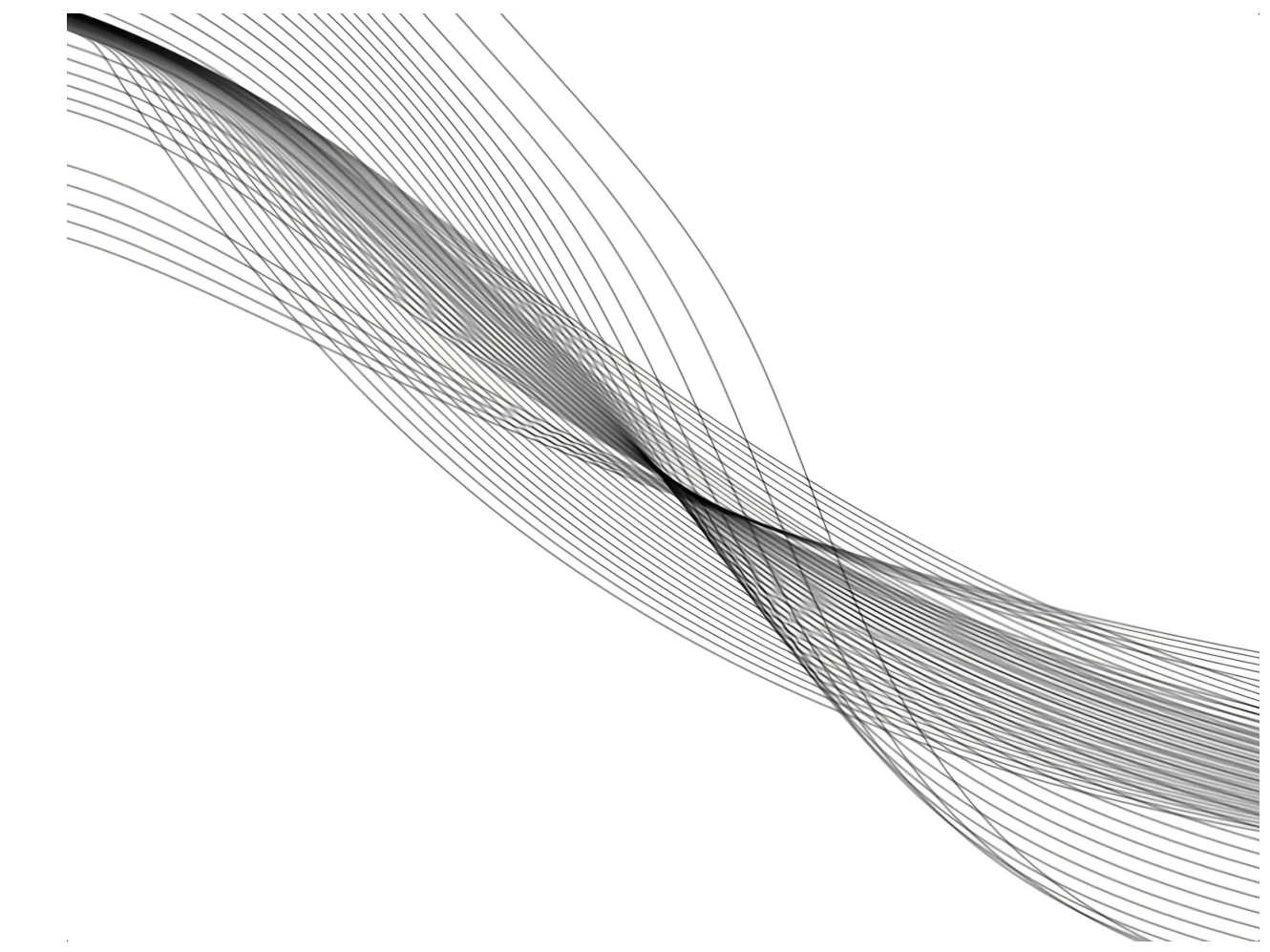




Characterization of the sequential nature of neuronal dynamics: Experimental recordings, computational models and novel stimulation neurotechnologies



Alicia Garrido Peña
Supervisor: Pablo Varona Martínez

PhD thesis. Ingeniería Informática y Telecomunicaciones
Universidad Autónoma de Madrid

Characterization of the sequential nature of neuronal dynamics: Experimental recordings, computational models and novel stimulation neurotechnologies

By

Alicia Garrido Peña



PhD thesis

Doctorado en Ingeniería Informática y de Telecomunicación

Supervisor

Pablo Varona Martínez

Departamento Ingeniería Informática
Escuela Politécnica Superior (EPS),
Universidad Autónoma de Madrid (UAM)
Madrid, Spain.

(July 2024)

“That is all as it should be, for in a question like this truth is only to be had by laying together many varieties of error.” - Virginia Woolf. A room of one’s own

Abstract

In the context of the multidisciplinary and combined efforts to understand the brain, we focus in a bottom-up approach to explain neural dynamics at low description levels. In particular, we study the sequential nature of neuronal dynamics, an essential point of view since many neural processes at different time and spatial scales occur in a sequential manner. To explore this sequentiality at different scales, we need adequate cases of study, approaches and techniques. In this thesis, we have addressed this topic using neurons and circuits of Central Pattern Generators (CPGs) to explore their robust sequential rhythm generation and a novel neurotechnology for the noninvasive modulation of neural dynamics: continuous-wave near-infrared (CW-NIR) laser stimulation. Throughout this work, we have combined electrophysiology and computational techniques, exploiting the advantages of their joint use.

First, we examined the presence of robust linear relationships between intervals that build up the cycle-by-cycle bursting sequence of the feeding CPG of the great pond snail (*Lymnaea stagnalis*) characterizing emerging coordination constraints in the form of sequential dynamical invariants, which were recently reported in the pyloric CPG of *Carcinus maenas*. We provided evidence to support the universality of this phenomenon by exploring it in another system and in a modeling study. We quantified the variability of the intervals of the sequences and discuss its role in motor coordination under different contexts. We also discuss the necessity of reproducing intrinsic functional variability in computational models for a complete characterization of the system and the associated sequential dynamical features. To conclude this first part of the thesis, we propose the validation of sequential dynamical invariants as flexible autonomous coordination mechanisms for effective locomotion in biohybrid robotics.

In the aim of finding novel techniques and approaches to noninvasively modulate sequential neural activity, we present in the second part of the thesis a study of the effect of CW-NIR laser in the neuronal dynamics of single neurons. First, we quantified its action on single neurons proving its effectiveness in sustained stimulation to modulate neuronal dynamics by accelerating action potentials

and increasing the spiking rate. We analyzed the different biophysical candidates to explain the results with the help of a theoretical study that explored both the effect of each candidate and the global key role of temperature in the observed modulation. To assess the change in the sequential evolution of the spike generation, we designed a novel activity-dependent technique to deliver the illumination at specific time instants. This protocol allowed to dissect the effect of the CW-NIR illumination on the action potential. Beyond its potential as a research tool, we believe that this activity-dependent protocol could become a widely used neurotechnology in clinical applications, allowing the design of personalized treatments.

Overall, this work provides a comprehensive study of neural dynamics exploring its sequential nature. The identification of dynamical invariants and the non-invasive stimulation through CW-NIR laser can be key for future applications in neurorrehabilitation, for assisted robotic locomotion technologies, and for novel treatments in neural disorders.

Resumen

En el contexto de los esfuerzos multidisciplinares y combinados para entender el cerebro, en esta tesis nos centramos en un enfoque *bottom-up* para explicar la dinámica neuronal desde una descripción de procesos a bajo nivel. En particular, estudiamos la naturaleza secuencial de la dinámica neuronal, un punto de vista esencial ya que muchos procesos neuronales ocurren de manera secuencial en diferentes escalas temporales y espaciales. Para explorar esta secuencialidad en diferentes escalas, necesitamos casos de estudio, enfoques y técnicas adecuadas. Por tanto, abordamos este tema utilizando neuronas y circuitos Generadores Centrales de Patrones (CPGs, por sus siglas en inglés) para explorar la generación de sus ritmos secuenciales robustos, y una novedosa neurotecnología para la modulación no invasiva de la dinámica neuronal: la estimulación con láser infrarrojo cercano de onda continua (CW-NIR, por sus siglas en inglés). A lo largo de este trabajo, combinamos técnicas de electrofisiología y modelos computacionales, aprovechando las ventajas de su uso conjunto.

En primer lugar, examinamos la presencia de relaciones lineales robustas entre intervalos que componen la secuencia de las ráfagas ciclo a ciclo del CPG alimentario del gran caracol de estanque (*Lymnaea stagnalis*), caracterizando las restricciones de coordinación emergentes en forma de invariantes dinámicos secuenciales, recientemente reportados en el CPG pilórico de *Carcinus maenas*. Aportamos evidencias que apuntan a la universalidad de este fenómeno explorándolo en otro sistema y en un estudio teórico. Cuantificamos la variabilidad de los intervalos que forman las secuencias y abordamos su papel en la coordinación motora bajo diferentes contextos. También discutimos la necesidad de reproducir la variabilidad funcional intrínseca en modelos computacionales para una caracterización completa del sistema y de las propiedades dinámicas de las secuencias asociadas a esa variabilidad. Finalmente, en esta primera parte de la tesis, proponemos la validación de los invariantes dinámicos secuenciales como mecanismos de coordinación autónoma y flexible para la locomoción efectiva en robótica biohíbrida.

Con el objetivo de encontrar nuevas técnicas y enfoques para una modulación no invasiva de la actividad neural secuencial, presentamos en la segunda parte de la tesis un estudio del efecto del láser

infrarrojo continuo (CW-NIR) en la dinámica neuronal de neuronas individuales. Primero, ilustramos su efecto en estas neuronas, demostrando su eficacia mediante iluminación sostenida para modular la dinámica neuronal al acelerar los potenciales de acción e incrementar su frecuencia. Analizamos los diferentes candidatos biofísicos para explicar los resultados con la ayuda de un estudio teórico en el que se explora tanto el efecto de cada candidato como el papel clave de la temperatura en la modulación observada. Para evaluar el cambio en la evolución secuencial de la generación de *spikes*, diseñamos una nueva técnica para iluminar las neuronas solo en instantes de tiempo específicos dependientes de su actividad. Este protocolo permitió disecionar por etapas el efecto de la iluminación CW-NIR en el potencial de acción. Más allá de su potencial como herramienta de investigación, creemos que este protocolo de ciclo cerrado puede convertirse en una neurotecnología ampliamente utilizada en aplicaciones clínicas, permitiendo el diseño de tratamientos personalizados.

En resumen, este trabajo proporciona un estudio exhaustivo de la dinámica neuronal explorando su naturaleza secuencial. La identificación de invariantes dinámicos y la estimulación no invasiva a través de láser CW-NIR pueden ser claves para futuras aplicaciones en neurorrehabilitación, para el diseño de tecnologías robóticas de locomoción asistida, y para el desarrollo de nuevos tratamientos en trastornos neurológicos.

Agradecimientos

Casi más difícil que el propio documento es resumir en una página en forma de agradecimientos los esfuerzos de mi entorno durante esta tesis. En este tiempo he aprendido mucho sobre neurociencia, programación, modelos dinámicos, láseres... Pero también mucho a nivel personal, y por supuesto no ha sido sola. Así que a toda persona con la que me he cruzado o he compartido camino y ha vivido esto conmigo, muchas gracias.

Concretando... Gracias a Pablo Varona, por abrirme las puertas del mundo de la neurociencia y darme espacio y apoyo para desarrollarme en el mundo de la investigación. A Rafi por darle la oportunidad a una informática de aprender electrofisiología y por enseñarme tanto en tantas horas de laboratorio, experimentos y análisis. A Paco por tantas ideas y por el apoyo y cariño durante todo el trabajo de esta tesis. A Jesús y Javier por todas esas horas ajustando el láser. A todos los demás miembros del GNB por acogerme tan bien desde el principio. A Roy por tantas conversaciones recién llegada a "primera hora". A Irene por dedicar tanto tiempo en su final de tesis a enseñarme. A Pablo por tantas horas de experimentos y trabajo, sobre todo por todo el apoyo mutuo en todas esas jornadas. A Sara por el caos que he tenido la suerte de conocer en estos años. A Ángel por tantas ideas, escucha y aportaciones a este trabajo, pero también por los cafés y el deporte para recargar pilas. A Carlos, Alberto, Fabiano, Aaron, Jessica, Manu, Angel F. Habéis hecho más fácil ir cada día al lab y un gusto siempre veros fuera de él.

Y fuera del lab, a todos los que habéis estado presentes. A Irene, por haber acompañado tan de cerca estos años de perderme las fiestas de Moratalla por el congreso, de desaparecer volviendo a las tantas de trabajar y por haber hecho de los ratos de ocio y COVID en Madrid un espacio de casa, convivencia y cariño. A mi MAPS, por haber sido refugio emocional tantas veces y conseguir encontrarnos siempre pese al tiempo que pase (y la falta de él). A Alba y Pablo por lo divertido que es siempre el cameo. A Jorge y Carmen, que también habéis vivido esto muy de cerca, pero sobre todo habéis sido parte de esos ratos de fuga. A María y Sara por los daños colaterales. A Rodri por acompañarme desde el principio de mi etapa en Madrid. A María G., por estar siempre

en la misma onda vital y comprenderme tan bien. A mi Granada querida y todos los que sé que me apoyáis y mantenéis desde allí (incluso aunque ya no la habitéis). A RadioPalacio, Rumanía, Luis, María, Palolo, Migue... por conseguir que el tiempo no consiga cambiar nada al volver a vernos. A Jelen y Ro, por cuidarme tanto en la distancia, gracias por toda la confianza y el cariño con el que me la demostráis. A Cris, o como diría ella 'mi amiga más antigua', por todo el apoyo que siento de tu parte. A Miguel y Zapa, porque desde que os conozco habéis sido un oasis de escape, desarrollo personal y cable a tierra. A Isa, que siempre consigue estar presente aunque ni la constancia ni el tiempo sean nuestro punto fuerte. A Mai, Const y Anita, por los ratitos breves pero tan casa que hemos compartido estos años. A las conspiradoras por abrirme al final de esta etapa un ventanal a otras realidades y dejarme acompañarlos a descubrirlas.

A mi familia, a mis padres y mis hermanas, por su cuidado y apoyo incondicional durante este proceso y en todos los demás aspectos, retos y cambios de la vida.

Y por supuesto a Ángel, por su ayuda durante todo este trabajo, porque has sido apoyo indiscutible desde la primera charla online en el congreso del CNS hasta el seminario de fin de tesis. Por ser motor, soporte e impulso constante, y la compañía que quiero en cualquier camino.

Contents

1	Introduction and State of the Art	1
1.1	Neuroscience, neurons and their dynamics	1
1.1.1	Neuronal dynamics	2
1.1.2	Network dynamics	5
1.2	The sequential nature of neural dynamics	6
1.3	Studying neural dynamics in computational models.	10
1.3.1	Conductance-based models	11
1.3.2	Variability in computational models	15
1.4	Vertebrate and invertebrate animal studies	16
1.5	Neural stimulation	18
1.5.1	Stimulation techniques	18
1.5.2	Neuromodulation and its need for clinical applications	19
2	Introducción y Estado del Arte	21
2.1	Neurociencia, neuronas y su dinámica	21
2.1.1	Dinámica neuronal	22
2.1.2	Dinámicas de redes	25
2.2	La naturaleza secuencial de la dinámica neuronal	26
2.3	Estudio de la dinámica neuronal mediante modelos computacionales.	30
2.3.1	Modelos basados en conductancia	31
2.3.2	Variabilidad en los modelos computacionales	36

CONTENTS

2.4	Estudios de animales vertebrados e invertebrados	37
2.5	Estimulación neuronal	39
2.5.1	Técnicas de estimulación	39
2.5.2	Neuromodulación y su necesidad para aplicaciones clínicas	40
3	Motivation and Objectives	43
4	Materials and Methods	47
4.1	The neural system of <i>Lymnaea stagnalis</i>	47
4.2	The feeding CPG of <i>Lymnaea stagnalis</i>	48
4.3	Electrophysiology in <i>Lymnaea stagnalis</i>	49
4.4	Conductance based models	50
4.4.1	Feeding CPG model	51
4.4.2	CGC neuron model	54
4.5	Neural data analysis	55
4.6	CW-NIR laser setup	59
5	Sequential constrains in CPG circuits: Dynamical invariants	61
5.1	Introduction	61
5.2	Methods	63
5.2.1	Time references, intervals and CPG sequence	63
5.2.2	Inducing variability in the model by current injection	65
5.2.3	Experimental recordings and stimulation	67
5.2.4	Models with chaotic activity	68
5.2.5	Hybrot structure	70
5.3	Sequential dynamical invariants in computational models	72
5.3.1	N1M driven variability	73
5.3.2	N3t driven variability	74
5.3.3	SO driven variability	76

CONTENTS

5.3.4	Cycle-by-cycle interval relations not only involving the period	77
5.3.5	Comparison with two-phase intervals	81
5.4	Experimental results in <i>Lymnaea Stagnalis</i>	83
5.4.1	Invariants in spontaneous activity	86
5.4.2	Invariants in SO driven activity	92
5.4.3	Invariants in MLN stimulation driven activity	98
5.4.4	Invariants in CVa1 driven activity induced by electrical stimulation	101
5.4.5	Summary of changes in the invariants due to stimulation	107
5.4.6	Invariant resetting	109
5.5	Characterization of variability in bursting models and its functionality	111
5.6	Transformation of sequential intervals into effective robot movement	113
5.7	Discussion	116
6	CW-NIR laser as an effective neuromodulation technique	121
6.1	Introduction	121
6.2	Methods	123
6.2.1	Sustained CW-NIR stimulation protocol	123
6.2.2	Activity-dependent laser stimulation protocol	124
6.2.3	Spike waveform characterization parameters	126
6.2.4	Statistical Analysis	127
6.3	Temperature estimation for analyzing laser neuromodulation	129
6.4	Sustained CW-NIR laser stimulation effect on single neuron dynamics	130
6.4.1	CW-NIR laser effect on spike waveform	130
6.4.2	CW-NIR laser effect on spiking rate	133
6.4.3	Effect of CW-NIR stimulation in a minimal circuit	136
6.4.4	Effect of CW-NIR stimulation at different wavelengths	137
6.5	Model analysis for constraining candidates to explain the effect of CW-NIR laser illumination in the spike dynamics	139

CONTENTS

6.5.1	Parameter range modification for the biophysical candidates in the model	139
6.5.2	Change of spike dynamics considering temperature modulation in the model	145
6.6	Activity-dependent stimulation to assess the laser effect at distinct stages of the spike dynamics	149
6.6.1	Model simulation of activity-dependent stimulation	149
6.6.2	Experimental activity-dependent stimulation	151
6.7	Discussion	154
6.7.1	Singularity of the sustained and activity-dependent CW-NIR stimulation on neural dynamics	154
6.7.2	Biophysical explanation of the CW-NIR modulation through modeling and activity-dependent stimulation	155
6.7.3	Applications for research and clinical use	157
7	Conclusion and Discussion	159
8	Conclusiones y Discusión	167
A	Publications	195
B	Supplementary figures for chapter 4	199

List of Tables

1.1	Equations of Hodgkin and Huxley formalism for the voltage and conductance gating variables.	13
2.1	Ecuaciones del formalismo de Hodgkin y Huxley para el voltaje y las variables de conductancia.	34
5.1	List of i_{inj} values that yield realistic bursting rhythms for each neuron in the model CPG used in the stimulation protocols reported in this chapter. The left section of the table displays the i_{inj} values applied to each neuron (columns) during each simulation condition (rows). Ramp values on the right section refer to the minimum and maximum values of the ramp variable c in each simulation, increasing i_{inj} in the specified step every 4.6 seconds (the approximate duration of two N3t burst) to induce variability.	67
5.2	Time reference boundaries for the three phases in the feeding CPG.	85

LIST OF TABLES

List of Figures

1.1	Illustration by Ramon y Cajal intended to show the probable course of information flow in the bee retina (Ramón y Cajal & Sánchez, 1915) (Available via license: CC BY 4.0).	2
1.2	Representation of the sequential phases and terminology of an action potential, along with the ionic currents involved in its generation (I_K, I_{Na} and $I_{leakage}$). In each of these phases of the action potential generation, different ionic channels are activated sequentially, e.g. the sodium channel is involved during the depolarization phase and its activity decays as the potassium channel activates mostly in the repolarization phase.	3
1.3	Examples of different spike shapes. Representation of two recordings from two different cells in the right parietal ganglion of <i>Lymnaea stagnalis</i> . a) Symmetrical shaped spike. b) Shoulder shaped spike.	4
1.4	Examples of different types of neuronal spiking activity. a) Two simultaneous intracellular recordings in <i>Lymnaea stagnalis</i> showing tonic firing at two different frequencies. b) Example of bursting activity from <i>Lymnaea stagnalis</i> . c) Example of bursting activity in the PD neuron from <i>Carcinus maenas</i>	5
1.5	Representation of synapse types. Left. Illustration of an electrical synapse between two cells and diagram of a gap junction (Adapted from Wikimedia Commons). Right. Illustration of the structure of a chemical synapse (Adapted from Wikimedia Commons)	6
1.6	Left. Gastric and pyloric CPG connection scheme of crustacean, probably the best known circuits in neuroscience research (Huerta et al., 2001). Right. Conectome in human brain rendered from 20 subjects showing the complexity in the connectivity of a larger network (By Andreashorn CC BY-SA 4.0).	6

LIST OF FIGURES

1.7 Illustration of the sequential feeding process at different time scales in <i>Lymnaea stagnalis</i>	8
1.8 Superimposition of bursts at different time instants aligned by the first spike in an intracellular recording of an LP neuron in the pyloric CPG of <i>Carcinus maenas</i>	9
1.9 Neural and network models classified by biophysical detail, structure modeled and size of the network. Figure adapted from Fig. 2 in Gleeson et al. (2019) under Creative Commons CC-BY license. Models are classified by their level of biophysical detail (the less specific ones are placed at the bottom of the y-axis), by the size of the network modeled (x-axis), and by the brain-structure they model (represented in colored boxes). The shape of the box also classifies the model in network model or individual cell model. The spiral, added as a new model category, indicates the ability of the model to produce chaotic activity without external perturbations, i.e., the ability to reproduce intrinsic variability. Although the figure does not contain all model approaches, it illustrates key milestones in neuronal modeling.	11
1.10 a) Electrical circuit describing the membrane voltage in a conductance-based neuron model. b) Electrical circuit representing the scheme for intracellular recordings.	12
1.11 Simulations of two distinct action potential types: no shoulder (a) and shoulder shaped spike (b), described by equations in Hodgkin and Huxley (1952) and Vavoulis et al. (2010), respectively.	14
1.12 a) Photograph of <i>Lymnaea Stagnalis</i> . b) Representation of <i>L. stagnalis</i> life cycle. Figure 2A from Fodor et al. (2020) (Creative Commons license).	18
2.1 Ilustración de Ramón y Cajal que muestra el posible curso de información en la retina de la abeja (Ramón y Cajal & Sánchez, 1915) (Disponible bajo la licencia: CC BY 4.0).	22
2.2 Representación de las fases secuenciales y terminología de un potencial de acción junto con las corrientes que lo generan (I_K, I_{Na} and $I_{leakage}$). En cada una de estas fases de la generación del potencial de acción, se activan secuencialmente diferentes canales iónicos, por ejemplo, el canal de sodio está involucrado durante la fase de despolarización y su actividad disminuye a medida que el canal de potasio se activa principalmente en la fase de repolarización.	24

LIST OF FIGURES

2.3 Ejemplos de diferentes formas de onda de potenciales de acción. Representación de dos registros de dos células diferentes en el ganglio parietal derecho de <i>Lymnaea stagnalis</i> . a) <i>Spike</i> con forma de onda simétrica; b) <i>Spike</i> con forma de onda con "hombro".	24
2.4 Representación de dos ejemplos de diferentes actividades neuronales de disparo. a) Dos registros intracelulares simultáneos en <i>Lymnaea stagnalis</i> mostrando disparo tónico a dos frecuencias diferentes. b) Ejemplo de actividad en ráfagas en un registro intracelular en <i>Lymnaea stagnalis</i> . c) Ejemplo de actividad en ráfagas en un registro intracelular en la neurona PD en <i>Carcinus maenas</i>	25
2.5 Representación de tipos de sinapsis. Izquierda: Ilustración de una sinapsis eléctrica entre dos células y diagrama de la unión gap (Adaptado de Wikimedia Commons). Derecha: Ilustración de la estructura de una sinapsis química (Adaptado de Wikimedia Commons).	26
2.6 Izquierda: Esquema de la conectividad del CPG pilórico y gástrico del crustáceo, probablemente uno de los circuitos mejor conocidos en neurociencia (Huerta et al., 2001). Derecha: Conectoma en el cerebro humano renderizado a partir de 20 sujetos que representa una red de conexiones más compleja (Por Andreashorn - Trabajo propio, CC BY-SA 4.0).	27
2.7 Ilustración del proceso de alimentación secuencial en diferentes escalas de tiempo en <i>Lymnaea stagnalis</i>	29
2.8 Superposición de ráfagas en diferentes instantes de tiempo alineadas por el primer <i>spike</i> en la ráfaga para grabaciones intracelulares de una neurona LP en el CPG pilórico.	30

LIST OF FIGURES

2.9 Modelos neuronales y de red clasificados por su nivel de detalle biofísico (los menos específicos están situados en la parte inferior del eje y), por estructura modelada (color de las cajas) y por el tamaño de la red (eje x). Figura adaptada de la Fig. 2 (Gleeson et al., 2019) bajo licencia Creative Commons CC-BY. Los modelos están clasificados por el detalle biofísico, siendo los modelos en la parte inferior los menos específicos; por el tamaño de la red modelada, de izquierda a derecha, una célula a cientos de células; y por la estructura cerebral que modelan, representada en cajas de colores. La forma de la caja también clasifica en modelo de red o célula individual. La espiral representa actividad caótica y ha sido incluida modificando la figura original. Una espiral en la caja indica la capacidad del modelo para producir actividad caótica sin alteraciones externas, es decir, reproducir variabilidad intrínseca espontánea. Aunque la figura no contiene todos los enfoques de modelos, ilustra hitos clave en el modelado neuronal.	32
2.10 a) Circuito eléctrico que describe el potencial de membrana en un modelo de neurona basado en conductancia. b) Circuito eléctrico que representa el esquema para registros intracelulares.	33
2.11 Simulaciones de dos tipos distintos de potencial de acción: sin hombro (a) y con forma de hombro (b), descritos por las ecuaciones en Hodgkin and Huxley (1952) y Vavoulis et al. (2010), respectivamente.	35
2.12 a) Fotografía del animal <i>Lymnaea stagnalis</i> . b) Representación del ciclo de vida de <i>L. stagnalis</i> . Figura 2A de Fodor et al. (2020) (Creative Commons license).	39
4.1 Neural system of <i>Lymnaea stagnalis</i> . a) Diagram of the neural system labeled for all ganglia. b) Top panel: photograph of the buccal ganglia. Bottom panel: photograph of the two parietal ganglia and visceral ganglion.	48
4.2 Example of fabrication of a sharp micro-electrode glass in a pipette puller.	50

LIST OF FIGURES

4.3 Panel (a). Ionic channel distribution in the two-compartment description for the individual neurons in the Vavoulis et al. (2007) model used in this study. At the soma: I_{ACh} , acetylcholine ionic channel; I_{NaL} , slowly inactivating sodium ionic channel; I_T , low-threshold calcium current; I_{inj} , injected current; $I_{L,S}$, leakage current in the soma; I_{syn} , synaptic current. At the axon: I_{NaT} , fast inactivating sodium current; I_K , delayed rectifier potassium current; $I_{L,A}$, leakage current in the axon. The color for each I_X current represents the CPG neuron that includes it at the soma, N1M, N2v and N3t, respectively. Panel (b). Connection scheme for the <i>Lymnaea stagnalis</i> feeding CPG circuit model. The colors indicating each neuron in the circuit match those in the representation of their corresponding somatic membrane potential traces in section 4.4.1.	53
4.4 Triphasic feeding rhythm as produced by the circuit CPG model described in Fig. 4.3. In this simulation, i_{inj} values applied to each neuron are 8.5, 6, 2 and 0 mV, respectively.	53
4.5 Simulation of the CGC-model representing the voltage dynamics during an action potential and the corresponding ionic currents defined in the model ($I_{NaP}, I_{NaT}, I_A, I_D, I_{LVA}, I_{HVA}$). The units in the y-axis are specified in the legend.	55
4.6 Illustration of the laser beam focused on a neuron in the right parietal ganglia.	60
4.7 Image of the CW-NIR laser stimulation setup. On the left, there is the micromanipulator with the electrode and the glass micropipette for the intracellular recording. In the center of the image under the microscope lens, there is the preparation of the CNS of <i>Lymnaea stagnalis</i> . On the right side, the laser fiber is attached to the collimator and at the end of the holder there is a lens to focus the laser beam. This is also attached to a micromanipulator for a precise focusing.	60
5.1 Example of robust sequential bursting dynamics in CPGs. Representation of burst duration in three neurons in a CPG model, the sequential activation of the three neurons produces cycles (indicated as gray boxes in the sequence). The connections between the three neurons are represented in the diagram on the right side of the panel.	62

LIST OF FIGURES

5.2 Panel A. Individual neuron sequence interval definitions. Each BD label represents the burst duration, defined as the time interval from the first spike to the last spike in the neuron's burst. Period was measured as the interval from the first spike of N1 burst to the first spike of the next N1 burst, covering three phases in relation to the activity of the other neurons. IBI represents the interburst interval, defined as the time from the last spike of a neuron's burst to the first one of the next burst in the same neuron. Panel B. Definition of intervals involving pairs of neurons. NXNY interval represents interval from NX start to NY start. NXNY delay represents interval from NX end to NY start. Period was measured from N1 start to N1 start, covering the three phases of the CPG rhythm.	64
5.3 Illustration of the CPG activity when a current ramp i_{inj} is applied to N3t. Variability in the sequence intervals was induced by applying two consecutive ramps as the one shown in this Figure to a specific cell. The ramp current was applied only to one of the cells at a time.	65
5.4 Hybrot experiment design Top panel: illustration of the experimental setup for the FLC-Hybrot implementation: A) Computer controlling the closed-loop interaction between the living CPG and the robot. B) DAQ and signal amplifiers; C) Microscope; D) Testing track with light and shadow regions. Middle panel: Detail of the elements of the setup: E) Hexapod robot, receives the neural information from the computer and sends back the sensory feedback through a Bluetooth connection; F) <i>In vitro</i> pyloric CPG preparation with three electrodes to: (1) record extracellular activity from the nerve which includes the activity from the LP neuron (blue) (2) to record intracellular activity from the PD neuron (green) and (3) to introduce the feedback current into a PD neuron (red). The signal recorded from the electrode is received through the DAQ device. Bottom panel: detail of the elements of the robot and the preparation. PD neuron (intracellular recording, green trace) and LP neuron (extracted from the extracellular recording, blue trace) the activity is analyzed online by the computer and used to modulate the movement of the robot. Meanwhile, robot's light sensor detects the presence of light or shadow over it and the Arduino board sends that information to the computer, which injects feedback current into the PD neuron (red trace) accordingly.	71

LIST OF FIGURES

5.5 N1M stimulation: a) Box-plots of the sequence intervals under N1M neuron stimulation. b) Interval correlations to period for N1M-driven simulation. First row: Burst durations. Second and third row: Two-neuron <i>intervals</i> . Forth and fifth row: Two-neuron <i>delays</i> . Linear relationships are quantified by the R^2 values of the linear regression.	73
5.6 N3t stimulation: a) Box-plots of the sequence intervals under N3t neuron stimulation. b) Interval correlations to Period for N3t-driven simulation. First row: Burst durations. Second and third row: Two-neuron <i>intervals</i> . Forth and fifth row: Two-neuron <i>delays</i> . Linear relationships are quantified by the R^2 values of the linear regression.	75
5.7 SO stimulation: a) Box-plots of the sequence intervals under SO modulatory neuron stimulation. b) Interval correlations to Period for SO-driven simulation. First row: Burst durations. Second and third row: Two-neuron <i>intervals</i> . Forth and fifth row: Two-neuron <i>delays</i> . Linear relationships are quantified by the R^2 values of the linear regression.	76
5.8 N1M stimulation: Pairplot with all possible combination between time intervals within a cycle.	78
5.9 N3t stimulation: Pairplot with all possible combination between time intervals within a cycle.	79
5.10 SO stimulation: Pairplot with all possible combination between time intervals within a cycle.	80
5.11 a) Representation of the intervals for each cycle when considering three or two phases (left and right, respectively). b) Interval correlations to period for SO-driven simulation for three phases. First row: Burst duration. Second and third row: Two-neuron intervals. Forth and fifth row: Two-neuron delays (data shown in Fig. 5.5). c) Interval correlations to period for N1M-driven simulation for two phases. First row: Burst duration. Second row: Two-neuron <i>intervals</i> . Third row: Two-neuron <i>delays</i> . For b) and c) the linear relationships are quantified by the R^2 values of the regression.	82

LIST OF FIGURES

LIST OF FIGURES

5.16 Spontaneous case 3: Panel of interval distributions and dynamical invariants for the three phases in the CPG for spontaneous activity. a) Voltage traces for the intracellular recording analyzed for this panel. b) Representation of the time-intervals described. c) Duration of each time interval (<i>y – axis</i>) at each cycle. d) Box-plot with the variability distribution of the duration of each time-interval. e) Time-intervals duration against the period for NX-Burst duration (blue), NXNY-Interval (green) and NXNY-Delay (red).	90
5.17 Spontaneous activity summary: Panel of the pairplots for all possible combinations between the time intervals defined for two phases (N1 and N3) in the CPG recordings for the three examples of spontaneous activity recordings.	91
5.18 Representation of recordings of the spontaneous activity with lapses of SO modulation. The parts of the recording with yellow background highlight when the activity was modulated by the SO neuron. From top to bottom: intracellular recording of a neuron from the B4 cluster, B3 motoneuron, B1 motoneuron, B8 motoneuron, and N1M interneuron.	92
5.19 SO neuron driven spontaneous activity: Panel of interval distributions and dynamical invariants for the two phases in the CPG for spontaneous activity driven by SO neuron. a) Voltage traces for the intracellular recording analyzed for this panel. b) Representation of the time-intervals described. c) Duration of each time interval (<i>y – axis</i>) at each cycle. d) Box-plot with the variability distribution of the duration of each time-interval. e) Time-intervals duration against the period for NX-Burst duration (blue), NXNY-Interval (green) and NXNY-Delay (red).	94
5.20 Spontaneous activity when the SO-driven modulation ceases: Panels illustrate the interval distribution and dynamical invariants for the two phases in the CPG during spontaneous activity without SO modulating the rhythm. a) Voltage traces for the intracellular recording analyzed for this panel. b) Representation of the time-intervals described. c) Duration of each time interval (<i>y – axis</i>) at each cycle. d) Box-plot with the variability distribution of the duration of each time-interval. e) Time-intervals duration against the period for NX-Burst duration (blue), NXNY-Interval (green) and NXNY-Delay (red).	95

LIST OF FIGURES

<p>5.21 Spontaneous SO neuron modulation restarts: Panel of interval distributions and dynamical invariants for the two phases in the CPG for spontaneous activity driven by SO neuron. a) Voltage traces for the intracellular recording analyzed for this panel. b) Representation of the time-intervals described. c) Duration of each time interval (<i>y – axis</i>) at each cycle. d) Box-plot with the variability distribution of the duration of each time-interval. e) Time-intervals duration against the period for NX-Burst duration (blue), NXNY-Interval (green) and NXNY-Delay (red).</p> <p>5.22 SO neuron stimulation: Panel of interval distributions and dynamical invariants for the two phases in the CPG for activity driven by SO neuron induced by its electrical stimulation. a) Voltage traces for the intracellular recording analyzed for this panel. b) Representation of the time-intervals described. c) Duration of each time interval (<i>y – axis</i>) at each cycle. d) Box-plot with the variability distribution of the duration of each time-interval. e) Time-intervals duration against the period for NX-Burst duration (blue), NXNY-Interval (green) and NXNY-Delay (red).</p> <p>5.23 Panel of the pairplots for all possible combinations between the time intervals for two phases in the CPG recordings for (left) spontaneous SO rhythm modulation and (right) the induced SO rhythm modulation.</p> <p>5.24 MLN stimulation: Panel of interval distributions and dynamical invariants for the three phases in the CPG under MLN Medium Lip Nerve (MLN) stimulation. a) Voltage traces for the intracellular recording analyzed for this panel. b) Representation of the time-intervals described. c) Duration of each time interval (<i>y – axis</i>) at each cycle. d) Box-plot with the variability distribution of the duration of each time-interval. e) Time-intervals duration against the period for NX-Burst duration (blue), NXNY-Interval (green) and NXNY-Delay (red).</p> <p>5.25 MLN stimulation: Pairplot with all possible combinations in the intervals.</p> <p>5.26 CV1a driven case 1: Panel of interval distributions and dynamical invariants for the two phases in the CPG under CV1a stimulation. a) Voltage traces for the intracellular recording analyzed for this panel. b) Representation of the time-intervals described. c) Duration of each time interval (<i>y – axis</i>) at each cycle. d) Box-plot with the variability distribution of the duration of each time-interval. e) Time-intervals duration against the period for NX-Burst duration (blue), NXNY-Interval (green) and NXNY-Delay (red).</p>	<p>96</p> <p>97</p> <p>98</p> <p>99</p> <p>100</p> <p>102</p>
--	---

LIST OF FIGURES

5.27 CV1a driven case 2: Panel of interval distributions and dynamical invariants for the two phases in the CPG under CV1a stimulation. a) Voltage traces for the intracellular recording analyzed for this panel. b) Representation of the time-intervals described. c) Duration of each time interval (<i>y – axis</i>) at each cycle. d) Box-plot with the variability distribution of the duration of each time-interval. e) Time-intervals duration against the period for NX-Burst duration (blue), NXNY-Interval (green) and NXNY-Delay (red).	103
5.28 CV1a driven case 3: Panel of interval distributions and dynamical invariants for the two phases in the CPG under CV1a stimulation. a) Voltage traces for the intracellular recording analyzed for this panel. b) Representation of the time-intervals described. c) Duration of each time interval (<i>y – axis</i>) at each cycle. d) Box-plot with the variability distribution of the duration of each time-interval. e) Time-intervals duration against the period for NX-Burst duration (blue), NXNY-Interval (green) and NXNY-Delay (red).	104
5.29 CV1a driven case 4: Panel of interval distributions and dynamical invariants for the two phases in the CPG under CV1a stimulation. a) Voltage traces for the intracellular recording analyzed for this panel. b) Representation of the time-intervals described. c) Duration of each time interval (<i>y – axis</i>) at each cycle. d) Box-plot with the variability distribution of the duration of each time-interval. e) Time-intervals duration against the period for NX-Burst duration (blue), NXNY-Interval (green) and NXNY-Delay (red).	105
5.30 Panel of the pairplots for all possible combinations between the time intervals for two phases (N1 and N3) in the CPG recordings for the four examples of induced CV1a neuron modulation recordings.	106
5.31 Summary of the results discussed for different rhythm modulations. Each pairplot shows all possible interval combinations, the upper right connection diagram shows the neuron stimulated for each case. The examples shown here correspond to (from left to right and top to bottom): Spontaneous activity example 1 (Fig. 5.14), SO induced modulation (Fig. 5.22), MLN stimulation (Fig. 5.24) and CVa1 stimulation example 1 (Fig. 5.26).	108

LIST OF FIGURES

5.32 Absence of dynamical invariants between non-overlapping intervals in consecutive cycles. For each pairplot, the lower triangle represents interval relationships in the same cycle and the upper triangle represents relationships between intervals of one cycle against intervals of the next cycle. The examples shown here correspond to (from left to right and top to bottom): Spontaneous activity example 1 (Fig. 5.14), SO induced modulation (Fig. 5.22), MLN stimulation (Fig. 5.24) and CVa1 stimulation example 1 (Fig. 5.26).	110
5.33 Example of variability in waveforms from intracellular recordings of the LP and PD neurons in the pyloric CPG.	111
5.34 Example of bursts with no waveform variability in the Ghigliazza and Holmes (2004) model from the ODEs neurons in the insect locomotion CPG and in the N1M neuron model from Vavoulis et al. (2007) with no ramp stimulation in the CPG circuit. The equations for both models can be found in Secs. 5.2.4 and 4.4.1, respectively.	112
5.35 Example of variability in waveforms from model simulation of neuron from Nowotny et al. (2008) model in chaotic mode and N1M neuron from Vavoulis et al. (2007) under current stimulation in the CPG circuit. The equations for both models can be found in Secs. 5.2.4 and 4.4.1, respectively.	112
5.36 Representation of the FLC-Hybrot paradigm design. Neural dynamics from a functional living CPG circuit are recorded online and used to coordinate the robot movement in real-time. Activity from the PD neuron is recorded intracellularly (green trace), while the LP bursts are extracted from the nerve's extracellular signal (blue trace). This robot walks through a trial track with interspersed light and shadow regions. When the robot's light sensor detects that it is located under a shadow, it sends feedback current to the living circuit. CPG dynamics change as a reaction to the injected current, thus modifying the robotic locomotion. The following video shows an example of this experiment https://youtu.be/ny2dJGbG8lo	114

LIST OF FIGURES

5.37 Flexible hybrot adaptation to environmental changes when noticed by the robot sensors and associated coordinated locomotion. When the robot entered a shadow section, it sent sensory feedback to the living CPG in the form of positive electrical current (red trace). Blue and green traces are recordings of the extracellular and intracellular (PD neuron) activity of the circuit and display the change caused by the feedback current injection in the PD neuron, slowing down the CPG rhythm. The oscillatory movement of the robot legs is represented in the brown trace and it can be observed that a variation in the CPG rhythm leads to a change in the robotic locomotion, modifying both the period and the amplitude of the oscillation.	115
5.38 Left: dynamical invariant present in the living CPG activity during the validation test, represented as a cycle-by-cycle linear relation between the LP neuron bursting period and the LPPD interval. Right: dynamical invariant present in the FLC-Hybrot locomotion during the validation test, represented as a cycle-by-cycle linear relation between its legs' oscillation period and amplitude. The dynamical invariant property is effectively translated from the living CPG to the robot locomotion, encoded as: Robot period = LP period, Robot amplitude = LPPD interval * factor.	116
6.1 CW-NIR laser stimulation protocol sequence: Control, laser stimulation and recovery.	124
6.2 Activity-dependent protocol scheme. Neurons were recorded intracellularly and their voltage signals were processed in real-time with the RTXI software. Using the spike prediction algorithms, the shutter was triggered at the desired action potential phase illuminating the neurons.	125
6.3 Examples of illumination offset, defined as the time interval from the end of the illumination to the peak of the spike.	126
6.4 Representation of waveform shape's metrics: a) Spike duration at half width. b) Spike amplitude between the maximum and minimum voltage values. c) Depolarization slope at half width. d) Repolarization slope at half width.	127
6.5 Open-pipette temperature estimation method. Each row in the panel represents pulsed and continuous current delivery for the estimation, respectively. For both examples: left column, temperature and voltage relation. Right column filtered mean of voltage recordings from short illumination intervals in the pipette.	129

LIST OF FIGURES

- 6.6 Effect of sustained CW-NIR laser stimulation on the spike waveform for two distinct neuron types. For all panels: control, laser and recovery are color coded in blue, red and green, respectively. Panel A. Characterization of no shoulder shape type neuron. Panel B. Characterization of shoulder shape type neuron. Ai) and Bi) Superimposition of spike waveforms in a single trial recording corresponding to a symmetrical and shoulder spike neuron, respectively. The spikes were aligned to the peak for the x axis and to the onset for the y axis, the mean is depicted in darker colors. Aii) and Bii) barcharts quantify the change using the difference from laser to control normalized by the mean control value for metrics: duration, depolarization and repolarization slopes, and amplitude. Panel C, violin plots representing the variation of the experiments with respect to the control ($N = 23$) for shoulder and symmetrical types together. For each metric of the waveform, the control, laser and recovery recordings are normalized to the first control. From left to right: duration, depolarization slope, repolarization slope and amplitude. Asterisks over the violins indicate that the metric change was highly significant (Bonferroni correction, $(\rho < 0.01/4)$, see Statistical Analysis Sec. 6.2.4 in Materials and Methods). 131

6.7 Segregation of data into shoulder and symmetrical neural types. Violin plots for the four metrics -duration, depolarization slope, repolarization slope and amplitude- grouped by control, laser and recovery trials. Spikes metrics are normalized to the first control, as in Fig. 6.6 panel C. 133

6.8 Firing rate and interspike interval (ISIs) analysis for the CW-NIR laser stimulation. A. Absolute firing rate in all experiments ($N=23$). B. Absolute firing rate for cases from the experiments in A with no change during laser illumination ($N=11$); C. Absolute firing rate for experiments from A showing an increase in the firing rate ($N=12$); D. ISI histograms for control, laser and recovery for each experiment. Cases showing increased excitation in their firing rate (sample in panel C) when illuminated by the CW-NIR laser are highlighted in a red square. 135

6.9 Microscope image of the three cases of illumination in electrically coupled neurons. From left to right: illumination of VD1 neuron, RPD2 neuron and the gap junction of their electrical coupling. The electrode recording each cell can be seen in these images, filaments approaching the cells from the bottom right and from the top left. 136

LIST OF FIGURES

- 6.10 Electrically coupled neurons illumination: superposition of the averaged waveform for control, laser and recovery in the three different illumination scenarios (three examples are shown for each case): spike waveforms of VD1 and RPD2 illuminating VD1 (left column); waveforms of VD1 and RPD2 illuminating RPD2 (middle column); and finally neuronal waveforms illuminating the gap junction (right column). Each plot follows the previous color code for control, laser and recovery: blue, red and green, respectively) 137
- 6.11 Water absorption for different wavelengths values. 138
- 6.12 Representation of the effect of sustained laser stimulation at 830nm at 90mW and 1450nm at 120mW. In terms of power density, the corresponding values are: 194.88 W/cm² and 315.78 W/cm², respectively. The left panel in each row is the superimposition of the spike waveforms aligned to the first point, during a control recording with no stimulation, a laser recording during the illumination at the specific wavelength and a recovery control, again with no stimulation. The four panels in each row correspond to the mean value for each trial of control, laser and recovery for the spike waveform metrics: duration, amplitude, depolarization and repolarization slopes. 139
- 6.13 Modeling study of the CW-NIR laser stimulation effects due to isolated biophysical changes that alter the spike waveform. Panels A, B, C and D: Superposition of spike waveforms in each model by modulating a single biophysical candidate. The background colors correspond to each simulated model. In Panel A, the capacitance is changed for the HH and CGC neuron models, and in the two compartments for the N3t neuron model. Panel B shows the spike waveforms changing the conductances of *Na* channel currents: I_{Na} from the HH-model, I_{NaP} and I_{NaT} , from the CGC-model. Panel C, displays the modulation of *K* conductances in ionic currents: I_K in the HH-model and I_D and I_A for the CGC-model (from left to right). Panel D shows the modification of the calcium current conductances in the CGC-model (I_{HVA} and I_{LVA}). Table in panel E represents the quantification of the changes in the spike metrics when tuning each parameter for every model. Each cell contains the waveform change normalized to the maximum. The color gradient represents similarity based on the standard deviation of the normalized experimental change. Dark purple corresponds to low similarity ($2\sigma_{MEC}$ or larger) and white to high similarity. The quantified experimental reference (MEC) is annotated in the first row of the table. . . 141

LIST OF FIGURES

6.14 Waveform change in the CGC-model due to ΔT temperature variation. Panel Ai) shows the spike waveform superposition for distinct ΔT values. Spikes are aligned to the initial value of each waveform. In panel Aii) the normalized change in the waveform is depicted for all metrics (duration, depolarization and repolarization slopes and amplitude). Panel B shows the change in response to temperature variation from 1 to 10°C ($Q_{10} = 3$) in the normalized metrics.	146
6.15 Simulation of the effect of individual channels on the spike waveform under temperature modulation. Panel A.i) Waveform modulation in the CGC-model excluding temperature dependency in one channel at a time, from left to right: I_{NaT} , I_A , I_{HVA} , I_{LVA} , I_D respectively. Panel A.ii) Waveform modulation in the CGC-model with temperature dependency only in one channel at a time, from left to right: I_{NaT} , I_A , I_{HVA} , I_{LVA} and I_{NaP} , respectively. Note that I_{NaP} is not in panel A.i) and neither is I_D in A.ii), as for these two particular simulations there was no spike generation. Panels B.i) and B.ii) show the quantification of the waveform change for $\Delta T = 5^\circ\text{C}$ in duration, depolarization slope, repolarization slope and amplitude for all channels in panel A. Both figures include, as reference, the experimental mean and STD (shown in black) and, for case B.ii) (only one channel at a time), the quantification when all channels have the same temperature dependency (all with $\Delta T = 5^\circ\text{C}/3^\circ\text{C}$, data used in Fig. 6.14) is depicted in light and dark red bars.	147
6.16 Simulation of the effect of CW-NIR laser in the CGC-model. Stimulating only during the depolarization or only during repolarization phases for first and second rows respectively.	150
6.17 Results in the spike waveform for the simulation of the effect of CW-NIR laser in the CGC-model. Stimulating only during the depolarization (light green trace) or repolarization (dark green trace) phases and simulating a constant change value (red trace).	150

LIST OF FIGURES

- 6.18 Study of the laser effect at different stages of the spike waveform with an activity-dependent stimulation protocol. The panels quantify the change induced by the laser stimulation at distinct illumination offsets, –time intervals from the end of the illumination to the peak of the spike–. Top panel shows a spike waveform from the experiment as a time reference for the offset –time 0 corresponds to the spike peak. Boxplots represent the difference of each metric with respect to the control. All illumination intervals, pictured in the blue boxes, had the same duration of 58 ms and spikes were grouped by the illumination offset. Recovery and continuous laser reference are also shown in green and red boxes at left and right in the figure, respectively. The spike metrics selected here were duration, depolarization and repolarization slopes, –second, third and fourth rows, respectively. 152
- 6.19 Normalized change for grouped values of spike duration, depolarization and repolarization slopes at distinct illumination offsets in the activity-dependent stimulation protocol. Each value in each group was normalized to the mean of its corresponding day controls as minimum value and the mean of the continuous laser recordings for each day as the maximum value. The maximum value for each metric is marked by a black circle. 153

LIST OF FIGURES

7.1	Schematic summary of the results presented in this work. In the feeding CPG of <i>Lymnaea stagnalis</i> , we explored in (1) experimental and (2) computational data the presence of dynamical invariants (Secs. 5.4 and 5.3), showing strong linear relations in sequence intervals and associating them to the possible functional role of this dynamical phenomenon. The experimental results were complemented by exploring the translation of (3) cycle-by-cycle invariant intervals into effective robot movement maintaining these strong linear relations (Sec. 5.6). We also showed the (4) importance of reproducing the functional variability in computational models (Sec. 5.5). As a way to modulate neural dynamics, we characterized the effect of the CW-NIR laser in single neurons in sustained and activity dependent illumination protocols. We showed that (5) the spike waveform is modified during the laser illumination, as well as the firing rate (Sec. 6.4), and discussed the effect at (6) different wavelengths (Sec. 6.4.4). We showed also (7) preliminary results in the stimulation of a minimal circuit (Sec. 6.4.3). The computational model analysis (8) revealed the combination of candidates to reproduce the effect and the importance of the role of temperature (Sec. 6.5). (9) The activity-dependent protocol (10) allowed to assess the laser effect at different phases of the action potential generation (Sec. 6.6).	165
B.1	N1M stimulation: Pairplot illustrating the invariant relation resetting within consecutive cycles. Lower triangle represents the relationships between intervals within the same cycle. Upper triangle represents the relations between intervals of one cycle and those in the next one.	199
B.2	Spontaneous case 1: Panel of interval distribution and dynamical invariants for the three phases in the CPG for spontaneous activity.	200
B.3	Spontaneous case 2: Panel of interval distribution and dynamical invariants for the three phases in the CPG for spontaneous activity.	201
B.4	Spontaneous case 3: Panel of interval distribution and dynamical invariants for the three phases in the CPG for spontaneous activity.	202
B.5	CV1a driven case 4: Panel of interval distribution and dynamical invariants for the three phases in the CPG under CV1a stimulation.	203
B.6	Table of R^2 values for the linear regression between the period and each interval for all experimental recordings discussed in this section.	203

CHAPTER 1

Introduction and State of the Art

1.1 Neuroscience, neurons and their dynamics

Neuroscience is a wide and challenging field in science. It faces crucial questions, such as the study of the neural mechanisms underlying brain activity, how can those mechanisms outcome as human cognition or behavior, how information is sensed, processed, created and converted into action through neural activity, how are neural diseases generated and how can we detect and treat them. These questions and many more have been open problems that have intrigued the neuroscience community since the first steps in this field. Neuroscience was born as a modern discipline from anatomy, physiology, biochemistry and biophysics. As a broad field, it is approached from distinct perspectives and it is usually referred to by its subfields, e.g. Neurobiology, Neuropharmacology, Clinical Neuroscience, Developmental Neuroscience, Systems Neuroscience, Cognitive Neuroscience, Computational Neuroscience, Neurotechnology, etc. All these fields aim to explain or repair brain function either as a whole or in parts. They use different techniques and approaches where some of which give rise to entirely new fields, like Neuroimaging.

We cannot think or discuss about neuroscience without highlighting the work by Santiago Ramón y Cajal, crucial in the firsts steps on the understanding the brain (Ramón y Cajal, 1899; De Carlos & Borrell, 2007; Delgado-García, 2015; de Castro & Merchán, 2016; de Castro, 2019). The idea of the "neuron doctrine" boosted the study of the brain, explaining and describing the structure of individual cells called *neurons* that are able to connect and thus communicate by *synapses*. Figure 1.1 shows one of Cajal's drawings describing the bee retina with arrows indicating a possible information flow.

The brain is a complex system that we can study from many different prisms. In this thesis, we follow a bottom-up approach. So we will analyze experimentally and theoretically the neural activity at ionic channels and small circuits (with few synapses). Moreover, we will follow a Neurocomputational

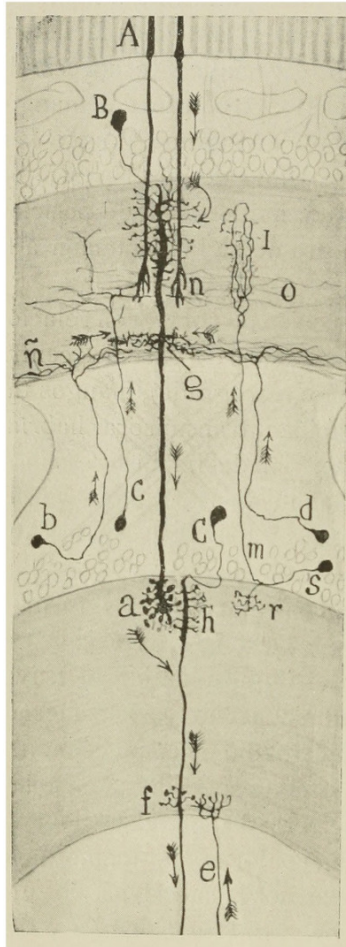


Figure 1.1: Illustration by Ramon y Cajal intended to show the probable course of information flow in the bee retina (Ramón y Cajal & Sánchez, 1915) (Available via license: [CC BY 4.0](#)).

perspective based on hierarchical sequential information processing, which will be defined in detail in subsection 1.3. In the following lines we will approach the basis of neural activation from a computational perspective necessary for the reading flow of this document. We will focus in the dynamics of voltage that neurons produce and how that inter-operates to give rise to neural activity.

1.1.1 Neuronal dynamics

Neurons are cells morphologically composed by dendrites, where the connections from other neurons are received through synapses, a soma or cellular body (where information is typically integrated) and an axon (where the information is conveyed as output). Since neurons are the cells that present the largest diversity in morphology, this description does not apply to all neuronal types but serves to start highlighting the importance of spatial scales in the nervous system.

Neuronal electrical activity is often described in terms of the evolution of membrane voltage caused by the flow of ionic channels between the inside and outside of the cell (Kandel et al., 2012). The

characteristic fast change in the membrane voltage when a neuron fires an output signal is called an action potential or a spike. They are often seen as the minimal pieces of information for reception, processing and transmission carried out by neurons. A more concrete definition of spike could be "an abrupt and transient change of membrane voltage that propagates to other neurons via a long protrusion called an axon" (Izhikevich, 2007). Thus, when no inputs are received, the membrane potential of a neuron is negative and it is called resting potential. When this potential is altered by an input that makes the voltage increase, it is known as depolarization. After reaching a peak of voltage, typically a positive value of around 40mV, the potential starts decreasing again. When the potential is more negative than the resting potential, it is known as hyperpolarization. Figure 1.2 illustrates the sequential phases of the action potential generation.

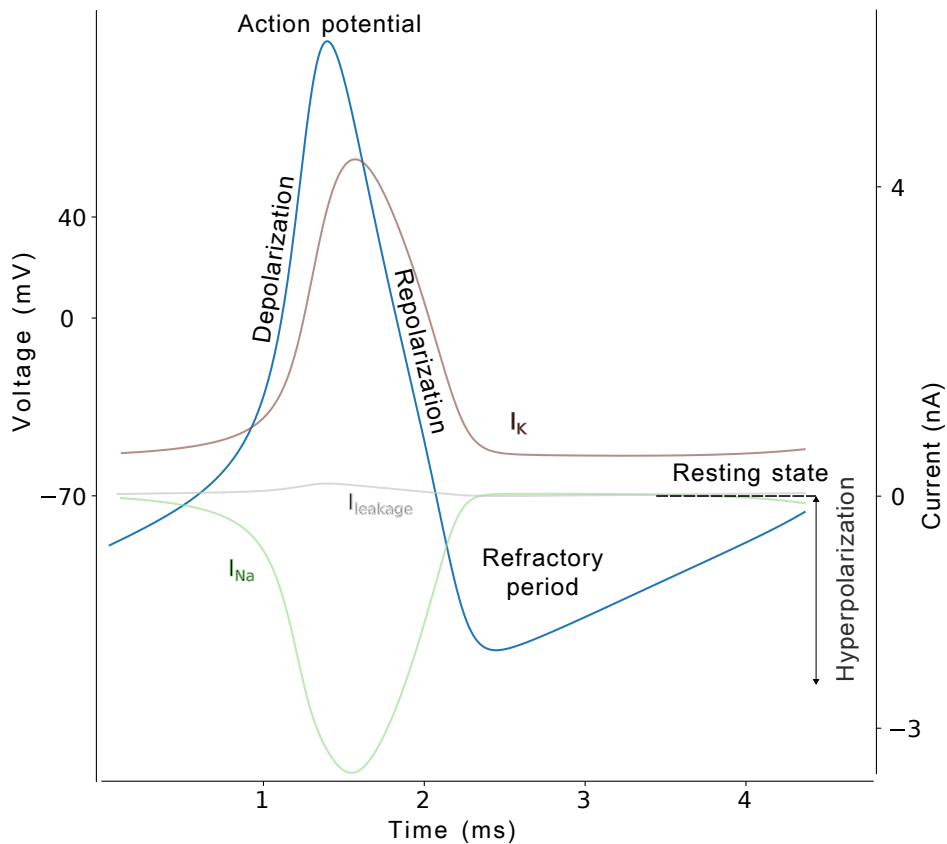


Figure 1.2: Representation of the sequential phases and terminology of an action potential, along with the ionic currents involved in its generation (I_K, I_{Na} and $I_{leakage}$). In each of these phases of the action potential generation, different ionic channels are activated sequentially, e.g. the sodium channel is involved during the depolarization phase and its activity decays as the potassium channel activates mostly in the repolarization phase.

The neural activity is generated by the flow of different ionic channels that counterbalance the voltage value generating the action potential (Koch, 1999). The membrane can be composed by different ionic channels, and their dynamics are conditioned by that combination and the possible synaptic

connections. These changes in dynamics can be manifested in different ways, but the most characteristic ones are the shape and temporal evolution of the action potential. For example, Figure 1.3 shows examples of two distinct action potentials with visible differences in their shape: Fig. 1.3a) presents a symmetrical shape, where depolarization and repolarization slopes are similar, whereas in Fig. 1.3a), there is a notable shoulder in the repolarization and its timescale is almost double in comparison with the example shown in Fig. 1.3a).

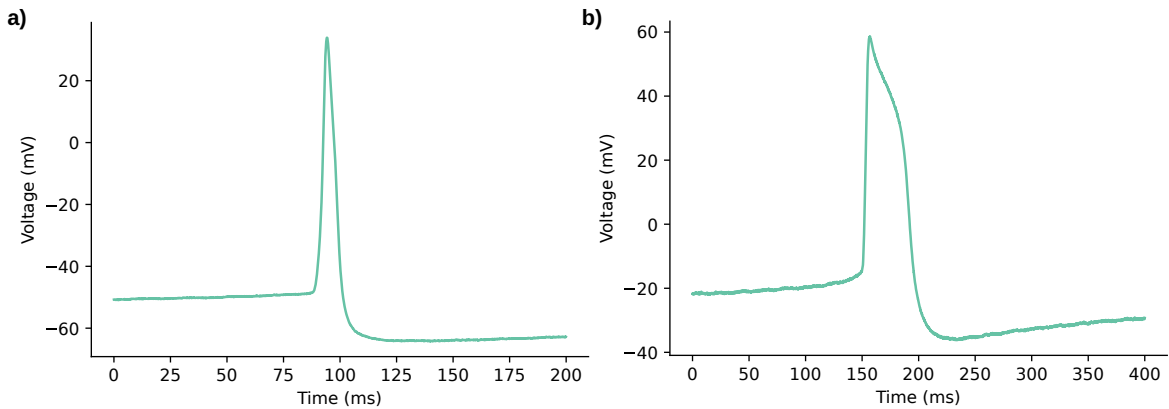


Figure 1.3: Examples of different spike shapes. Representation of two recordings from two different cells in the right parietal ganglion of *Lymnaea stagnalis*. a) Symmetrical shaped spike. b) Shoulder shaped spike.

If spikes are considered minimal pieces of information when coding in neural activity, their combination leads to new forms of aggregated information, known as bursts. Although there is not a fixed description of a burst, and depending on the animal and system a burst might look different (Russell & Hartline, 1978; Palmu et al., 2010; Lundqvist et al., 2016), there are some common features in bursts: they typically consist of a group of spikes (more than two) on top of a sustained depolarization, and these groups are separated by a hyperpolarized quiescent period called inter-burst interval (IBI). Figure 1.4 shows several examples of distinct neuronal activities observed in intracellular recordings. Depending on the specific cell and circuit, neurons can present tonic firing at different rates as shown in panel a), or bursting activity shown in panels b) and c).

Traditionally, neural codes have been studied with a focus on single spike activation, e.g., by the binarization of the activity (the neuron generates a spike or it does not). Burst can also be informative in terms of the neural activity, either as a whole piece of information or as a complex box of data itself: "bursts are a family of firing patterns that trigger physiological mechanisms not engaged by the same number of spikes in relative isolation" (Friedenberger et al., 2023). Bursts can be originated either by internal activation, mostly by calcium channels or/and by the synaptic dynamics involving the corresponding cell (inhibition/excitation), for an extended review see (Friedenberger et al., 2023). Bursting activity is very common in Central Pattern Generator circuits (CPGs) (Katz, 2016; Steuer

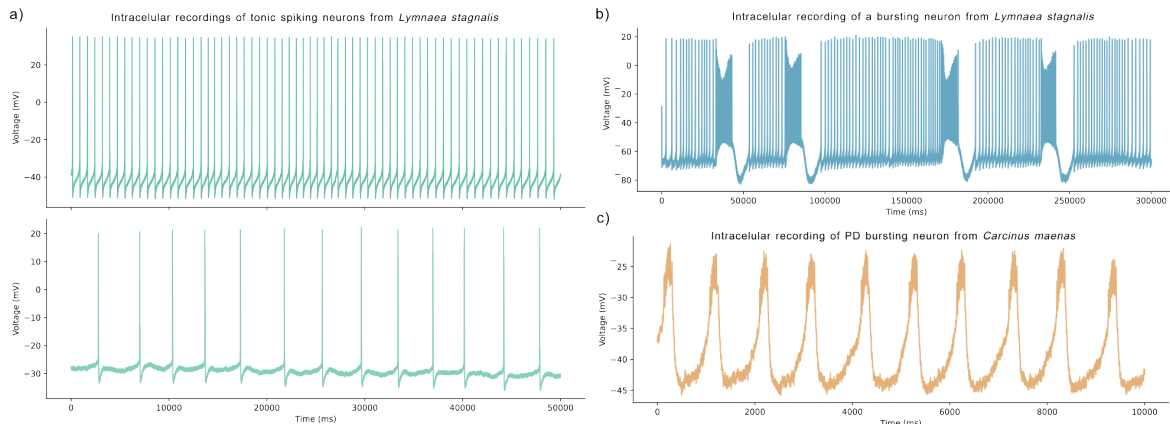


Figure 1.4: Examples of different types of neuronal spiking activity. a) Two simultaneous intracellular recordings in *Lymnaea stagnalis* showing tonic firing at two different frequencies. b) Example of bursting activity from *Lymnaea stagnalis*. c) Example of bursting activity in the PD neuron from *Carcinus maenas*.

& Guertin, 2018), which will be discussed in detail below and in chapter 5.

1.1.2 Network dynamics

Although analyzing the activity of a single neuron is important in terms of characterizing its dynamics, when talking about information processing and behavior, it is also crucial to study the overall circuit dynamics. A circuit of neurons is defined by nervous cells interconnected by synapses. There are two main types of synapses in the nervous system: electrical and chemical connections, see Fig. 1.5. The main difference between them relies on how the communication takes place. Chemical synapses occur through the mediation of *neurotransmitters*, where a presynaptic neuron releases these molecules that are bound to neuroreceptors to produce an alteration in the postsynaptic neuron. Thus, this connection is asymmetrical and unidirectional, whereas electrical synapses can implement symmetrical and bidirectional connections. In those synapses, the neurons are attached by a structure called *gap junction*, which "pipes" both neurons, in a tissue structure that constrains the leakage to the extracellular space. This communication allows electric charge to flow from one neuron to the other and is thus faster than the chemical synapses, which in comparison has no delay. The activity of electrically coupled is usually synchronous (Levitin & Kaczmarek, 2002).

Neurons can be connected by several types of both chemical and electrical synapses, and they involved in multiple circuits under the action of modulatory cells. Figure 1.6 illustrates two examples of circuits at the cellular and whole brain levels. In any nervous system, there are complex aggregates of networks of networks, which work at different time scales and can take part in multiple functionalities. This interconnection of networks, from a lower local level up to the whole brain, leads to organized sequential neural activity built out of sequences of sequences (Rabinovich et al., 2020).

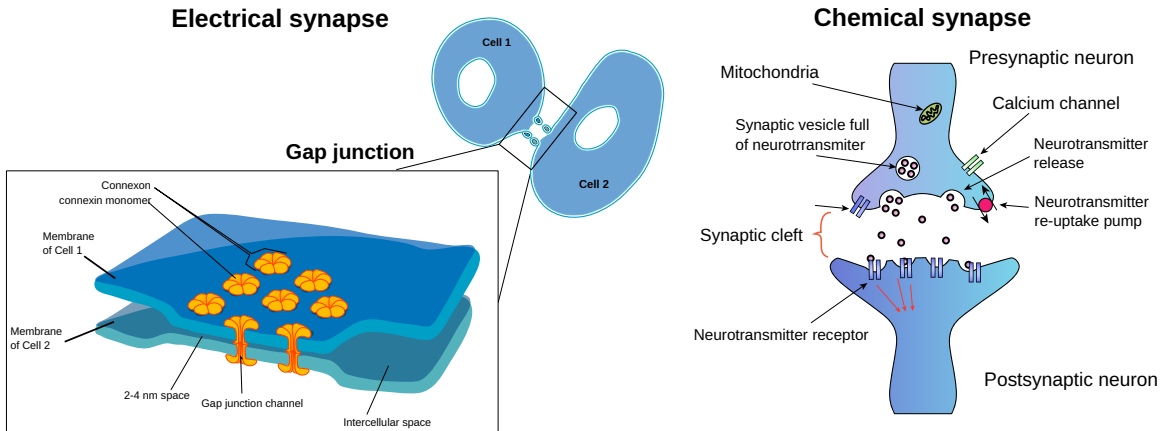


Figure 1.5: Representation of synapse types. Left. Illustration of an electrical synapse between two cells and diagram of a gap junction (Adapted from [Wikimedia Commons](#)). Right. Illustration of the structure of a chemical synapse (Adapted from [Wikimedia Commons](#))

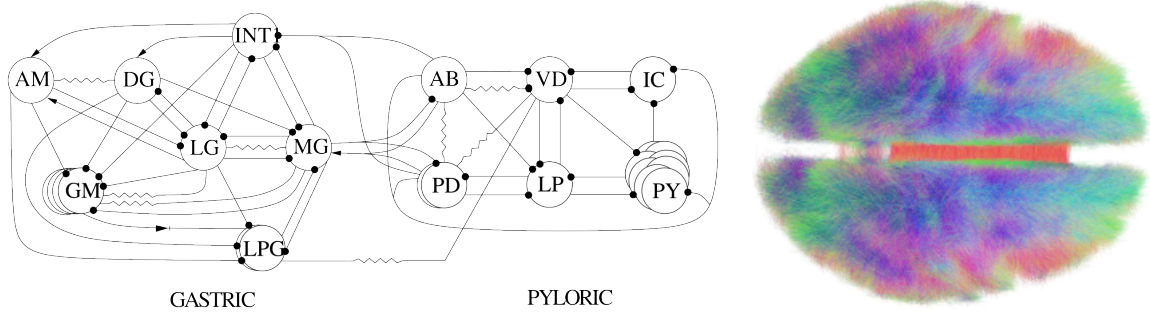


Figure 1.6: Left. Gastric and pyloric CPG connection scheme of crustacean, probably the best known circuits in neuroscience research (Huerta et al., 2001). Right. Conectome in human brain rendered from 20 subjects showing the complexity in the connectivity of a larger network (By Andreashorn [CC BY-SA 4.0](#)).

1.2 The sequential nature of neural dynamics

Brain dynamics can be described as sequences of interactions, from molecules and neurons to motor control and behavior, involving a coordinated hierarchy of temporal and spatial scales (Yuste et al., 2005; Kiebel et al., 2008; Rabinovich & Varona, 2018; Rabinovich et al., 2023), from ionic channel activations to sensory encoding, processing, and decision making. Its study reveals fundamental aspects of brain function and cognition, e.g., impulse transmission, executive function, spatial processing, memory, etc.

A common example of sequential processing is speech, where sequential patterns are present in the structure of phrases, as a sequences of sequences of syllables, words and silences (Kiebel et al., 2009). In this line, an extended case study is the birdsong, which has similarity to human's speech, as they involve sequences of coordinated sounds (Prather et al., 2017; Fishbein et al., 2019). Beyond speech, sequential processing is also present in motor control, from muscle activation to repetitive

CHAPTER 1: INTRODUCTION AND STATE OF THE ART

coordinated actions such as rhythmic tapping or music performance (Ding et al., 2017). Also, there are many important cognitive processes that rely in sequential mechanisms such as perception, memory, decision making, attention and emotion (Varona & Rabinovich, 2016; He, 2018; Rabinovich et al., 2020).

It is not clear yet how exactly the brain processes time. In contrast to the theory of a central clock that manages time for every behavioral task, the theory of a distributed time processing (Buonomano & Merzenich, 1995; Ivry, 1996) is well accepted. In this framework, especially in movement coordination, neural circuits manage sequential rhythmic activity. This is the case of Central Pattern Generators (CPGs), circuits of neurons with closed-topology that sequentially activate neurons and generate coordinated motor activity (Selverston et al., 2000). They are present in many systems, from insects to humans (Pearson, 1972; Marder & Bucher, 2001; MacKay-Lyons, 2002; Minassian et al., 2017). There are several key aspects that make these circuits an interesting case study. First, their neurons are organized in closed-topologies receiving all feedback from companion cells (Huerta et al., 2001). These circuits are able to maintain a rhythmic activity in an autonomous manner, typically by mutual inhibitory interactions (Katz, 2016). Secondly, their activity is flexible enough to adapt to changes in the environmental context, e.g., variations in the terrain while walking. Finally, they are present in many systems and in some of them there is a direct relationship between the activity of the neurons in the circuit and the motor movement that they produce. For example, in the case of the pyloric CPG in the crab *C. maenas*, they are in charge of the pylorus movement: the PD (pyloric dilator), LP (Lateral Pyloric) and PY (PYloric) neurons control the pylorus dilatation, and the closing and contraction of the rostral constrictor to move food in the digestive system (Moulins & Selverston, 1987; Selverston & Ayers, 2006).

The sequential activity in the brain goes from the sub-millisecond scale to days (the time scale of circadian rhythms (Mauk & Buonomano, 2004)). Figure 1.7 shows an illustrative example of the sequential nature of neural activity at different scales in the generation of coordinated motor activity in the feeding of a snail. At the sub-millisecond scale, there is a flow of ions that generate a sequence of ionic channel activation, which in the scale of milliseconds produces action potentials. Their combination in form of rhythmic bursts, activate the corresponding muscles at the scale of seconds and generate the necessary sequential movement to eat: open the mouth, rasp food and swallow, which is repeated along the day.

The study of the action potential dynamics and the interaction between ionic channels and synapses is crucial, since they are key elements in any brain process. The alteration of the dynamics of these channels at different levels can affect synaptic inputs/outputs, how neurons communicate and the

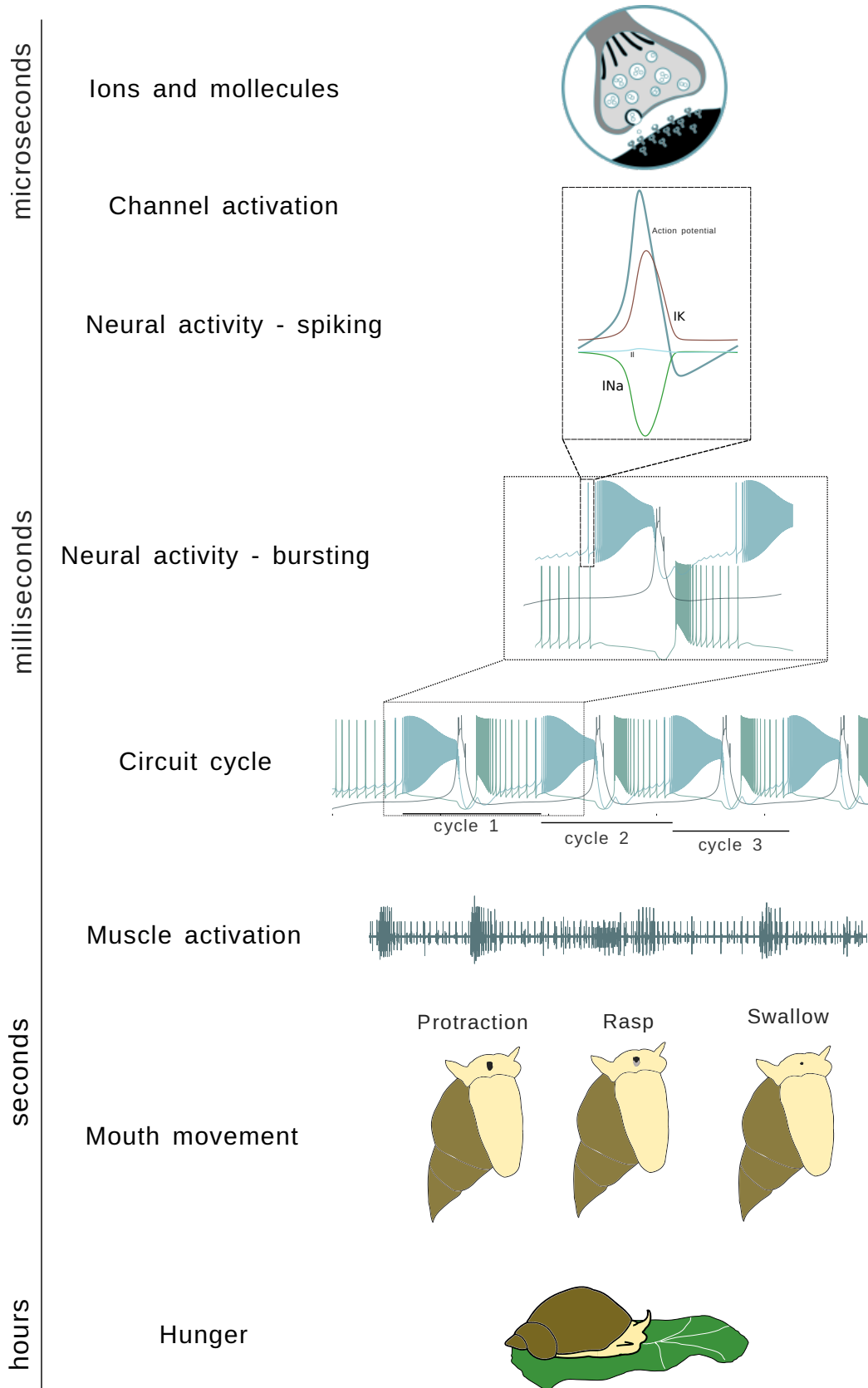


Figure 1.7: Illustration of the sequential feeding process at different time scales in *Lymnaea stagnalis*.

resulting process. Ionic channels are the starting point of the electrical signals underlying neuronal network activity, and their malfunction can contribute to neural disorders (Kecske et al., 2023). Thus, understanding brain activity not only at large scales but also from the stage of voltage generation dynamics can be crucial for a real and complete comprehension of neural systems. Their study can also help distinguish between short- and long-term modulation, a key aspect in neural plasticity and the application of neuromodulatory techniques (Chambers & Kramer, 2008; Burke & Bender, 2019).

It is important to explore the mechanisms that allow sustaining a robust sequential activity despite changes in the input informational context and the variability underlying the neural dynamics. Action potentials and bursts can be classified depending on their waveform and overall temporal characteristics. However, in those subgroups there is a high intra-variability, where, for example, bursting activity can differ in shape, duration, and number of spikes in a given burst. Figure 1.8 shows an example of the variability in the burst waveform and duration for a sequence of several bursts.

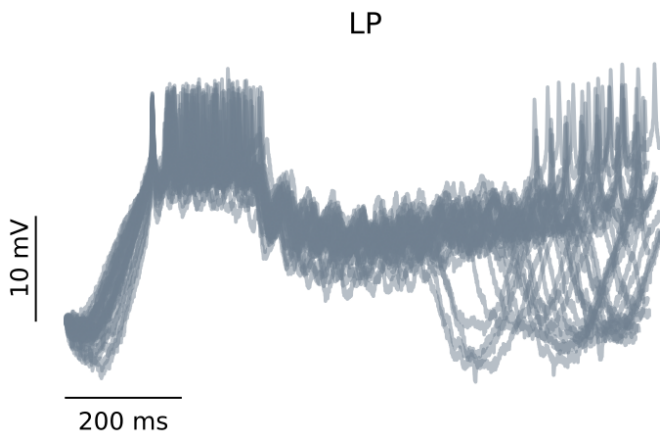


Figure 1.8: Superimposition of bursts at different time instants aligned by the first spike in an intracellular recording of an LP neuron in the pyloric CPG of *Carcinus maenas*.

The study of this variability unveils key factors in the sequentiality and how it is maintained despite different intrinsic or external modulations. This is the case for example of sequential dynamical invariants, i.e., robust relationships between time intervals that conform a neural sequence when analyzing the activity cycle-by-cycle (Reyes et al., 2008; Elices et al., 2019; Garrido-Peña et al., 2021; Berbel et al., 2024). Sequential dynamical invariants might have a crucial role in neural coordination to autonomously establish a balance between the robustness of a sequence and the flexibility of its constituent time intervals required for effective function in many brain processes (Ullén et al., 2003; Tatsuno, 2015; Dragoi, 2020; Zhou et al., 2020; Zimnik & Churchland, 2021). We will discuss in detail these phenomena in the feeding CPG of *Lymnaea stagnalis* in chapter 5.

1.3 Studying neural dynamics in computational models.

Computational Neuroscience is a subfield of neuroscience that uses theoretical and computational techniques to address the study of nervous systems at multiple levels, from the molecular level all the way to the complex networks that shape behavior. It is thus a multi-disciplinary field. The bases of Computational Neuroscience lay in the understanding of brain dynamics from its electrical signals and the information they carry (Shannon, 1948; Hodgkin & Huxley, 1952; Dimitrov et al., 2011; Caterall et al., 2012; Schwiening, 2012). Computational Neuroscience has extended its scope, leading to new paths of research including the use of tools from complex networks, graph theory, causality analysis and machine learning (“30th Annual Computational Neuroscience Meeting”, 2021). There is also a symbiotic relationship with Artificial Intelligence where both fields inspire and help each other grow (Amunts et al., 2019; Gonçalves et al., 2020; Woźniak et al., 2020).

An important part of Computational Neuroscience is the description of neural systems with theoretical models and the reproduction of key phenomena by model simulations. The simulation of neural activity is a powerful tool to explore neuronal dynamics, its biophysical sources, the possible mechanisms underlying neural signaling, and the observed complex information processing. Its strength relies on the complete accessibility to the variables of the model, the typical extensive range of tunable parameters in the model, which can be explored, and the ability to assess the role of distinct elements in the system or circuit by including or excluding them in the simulations. Although models cannot fully substitute research on living systems, they do lead us closer to the understanding of complex neural dynamics, being a convenient, effective and a low cost methodology to advance in science. Also, models are an essential complement to experimental neuroscience reaching detailed descriptions where experimental approaches such as electrophysiology have limitations arising from the unavoidable partial observability of the brain.

Models can be classified by their level of description, i.e., their level of simplification/abstraction, the detail of the structure/phenomenon being simulated, the size of the network, or their ability to reproduce the observed neural activity, e.g. chaotic dynamics. Figure 1.9 illustrates such kind of classification, with examples of models of large networks as Potjans and Diesmann (2014) and Bezaire et al. (2016), of single but highly detailed cells as in Smith et al. (2013), and more abstract descriptions such as the one proposed in Izhikevich (2003). Regarding the level of description, in the different biophysical models there is always a choice between a detailed description of nonlinearities, channels and excitability properties, and efficiency in computation. In this line, researchers can choose from conductance-based models as the Hodgkin and Huxley (1952) paradigm, rich in the description of nonlinearities or simplified dynamical models such as the FitzHugh (1961) and Hindmarsh and

Rose (1984) descriptions, which typically represent nonlinearities with polynomial simplifications (see Torres and Varona (2012) for a review of different levels of neuronal modeling).

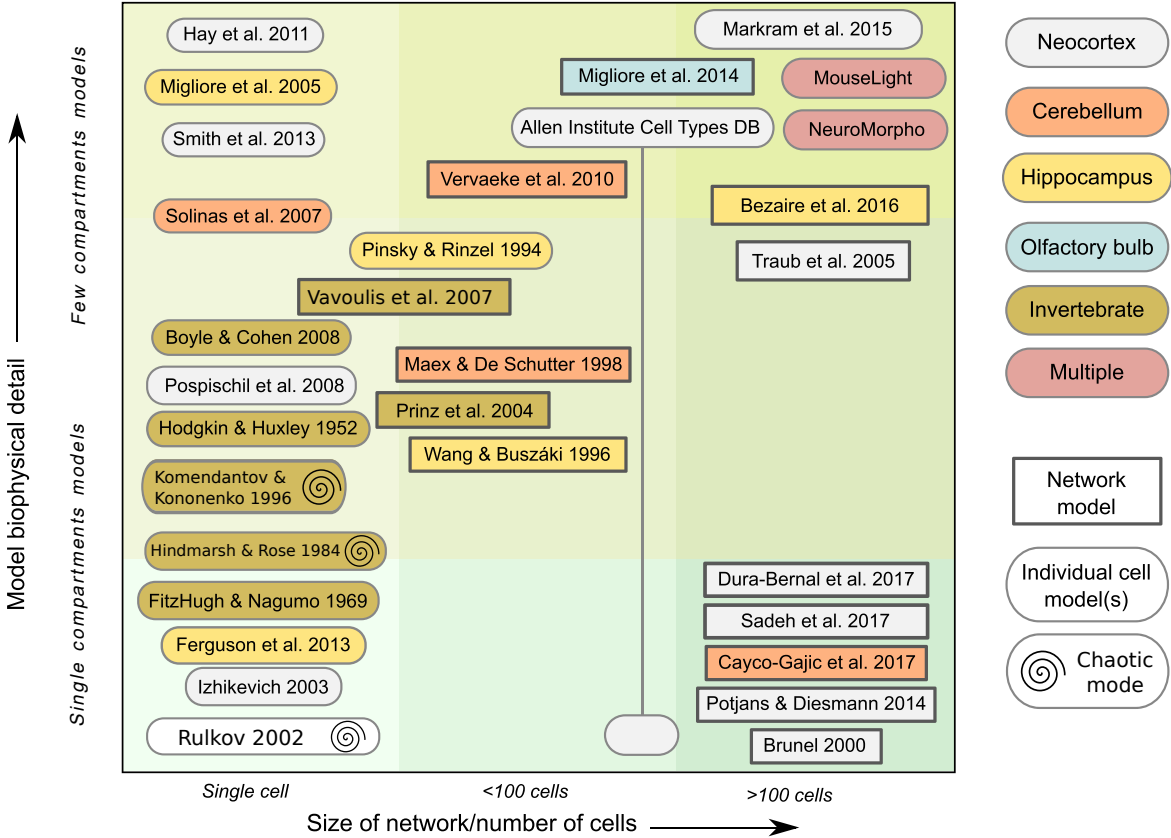


Figure 1.9: Neural and network models classified by biophysical detail, structure modeled and size of the network. Figure adapted from Fig. 2 in Gleeson et al. (2019) under Creative Commons CC-BY license. Models are classified by their level of biophysical detail (the less specific ones are placed at the bottom of the y-axis), by the size of the network modeled (x-axis), and by the brain-structure they model (represented in colored boxes). The shape of the box also classifies the model in network model or individual cell model. The spiral, added as a new model category, indicates the ability of the model to produce chaotic activity without external perturbations, i.e., the ability to reproduce intrinsic variability. Although the figure does not contain all model approaches, it illustrates key milestones in neuronal modeling.

1.3.1 Conductance-based models

In this thesis, all experimental recordings have been supported with simulations of conductance-based models. They are mathematical descriptions of the ionic channel dynamics based on their voltage-dependent conductance. The pioneer study by Hodgkin and Huxley (1952) defined dynamical equations based on the equivalent electrical circuit of the neuronal membrane of the giant squid axon, see Fig. 1.10.a). This modeled circuit is also used to describe the intracellular recording configuration, where the pipette is included as an extra current compensated by the electrode in the bath

(see Fig. 1.10.b).

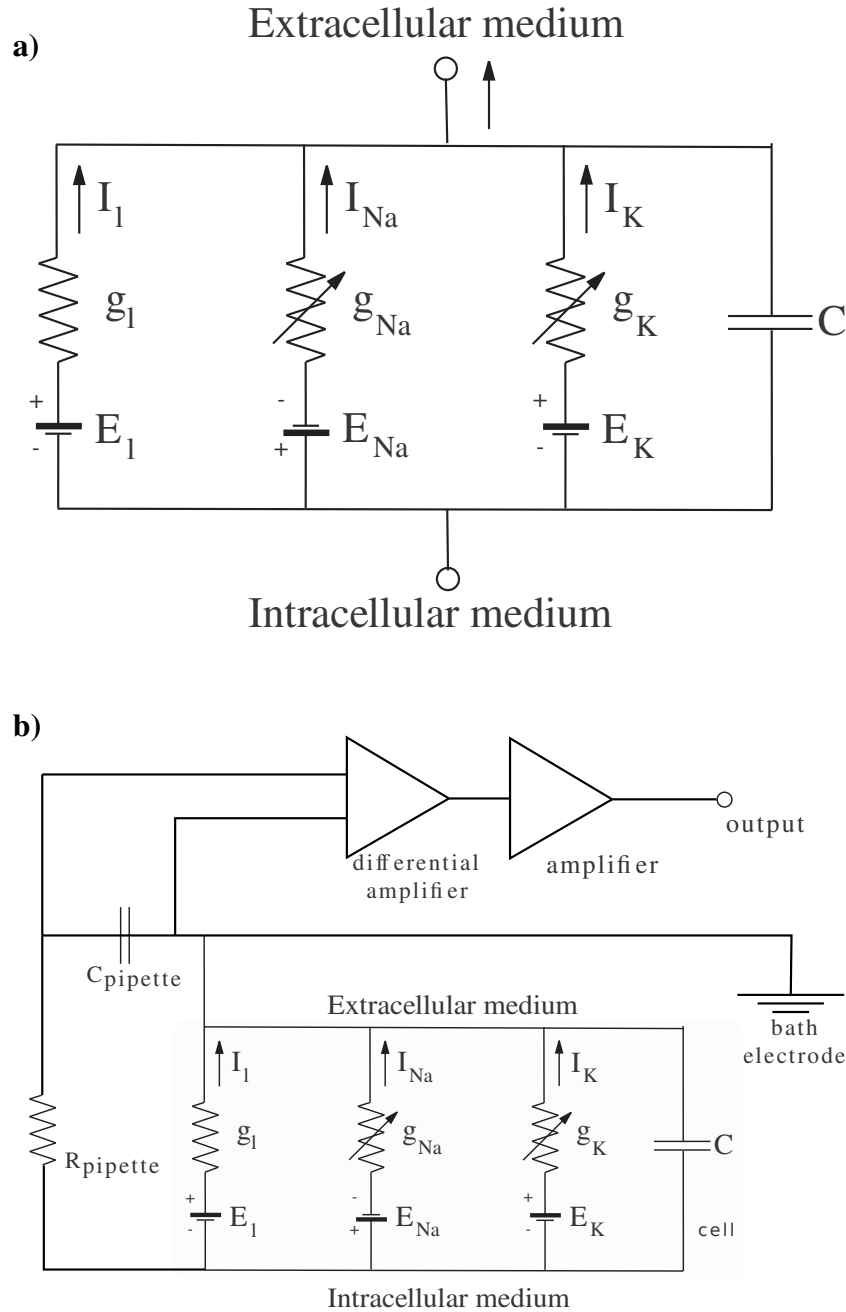


Figure 1.10: a) Electrical circuit describing the membrane voltage in a conductance-based neuron model. b) Electrical circuit representing the scheme for intracellular recordings.

In these models, the simulation of neural electrical activity is based on the mathematical description of different ionic channels in the circuit, whose dynamics are well defined by activation gates. First, there is a mathematical description of the voltage dependency on time, as described by the equation 1.3.1:

$$C_m \frac{dV}{dt} = -I - \sum I_x; : \quad (1.3.1)$$

where V is the membrane potential, I is an external current, e.g. an external stimulus or a synaptic current, and I_x is the current description for each channel involved in the action potential generation, e.g., sodium, potassium, calcium (I_K, I_{Na}, I_{Ca}).

Second, each channel is also described with voltage-dependent activation-gate dynamics:

$$I_x = g_x m^n h^n (V - E_x), \quad (1.3.2)$$

where g_x is the corresponding maximum conductance of the channel, E_x is the reversal potential for that channel and m and h represent activation and inactivation conductance variables, respectively. These gates usually have a nonlinear (exponential tendency) description dependent on voltage and time. They typically follow the structure in equation 1.3.3:

$$\frac{dm}{dt} = \frac{m_{\infty,i} - m_i}{\tau_{m,i}} \quad (1.3.3)$$

where $\tau_{m,i}$ are relaxation time constants which are usually voltage-dependent and modeled using Sigmoid or Gaussian functions. Note that m was used here but this formula also applies to inactivation variables.

Following the Hodgkin and Huxley formalism, the equations that describe the voltage dynamics and the conductance dynamics of the active channels (Na and K) in the circuit shown in Fig. 1.10a) are described in table 1.1.

Voltage equation	$C \frac{dV}{dt} = I - g_K n^4 (V - E_K) - g_{Na} m^3 h (V - E_{Na}) - g_L (V - E_L)$		
	Activation variables		Inactivation variable
gating variables	$\frac{dm(t)}{dt} = \frac{m_{\infty}(V(t)) - m(t)}{\tau_m(V(t))}$	$\frac{dn(t)}{dt} = \frac{n_{\infty}(V(t)) - n(t)}{\tau_n(V(t))}$	$\frac{dh(t)}{dt} = \frac{h_{\infty}(V(t)) - h(t)}{\tau_h(V(t))}$

Table 1.1: Equations of Hodgkin and Huxley formalism for the voltage and conductance gating variables.

This combination of channels generates the spike waveform shown in Fig. 1.11a but, as in living neurons, the combination of different channels leads to distinct outputs, e.g. shoulder and no-shoulder type neurons (see previous section, Fig. 1.3). This is the case of waveform shown in Fig. 1.11b. This shoulder shape could be reproduced in models by including calcium channels in their description.

Modeling networks

In addition to the modeling of the action potential generation, synapses can also be described with different mathematical representations depending on their type and the level of specificity. A combination of conductance-based models and synapses can modulate neural networks at different levels of

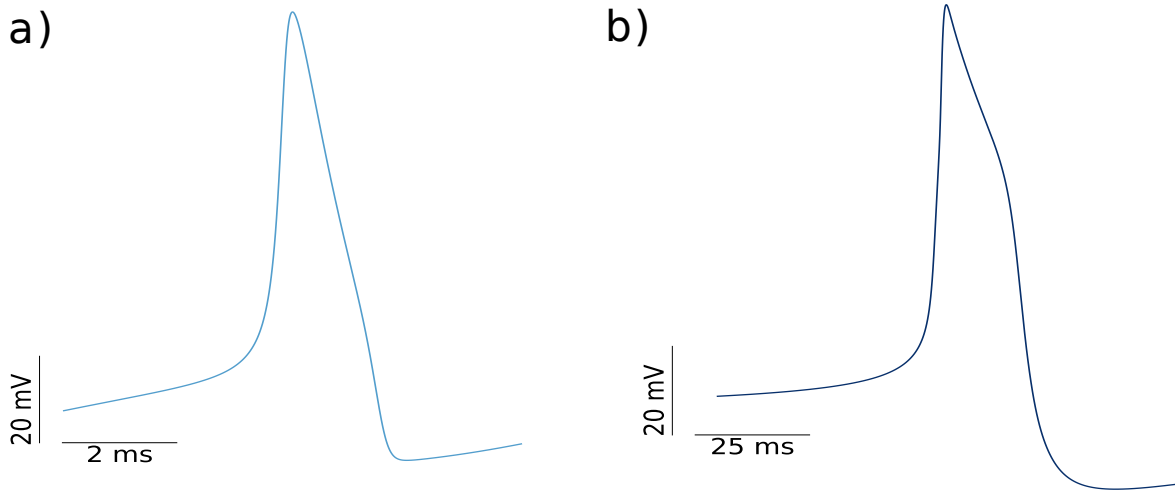


Figure 1.11: Simulations of two distinct action potential types: no shoulder (a) and shoulder shaped spike (b), described by equations in Hodgkin and Huxley (1952) and Vavoulis et al. (2010), respectively.

complexity (Huerta et al., 2001; Aguirre et al., 2007; Latorre et al., 2013). Synapses are introduced in conductance-based models as an extra current that simulates the effect in the neuron dynamics of incoming chemical or electrical inputs. In conductance based models, electrical synapses or gap junctions are usually defined by the following equation:

$$I_{ij}(t) = \bar{G}_{ij}(V_i(t) - V_j(t)) \quad (1.3.4)$$

where i and j represent the two neurons conforming the electrical synapse and \bar{G}_{ij} is a constant representing the maximum value of the synaptic conductance in the connection. For symmetrical gap junctions, the other cells receives exactly the same current with inverse sign.

On the other hand, chemical synapses are by definition asymmetrical and can be described as in equation 1.3.5:

$$I_{ij}(t) = G_{ij}(t)(V_i - E_j^{\text{syn}}) \quad (1.3.5)$$

where E_j^{syn} is the reversal potential of the synapse, the voltage value at which the synaptic current cancels, and G_{ij} can now have complex dynamics considering the trafficking of neurotransmitters, e.g. as in equation 1.3.6 (Torres & Varona, 2012).

$$G_{ij}(t) = \bar{G}_{ij}\Theta(t - t_j^{\text{sp}})\alpha(t - t_j^{\text{sp}}) \quad (1.3.6)$$

where \bar{G}_{ij} is the constant value for the conductance, t_j^{sp} is the time at which the presynaptic spike occurs. $\Theta(x)$ is the Heaviside step function and $\alpha(t)$ is a function to model an evoked postsynaptic responses, which can be defined with a nonlinear dependency, e.g. by exponential functions.

Thus, depending on the selection of this level of specification, the neuron can be activated by a (i) binary cause: occurrence or absence of an action potential, (ii) a dynamic model that is also

dependent on the postsynaptic voltage level like a graded synapse where the concentration of neurotransmitters depends on the presynaptic voltage, or (iii) a model describing other more complex dynamic synaptic phenomena such as synaptic depression and/or facilitation. In the later cases, the level of specification is higher, with a richer description of the synapse dynamics. This is the case for example of the gradual synapse in the CPG model by Vavoulis et al. (2007), discussed in the methods chapter, section 4.4.1, or the Tsodyks and Markram (1997) model , represented by equations 1.3.7 and 1.3.8:

$$\frac{dU}{dt} = -\frac{U}{\tau_{\text{rec}}} + U_{\infty}(1-U)\delta(t-t_{\text{spike}}) \quad (1.3.7)$$

$$\frac{dX}{dt} = -\frac{X}{\tau_{\text{fac}}} + (1-X)\frac{U(t_{\text{spike}})}{U_{\infty}}\delta(t-t_{\text{spike}}) \quad (1.3.8)$$

where U is the fraction of resources available for release, X is the fraction of available neurotransmitter resources in the synaptic terminal. τ_{rec} is the time constant of synaptic resource recovery and τ_{fac} the time constant of synaptic facilitation. U_{∞} is the steady-state value of U and t_{spike} is the time of presynaptic spike. The delta function considers that a spike arrives to the synapse at a fixed time.

1.3.2 Variability in computational models

Most studies use deterministic models that produce regular neural activity, which are sufficient for many research questions when exploring input/output responses, studying the role of different biophysical elements or supporting experimental results on steady state dynamics. However, living systems are highly variable, often working in transient regimes, and often displaying chaotic activity while still producing sequential and robust patterned activity (Selverston et al., 2000). Variability in the activity of living neurons has been proven to play an important role in relevant information processing tasks (Ding & Glanzman, 2011; Masquelier, 2013; Renart & Machens, 2014; Hutt et al., 2023; Ribeiro et al., 2024). While this is a key aspect in neural dynamics, models usually exclude intrinsic variability from their description, particularly in membrane potential waveforms and in collective adaptive dynamics. To induce some level of stochasticity, models typically include Gaussian noise as external input (Linaro et al., 2011; Pezo et al., 2014; Zheng et al., 2020). However, this is a limited approach when exploring the role of intrinsic functional variability, which is dynamically generated by the neurons and the circuits for specific computational tasks, e.g. for sequence coordination. There are several possibilities to include variability in neuronal intrinsic dynamics as it is the example of Hindmarsh and Rose (1984) or Komendantov and Kononenko (1996), where, in both descriptions, there is a combination of parameters that lead to a chaotic states, where the result-

ing activity is not regular. When the source of the variability in the system comes from its intrinsic properties, there is a possibility to study the associated dynamics and the role of this variability in the system without external perturbations such as stochastic noise or currents, and explore the specific properties of the channels from a intrinsic source of variability. Intrinsic variability from rich neuronal dynamics can be reflected in the functionality of the circuit. Also the combination of a regular dynamical model and stochasticity in the ionic channel description can also lead to intrinsic chaotic variability (Carelli et al., 2005).

1.4 Vertebrate and invertebrate animal studies

The study of neural dynamics and behavior is carried out using many different animal models. In addition to the hegemonic rodents models, there have been invaluable findings using invertebrates, such as in genetics and in developmental biology in *C. elegans* (Brenner, 1974), *Zebra fish* (Streisinger et al., 1981) and *Drosophila* (Nüsslein-Volhard & Wieschaus, 1980); neural dynamics in *Aplysia* (Wachtel & Kandel, 1967) or *Loligo* (Hodgkin & Huxley, 1952), motor activity in *Panulirus* (Selverston et al., 1976) and *Carcinus maenas* (Eisen & Marder, 1982) or *Lymnaea stagnalis* (Benjamin & Rose, 1979), the main animal model in this thesis. Besides those examples, these animal models have been used for a wide variety of fields including behavioral studies, ecotoxicology, evolution, human disease modeling, etc. (Romanova & Sweedler, 2018).

Despite brain differences between invertebrates and mammals, there are many universal characteristics of nervous systems that can be extrapolated to humans (Preuss, 2000). By using computational models and exploring different animal species, a ground truth can be set for the aspects that shape neuronal and thus behavioral dynamics.

Findings in invertebrates are sometimes overlooked, often under the excuse that features in invertebrates cannot be extrapolated to humans. However, invertebrates models have proven their utility not only in basic science. We can find examples of this in human diseases, memory, motor activity and neuromodulation. Particularly, in the study of neural processes, the ease of accessibility and the finite number of large neurons in the system have made invertebrates an interesting case study (Gelperin, 2019).

Invertebrate models have the advantage of longer survival times of the preparations, and easier accessibility to specific nervous system, as compared to vertebrate preparations, which facilitate many experimental goals. Also, the ease of breeding and reproduction or the simplicity of their biological features, that makes possible a full description of it, i.e. the genomic description of *C. elegans* or the

nervous system in *Lymnaea stagnalis*. Apart from this, some selected species were a main field of study in the last decades, so there is plenty of literature for each one even in different fields. Furthermore, despite the simplicity of these systems, their nervous system is still capable of generating robust sequential neural activity, preset behavior and even learning processes.

Apart from the possible advances in science from a productivist view, invertebrates models can also bridge the gap between resources and science, allowing low-income labs and countries to *do* science. This animal models are usually cheaper to obtain, maintain and there is usually a possibility of breeding own colonies. This makes their use extendable and breaks some economical barriers in science, where high-income countries usually centralize the science production with strong conventions (Stephan, 2015; Castillo & de la Guardia, 2017).

However, in any animal model, it is important to prioritize scientific advancement responsibly. Alternatives such as computational models should be considered alongside experimental studies, aiming to reduce the need for them and offering a less invasive path to extend our knowledge.

***Lymnaea stagnalis*, the great pond snail**

In this thesis, we work on the neural system of the great pond snail, *Lymnaea stagnalis* (see Fig. 1.12a). This mollusk has been an important case study since the late XX century, when it was used extensively to study neurobiological processes and nervous system functioning. This career-time effort lead to a detailed description of the buccal ganglia and its CPG, including the three main interneurons conforming it (Benjamin et al., 1979; Rose & Benjamin, 1979; Benjamin & Elliott, 1989; Brierley et al., 1997) and the modulatory neurons that influence the CPG activity such as SO and CGC neuron in the cerebral ganglia (McCrohan & Benjamin, 1980; Rose & Benjamin, 1981; Kemenes et al., 2001)). Besides the buccal ganglia, other neurons in different ganglia are also well identified, with specific characteristics such as electrical coupling or dopamine containing neurons as in the Right Parietal Ganglia (Winlow et al., 1981; Benjamin & Pilkington, 1986).

As an animal model, *L. stagnalis* has been key in other fields, such as host-parasite or genome editing studies. This last case is thanks to the short and well studied life-cycle of *L. stagnalis* (see Fig. 1.12), as well as the easiness to lab-bread them, without losing its main characteristics through generations (Noland & Carriker, 1946). Recordings and analyses in this thesis are framed in the study of the neural activity in its central nervous system (CNS). *L. stagnalis* CNS is composed by 11 ganglia: symmetrical pairs of buccal, pedal, cerebral, pleural and parietal ganglia, and a single visceral ganglion (see Sec. 4.1). We will focus specially in its feeding CPG, which, by a distributed combination of motor- and inter-neurons allocated mainly in buccal and cerebral ganglia, produces

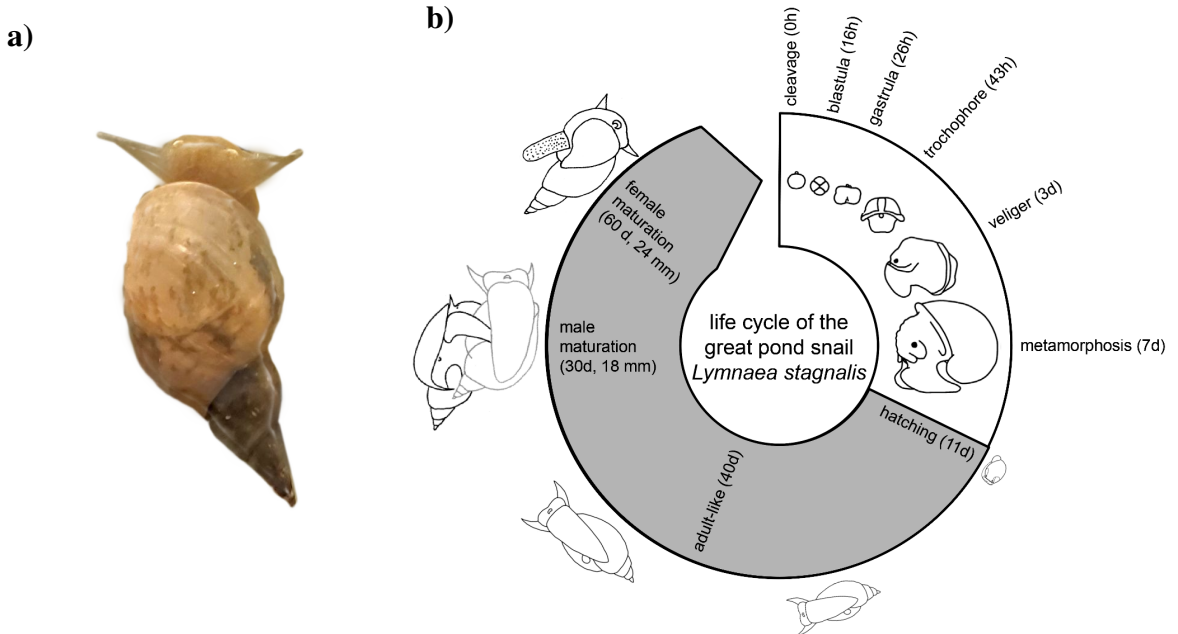


Figure 1.12: a) Photograph of *Lymnaea Stagnalis*. b) Representation of *L. stagnalis* life cycle. Figure 2A from Fodor et al. (2020) ([Creative Commons license](#)).

a rhythmic pattern movement that allows feeding in three phases (protraction, rasp and swallow). Beyond this study of the CPG, we will work on the giant neurons located in the right parietal ganglia (RPG), taking advantage of the membrane high-voltage (up to 80mV) and slow activity (20 to 100 ms per spike) to analyze in detail the action potential dynamics.

1.5 Neural stimulation

1.5.1 Stimulation techniques

Neural stimulation have been an essential aspect in the study of neural dynamics, allowing the modulation of the neural system to explore, reproduce and alter its dynamics for the assessment of information processing in nervous systems. There are several techniques to produce stimulation, we could classify them in chemical –using chemical components to block/enhance neural mechanisms–, electrical –injecting current in the cell membrane or close to the nerves–, magnetic –subjecting the system to magnetic fields–, mechanical –introducing movement as a perturbation–, or optical –where neurons or circuits are stimulated though an illumination process. In this thesis, we focus in electrical and optical stimulation. In the electrical techniques, since the firsts applications of electrophysiology (Marmont, 1949; Cole, 1955; Neher & Sakmann, 1976) and the subsequent apparition of patch-clamp technique (Hamill et al., 1981), many different techniques have been developed, for distinct systems.

Voltage-clamp, current clamp and patch clamping modified the paradigm in physiology and basic medicine in the study of the cell membrane dynamics with an exceptional detail that still today is heading ranges of precise recording and stimulation (Hamill et al., 1981). To Voltage-clamp followed variations such as dynamic-clamp, that enhances the electrophysiology possibilities by combining it with the possibilities of computing through a closed-loop protocol in real-time (Nowotny & Varona, 2022). This allows implementing specific algorithms to intervene the neural activity and test it to different approaches (Chamorro et al., 2012). Regarding optical stimulation, a novel and widespread technique is opto-genetics, that by genetically modifying the animals, neurons are reactive to light and have had great achievements in the last decades using for both stimulation and exploration (Chen et al., 2022). Other example still under study is near-infrared laser, a novel technique that will be explored in detail along this thesis. This technique has proven its potential for neuronal stimulation in different systems such as the hippocampus (Liang et al., 2009), spinal ganglia in the cochlea (Goyal et al., 2012; Barrett et al., 2018; Brown et al., 2020) and other systems (Shapiro et al., 2012; Cayce et al., 2014; Begeng et al., 2022).

1.5.2 Neuromodulation and its need for clinical applications

Beyond the necessity for neural stimulation in basic research to understand and explore the brain signaling and dynamics, there is a direct societal impact of neural stimulation in clinical applications. In this context, Neuromodulation is an area of medicine involving many specialities that can be defined as "the science of how electrical, chemical and mechanical interventions can modulate distinct models of the nervous system function [and it is] inherently non-destructive, reversible, and adjustable" (Krames et al., 2009). This field is so important due to its possibilities in brain disorder treatments, for functional stimulation but also by the long-term modulation through neuronal plasticity. Neuromodulation can be classified, depending on the technology used for it, as invasive or non-invasive. Invasive technologies are those that require a direct interaction with the living system, which causes harm at some extent, e.g. including surgery. A well-known example of this type of neuromodulation is deep-brain stimulation (DBS), this technique has been effectively used for treating movement disorders by electrically stimulating the brain at certain brain areas after implanting a device (Limousin & Foltynie, 2019; Hariz & Blomstedt, 2022). In the case of non-invasive neuromodulation, we can find transcranial magnetic stimulation (TCM), which using electric fields stimulates certain areas of the brain. This stimulation has been successful for example in the treatment of depression or obsessive-compulsive disorders (Valero-Cabré et al., 2017; Clarke et al., 2018). Each type of technique has its own advantages, invasive techniques are usually more precise in space and time, whereas non-

CHAPTER 1: INTRODUCTION AND STATE OF THE ART

invasive techniques provide more flexibility and adaptability to different patients and contribute to the wide availability of the technique. In this context, optical techniques discussed for stimulation in basic research have been rising in popularity also for clinical applications. In this thesis we will explore near-infrared continuous-wave laser stimulation, a novel type of noninvasive neurotechnology.

CHAPTER 2

Introducción y Estado del Arte

2.1 Neurociencia, neuronas y su dinámica

La neurociencia es un campo amplio y desafiante. Afronta preguntas cruciales, tales como el estudio de los mecanismos neuronales subyacentes a la actividad cerebral, cómo pueden esos mecanismos resultar en procesos cognitivos o el comportamiento humano, cómo la información se percibe, procesa, transforma y crea, y finalmente se convierte en acciones a través de la actividad neuronal, cómo se originan las enfermedades neuronales y cómo podemos detectarlas y tratarlas. Estas preguntas y muchas más han sido problemas abiertos que han intrigado a la comunidad científica desde los primeros pasos en el campo. La neurociencia nació como una disciplina moderna a partir de la anatomía, la fisiología, la bioquímica y la biofísica. Por el amplio alcance del campo, se suele abordar desde distintas perspectivas y comúnmente se referencia por sus subcampos, por ejemplo, Neurobiología, Neurofarmacología, Neurociencia Clínica, Neurociencia del Desarrollo, Neurociencia de Sistemas, Neurociencia Cognitiva, Neurociencia Computacional, Neurotecnología, etc. Todos estos campos tienen como objetivo explicar o reparar la función cerebral, ya sea como un conjunto o en partes. En este proceso se utilizan diferentes técnicas y enfoques, algunos de los cuales dan lugar a campos completamente nuevos, como la Neuroimagen.

No podemos pensar o discutir sobre neurociencia sin destacar el trabajo de Santiago Ramón y Cajal, crucial en los primeros pasos para comprender el cerebro (Ramón y Cajal, 1899; De Carlos & Borrell, 2007; Delgado-García, 2015; de Castro & Merchán, 2016; de Castro, 2019). La idea de la "doctrina de la neurona" fue un impulso en el estudio del cerebro, explicando y describiendo la estructura de células individuales llamadas *neuronas* que son capaces de conectarse y, por lo tanto, comunicarse mediante *sinapsis*. La Figura 2.1 muestra uno de los dibujos de Cajal que ilustra la retina de la abeja y una primera aproximación al posible curso del flujo de información en este sistema.



Figure 2.1: Ilustración de Ramón y Cajal que muestra el posible curso de información en la retina de la abeja (Ramón y Cajal & Sánchez, 1915) (Disponible bajo la licencia: CC BY 4.0).

El cerebro es un sistema complejo que podemos estudiar desde diferentes prismas. En esta tesis, seguimos un enfoque *bottom-up* (de abajo hacia arriba), en el que analizamos de forma experimental y teórica la actividad neuronal desde una descripción de la dinámica de canales iónicos y la de pequeños circuitos (con pocas sinapsis). Además, seguimos una perspectiva neurocomputacional basada en el procesamiento secuencial jerárquico de la información, que se definirá en detalle en la subsección 2.3. En las siguientes líneas abordaremos las bases de la activación neuronal desde esta perspectiva computacional necesaria para la comprensión de este documento. Nos centraremos en la dinámica de voltaje que las neuronas son capaces de producir y en su interrelación para dar lugar a su actividad secuencial colectiva.

2.1.1 Dinámica neuronal

Las neuronas son células morfológicamente compuestas por dendritas, donde se reciben las conexiones de otras neuronas a través de sinapsis; un soma o cuerpo celular (donde normalmente se integra

la información) y un axón (donde la información se transmite como salida). Dado que las neuronas son las células que presentan la mayor diversidad en morfología, esta descripción no se aplica a todos los tipos neuronales, pero nos sirve para comenzar a destacar la importancia de las escalas espaciales en el sistema nervioso.

La actividad eléctrica neuronal a menudo se describe en términos de la evolución del voltaje de la membrana causada por el flujo de canales iónicos entre el interior y el exterior de la célula (Kandel et al., 2012). El cambio rápido característico en el voltaje de la membrana cuando una neurona emite una señal de salida se llama potencial de acción o *spike*. Estos potenciales de acción suelen considerarse como la unidad mínima de información para la recepción, procesamiento y transmisión por parte de las neuronas. Una definición más concreta de *spike* podría ser "un cambio abrupto y transitorio del voltaje de la membrana que se propaga a otras neuronas a través de una extensión larga llamada axón" (traducción del texto original) (Izhikevich, 2007). Así, cuando no se reciben entradas, el potencial de la membrana de una neurona es negativo y se llama potencial de reposo. Cuando este potencial se altera por una entrada que hace que el voltaje aumente, se conoce como despolarización. Después de alcanzar un pico de voltaje, típicamente un valor positivo de alrededor de 40mV, el potencial comienza a disminuir nuevamente. Cuando el potencial toma valores por debajo del potencial de reposo, se conoce como hiperpolarización. La Figura 2.2 ilustra las fases secuenciales de la generación del potencial de acción.

La actividad neuronal se produce por el flujo de diferentes canales iónicos que provocan la generación de potenciales de acción (Koch, 1999). La membrana puede estar compuesta por diferentes canales iónicos, y su dinámica está condicionada por esa combinación y las posibles conexiones sinápticas a las que está sujeta la neurona. Estos cambios en la dinámica se ponen de manifiesto de diferentes maneras, pero las más representativas son la forma de onda y la evolución temporal de los potenciales de acción. Por ejemplo, en la Fig. 2.3 muestra dos potenciales de acción distintos con diferencias visibles en su forma de onda. En la Figura 2.3a) se muestra un potencial que presenta una forma simétrica, donde las pendientes de despolarización y repolarización son similares, mientras que en la forma de onda de Fig. 2.3b), hay un "hombro" característico en la repolarización y su escala temporal es casi el doble en comparación con el ejemplo mostrado en la Fig. 2.3a).

Si consideramos los potenciales de acción como piezas mínimas de información al codificar la actividad neuronal, la combinación de estas piezas mínimas de información lleva a nuevas formas de información, también conocidas como ráfagas. Aunque no hay una descripción fija de una ráfaga, y dependiendo del animal y el sistema una ráfaga puede verse diferente (Russell & Hartline, 1978; Palmu et al., 2010; Lundqvist et al., 2016), hay algunas características comunes en ellas: normal-

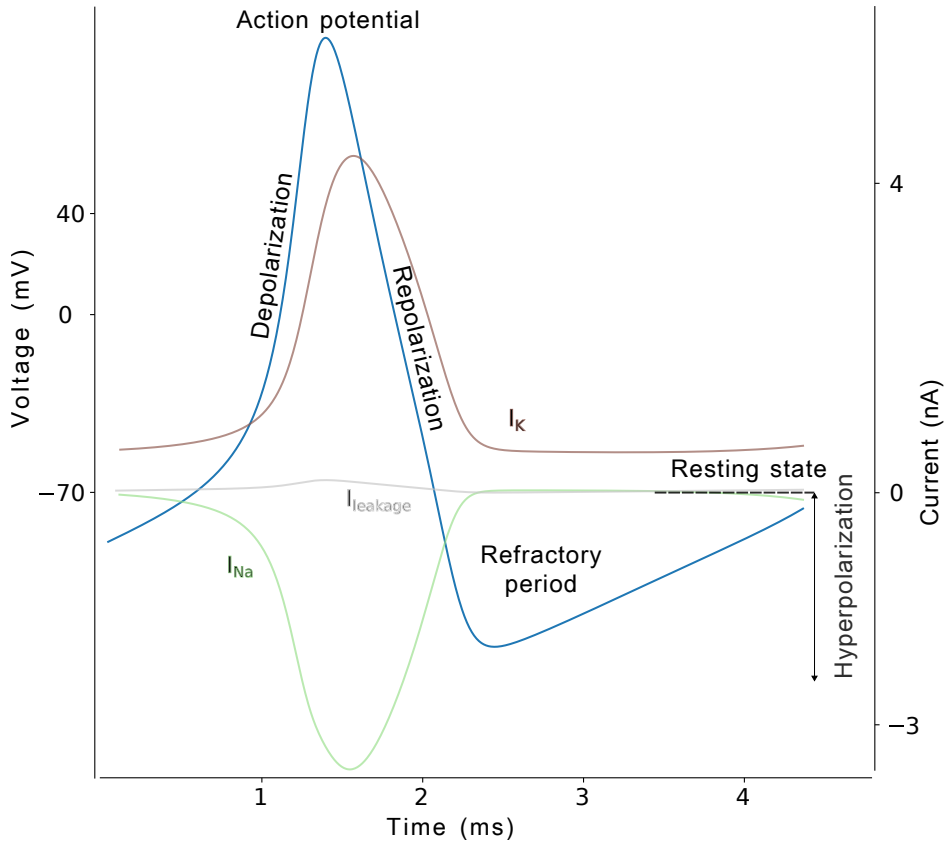


Figure 2.2: Representación de las fases secuenciales y terminología de un potencial de acción junto con las corrientes que lo generan (I_K, I_{Na} and $I_{leakage}$). En cada una de estas fases de la generación del potencial de acción, se activan secuencialmente diferentes canales iónicos, por ejemplo, el canal de sodio está involucrado durante la fase de despolarización y su actividad disminuye a medida que el canal de potasio se activa principalmente en la fase de repolarización.

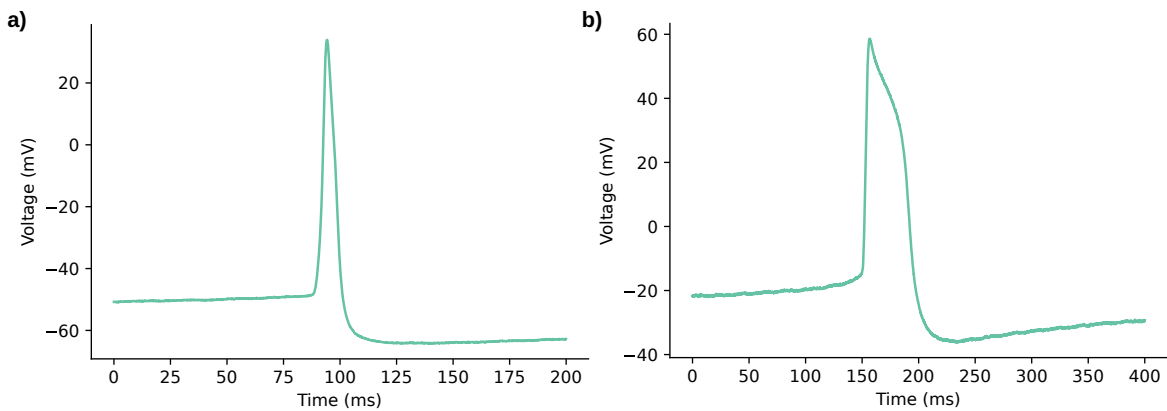


Figure 2.3: Ejemplos de diferentes formas de onda de potenciales de acción. Representación de dos registros de dos células diferentes en el ganglio parietal derecho de *Lymnaea stagnalis*. a) Spike con forma de onda simétrica; b) Spike con forma de onda con "hombro".

mente consisten en un grupo de *spikes* (más de dos) sobre una despolarización sostenida, y estos grupos están separados por un período de quiescencia de hiperpolarización llamado intervalo en-

tre ráfagas (IBI). La Figura 2.4 muestra varios ejemplos de distintas actividades neuronales observadas en grabaciones intracelulares. Dependiendo de la neurona específica y el circuito, las neuronas pueden presentar disparo tónico a diferentes frecuencias como el mostrado en el panel a), o actividad en ráfagas en los paneles b) y c).

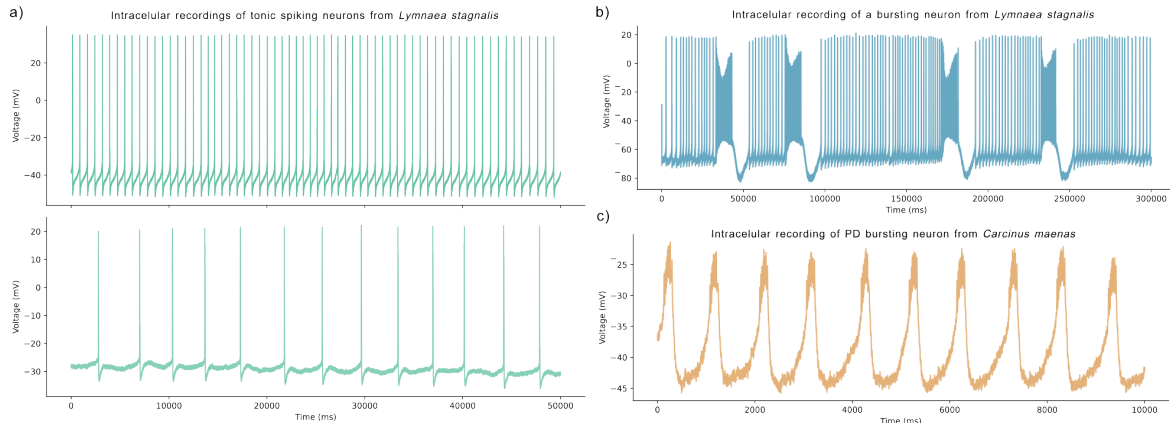


Figure 2.4: Representación de dos ejemplos de diferentes actividades neuronales de disparo. a) Dos registros intracelulares simultáneos en *Lymnaea stagnalis* mostrando disparo tónico a dos frecuencias diferentes. b) Ejemplo de actividad en ráfagas en un registro intracelular en *Lymnaea stagnalis*. c) Ejemplo de actividad en ráfagas en un registro intracelular en la neurona PD en *Carcinus maenas*.

Tradicionalmente, los códigos neuronales se han estudiado centrándose en la activación de *spikes* individuales, por ejemplo, mediante la binarización de la actividad (la neurona genera un *spike* o no). Las ráfagas también pueden ser informativas en términos de la actividad neuronal, ya sea como una pieza completa de información o como una caja de datos compleja en sí misma: "las ráfagas son una familia de patrones de disparo que desencadenan mecanismos fisiológicos que no se activan con el mismo número de *spikes* en relativo aislamiento" [traducido del texto original] (Friedenberger et al., 2023). Las ráfagas pueden originarse por activación interna, principalmente por canales de calcio y/o por la dinámica sináptica que involucra a la célula correspondiente (inhibición/excitación), para una revisión extendida ver (Friedenberger et al., 2023). La actividad en ráfagas es muy común en circuitos Generadores Centrales de Patrones (CPGs) (Katz, 2016; Steuer & Guertin, 2018), que se discutirán en detalle a continuación y en el Capítulo 5.

2.1.2 Dinámicas de redes

Aunque el análisis de la actividad de una sola neurona es importante para caracterizar su dinámica, cuando se habla de procesamiento de información y comportamiento, también es crucial estudiar la dinámica general del circuito. Un circuito de neuronas se define por células nerviosas interconectadas por sinapsis. Existen dos tipos principales de sinapsis en el sistema nervioso: conexiones eléctricas

y químicas, como se muestra en la Fig. 2.5. La principal diferencia entre ellas radica en cómo se lleva a cabo la comunicación. Las sinapsis químicas ocurren mediante la mediación de *neurotransmisores*, donde una neurona presináptica libera estas moléculas que se unen a los neuroreceptores para producir una alteración en la neurona postsináptica. Por lo tanto, esta conexión es asimétrica y unidireccional, mientras que en las sinapsis eléctricas encontramos una conexión simétrica y bidireccional. En estas sinapsis, las neuronas están casi unidas por una estructura llamada *unión gap* (*gap junction* en inglés), que conecta ambas neuronas en una estructura tisular que limita la fuga al espacio extracelular. Esta comunicación permite que la carga eléctrica fluya de una neurona a otra y es más rápida que las sinapsis químicas, con una comunicación sin retraso en comparación. La actividad de las neuronas acopladas eléctricamente suele ser sincrónica (Levitin & Kaczmarek, 2002).

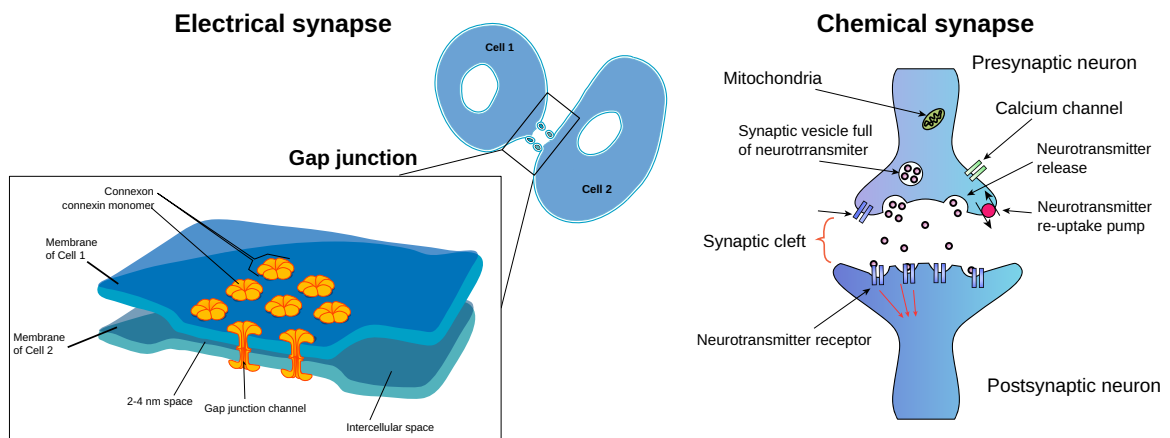


Figure 2.5: Representación de tipos de sinapsis. Izquierdo: Ilustración de una sinapsis eléctrica entre dos células y diagrama de la unión gap (Adaptado de [Wikimedia Commons](#)). Derecho: Ilustración de la estructura de una sinapsis química (Adaptado de [Wikimedia Commons](#)).

Las neuronas pueden estar conectadas varios tipos de sinapsis químicas y eléctricas, y generalmente también están conectadas a otros circuitos bajo el efecto de neuronas moduladoras. La Figura 2.6 ilustra dos ejemplos de circuitos a nivel celular y macroscópico. En cualquier sistema nervioso, se forman agrupaciones complejas de redes de redes, que pueden funcionar a diferentes escalas temporales y pueden participar en múltiples funcionalidades. Esta interconexión de redes y, a un nivel más bajo, de células, conduce a activaciones secuenciales y transferencias de acciones en secuencias de secuencias (Rabinovich et al., 2020).

2.2 La naturaleza secuencial de la dinámica neuronal

Las dinámicas cerebrales pueden describirse como secuencias de interacciones, desde moléculas, hasta neuronas, control motor y comportamiento, lo que implica una jerarquía coordinada de es-

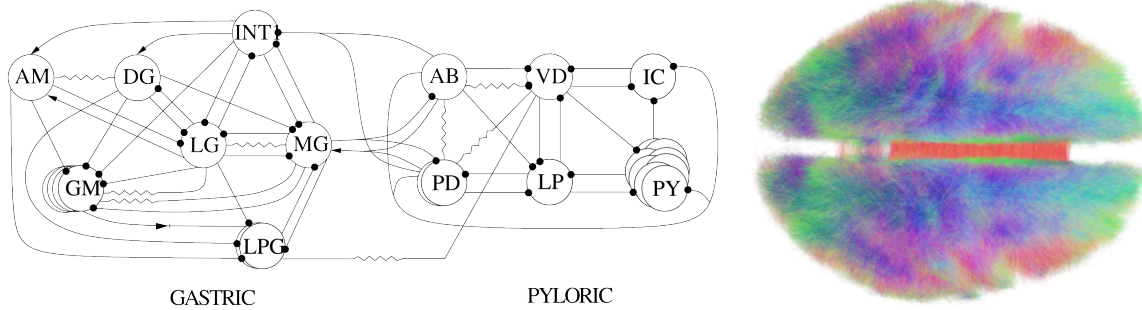


Figure 2.6: Izquierdo: Esquema de la conectividad del CPG pilórico y gástrico del crustáceo, probablemente uno de los circuitos mejor conocidos en neurociencia (Huerta et al., 2001). Derecha: Conectoma en el cerebro humano renderizado a partir de 20 sujetos que representa una red de conexiones más compleja (Por Andreashorn - Trabajo propio, CC BY-SA 4.0).

calas temporales y espaciales (Yuste et al., 2005; Kiebel et al., 2008; Rabinovich & Varona, 2018; Rabinovich et al., 2023), desde activaciones de canales iónicos hasta codificación sensorial, procesamiento y toma de decisiones. Su estudio revela aspectos fundamentales de la función cerebral y la cognición, por ejemplo, la transmisión de impulsos, la función ejecutiva, el procesamiento espacial, memoria, etc.

Un ejemplo común de procesamiento secuencial es el habla, donde los patrones secuenciales están presentes en la estructura de las frases, como secuencias de secuencias de sílabas, palabras y silencios (Kiebel et al., 2009). En esta línea, un caso de estudio extendido es el canto de los pájaros, que tiene similitud con el habla humana, ya que involucran secuencias de sonidos coordinados (Prather et al., 2017; Fishbein et al., 2019). Aparte de en el habla, el procesamiento secuencial también está presente en el control motor, desde la activación muscular hasta acciones coordinadas repetitivas como el golpeteo rítmico o la interpretación musical (Ding et al., 2017). Además, hay muchos procesos cognitivos importantes que dependen de mecanismos secuenciales como la percepción, la memoria, la toma de decisiones, la atención y la emoción (Varona & Rabinovich, 2016; He, 2018; Rabinovich et al., 2020).

Sin embargo, no está claro cómo procesa exactamente el cerebro el tiempo. En contraste con la teoría de un reloj central que gestiona el tiempo para cada tarea conductual, la teoría de un procesamiento temporal distribuido (Buonomano & Merzenich, 1995; Ivry, 1996) es bien aceptada. En este marco, especialmente en la coordinación del movimiento, existen circuitos que gestionan la actividad rítmica secuencial. Este es el caso de los Generadores Centrales de Patrones (CPGs), circuitos de neuronas con topología cerrada que activan secuencialmente neuronas y generan actividad motora coordinada (Selverston et al., 2000). Están presentes en muchos sistemas, desde insectos hasta humanos (Pearson, 1972; Marder & Bucher, 2001; MacKay-Lyons, 2002; Minassian et al., 2017). Hay

varios aspectos clave que hacen de estos circuitos un caso de estudio interesante. Primero, sus neuronas están organizadas en topologías cerradas recibiendo retroalimentación de células compañeras (Huerta et al., 2001). Estos circuitos pueden mantener una actividad rítmica de manera autónoma, típicamente mediante interacciones inhibitorias mutuas (Katz, 2016). Segundo, su actividad es lo suficientemente flexible como para adaptarse a cambios en el contexto, por ejemplo, variaciones en el terreno al caminar. Finalmente, están presentes en muchos sistemas y en algunos de ellos hay una relación directa entre la actividad de las neuronas en el circuito y el movimiento motor que producen. Por ejemplo, en el CPG pilórico en el cangrejo *C. maenas*, encargado del movimiento del píloro, las neuronas PD (dilatador pilórico), LP (pilórico lateral) y PY (PYlórico) corresponden a la dilatación del píloro, el cierre del píloro y la contracción del constrictor rostral para mover los alimentos en el sistema digestivo (Moulins & Selverston, 1987; Selverston & Ayers, 2006).

La actividad secuencial en el cerebro va desde la escala de sub-milisegundos hasta días (la escala temporal de los ritmos circadianos (Mauk & Buonomano, 2004)). La Figura 2.7 muestra un ejemplo ilustrativo de la naturaleza secuencial de la actividad neuronal en diferentes escalas en la generación de actividad motora coordinada en la alimentación de un caracol. A la escala de sub-milisegundos, hay un flujo de iones que genera una secuencia de activación de canales iónicos, que en la escala de milisegundos produce potenciales de acción. La combinación de ellos en forma de ráfagas rítmicas, activa los músculos correspondientes en la escala de segundos y genera el movimiento secuencial necesario para alimentarse: abrir la boca, raspar el alimento y tragarse, que se repite a lo largo del día.

El estudio de la dinámica de los potenciales de acción y la interacción entre los canales iónicos y las sinapsis es crucial, ya que es una parte clave en cualquier proceso cerebral, y no puede separarse del estudio de la actividad en su conjunto. La alteración de la dinámica de estos canales a diferentes niveles, puede afectar las entradas/salidas sinápticas, cómo se comunican las neuronas y el proceso resultante. Los canales iónicos son el punto de partida de las señales eléctricas subyacentes a la actividad de la red neuronal, y su mal funcionamiento puede contribuir a trastornos neuronales (Kecske et al., 2023). Por lo tanto, comprender la actividad cerebral no solo a gran escala sino también desde la etapa de generación de dinámicas de voltaje puede ser clave para una comprensión realmente completa de los sistemas neuronales. Su estudio también puede ayudar a distinguir entre la modulación a corto y largo plazo, un aspecto clave en la plasticidad neuronal y la aplicación de técnicas neuromoduladoras (Chambers & Kramer, 2008; Burke & Bender, 2019).

Es importante explorar los mecanismos que permiten mantener una actividad secuencial robusta a pesar de los cambios en el contexto informacional mediante la entrada de diferentes estímulos y la variabilidad subyacente en la dinámica neuronal. Los potenciales de acción y las ráfagas pueden

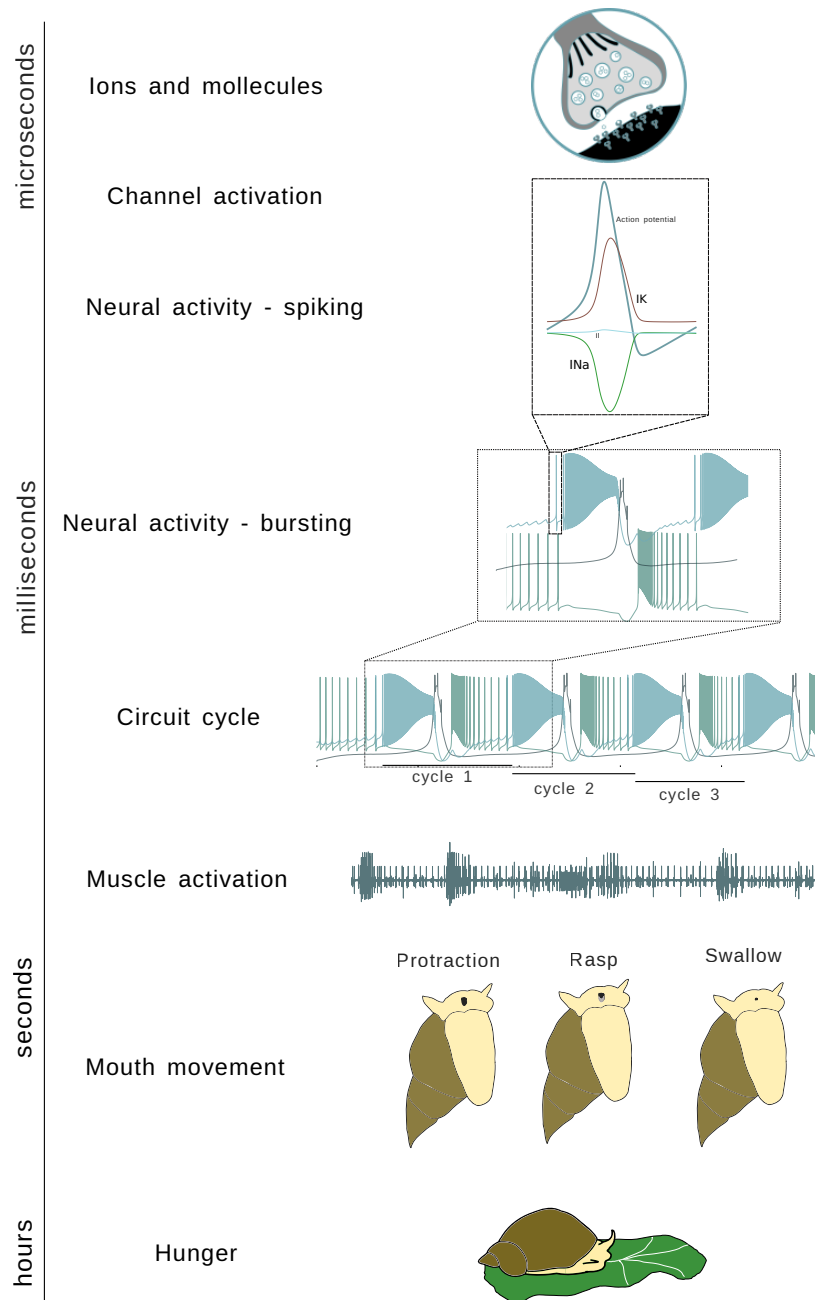


Figure 2.7: Ilustración del proceso de alimentación secuencial en diferentes escalas de tiempo en *Lymnaea stagnalis*.

clasificarse según su forma de onda y la actividad de disparo agrupada. Sin embargo, en esos subgrupos hay una alta intra-variabilidad, donde, por ejemplo, la actividad de ráfagas puede diferir en forma y duración, es decir, en el número de potenciales en una ráfaga. La Figura 2.8 muestra un ejemplo de la variabilidad en la forma de onda y la duración de la ráfaga para una secuencia de varias ráfagas.

El estudio de esta variabilidad revela factores clave en la secuencialidad y cómo se mantiene a pesar de diferentes modulaciones intrínsecas o externas. Este es el caso, por ejemplo, de los invariantes dinámicos secuenciales, es decir, relaciones robustas entre intervalos de tiempo que conforman una

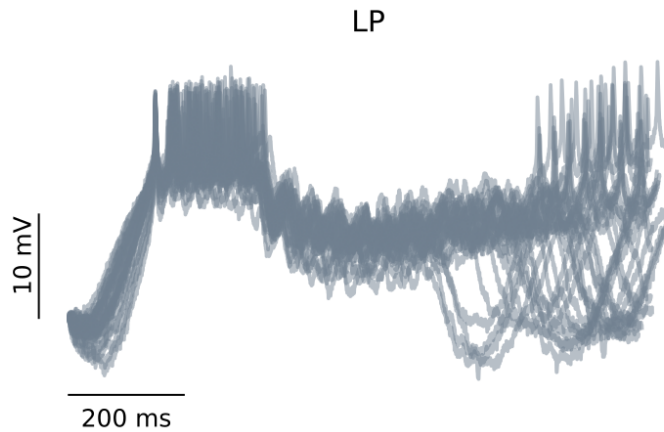


Figure 2.8: Superposición de ráfagas en diferentes instantes de tiempo alineadas por el primer *spike* en la ráfaga para grabaciones intracelulares de una neurona LP en el CPG pilórico.

secuencia neuronal, al analizar la actividad ciclo a ciclo (Reyes et al., 2008; Elices et al., 2019; Garrido-Peña et al., 2021; Berbel et al., 2024). Estos invariantes dinámicos secuenciales pueden tener un papel crucial en la coordinación de la actividad secuencial de forma autónoma, en el que se establece un equilibrio entre robustez y flexibilidad de sus intervalos temporales, requeridas para una función efectiva en muchos procesos cerebrales (Ullén et al., 2003; Tatsuno, 2015; Dragoi, 2020; Zhou et al., 2020; Zimnik & Churchland, 2021). Discutiremos en detalle este fenómeno en el CPG alimentario de *Lymnaea stagnalis* en el capítulo 5.

2.3 Estudio de la dinámica neuronal mediante modelos computacionales.

La Neurociencia Computacional es un subcampo de la neurociencia que utiliza técnicas teóricas y computacionales para abordar el estudio del sistema nervioso en múltiples niveles, desde el nivel molecular hasta redes complejas que dan forma al comportamiento. Es, por lo tanto, un campo multidisciplinar. La base de la Neurociencia Computacional radica en la comprensión de la dinámica cerebral a partir de sus señales eléctricas y la información que transportan (Shannon, 1948; Dimitrov et al., 2011; Catterall et al., 2012; Schwiening, 2012). Desde sus comienzos, la Neurociencia Computacional ha ampliado su alcance, llegando a nuevos caminos de investigación que incluyen redes complejas, teoría de grafos, análisis de células individuales y técnicas de aprendizaje automático (“30th Annual Computational Neuroscience Meeting”, 2021). En campos como la Inteligencia Artificial incluso existe una relación simbiótica entre ambos, en la que se inspiran y se ayudan mutuamente a crecer (Amunts et al., 2019; Gonçalves et al., 2020; Woźniak et al., 2020).

Una parte importante de la Neurociencia Computacional es la descripción de sistemas neuronales con modelos teóricos y la reproducción de fenómenos clave mediante la simulación del modelo. La

simulación de la actividad neuronal es una herramienta de gran potencial para explorar la dinámica neuronal, sus fuentes biofísicas, los posibles mecanismos subyacentes en la señal neuronal y el complejo procesamiento de la información observada. Su potencial radica en la completa accesibilidad a las variables del modelo, el rango típicamente extenso de parámetros ajustables en el modelo que se pueden explorar y la capacidad para evaluar el papel de elementos distintos en el sistema o circuito incluyéndolos o excluyéndolos de las simulaciones. Aunque los modelos no pueden sustituir completamente la investigación en sistemas vivos, sí nos acercan a la comprensión de la dinámica neuronal compleja, siendo una metodología conveniente, eficaz y de bajo coste para los avances científicos. Además, los modelos son un complemento esencial para la neurociencia experimental, alcanzando descripciones detalladas donde los enfoques experimentales como la electrofisiología tienen limitaciones debido a la observabilidad parcial subyacente al método.

Los modelos pueden clasificarse según su nivel de descripción, es decir, qué nivel de simplificación/abstracción se utiliza, el detalle de la estructura/fenómeno que se modela y el tamaño de la red, o su capacidad para reproducir la actividad neuronal observada, por ejemplo, dinámicas caóticas. La Figura 2.9 ilustra este tipo de clasificación, con ejemplos de modelos de grandes redes como Potjans and Diesmann (2014) and Bezaire et al. (2016), de células individuales pero aún detallados como en Smith et al. (2013), y descripciones más abstractas como la propuesta en Izhikevich (2003). En cuanto al nivel de descripción, en los diferentes modelos biofísicos siempre hay una elección entre la descripción detallada de las no linealidades, canales y propiedades de excitación, y la eficiencia en la computación. En esta línea, los investigadores pueden elegir entre modelos basados en conductancia (Hodgkin & Huxley, 1952), ricos en la descripción de no linealidades, o modelos dinámicos simplificados (FitzHugh, 1961; Hindmarsh & Rose, 1984), que típicamente representan no linealidades con simplificaciones polinomiales (ver Torres and Varona (2012) para una revisión de diferentes niveles de modelado neuronal).

2.3.1 Modelos basados en conductancia

En esta tesis, todos los registros experimentales se han complementado con simulaciones mediante modelos basados en conductancia. Estos se definen como descripciones matemáticas de la dinámica de los canales iónicos, basadas en su conductancia dependiente del voltaje. El estudio pionero de Hodgkin and Huxley (1952) definió ecuaciones dinámicas basadas en el circuito eléctrico equivalente de las propiedades eléctricas de las neuronas en el axón gigante del calamar, ver Fig. 2.10.a). Este circuito también se puede utilizar para describir la configuración de registro intracelular, donde la pipeta se incluye como una corriente adicional compensada por el electrodo en la solución (ver Fig.

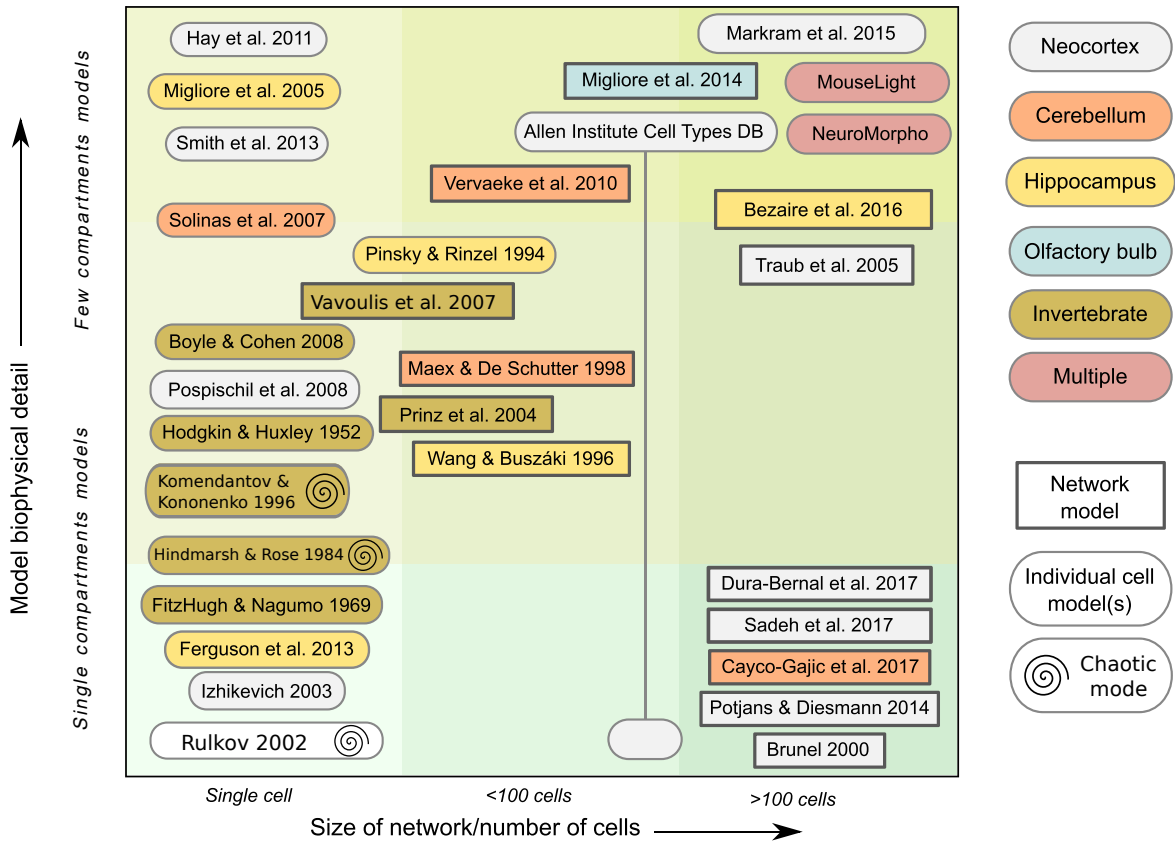


Figure 2.9: Modelos neuronales y de red clasificados por su nivel de detalle biofísico (los menos específicos están situados en la parte inferior del eje y), por estructura modelada (color de las cajas) y por el tamaño de la red (eje x). Figura adaptada de la Fig. 2 (Gleeson et al., 2019) bajo licencia Creative Commons CC-BY. Los modelos están clasificados por el detalle biofísico, siendo los modelos en la parte inferior los menos específicos; por el tamaño de la red modelada, de izquierda a derecha, una célula a cientos de células; y por la estructura cerebral que modelan, representada en cajas de colores. La forma de la caja también clasifica en modelo de red o célula individual. La espiral representa actividad caótica y ha sido incluida modificando la figura original. Una espiral en la caja indica la capacidad del modelo para producir actividad caótica sin alteraciones externas, es decir, reproducir variabilidad intrínseca espontánea. Aunque la figura no contiene todos los enfoques de modelos, ilustra hitos clave en el modelado neuronal.

2.10.b).

En estos modelos, la simulación de la actividad eléctrica neuronal se basa en la descripción matemática de diferentes canales iónicos en el circuito, cuya dinámica también está bien definida por compuertas de activación. Primero, hay una descripción matemática de la dependencia del voltaje en el tiempo, como se describe en la ecuación 2.3.1:

$$C_m \frac{dV}{dt} = -I - \sum I_x, : \quad (2.3.1)$$

donde V es el potencial de membrana, I es una corriente externa, por ejemplo, un estímulo externo

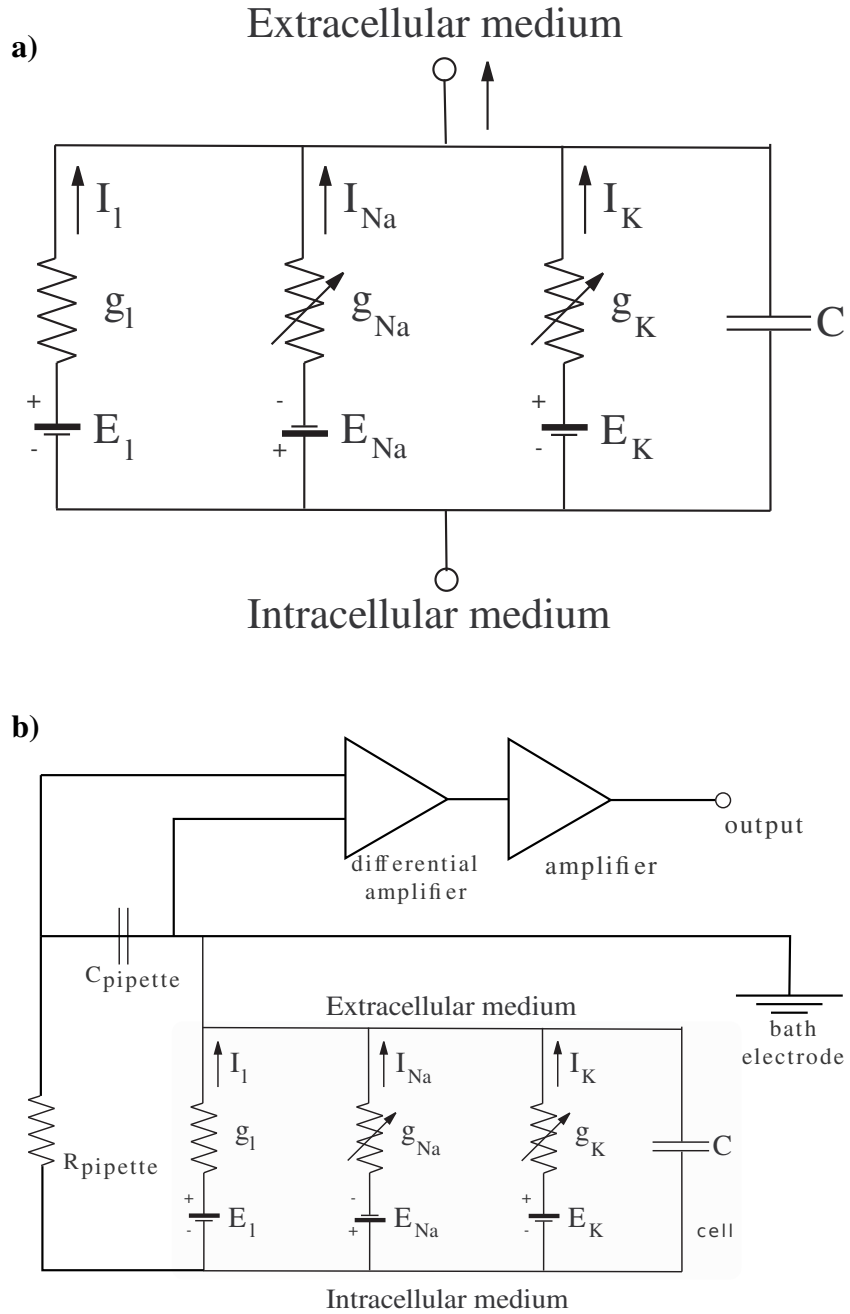


Figure 2.10: a) Circuito eléctrico que describe el potencial de membrana en un modelo de neurona basado en conductancia. b) Circuito eléctrico que representa el esquema para registros intracelulares.

o una corriente sináptica, I_x es la descripción de la corriente para cada canal involucrado en la generación del potencial de acción, por ejemplo, sodio, potasio, calcio (I_K , I_{Na} , I_{Ca}).

En segundo lugar, cada canal también se describe dependiente del voltaje compuesto por dinámicas de compuertas de activación:

$$I_x = g_x m^n h^n (V - E_x), \quad (2.3.2)$$

donde g_x es la conductancia máxima del canal, E_x es el potencial de reversión para ese canal y m y h representan las variables de activación e inactivación de la conductancia, respectivamente. Estas variables suelen tener una descripción no lineal (tendencia exponencial) dependiente del voltaje y el tiempo. Siguen generalmente la estructura en la ecuación 2.3.3:

$$\frac{dm}{dt} = \frac{m_\infty - m}{\tau_m} \quad (2.3.3)$$

donde $\tau_{m,i}$ son constantes de tiempo de relajación que suelen depender del voltaje y se modelan utilizando funciones sigmoides o gaussianas. Aunque aquí utilizamos m , esta fórmula también se aplica a las variables de inactivación.

Siguiendo el formalismo de Hodgkin y Huxley, las ecuaciones que describen la dinámica del voltaje y la dinámica de la conductancia de los canales activos (Na y K) en el circuito mostrado en la Fig. 2.10a) se describen en la tabla 2.1.

Ecuación de voltaje	$C \frac{dV}{dt} = I - g_K n^4 (V - E_K) - g_{Na} m^3 h (V - E_{Na}) - g_L (V - E_L)$		
	Variables de activación	Variable de inactivación	
variables de compuerta	$\frac{dm(t)}{dt} = \frac{m_\infty(V(t)) - m(t)}{\tau_m(V(t))}$	$\frac{dn(t)}{dt} = \frac{n_\infty(V(t)) - n(t)}{\tau_n(V(t))}$	$\frac{dh(t)}{dt} = \frac{h_\infty(V(t)) - h(t)}{\tau_h(V(t))}$

Table 2.1: Ecuaciones del formalismo de Hodgkin y Huxley para el voltaje y las variables de conductancia.

Esta combinación de canales genera la forma del *spike* mostrada en la Fig. 2.11a pero, como en las neuronas vivas, la combinación de diferentes canales produce salidas distintas, por ejemplo, neuronas de tipo con hombro y sin hombro (ver sección anterior, Fig. 2.3). Este es el caso de la forma de onda mostrada en la Fig. 1.11b. Esta forma de hombro puede reproducirse en modelos al incluir canales de calcio en su descripción.

Modelado de redes

Además del modelado de la generación de potenciales de acción, las sinapsis también pueden describirse con diferentes representaciones matemáticas dependiendo de su tipo y del nivel de especificidad. Una combinación de modelos basados en conductancia y sinapsis puede modular las redes neuronales en diferentes niveles de complejidad (Huerta et al., 2001; Aguirre et al., 2007; Latorre et al., 2013). Las sinapsis se introducen en modelos basados en conductancia como una corriente adicional que simula el efecto en la dinámica de la neurona de entradas químicas o eléctricas entrantes. En los modelos basados en conductancia, las sinapsis eléctricas o uniones gap generalmente

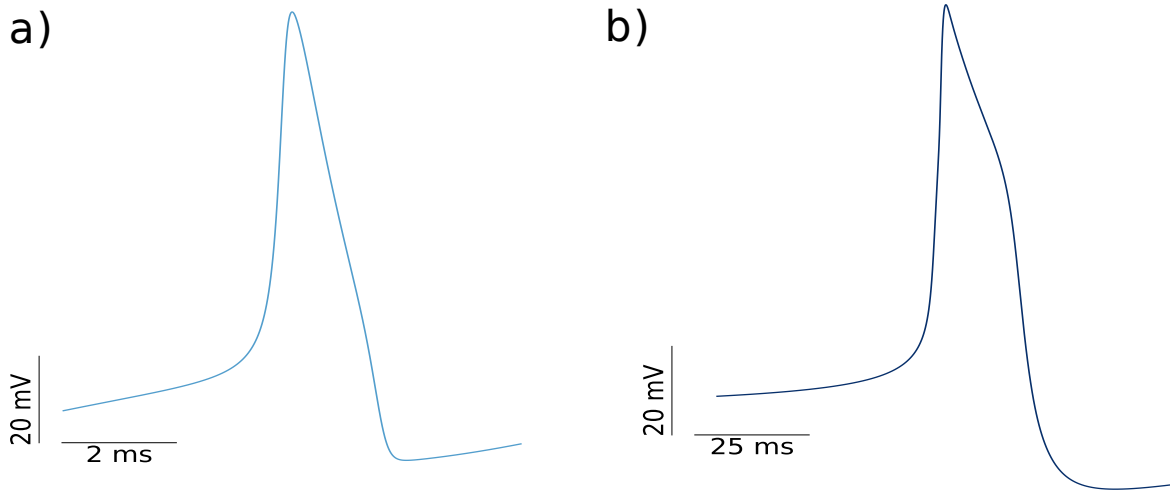


Figure 2.11: Simulaciones de dos tipos distintos de potencial de acción: sin hombro (a) y con forma de hombro (b), descritos por las ecuaciones en Hodgkin and Huxley (1952) y Vavoulis et al. (2010), respectivamente.

se definen por la siguiente ecuación:

$$I_{ij}(t) = \bar{G}_{ij}(V_i(t) - V_j(t)) \quad (2.3.4)$$

donde i y j representan las dos neuronas que conforman la sinapsis eléctrica y \bar{G}_{ij} es una constante que representa el valor máximo de la conductancia sináptica en la conexión. Para las uniones gap simétricas, la otra célula recibe exactamente la misma corriente con signo inverso.

Por otro lado, las sinapsis químicas son por definición asimétricas y pueden describirse como en la ecuación 1.3.5:

$$I_{ij}(t) = G_{ij}(t)(V_i - E_j^{syn}) \quad (2.3.5)$$

donde E_j^{syn} es el potencial de inversión de la sinapsis, el valor del voltaje en el cual la corriente sináptica se cancela, y G_{ij} puede ahora tener dinámicas complejas considerando el tráfico de neurotransmisores, por ejemplo, como en la ecuación 1.3.6 (Torres & Varona, 2012).

$$G_{ij}(t) = \bar{G}_{ij}\Theta(t - t_j^{sp})\alpha(t - t_j^{sp}) \quad (2.3.6)$$

donde \bar{G}_{ij} es el valor constante para la conductancia, t_j^{sp} es el momento en que ocurre el *spike* presináptico. $\Theta(x)$ es la función escalón de Heaviside y $\alpha(t)$ es una función para modelar las respuestas postsinápticas evocadas, que puede definirse con una dependencia no lineal, por ejemplo, mediante funciones exponenciales.

Así, dependiendo de la selección de este nivel de especificación, la neurona puede ser activada por (i) una causa binaria: ocurrencia o ausencia de un potencial de acción, (ii) un modelo dinámico que también depende del nivel de voltaje postsináptico como una sinapsis gradual donde la concentración de

neurotransmisores depende del voltaje presináptico, o (iii) un modelo que describa otros fenómenos sinápticos dinámicos más complejos como la depresión sináptica y/o facilitación. En los últimos casos, el nivel de especificación es más alto, con una descripción más rica de la dinámica sináptica. Este es el caso, por ejemplo, de la sinapsis gradual en el modelo CPG de Vavoulis et al. (2007), que se discutirá en el capítulo de métodos, sección 4.4.1, o el modelo de Tsodyks and Markram (1997), representado por las ecuaciones 2.3.7 y 2.3.8:

$$\frac{dU}{dt} = -\frac{U}{\tau_{\text{rec}}} + U_{\infty}(1-U)\delta(t-t_{\text{spike}}) \quad (2.3.7)$$

$$\frac{dX}{dt} = -\frac{X}{\tau_{\text{fac}}} + (1-X)\frac{U(t_{\text{spike}})}{U_{\infty}}\delta(t-t_{\text{spike}}) \quad (2.3.8)$$

donde U es la fracción de recursos disponibles para la liberación, X es la fracción de recursos de neurotransmisores disponibles en la terminal sináptica. τ_{rec} es la constante de tiempo de recuperación de recursos sinápticos y τ_{fac} la constante de tiempo de facilitación sináptica. U_{∞} es el valor de estado estacionario de U y t_{spike} es el momento del *spike* presináptico. La función delta considera que un *spike* llega a la sinapsis en un tiempo fijo.

2.3.2 Variabilidad en los modelos computacionales

La mayoría de los estudios utilizan modelos deterministas que producen actividad neural regular, los cuales son suficientes para muchas preguntas de investigación al explorar respuestas de entrada/salida, estudiar el papel de diferentes elementos biofísicos o apoyar resultados experimentales sobre dinámicas en estado estacionario. Sin embargo, los sistemas vivos son altamente variables, a menudo funcionan en regímenes transitorios y frecuentemente muestran actividad caótica mientras siguen produciendo actividad secuencial y robusta con patrones (Selverston et al., 2000), como es el caso de los CPGs. Se ha demostrado que la variabilidad en la actividad de las neuronas vivas juega un papel importante en tareas relevantes de procesamiento de información (Ding & Glanzman, 2011; Masquelier, 2013; Renart & Machens, 2014; Hutt et al., 2023; Ribeiro et al., 2024). Aunque este es un aspecto clave en la dinámica neural, los modelos generalmente excluyen la variabilidad intrínseca de su descripción, particularmente en las formas de onda del potencial de membrana y en las dinámicas adaptativas colectivas. Para inducir variabilidad, una solución común en la literatura es añadir ruido estocástico como entrada externa (Linaro et al., 2011; Pezo et al., 2014; Zheng et al., 2020). Sin embargo, este es un enfoque limitado cuando se explora el papel de la variabilidad funcional intrínseca, que es generada dinámicamente por las neuronas y los circuitos para tareas computacionales específicas, por ejemplo, para la coordinación de secuencias. Hay varias posibilidades para incluir

variabilidad en la dinámica intrínseca neuronal como es el caso de Hindmarsh and Rose (1984) o Komendantov and Kononenko (1996), donde, en ambas descripciones, hay una combinación de parámetros que conducen a estados caóticos, donde la actividad resultante no es regular. Cuando la fuente de la variabilidad en el sistema proviene de sus propiedades intrínsecas, existe la posibilidad de estudiar las dinámicas asociadas y el papel de esta variabilidad en el sistema sin fuentes externas aleatorias, que en las dinámicas ciclo a ciclo pueden anularse.

2.4 Estudios de animales vertebrados e invertebrados

El estudio de la dinámica neuronal y el comportamiento se lleva a cabo utilizando muchos modelos animales diferentes. Además de los modelos dominantes de roedores, se han realizado hallazgos de valor incalculable utilizando invertebrados, como en genética y biología del desarrollo en *C. elegans* (Brenner, 1974), *Zebra fish* (Streisinger et al., 1981) y *Drosophila* (Nüsslein-Volhard & Wieschaus, 1980); dinámica neuronal en *Aplysia* (Wachtel & Kandel, 1967) o *Loligo* (Hodgkin & Huxley, 1952), actividad motora en *Panulirus* (Selverston et al., 1976) y *Carcinus maenas* (Eisen & Marder, 1982) o *Lymnaea stagnalis* (Benjamin & Rose, 1979), el principal modelo animal en esta tesis. Además de estos ejemplos, estos modelos animales se han utilizado en una amplia variedad de campos, incluidos estudios conductuales, ecotoxicología, evolución, modelado de enfermedades humanas, etc. (Romanova & Sweedler, 2018).

A pesar de las diferencias cerebrales entre invertebrados y mamíferos, existen muchas características universales de los sistemas nerviosos que pueden extrapolarse a los humanos. Debemos tener en cuenta que cualquier modelo animal sigue siendo un marco de investigación, con diferencias respecto al enfoque real de estudio –el cerebro humano– y como modelo, existen diferencias en la estructura, incluso dentro de las especies de mamíferos (Preuss, 2000). Por lo tanto, mediante el uso de modelos computacionales o explorando más especies animales, se puede establecer una verdad "base" para los aspectos que conforman la dinámica neuronal y del comportamiento.

Los hallazgos en invertebrados no alcanzan la misma relevancia en muchas ocasiones, a menudo bajo la excusa de que las características en los invertebrados no pueden extrapolarse a los humanos. Sin embargo, los modelos de invertebrados han demostrado su utilidad no solo en ciencia básica. Podemos encontrar ejemplos de esto en los estudios de enfermedades humanas, memoria, actividad motora y neuromodulación. En concreto, en el estudio de procesos neuronales, la facilidad de accesibilidad y el número finito de neuronas de gran tamaño en estos sistemas han hecho de los invertebrados un caso de estudio interesante (Gelperin, 2019).

Entre las ventajas de usar invertebrados, cabe destacar el fácil acceso al sistema nervioso, la duración de la actividad espontánea después de la disección durante horas y la facilidad de cría y reproducción o la simplicidad de sus características biológicas, que hacen posible una descripción completa de ellas, como la descripción genómica de *C. elegans* o el sistema nervioso en *Lymnaea stagnalis*. Además, en algunas de estas especies se ha realizado un estudio exhaustivo en las últimas décadas, por lo que hay una gran cantidad de literatura para cada una, incluso en diferentes campos. Además, a pesar de la simplicidad de estos sistemas, su sistema nervioso sigue siendo capaz de generar actividad neuronal secuencial robusta, comportamiento automático e incluso procesos de aprendizaje.

Aparte de los posibles avances en la ciencia que pueden darse desde un punto de vista productivista, los modelos de invertebrados también pueden cerrar la brecha entre recursos y ciencia, permitiendo que laboratorios de bajos ingresos *hagan* ciencia. Estos modelos animales suelen ser más baratos de obtener y mantener, y generalmente hay posibilidad de criar colonias propias. Esto hace que su uso sea fácilmente generalizable y rompe algunas barreras económicas en la ciencia, donde los países de altos ingresos suelen centralizar la producción científica con fuertes convenciones en qué modelos animales y técnicas usar (Stephan, 2015; Castillo & de la Guardia, 2017).

***Lymnaea stagnalis*, el gran caracol de estanque**

En esta tesis, exploramos el sistema nervioso del "gran caracol de estanque", *Lymnaea stagnalis* (ver Fig. 2.12a). Este molusco ha sido un modelo de estudio relevante desde finales del siglo XX, cuando se utilizó de manera extensa para estudiar procesos neurobiológicos y el funcionamiento del sistema nervioso. Este esfuerzo de su estudio durante de años ha resultado en una descripción detallada de los ganglios bucales, incluyendo las tres principales interneuronas que lo conforman (Benjamin et al., 1979; Rose & Benjamin, 1979; Benjamin & Elliott, 1989; Brierley et al., 1997) y las neuronas modulatorias que influyen en la actividad del CPG alimentario, como la neurona SO y la neurona CGC en el ganglio cerebral (McCrohan & Benjamin, 1980; Rose & Benjamin, 1981; Kemenes et al., 2001). Además de los ganglios bucales, otras neuronas en diferentes ganglios también están bien identificadas, con características específicas como el acoplamiento eléctrico o neuronas que contienen dopamina como el ganglio parietal derecho (Winlow et al., 1981; Benjamin & Pilkington, 1986).

Además de estos estudios, este animal como modelo, ha sido clave en otros campos como el huésped-parásito o la edición del genoma. Este último campo se debe al ciclo de vida corto y bien estudiado en *L. stagnalis* (ver Fig. 2.12), así como a la facilidad para criárslos en laboratorio, sin perder sus principales características a lo largo de las generaciones (Noland & Carriker, 1946). Las grabaciones

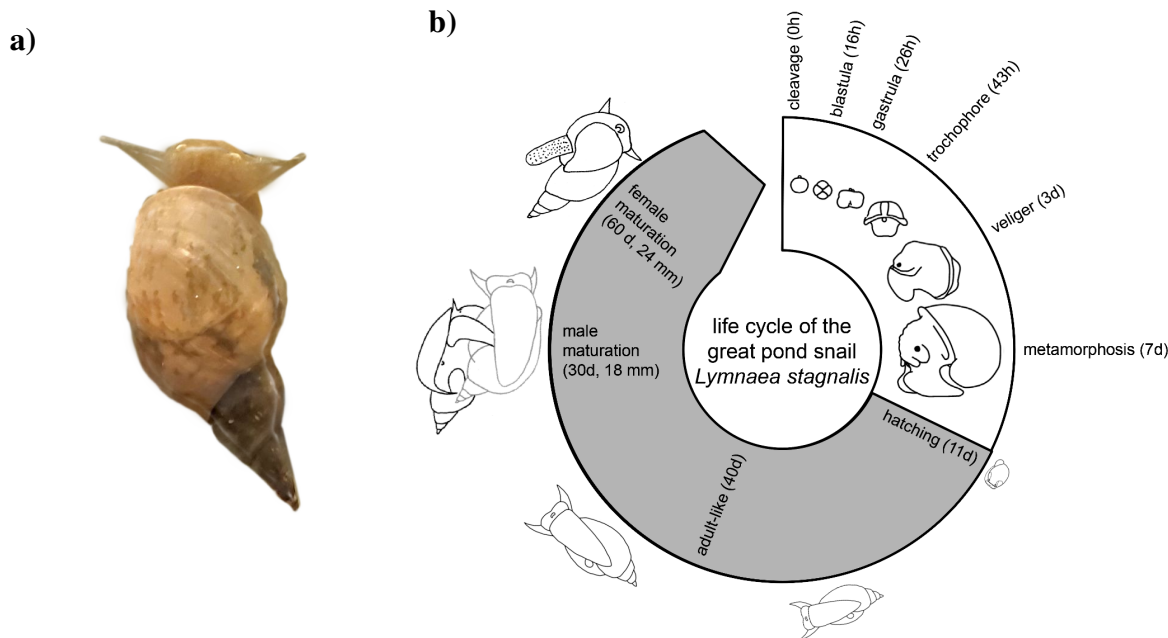


Figure 2.12: a) Fotografía del animal *Lymnaea stagnalis*. b) Representación del ciclo de vida de *L. stagnalis*.

Figura 2A de Fodor et al. (2020) ([Creative Commons license](#)).

y análisis en este trabajo están enmarcados en el estudio de la actividad neuronal en su sistema nervioso central (SNC). El SNC de *L. stagnalis* está compuesto por once ganglios que conforman el sistema: pares simétricos de ganglios bucal, pedal, cerebral, pleural y parietal, y un solo ganglio visceral (ver Sec. 4.1). Nos centraremos especialmente en su circuito CPG alimentario, que mediante una combinación distribuida de neuronas motoras e interneuronas ubicadas principalmente en los ganglios bucales y cerebrales, produce un patrón rítmico de movimiento que permite la alimentación en tres fases (protracción, raspado y deglución). Además de este estudio del CPG, trabajaremos en las neuronas gigantes ubicadas en el ganglio parietal derecho (RPG), aprovechando las características de la actividad: alto voltaje (hasta 80mV) y señal lenta (30 a 100 ms por spike) para analizar en detalle la dinámica del potencial de acción.

2.5 Estimulación neuronal

2.5.1 Técnicas de estimulación

La estimulación neuronal ha sido una parte esencial en el estudio de la dinámica neuronal, permitiendo la modulación del sistema nervioso para explorarla, reproducirla y alterarla. Hay varias técnicas para realizar esta estimulación, que podríamos clasificar en químicas –utilizando componentes químicos para bloquear/mejorar los mecanismos neuronales–, eléctricas –inyectando corriente

en la membrana celular o los nervios–, magnéticas –poniendo el sistema bajo el efecto de campos magnéticos–, mecánicas, –incluyendo el movimiento como perturbación–, u ópticas –donde se estimulan neuronas o circuitos a través de un proceso de iluminación. En esta tesis, nos centraremos en la eléctrica y la óptica. Con respecto a las técnicas eléctricas, desde las primeras aplicaciones de electrofisiología (Marmont, 1949; Cole, 1955; Neher & Sakmann, 1976) y la posterior aparición de la técnica de *patch-clamp* Hamill et al. (1981), se han desarrollado numerosas técnicas diferentes para distintos sistemas. El *voltage-clamp* y el *patch-clamp* modificaron el paradigma en la fisiología y la medicina básica en el estudio de la dinámica de la membrana celular con un gran detalle que todavía hoy lidera métodos de registro y estimulación precisos (Hamill et al., 1981). A la técnica de *voltage-clamp* le siguieron variaciones como el *dynamic-clamp*, que mejora las posibilidades de electrofisiología combinándolo con las posibilidades de computación a través de un protocolo de bucle cerrado en tiempo real (Nowotny & Varona, 2022). Esto permite implementar algoritmos específicos para intervenir en la actividad neuronal y probar diferentes enfoques (Chamorro et al., 2012). En cuanto a la estimulación óptica, una técnica novedosa y ampliamente utilizada es la optogenética, en la cual, mediante la modificación genética de los animales, se consigue que las neuronas sean reactivas a la luz y ha tenido grandes logros en las últimas décadas utilizando tanto para la estimulación como para la exploración y visualización de la actividad (Chen et al., 2022). Otro ejemplo aún en estudio es el láser infrarrojo cercano, una técnica novedosa que se explorará en detalle a lo largo de esta tesis. Esta técnica ha demostrado su potencial para la estimulación neuronal en diferentes sistemas como el hipocampo (Liang et al., 2009), ganglios espinales en la cóclea (Goyal et al., 2012; Barrett et al., 2018; Brown et al., 2020) y otros sistemas (Shapiro et al., 2012; Cayce et al., 2014; Begeng et al., 2022).

2.5.2 Neuromodulación y su necesidad para aplicaciones clínicas

Más allá de la necesidad de la estimulación neuronal en investigación básica para comprender y explorar la señalización y dinámica del cerebro, hay un impacto social directo de la estimulación neuronal en aplicaciones clínicas. En este contexto, la neuromodulación es un área de la medicina que involucra muchas especialidades y que puede definirse como "la ciencia de cómo las intervenciones eléctricas, químicas y mecánicas pueden modular las distintas funciones del sistema nervioso que es inherentemente no destructiva, reversible y ajustable" (traducida del texto original Krames et al., 2009). Este campo es tan importante debido a sus posibilidades en el tratamiento de trastornos neuronales, tanto por estimulación funcional como por la modulación a largo plazo a través de la plasticidad neuronal. La neuromodulación puede clasificarse, según la tecnología utilizada, como

invasiva o no invasiva. Las tecnologías invasivas son aquellas que requieren una interacción directa con el sistema vivo, lo que causa daño, por ejemplo, al requerir una cirugía. Un ejemplo conocido de este tipo de neuromodulación es la estimulación cerebral profunda (DBS), esta técnica se ha utilizado de manera efectiva para tratar trastornos del movimiento al estimular eléctricamente el cerebro en ciertas áreas cerebrales después de implantar un dispositivo (Limousin & Foltynie, 2019; Hariz & Blomstedt, 2022). En el caso de la neuromodulación no invasiva, podemos encontrar la estimulación magnética transcraneal (TMS), que mediante campos eléctricos estimula ciertas áreas del cerebro, exitosa, por ejemplo, en el tratamiento de trastornos como la depresión o el trastorno obsesivo compulsivo (Valero-Cabré et al., 2017; Clarke et al., 2018). Cada tipo de técnica tiene sus propias ventajas, las técnicas invasivas suelen ser más precisas en espacio y tiempo, mientras que las técnicas no invasivas ofrecen más flexibilidad y adaptabilidad a diferentes pacientes y contribuyen a la difusión de la técnica. En este contexto, las técnicas ópticas discutidas para la estimulación en la investigación básica también han ido ganando popularidad para aplicaciones clínicas. En esta tesis exploraremos un nuevo tipo de estimulación no invasiva con láser infrarrojo cercano de onda continua.

CHAPTER 3

Motivation and Objectives

During this work, we will analyze and explore neuronal activity focusing on its dynamics and following a bottom-up approach. In the state of art, we discussed the importance of sequential dynamics, and how we can describe this sequentiality at different scales, from milliseconds (ionic channels) up to hours or days in terms of behavior or life cycles. It is important to study neuronal dynamics at different spatial levels to understand the mechanisms behind the information processing and the subsequent outputs. To explore sequential activation at cell levels, we will use intracellular recordings of single neurons and cells from CPG circuits combining an experimental study with conductance-based models. In the case of CPG sequential activity, we will characterize and quantify cycle-by-cycle the variability of the sequence intervals. Although this approach has not always been typical in this kind of studies (Anwar et al., 2022), the assessment of the variability of sequence time-intervals can unveil important characteristics and constraints for motor coordination (Elices et al., 2019). Bursting activity is a good case study for this goal, since it is usually easier to define the phases associated to a specific motor activity based on burst events. In this work, we will discuss the generalization of the presence of sequential dynamical invariants, discovered in the pyloric CPG (Elices et al., 2019), exploring them in the feeding CPG of *Lymnaea stagnalis*, both in a computational model and in experimental recordings. We will explore the constraints underlying the CPG sequence time intervals but also the possible functional role of these flexible restrictions under different cases of activation of the CPG, e.g., feeding initiated by the presence of food or feeding activity initiated even in the absence of food.

On the other hand, we also reviewed in the previous chapter the importance of stimulation techniques to explore neural dynamics and behavior and also for possible clinical applications. In the second part of this work, we will explore Continuous-Wave Near-Infrared (CW-NIR) laser, a novel technique for neuronal dynamics modulation. This optical stimulation has a large potential for effective non-

invasive modulation of neuronal dynamics, but its exact mode of action is not known yet. There are different hypotheses, each one pointing to different biophysical candidates to explain the laser action during the signal modulation, such as calcium channels, capacitance or long-term processes such as mitochondria modulation, as well as different sources for the effect, such as photo-thermal or photo-chemical elements. During this work, we will characterize the CW-NIR effect in single neurons combining experimental and theoretical approaches to narrow down the possible candidates for the source of the effect. We will also present a novel approach for closed-loop stimulation to predict spikes and stimulate at different stages of the action potential generation.

In summary, the objectives of this thesis are:

1. To explore the sequential nature of neuronal dynamics at distinct description levels.
2. To study sequence interval variability constraints and relationships in neural models and living circuits.
3. To analyze the feeding CPG of *Lymnaea stagnalis* to provide evidence of the universality of sequential dynamical invariants found in the pyloric CPG by:
 - (a) Characterizing the sequential invariants cycle-by-cycle in a bursting CPG model.
 - (b) Analyzing intracellular recordings with spontaneous activity and with different rhythm initiation stimulation protocols.
4. To illustrate the possible functionality of sequential dynamical invariants in biohybrid robotics.
5. To test the capability of CW-NIR laser stimulation to modulate neuronal dynamics by:
 - (a) Characterizing the CW-NIR effect in the spike waveform dynamics.
 - (b) Analyzing the ability of this neurotechnology to change the spiking rate and the circuit dynamics.
6. To study the possible biophysical candidates underlying the CW-NIR effect in model simulations.
7. To design and implement a new technique for CW-NIR stimulation in closed-loop.

Understanding the sequential patterns at the level of CPGs and single neurons allows us to identify universal principles that can be applied to broader neural circuits and systems. The sequential dynamics explored in the first part of this thesis provides foundational insights into the intrinsic timing

CHAPTER 3: MOTIVATION AND OBJECTIVES

mechanisms that govern the coordination of sequential neural processes. By exploring novel modulatory mechanisms such as near-infrared laser stimulation, we bridge the gap between neural dynamics and novel noninvasive neurotechnologies. Finally, the activity-dependent laser illumination protocol allows a precise dissection of the laser effect on the sequential activation of ionic-channels.

CHAPTER 3: MOTIVATION AND OBJECTIVES

CHAPTER 4

Materials and Methods

This chapter will cover the common ground of the materials and methods applied in this thesis for the results described in chapters 5 and 6. The methods presented here will be complemented with a specific methodological description in those two chapters.

4.1 The neural system of *Lymnaea stagnalis*

The neural system of *Lymnaea stagnalis* (the great pond snail) is shown in Fig. 4.1. As in other mollusks, e.g. *Clione limacina*, the neural system is composed of several ganglia, each of them controlling (mainly, but not exclusively) some specific function of the snail. Figure 4.1.a shows a labeled image of the different ganglia in this system. Ganglia in the neural system are paired and distributed symmetrically, except from the visceral ganglion (unique) and the parietal, which is larger in the right side compared to that in the left side (see Fig. 4.1.b). All ganglia are interconnected by nerves (gray areas in the figure). As mentioned before, each ganglion has an associated behavioral task in the snail. From top to bottom, we find first the buccal ganglia (1), which control the buccal muscle involved in the processes of open-rasp-swallow, known as the feeding cycle, initiated by a CPG circuit contained in these ganglia. Located on the sides of the diagram, after cutting the cerebral commissure that joins them, we find the two cerebral ganglia (2) are involved in the activation and modulation of specific neurons, as well as neural circuits and processes. In the center of the figure we find the pedal ganglia (3) which control the snail pedal movements as crawling or swimming. The pleural ganglia (4), which contain sensory neurons, are connected to the mantle. Finally, at the bottom of the diagram, we find the parietal (5) and visceral (6) ganglia –connected to organs such as the intestine, the heart, and part of the genital system, and are involved in respiration, control of heartbeat and other visceral functions (Benjamin, 2008).

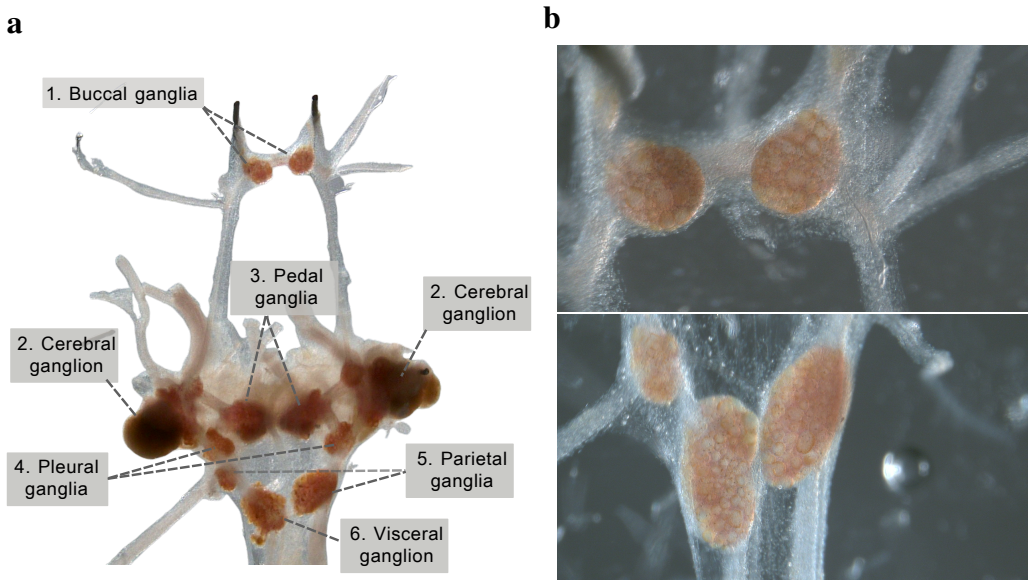


Figure 4.1: Neural system of *Lymnaea stagnalis*. a) Diagram of the neural system labeled for all ganglia. b) Top panel: photograph of the buccal ganglia. Bottom panel: photograph of the two parietal ganglia and visceral ganglion.

Neuronal recordings shown in this work are from the CPG in the buccal ganglia in chapter 5. In chapter 6 the recordings are from the right parietal ganglia (RPG), containing large neurons with tonic firing and a pair of electrically coupled giant cells in the RPG, and from the visceral ganglia. These ganglia are illustrated in Fig. 4.1b.

4.2 The feeding CPG of *Lymnaea stagnalis*

The feeding activity of the *L. stagnalis*, concerning the buccal mass, is classified in three main steps: protraction, rasp and swallow, alternating with states of "rest". This sequence of buccal movements in the snail is generated by the motoneurons distributed in the ganglia. Each of these phases is associated to the activation of one interneuron from the CPG: N1M, N2v, N3t, and followed by the motoneurons associated to them. This is a complex distributed system where motoneurons do not exclusively follow the interneurons but are also implied in the feeding cycle activation (Staras et al., 1998). In this circuit, there are also some modulatory neurons involved such as the SO neuron (in the same buccal ganglia), CGC or CV1a neurons (in the cerebral ganglia). Initial resting states, where the CPG as well as the motoneurons have no activity, may change due to a sensory input.

This CPG circuit can be studied in a dissected preparation, since the neurons are active for a long time after the isolation of the system. Particularly, the CPG rhythm is maintained after its activation and it is generated autonomously by the neurons in the circuit. However, due to the slow dynamics of

the system and the nature of the experimental setting, different ways to initiate the rhythm are have also been described. Previous literature in *L. stagnalis* proposed several solutions to this problem. The first solution is stimulating the neurons responsible for the initiation of the feeding rhythm, such as the SO modulator neuron on the buccal ganglia, the CBC, or the CVs neurons, located on brain ganglia (Benjamin, 2012). However, access to these neurons is not always easy and keeping them in constant stimulation might be necessary. Thus, another option for activation discussed in the literature is applying octopamine. Some neurons in the buccal ganglia are sensitive to octopamine and, as a result, this procedure activates the rhythm (Vehovszky et al., 2004). Alternatively, in a semi-intact preparation, sucrose can be applied to activate the rhythm (Straub et al., 2002; Vehovszky et al., 2004; Vavoulis et al., 2007). A similar approach performing a complete dissection consists in stimulating the Medium Lip Nerve (MLN). The recordings analyzed in chapter 5 correspond to either spontaneous activity or to electrical stimulation in CV1a, SO neuron, or the Medium Lip Nerve (MLN).

4.3 Electrophysiology in *Lymnaea stagnalis*

In this thesis, intracellular neuronal recordings have been mainly carried out in the mollusk *Lymnaea stagnalis*. Beyond the advantages of invertebrates discussed in section 1.4 – its easily accessible neural system, and the size and resistance of its neurons to electrode impaling –, the great pond snail's neural system has been extensively described including the feeding CPG, which is the model of study in chapter 5 of this work. Also its slow dynamics are convenient when studying the sequential evolution of the modulation in high temporal resolution, as in the case of the laser stimulation described in chapter 6.

The technique followed for neural activity acquisition was intracellular recordings with sharp electrodes filled with 3 M KCl. In this technique, a glass micropipette penetrates the cell to measure its electrical activity, with a minimal damage to the cell, and the evolution of the membrane potential is then recorded using a DC amplifier (ELC-03M, NPI Electronic, Hauptstrasse, Tamm, Germany). Glass micropipettes were pulled using a Sutter Instruments puller (Model P-97) (see Figure 4.2). Membrane potential recordings were acquired at 10 KHz using an A/D board (PCI-625 with a BNC-2090A DAQ device, National Instruments).

To facilitate the access to the cell, the sheath above it was reduced using protease (Sigma XVII) over the ganglion for ~1 min and then washed out with fresh saline (leaving the protease for longer time makes the impalement even more complicated due to the softness of the tissue). In order to record

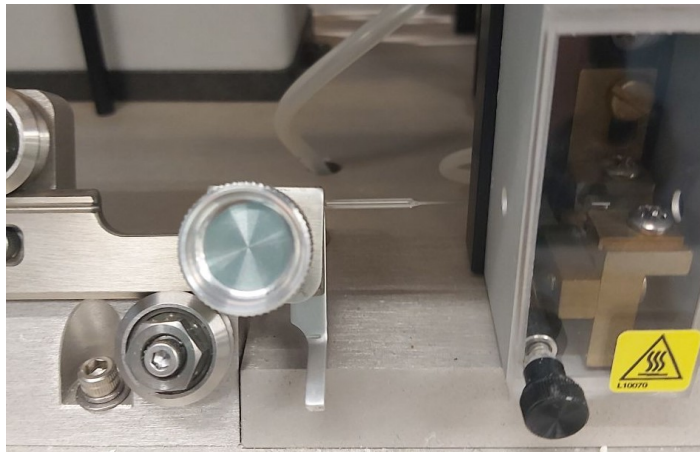


Figure 4.2: Example of fabrication of a sharp micro-electrode glass in a pipette puller.

cell signals extra- and intracellularly, it is necessary to have full access to the neural system (see Garrido-Peña, 2022 for more details). The preparation was immersed in a saline solution (in mM: 51.3 $NaCl$, 1.7 KCl , 1.5 $MgCl_2 \cdot 6H_2O$, 4.1 $CaCl_2 \cdot 2H_2O$, 5 HEPES, corrected to pH 7.8 with 4 M $NaOH$). All procedures followed the European Commission and Universidad Autónoma de Madrid animal treatment guidelines.

The recordings analyzed in section 5.4 were carried out using a equivalent procedure by Dr. Michael Crossley at the University of Sussex.

4.4 Conductance based models

For the theoretical analyses in this work, we used simulations of conductance-based models. As discussed in section 1.3, this kind of models are based on a specific combination of ionic channels with time-dependent conductance dynamics that provide a highly realistic description of the action potential generation. There are many different conductance-based models and formalisms depending on the specific combination of channels. Models used in this work, for both chapters 5 and 6, were designed for neurons in *Lymnaea stagnalis*, particularly for the neurons in the feeding CPG of the buccal ganglia –SO, N1M, N2v, N3t, (Vavoulis et al., 2007), for a neuron in the cerebral ganglia, CGC (Vavoulis et al., 2010), and we also employed the classical model by Hodgkin and Huxley (1952) and the described in Sec. 5.2.4. The feeding CPG model is a detailed description of the circuit with a combination of two-compartment neuron and gradual synapse models, which allows sufficient flexibility in the circuit to induce variability from a current ramp stimulus –this will be discussed in detail in section 5.3. The second model –CGC model– simulates a tonic firing and shoulder shaped spike waveforms, similar to the activity in some neurons in the right parietal ganglion characterized

in chapter 6.

4.4.1 Feeding CPG model

The Vavoulis et al. (2007) description of *Lymnaea stagnalis* individual neurons considers a two-compartment model to represent the soma and the axon as differentiated structures coupled by an axial resistance. This separation of the soma and the axon is used to regulate the interaction between the fast and slow dynamics in the model. The slow dynamics are located at the soma, whereas the fast dynamics are included in the axon compartment. This distributed formalism is represented in Fig. 4.3a., where each circle represents either soma or axon, containing the different ionic currents for each one. The description of the voltage dynamics is provided for soma (Eq. 4.4.1) and axon (Eq. 4.4.2) compartments:

$$\tau_m \frac{dV_S}{dt} = i_{inj} - i_{L,S} - i_X - i_{ec,S} - i_{syn}, \quad \text{with} \quad i_X = [i_{ACh}, i_{NaL}, i_T] \quad (4.4.1)$$

$$\tau_m \frac{dV_A}{dt} = -i_{L,A} - i_{NaT} - i_K - i_{ec,A} \quad (4.4.2)$$

Here we follow the notation of the original work where τ_m represents the time constant of the membrane (in ms) given by the ratio of the membrane capacitance (in nF) and the leakage conductance (in μ S). In equations 4.4.1 and 4.4.2, i variables (given in mV) are the product of the corresponding currents (in nA) times the passive input resistance given in $M\Omega$. Below we will refer to the currents in capital letters as I , following the common notation.

The soma compartment contains a slow current I_X whose ionic nature depends on the specific CPG neuron described (see Fig. 4.3a.). Thus, I_X represents one channel, either I_{ACh} , I_{NaL} or I_T , responsible of the specific slow dynamics associated with neurons N1M, N2v and N3t, respectively. Along with the slow ionic channel and the leakage channel $I_{L,S}$, the soma compartment also receives the synaptic current I_{syn} and the injection current I_{inj} . All currents are explained in detail below.

On the other hand, fast channels are part of the axon compartment: a fast inactivating sodium current I_{NaT} and a delayed rectifier potassium current I_K . These channels, along with the axon leakage channel $I_{L,A}$ follow the definition in Hodgkin and Huxley (1952) model. The model cells as described above are not endogenously bursters so to achieve bursting activity, a distinct constant value of i_{inj} is applied to the cells.

The CPG topology scheme is shown in Fig. 4.3, where the connections between neurons are represented by dashed or solid lines, depending on whether the connection is slow or fast, respectively, and

filled or empty circles at their end denoting the direction and the effect on the postsynaptic neuron: excitation (empty circles) or inhibition (filled circles). Individual neurons following the previous description are connected by graded synapses, defined by equations 4.4.3-4.4.6 (Vavoulis et al., 2007). The differential point of a graded synapse is that it is dependent on voltage values and time, many synapses models used are just dependent on a trigger voltage value, that activates the synapse (see chapter 1.3.1 for details). This model of synapse allows dynamical adaptation of neurons in the circuit to maintain the rhythm despite even under induced variability.

$$i_{syn} = \sum_j \gamma_{syn,j} s_j (V_S - E_{syn,j}) \quad (4.4.3)$$

$$\frac{ds_j}{dt} = \frac{r_j - s_j}{\tau_{syn,j}} \quad (4.4.4)$$

$$\frac{dr_j}{dt} = \frac{r_{\infty,j} - r_j}{\tau_{syn,j}} \quad (4.4.5)$$

$$r_{\infty,j} = \frac{1}{1 + e^{(-40 - V_{prev_S})/2.5}} \quad (4.4.6)$$

where index j runs over all presynaptic neurons and $\gamma_{syn,j}, E_{syn,j}, \tau_{syn}, V_{prev_S}$ are the product of input resistance and maximal synaptic conductance, the synaptic reversal potential, the synaptic time constant and the presynaptic potential, respectively.

The three inter-neurons described in this circuit have different waveform shapes, determined by their corresponding ionic channel and the axon connectivity, in Fig. 4.4 there is an example of a simulation with all neurons in the circuit. First, N1M voltage characteristics are provided by an acetylcholine sensitive channel ($i_{ACh} = 200 * p^3 * (V_S + 30)$), which causes the gradual spiking frequency increase as well as the visible plateau, i.e., the slow wave is sustained before hyperpolarization. On the other hand, N2v has a slowly inactivating sodium channel ($i_{NaL} = 2 * p^3 * q^3 * (V_S - 55)$), which causes the slow depolarization in this neuron. N2v neuron has a lower spiking frequency caused by the conductance value given for the axial g_{ec} linking the two compartments, which is much lower in this cell. Finally, the N3t neuron has the particularity of a post inhibitory rebound, which generates an initial fast spiking followed by a decrease in the firing rate as the burst evolves. This latter property is caused by a low-threshold calcium channel ($i_T = 3.27 * p^3 * q * (V_S - 80)$). SO neuron has no particular I_X channel (in contrast to N1M, N2v, and N3t neurons) so its activity is the result of the combination of the common ionic channels in the axon and the soma.

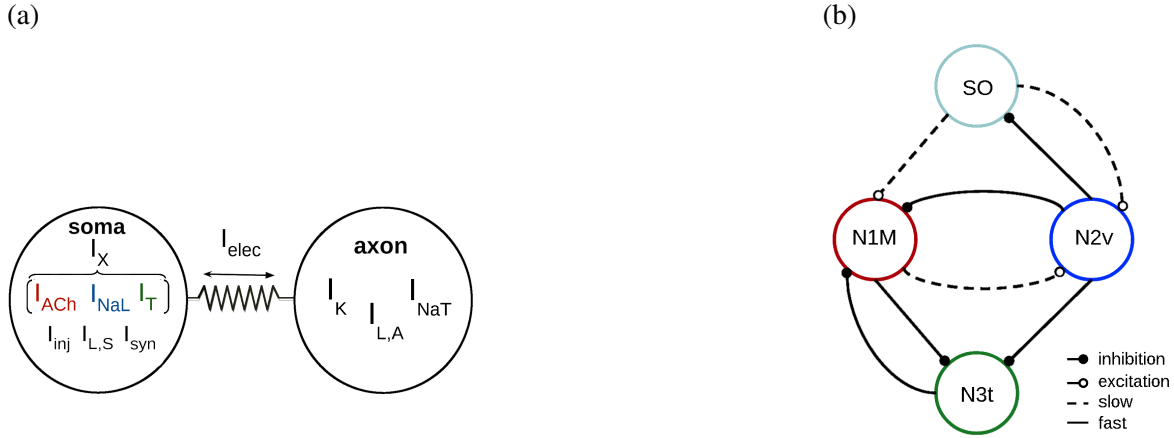


Figure 4.3: **Panel (a).** Ionic channel distribution in the two-compartment description for the individual neurons in the Vavoulis et al. (2007) model used in this study. At the soma: I_{ACh} , acetylcholine ionic channel; I_{NaL} , slowly inactivating sodium ionic channel; I_T , low-threshold calcium current; I_{inj} , injected current; $I_{L,S}$, leakage current in the soma; I_{syn} , synaptic current. At the axon: I_{NaT} , fast inactivating sodium current; I_K , delayed rectifier potassium current; $I_{L,A}$, leakage current in the axon. The color for each I_X current represents the CPG neuron that includes it at the soma, N1M, N2v and N3t, respectively. **Panel (b).** Connection scheme for the *Lymnaea stagnalis* feeding CPG circuit model. The colors indicating each neuron in the circuit match those in the representation of their corresponding somatic membrane potential traces in section 4.4.1.

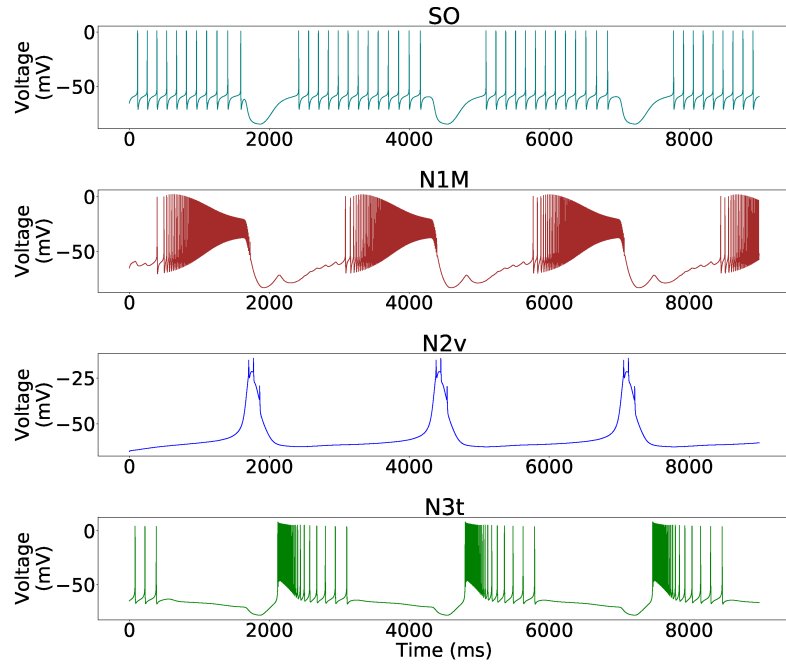


Figure 4.4: Triphasic feeding rhythm as produced by the circuit CPG model described in Fig. 4.3. In this simulation, i_{inj} values applied to each neuron are 8.5, 6, 2 and 0 mV, respectively.

4.4.2 CGC neuron model

This CGC model by Vavoulis et al. (2010) is described by six different ionic channels: Persistent and transient sodium currents (I_{NaP} , I_{NaT}), that primarily drive depolarization and action potential initiation; transient and delayed rectifier potassium currents (I_A , I_D), key for repolarization and contribute to the shoulder shape waveform in this neuron (specially I_D); and a low-voltage-activated and high-voltage-activated calcium currents (I_{LVA} , I_{HVA}), which are crucial for both immediate excitability and long-term plasticity. These channels are described by Eqs. 4.4.7 to 4.4.13.

$$C_m \frac{dV}{dt} = I_{inj} - I_{NaT} - I_{NaP} - I_A - I_D - I_{LVA} - I_{HVA}, \quad (4.4.7)$$

$$I_{NaT} = g_{NaT} m_\infty^3 h (V - E_{Na}), \quad (4.4.8)$$

$$I_{NaP} = g_{NaP} r^3 (V - E_{Na}), \quad (4.4.9)$$

$$I_A = g_A a^4 b (V - E_K), \quad (4.4.10)$$

$$I_D = g_D n^4 (V - E_K), \quad (4.4.11)$$

$$I_{LVA} = g_{LVA} c_\infty^3 d_\infty (V - E_{Ca}), \quad (4.4.12)$$

$$I_{HVA} = g_{HVA} e^3 f (V - E_{Ca}). \quad (4.4.13)$$

Inactivation and activation dynamic variables r, a, n, e and h, b, f are defined by:

$$\frac{dx}{dt} = \frac{x_\infty - x}{\tau_x}, \quad (4.4.14)$$

where $x = h, r, a, b, n, e$ or f and x_∞ and τ_{x_∞} are defined by:

$$x_\infty = \left(1 + \exp\left(\frac{V_H^x - V}{V_S^x}\right)\right)^{-1} \quad (4.4.15)$$

See Supplementary Material in Vavoulis et al. (2010) for more details.

The implementation of this model is available at Neuron library github.com/GNB-UAM/neun (Vavoulis-CGCModel).

Temperature dependence description in the model

To simulate the temperature dependency in the neuronal activity, a Q_{10} factor was incorporated to every dynamical equation in the model (i.e., conductances and activation gates). Q_{10} represents temperature sensitivity in each channel and it was included as a new factor as shown in Eqs. 4.4.16 and

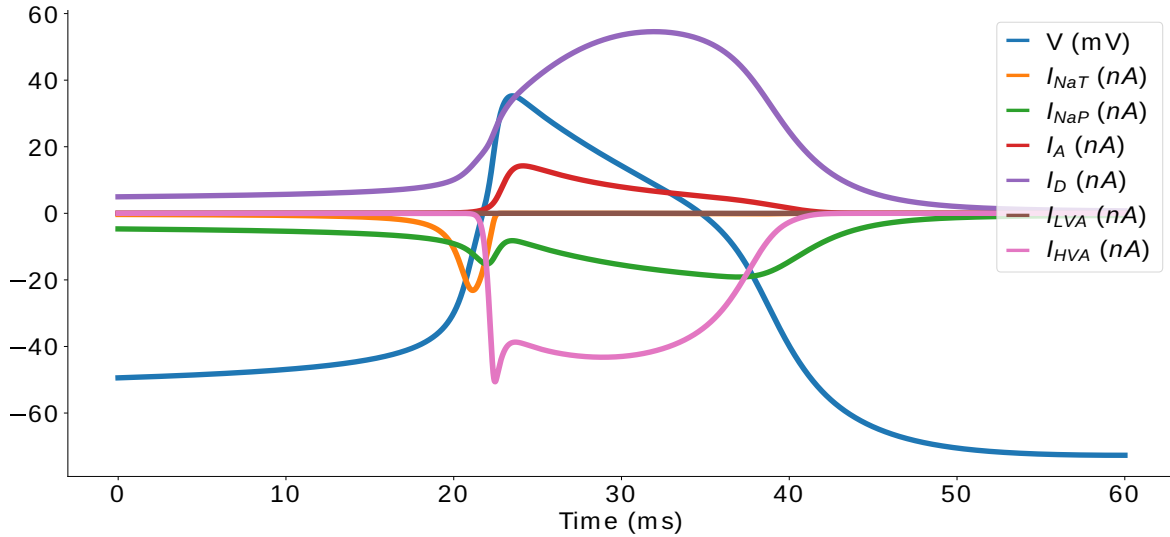


Figure 4.5: Simulation of the CGC-model representing the voltage dynamics during an action potential and the corresponding ionic currents defined in the model ($I_{NaP}, I_{NaT}, I_A, I_D, I_{LVA}, I_{HVA}$). The units in the y-axis are specified in the legend.

4.4.17, with $i = Na_T, Na_P, A, D, LVA, HVA$ for Eq. 4.4.16 and $i = h, r, a, b, n, d, e, f$ for Eq. 4.4.17. The capacitance was also defined as temperature dependent (C_T) with a linear relation to the difference of temperature:

$$g_i(T) = \bar{g}_i Q_{10}^{i \frac{T-T_0}{10}}, \quad (4.4.16)$$

$$\phi_i(T) = \bar{\phi}_i Q_{10}^{i \frac{T-T_0}{10}}, \quad (4.4.17)$$

$$C_T = c_0 + c_0 \gamma (T - T_0). \quad (4.4.18)$$

where $\bar{g}_i, \bar{\phi}_i, c_0$ are the original values used in the model and $\gamma = 0.05$.

4.5 Neural data analysis

To analyze the recordings of intracellular signals and the outputs of the models' simulations, we relied on the detection of single events, mainly spikes. Thus, we either defined time-intervals for the CPG rhythm or analyze each single spike based on waveform metrics as described in chapter 6. The detection of these time references (e.g., the duration of a spike or the first and last spike in a burst) allowed us to study the sequentiality of neural dynamics at different time-scales. In the cycle-by-cycle analysis, we focused on each event and cycle, avoiding the averaging of the results, since we consider this hinders information in the analysis of the sequential activity.

For the study of the time-intervals variability and the presence of sequential dynamical invariants, the spikes of the recording were detected by a voltage threshold, i.e., all peaks over a voltage value were considered action potential peaks and spikes in the model simulation of the bursting activity were detected using the change in the derivative along with a similar voltage threshold condition. Then, bursts were identified from the temporal structure of the spikes, and intervals were characterized by the timing of the first and last spike in each burst. In some recordings these temporal references were adjusted to the needs of the data available, this will be specified in the corresponding section 5.4.

All intervals defined in section 5.2.1 were defined by the spike events at the *beginning* and *end* of each burst. The quantification of the sequential time-intervals was implemented in *Python* as follows:

```

1 ##### SINGLE INTERVALS
2 # on = 0; off = 1
3
4 # off1 - on1 of the burst duration
5 def get_burst_duration(data):
6     return np.array([b - a for a, b in zip(data[:, 0], data[:, 1])])
7
8 # on2 - off1 of one burst and the next one, respectively
9 def get_burst_interval(data):
10    return np.array([a - b for a, b in zip(data[1:, 0], data[:, 1])])
11
12 # on2 - on1 of one burst and the next one, respectively
13 def get_burst_period(data):
14    return np.array([a - b for a, b in zip(data[1:, 0], data[:, 0])])
15
16 ##### PAIRED INTERVALS
17 def get_intervals(d1,d2):
18     if d1.size == 0 or d2.size == 0:
19         return [],[]
20
21     d1d2_interval = np.array([b-a for a,b in zip(d1[:,0],d2[:,0])])
22     d1d2_delay = np.array([b-a for a,b in zip(d1[:,1],d2[:,0])])
23     d2d1_interval = np.array([a-b for a,b in zip(d1[1:,0],d2[:-1,0])])
24     d2d1_delay = np.array([a-b for a,b in zip(d1[1:,0],d2[:-1,1])])
25
26     return [d1d2_interval,d1d2_delay],[d2d1_interval,d2d1_delay]
```

On the other hand, to analyze the data obtained from recordings and model simulations of the tonic firing activity for the CW-NIR laser effect analysis, we based on the spike waveform. To detect the spike times, it was usually enough with a voltage threshold to detect the events in the sequence –

CHAPTER 4: MATERIALS AND METHODS

regarding the stereotyped spike waveform. To analyze the waveform after the detection of the events, each time event in the voltage signal was segmented by considering N milliseconds before and after the event, thus defining segments that capture the shape of the waveform. The characterization of that waveform was carried by defining four metrics: duration, amplitude, and depolarization and repolarization slopes. The characterization of these metrics was implemented as in the following *Python* code:

```
1 # Description:
2 #   Receives spike voltage values and return the time values to get the duration
3 #   time
4 # measured at the mid point of the spike waveform
5 # Parameters:
6 #   spike: voltage values
7 #   dt: time rate
8 #   thres_val: voltage value where to measure the duration. By default mid
9 #   point.
10 # v_scale: scale of the voltage, assumes mV
11 # Return:
12 # time points at middle point of the spike waveform.
13 def get_spike_duration(spike, dt, thres_val=0.5, v_scale=1):
14     spike = spike[~np.isnan(spike)]
15
16     # Detects the peak of the waveform
17     peaks, properties = find_peaks(spike, prominence=1*v_scale, width=20)
18
19     if len(peaks)>1: # in case spike has several peaks, gets mid one.
20         mid_peak = np.isclose(len(spike)//2, peaks, atol=10)
21         peaks = peaks[mid_peak]
22
23         # peak_widths detects the width at "rel_height" of a signal given the peak.
24         results_half = peak_widths(spike, peaks, rel_height=thres_val)
25
26     # get the two time points corresponding to the waveform at midpoint
27     try:
28         duration_vals = np.array([results_half[2][0], results_half[3][0]])
29         th = results_half[1]
30     except Exception as e: # Exception in case the detection did not work.
31         duration_vals = np.array([])
32         th = 0
```

CHAPTER 4: MATERIALS AND METHODS

```

33     if duration_vals.size == 0: #Safety comprobation
34         return (0,0),th
35     else:
36         return (duration_vals[0]*dt,duration_vals[-1]*dt),th
37
38 # Description:
39 #   Calls get_spike_duration function and returns a single time value of the
40 #   duration
41 #   with the difference of the two points returned by the previous function.
42 def get_spike_duration_value(waveform, dt, plot=False, v_scale=1):
43     dur_refs,th = get_spike_duration(waveform, dt, plot=plot, v_scale=v_scale)
44
45     # Computes the time duration between the two points obtained from
46     # get_spike_duration
47     duration = dur_refs[1]-dur_refs[0]
48
49     return duration
50
51 # Description:
52 #   Receives spike values and return the amplitude value measured as the distance
53 #   between
54 #   maximum and minimum voltage value.
55 # Parameters:
56 #   spike voltage values
57 #   dt time rate
58 # Return:
59 #   amplitude
60 def get_spike_amplitude(spike,dt, v_scale=1):
61     # Cleans nan values (in case they are present)
62     spike = spike[~np.isnan(spike)]
63
64     # Gets min and max values from the waveform segments and compute the
65     # difference.
66     mx_value = np.max(spike) #maximum V value (spike)
67     mn_value = np.min(spike) #minimum V value (spike)
68
69     return mx_value-mn_value
70
71 # Description:
72 #   Receives spike values and return the increasing and decreasing slope values at
73 #   the
74 #   two points matching a threshold in "the middle" of the spike maximum and
75 #   minimum voltage value.

```

```

69 # Parameters:
70 #   spike voltage values
71 #   dt time rate
72 #   n_points: number of points around position to calculate slope
73 #   slope_position: where to calculate slope: defalult value, mid of spike.
74 # Return:
75 # depolarization slope, repolarization slope
76
77 def get_slope(spike,dt,n_points=10, slope_position=0.5, plot=False, v_scale=1):
78     spike = spike[~np.isnan(spike)]
79
80     # Get the mid points of the waveform as in "duration"
81
82     mid_ps,th = get_spike_duration(spike,dt,thres_val=slope_position, v_scale=
83                                     v_scale)
84     indx1 = int(mid_ps[0]/dt) #From ms to point ref
85     indx2 = int(mid_ps[1]/dt) #From ms to point ref
86
87     # Transforms n_points variable to compute the slopes
88     scale = int(0.1/dt)
89     n_points *= scale
90     n_ms = n_points*dt
91
92     # Computes the slope from the mid point at n_points before and after it
93     slope1 = (spike[indx1+n_points]-spike[indx1-n_points])/(n_ms*2)
94     slope2 = (spike[indx2+n_points]-spike[indx2-n_points])/(n_ms*2)
95
96     return (slope1,slope2)

```

Finally, the models were implemented in C++ taking advantage of its computational speed. Most analyses were performed in Python3, since it is a frequently used tool and libraries such as Pandas are very effective for data analysis. Some spike detection analysis of the intracellular recordings of the CPG were performed in the visual analysis tool DataView (Heitler, 2007). Scripts used in this work are available at github.com/agarpe/neural-dynamics-utils and all conductance-based models are included in Neun github.com/GNB-UAM/Neun

4.6 CW-NIR laser setup

The experimental results presented here were obtained using a continuous-wave (CW) NIR diode laser in single TEM00 operation and 830nm wavelength output (Integrated Optics 0830L-13A-NI-

PT-NF).

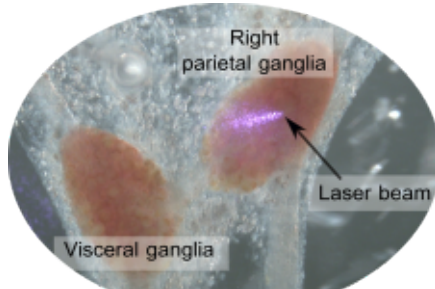


Figure 4.6: Illustration of the laser beam focused on a neuron in the right parietal ganglia.

The grazing incidence of the laser beam on the sample created a quasi-elliptical spot, with a minor axis of approximately $34\mu\text{m}$, as shown in Fig. 4.6.

Figure 4.7 shows the experimental setup. The diode laser output was coupled to a single-mode optical fiber to efficiently guide the laser beam to the sample. To adapt the divergence of the laser beam to the fiber optic output, an aspherical lenses-collimator (Thorlabs, F280FC-850) was installed. An achromatic doublet with focal length $f=50\text{mm}$ was used to focus the laser beam on the sample (Thorlabs AC127-050-B-ML). The experiments were performed with a laser output power of $\sim 90\text{ mW}$ and a power density over the sample of 146 W/cm^2 .

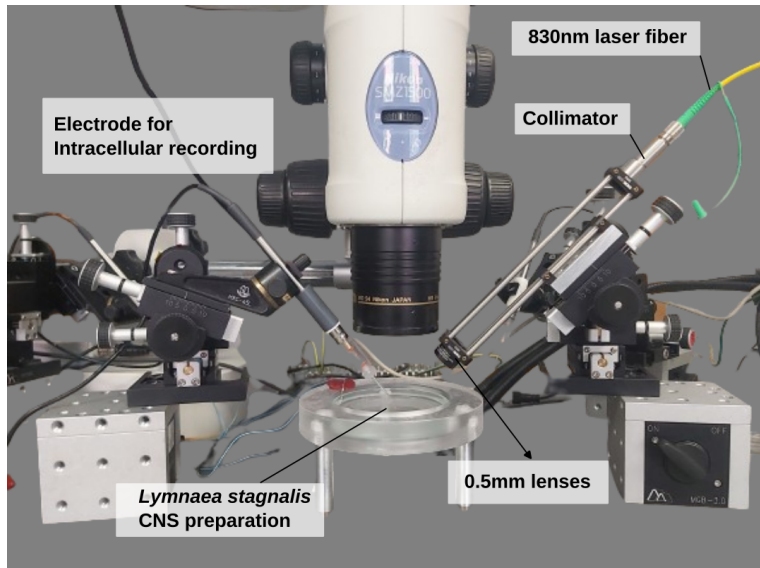


Figure 4.7: Image of the CW-NIR laser stimulation setup. On the left, there is the micromanipulator with the electrode and the glass micropipette for the intracellular recording. In the center of the image under the microscope lens, there is the preparation of the CNS of *Lymnaea stagnalis*. On the right side, the laser fiber is attached to the collimator and at the end of the holder there is a lens to focus the laser beam. This is also attached to a micromanipulator for a precise focusing.

The laser was attached to a micro-manipulator (Siskiyou MX160), allowing micrometer precision of the beam placement over the neuron and optimization of the beam focus. The focusing was performed using a binocular microscope (Nikon SMZ-1500) coupled to a CCD camera (XCAM1080PHA, TouTek Photonics, Zhejiang, China).

CHAPTER 5

Sequential constraints in CPG circuits: Dynamical invariants

In this chapter, we will analyze and discuss the temporal constraints in the sequential activity of the feeding CPG circuit of *Lymnaea stagnalis*. The presence of cycle-by-cycle sequential dynamical invariants was previously reported in the pyloric CPG of *Carcinus maenas*. We will address this research through computational models and experimental recordings to analyze the phenomena of sequential dynamical invariants during spontaneous activity and under different stimulation scenarios. We will also discuss the need of models able to simulate the intrinsic variability of neural activity without stochastic inputs and the possibility to explore the functional role of sequential dynamical invariants through effective robotic locomotion.

5.1 Introduction

Although often disregarded in many experimental and theoretical studies, neural sequences are key elements of brain activity which, in many cases, have a direct relationship to behavior (Hahnloser et al., 2002; Venaille et al., 2005; Buzsáki & Tingley, 2018; Paton & Buonomano, 2018; Rabinovich & Varona, 2018; Elices et al., 2019). The study of neural sequences involves the assessment of time references, time intervals and the associated temporal structure of individual neurons, groups of neurons or large neural ensembles, which typically hinder their characterization due to experimental limitations. In this context, Central Pattern Generators (CPGs) are adequate neural circuits to study the generation and coordination of neural sequences.

CPGs are neural structures capable of generating rhythmic activity that involves robust motor sequences in a highly autonomous manner (Hartline & Maynard, 1976; Selverston et al., 2000; Marder

& Bucher, 2001). This kind of circuits is found in many different organisms including humans (Dimitrijevic et al., 1998; Pavlidis et al., 2016; Arichi et al., 2017). The neurons in CPG circuits have rich intrinsic dynamics and their connections form non-open circuit topologies in which all members of the circuit receive information from at least another member in the ensemble (Selverston et al., 2000; Huerta et al., 2001). This favors rhythm coordination through closed-loop computation and endows CPGs with the ability to produce robust yet flexible rhythms where intervals building the sequences can be adapted in different behavioral contexts (Elices et al., 2019). Figure 5.1 illustrates an example of the robust sequential generation of bursts in a CPG.

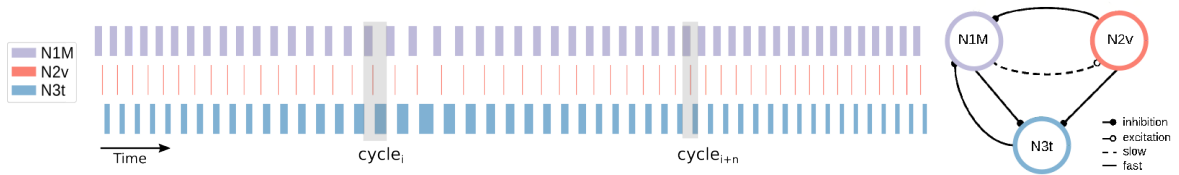


Figure 5.1: Example of robust sequential bursting dynamics in CPGs. Representation of burst duration in three neurons in a CPG model, the sequential activation of the three neurons produces cycles (indicated as gray boxes in the sequence). The connections between the three neurons are represented in the diagram on the right side of the panel.

The sequence of intervals underlying CPG rhythms presents variability in terms of the duration of each cell activation/inactivation, which has been identified in different nervous systems, e.g. see Elliott and Andrew, 1991; Reyes et al., 2008; Martinez et al., 2019. Consequently to the study of variability in cycle-by-cycle sequences, sequential dynamical invariants have been recently found in the form of robust linear relationships between specific sequence intervals and the period in the pyloric CPG of shore crabs (*Carcinus maenas*) (Elices et al., 2019). Dynamical invariants represent constraints of particular sequence intervals in relation to different intervals in the same cycle, as the instantaneous duration of the period, and build rules for the overall flexibility of the rhythm. It is important to note that not all intervals conforming the sequence display such constraints. The presence of invariants in the crustacean pyloric CPG are observed in all control conditions as well as in experiments under the effect of ethanol and other perturbations, which induce irregular rhythms (Elices et al., 2019).

While the existence of phase maintenance and linear relationships between rhythm intervals and the period have been discussed before in convenient animal models, e.g. Grillner and Kashin, 1976; Hooper, 1997; Vavoulis et al., 2007, detailed characterization of cycle-by-cycle variability to understand the existence of these relationships and the corresponding analysis of the universality of robust dynamical invariants are pending in both computational models and living recordings. The observation of these relationships in other animal models can also support the association of these temporal

restrictions to a functional, biological meaning.

Throughout this chapter we will characterize the sequence interval variability in a model of the *L. stagnalis* feeding CPG. We will induce variability with a ramp current injection. We will also address the issue of variability in neuronal models to study this kind of phenomena, and explore and discuss the presence of sequential dynamical invariants in intracellular recordings. The possible functional role will be assessed by inducing the activity through different methods but also from a practical approach in biohybrid robotics.

5.2 Methods

5.2.1 Time references, intervals and CPG sequence

The variability study addressed in this chapter is based on the characterization of cycle-by-cycle intervals in the rhythm produced by the CPG circuit. In our analysis of variability, we assess the presence of linear relationships between the intervals that build the sequence to characterize and unveil similar dynamical invariants as those found in the stomatogastric CPG (Elices et al., 2019). The intervals here analyzed can be measured for any two or three neurons following a robust triphasic rhythm. In the feeding CPG, N1, N2 and N3 represent the three phases, represented in the activity of interneurons N1M, N2v and N3t, respectively (simulated in the model) and in the experimental data by different combinations of moto- and interneurons (see Sec. 5.2.3).

Figure 5.2 shows the intervals described from single neuron intervals and intervals defined between two neurons. The definition of each interval is as follows:

1. **Burst Duration (BD)**, measured as the time interval between the first and the last spike of the burst (start to end in the trace of a given neuron).
2. **Inter Burst Interval (IBI)**, characterized as the time difference between the last spike of a burst and the first one of the next one (end to start in the trace of a given neuron).
3. **Period**, which covers the bursts from the three neurons and correspond to a cycle. It is measured as the time interval between the first spike of one burst in a neuron and the first spike of the next one on that neuron (start to start).
4. **NeuronX-NeuronY interval**, this interval is measured from the start of the burst of neuron X to the start of the burst of neuron Y (start X to start Y).

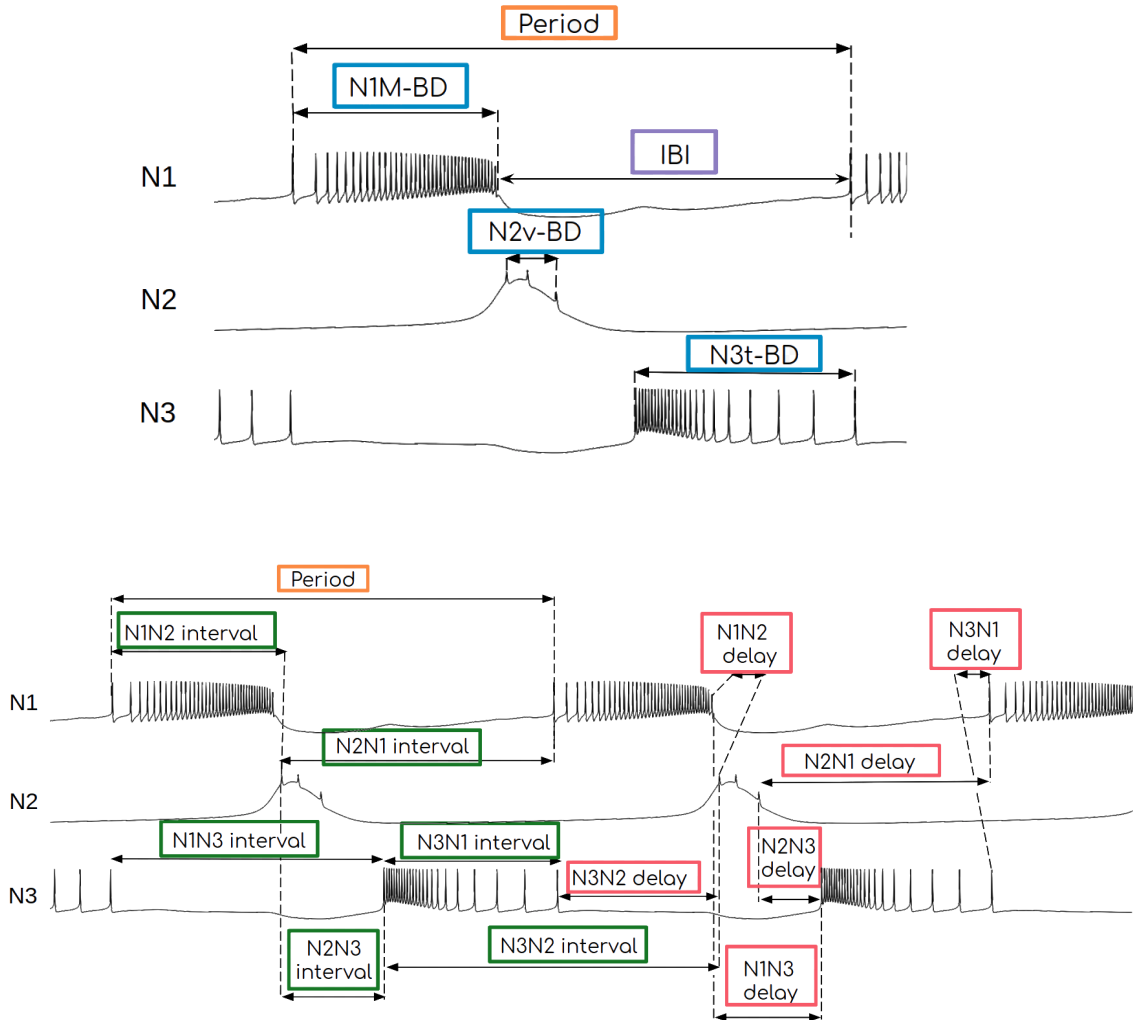


Figure 5.2: Panel A. Individual neuron sequence interval definitions. Each BD label represents the burst duration, defined as the time interval from the first spike to the last spike in the neuron's burst. Period was measured as the interval from the first spike of N1 burst to the first spike of the next N1 burst, covering three phases in relation to the activity of the other neurons. IBI represents the interburst interval, defined as the time from the last spike of a neuron's burst to the first one of the next burst in the same neuron. **Panel B.** Definition of intervals involving pairs of neurons. NXNY interval represents interval from NX start to NY start. NXNY delay represents interval from NX end to NY start. Period was measured from N1 start to N1 start, covering the three phases of the CPG rhythm.

5. **NeuronX-NeuronY delay**, being the time lapse between the burst end of a neuron X and the burst beginning of neuron Y. (end X to start Y).

Note that it is also possible to define those intervals only with the references from two neurons. For example, the intervals defined based on N1 and N3 time references would be: N1N3 and N3N1 intervals and N1N3 and N3N1 delay. The intervals corresponding to the third neuron are enclosed

in the others defined, e.g., in this example N2 burst and N2N1 delay would be contained in N1N3 delay. This consideration allows the characterization of the cycle-by-cycle variability in cases where it is not possible to define time references for the three neurons in the circuit.

5.2.2 Inducing variability in the model by current injection

The spiking-bursting activity of the model CPG neurons can be modulated by using an additional current injection on each cell, implemented in the i_{inj} term of equation (4.4.1). Depending on the current value applied, the corresponding neuron dynamics changes. While for N2v a change in this injection corresponds to a change in burst frequency (i.e. the number of bursts increases/decreases), for the rest of the neurons in the model a change in i_{inj} affects burst duration for N3t and SO, and the duration of the depolarization phase in N1M.

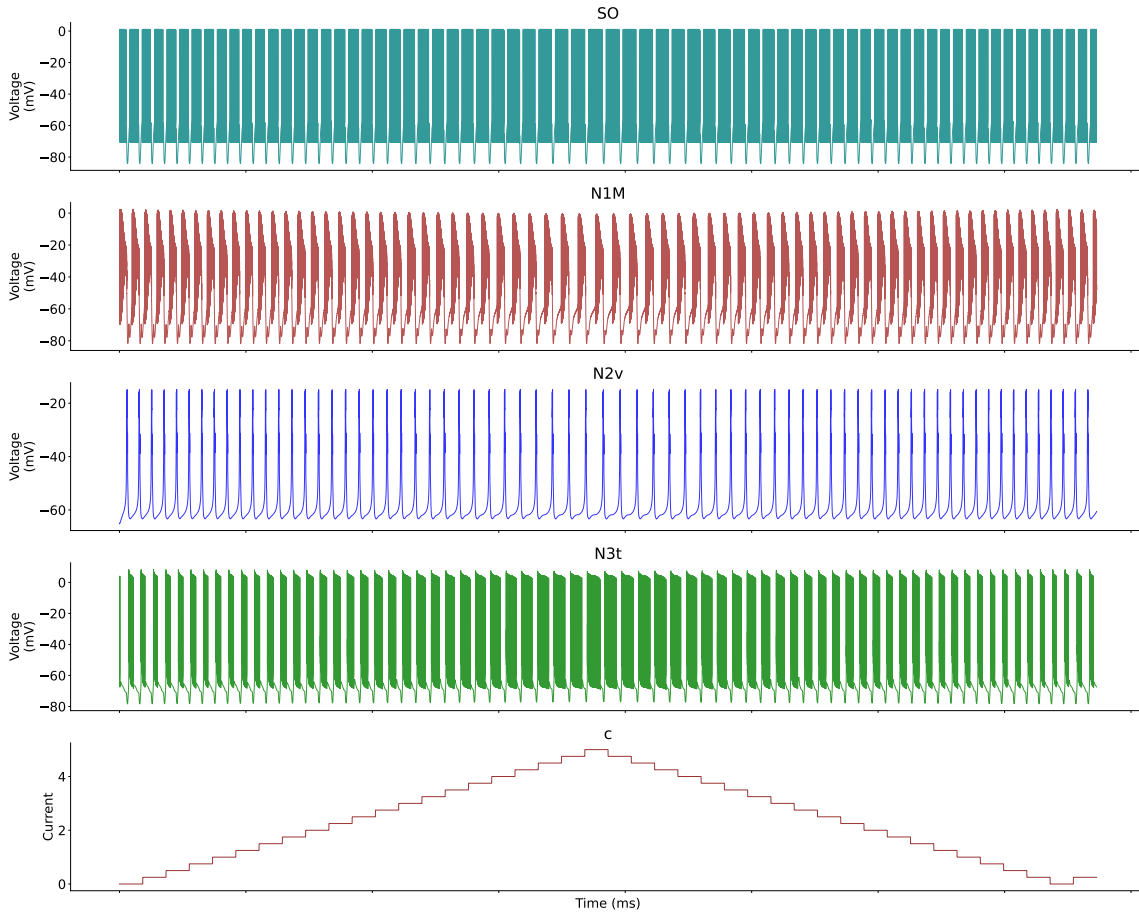


Figure 5.3: Illustration of the CPG activity when a current ramp i_{inj} is applied to N3t. Variability in the sequence intervals was induced by applying two consecutive ramps as the one shown in this Figure to a specific cell. The ramp current was applied only to one of the cells at a time.

Whilst the single neuron model descriptions have no intrinsic variability, the effect produced by the

modulation of the injected current in each neuron induces variability into the circuit, which allows characterizing the sequence intervals and the period, the associated robustness of the rhythm and the presence of dynamical invariants. Such stimulation has been used previously in the living circuit, as reported by Elliott and Andrew (1991). The authors of this work showed that it is possible to activate the feeding CPG with variability caused by current injection into individual cells in the circuit. CPG rhythms obtained under this type of stimulation differ depending on which neuron is being stimulated. To induce variability in the model we used a ramp protocol resulting in circuit time-interval variations as shown in Fig. 5.3.

By varying the current injected into N1M, its burst duration is kept nearly constant, but its depolarization phase before the spiking activity begins becomes longer. Since N3t is the neuron fitting in the sequence in that phase (see Fig. 4.4), it also increases its burst duration, being the most variable one in the CPG rhythm.

When value i_{inj} is increased on neuron SO, its burst duration becomes longer. Since SO has a modulator effect over N3t and N1M, it also alters the burst duration of these two neurons.

Neuron N3t also shows variable burst duration when an evolving current is injected. When i_{inj} value on N3t is larger, its burst duration increases, elongating the N1M depolarization phase.

Finally, when current is applied to N2v, the effect on its burst duration or the burst duration of the rest of the neurons is rather small. However, i_{inj} modulates N2v burst frequency through the hyperpolarization phase.

Therefore, we used a current ramp protocol to induce variability in the CPG model defined as follows: a ramp variable c as the current injection value ($i_{inj} = c$) on the neuron being stimulated, was increased from a minimum to a maximum value, and then decreased back to the initial value. This was repeated twice in each simulation. The ramp variable was modified with a fixed step value every 4.6 seconds (the approximate duration of two N3t bursts). The minimum and maximum c values were different in each cell and were tuned to generate realistic spiking-bursting behavior. All parameters used for the simulation analyses reported in this section are summarized in Table 5.1.

Simulations of Vavoulis et al. (2007) model were implemented in C++. The code of the feeding CPG model implementation is available at <https://github.com/GNB-UAM/CPG-feeding-Lymnaea>. This model was also included in Neun library in a Github repository <https://github.com/GNB-UAM/Neun>. Each simulation had the duration of two consecutive cycles of up and down ramps as the one shown in Fig. 5.3 using the parameters described in Table 5.1. The number of bursts in each simulation was approximately 140 (this number slightly depends on the neuron stimulated). Parameter values

Neuron stimulated	<i>i_{inj}</i> value				Ramp values (c)
	SO	N1M	N2v	N3t	
N1M	8.5	<i>c</i>	2	0	Min 0
N3t	9	10	1	<i>c</i>	Max 10.5
SO	<i>c</i>	10	1	4	Step 0.5
					0 5 0.25
					8.2 13 0.25

Table 5.1: List of i_{inj} values that yield realistic bursting rhythms for each neuron in the model CPG used in the stimulation protocols reported in this chapter. The left section of the table displays the i_{inj} values applied to each neuron (columns) during each simulation condition (rows). Ramp values on the right section refer to the minimum and maximum values of the ramp variable c in each simulation, increasing i_{inj} in the specified step every 4.6 seconds (the approximate duration of two N3t burst) to induce variability.

such as reversal potentials and synaptic conductances were the same ones specified in Vavoulis et al. (2007).

5.2.3 Experimental recordings and stimulation

The experimental recordings analyzed in section 5.4 were performed by Michael Crossley, University of Sussex, and were kindly provided for this work.

Each recording had at least 5 microelectrodes, which allowed to characterize the rhythm based on combinations of different neuron's activity. The experiments discussed in that section correspond to:

- Spontaneous activity: After the isolation of the CNS, the electrodes impaled in the neurons recorded the spontaneous activity in the CPG, with no further stimulation.
- Nerve electrical stimulation: For the activation of the rhythm, it is possible to stimulate the median lip nerve (MLN). The data analyzed in this case corresponds to a 4V stimulus at 1Hz.
- Neuron electrical stimulation: To modulate the CPG rhythm, SO and CV1a neurons where stimulated (in different experiments) by injecting a constant depolarizing current.

To define each phase, we used different neurons and bursting references, depending on the ones available on the circuit, following the interval definitions in table 5.2.

For each recording, each phase was characterized as follows:

- Spontaneous Activity Example 1 and 3: N1 phase was analyzed from B1 activity (bursting and depolarization); N2 phase was analyzed from B5 hyperpolarization, which has a strong

inhibition from N2v; N3 phase was analyzed from the bursting activity of B8 that replicates the N3t duration.

- Spontaneous Activity Example 2: N1 phase was analyzed from B1 activity (bursting and depolarization); N2 phase was analyzed from B1 hyperpolarization, which has a strong inhibition from N2v; N3 phase was analyzed from the bursting activity of B8, that replicates the N3t duration. Since the reference for N2 here coincides with N1 reference, we display here only the intervals corresponding to N1 and N3 phases, the intervals that correspond to three phases, such as N1-N2 delay or N2-N3 delay, either are already represented in the defined intervals or have a duration close to 0 ms.
- SO driven by stimulation and spontaneous activity: N1 phase was analyzed from B1 activity (bursting and depolarization) and N3 phase was analyzed from the bursting activity of B8 that replicates the N3t duration. N2 phase could not be clearly defined.
- MLN driven and CV1a driven 1-4: N1 phase was analyzed from N1M activity by a threshold helped by the derivative of the signal; N3 phase was analyzed from the bursting activity of B8 (analogously to the cases above). In CV1a stimulation for cases 1 and 3, N2 phase was also characterized from the inhibition of N1M.

5.2.4 Models with chaotic activity

As we discussed in the introduction, there are several models that are able to reproduce intrinsic variability in the voltage dynamics without the introduction of external perturbations such as stochastic noise. These models produce deterministic chaos which is useful to reproduce observed biological variability. In this subsection, we include the equations of the models used in Sec. 5.5 to represent variable and non-variable voltage activity.

LP model by Nowotny et al. (2008) with chaotic activity

To illustrate the variability displayed by chaotic models, in Sec. 5.5 we used the model by Nowotny et al. (2008), which reproduces the activity of LP neuron in the pyloric CPG. The membrane potential of the axon and soma compartments, V_{axon} and V_{soma} respectively, are described in this model by the following equations:

$$\frac{dV_{\text{axon}}}{dt} = \frac{1}{C_a} (-I_{\text{Na}} - I_{\text{Kd}} - I_M - I_{\text{leak,a}} + I_{VV}) \quad (5.2.1)$$

$$\frac{dV_{\text{soma}}}{dt} = \frac{1}{C_s} (-I_{\text{Ca}} - I_{\text{KCa}} - I_A - I_h - I_{\text{leak,s}} - I_{VV}) \quad (5.2.2)$$

All ionic currents except for the ones mentioned explicitly below are given by:

$$I_x = g_x m^p h^q (V - V_x) \quad (5.2.3)$$

where g_x is the maximal conductance of the current, V is the membrane potential of either the axon compartment (I_{Na} , I_{Kd} , and I_M) or the soma compartment (the rest of the ionic currents), and V_x is the ionic reversal potential. The activation and inactivation variables are described by:

$$\frac{dm}{dt} = \alpha_m(1-m) - \beta_m m \quad (5.2.4)$$

$$\frac{dh}{dt} = \alpha_h(1-h) - \beta_h h \quad (5.2.5)$$

for I_{Na} and I_{Kd} , and

$$\frac{dm_x}{dt} = \frac{m_{\infty,x}(V) - m_x}{\tau_{m_x}} \quad (5.2.6)$$

for the rest of the currents indicated by x .

The simulations with this model were performed using the code originally published by the authors, available at <https://modeldb.science/116957>.

Non chaotic model by Ghiglazza and Holmes (2004)

The Ghiglazza and Holmes (2004) model for motoneurons in the insect locomotion CPG is described by the following equations:

1. Membrane Potential Equation

$$C \frac{dv}{dt} = -[I_{\text{Ca}} + I_{\text{K}} + I_{\text{L}} + I_{\text{KS}}] + I_{\text{ext}} \quad (5.2.7)$$

2. Ionic Currents

$$I_{\text{Ca}} = \bar{g}_{\text{Ca}} m_{\infty}(v)(v - E_{\text{Ca}}) \quad (5.2.8)$$

$$I_{\text{K}} = \bar{g}_{\text{K}} n(v - E_{\text{K}}) \quad (5.2.9)$$

$$I_L = \bar{g}_L(v - E_L) \quad (5.2.10)$$

$$I_{KS} = \bar{g}_{KSC}(v - E_K) \quad (5.2.11)$$

3. Gating Variables Dynamics

$$\frac{dm}{dt} = \frac{\epsilon}{\tau_m(v)} [m_\infty(v) - m] \quad (5.2.12)$$

$$\frac{dc}{dt} = \frac{\delta}{\tau_c(v)} [c_\infty(v) - c] \quad (5.2.13)$$

4. Steady-State Activation and Time Constants

$$w_\infty(v; k_{i0}, v_{th}) = \frac{1}{1 + e^{-k_{i0}(v - v_{th})}} \quad (5.2.14)$$

$$\tau_i(v; k_{i0}, v_{th}) = \text{sech}(k_{i0}(v - v_{th})) \quad (5.2.15)$$

5.2.5 Hybrot structure

The experimental paradigm designed in order to test the correct behavior and locomotion of the FLC-Hybrot –FLC stands for Functional Living Circuit (Soëtard et al., 2023)– established a real-time closed-loop interaction between the robot and a living pyloric CPG of *Carcinus maenas* (Elices et al., 2019). During the experiment, the FLC-Hybrot had to walk through a straight and flat line, with no obstacles, along which there were interspersed sections with lights and shadows. Neural activity was recorded online from the living circuit and used to modulate the robot movement. At the same time, feedback current was injected into the living circuit when the robot’s light-sensor detected a shadow.

Top panel of Figure 5.4 shows an illustration of the experimental setup for the FLC-Hybrot implementation. In the real-time configuration, a computer was the link between the robot and the living preparation (Fig. 5.4A). The processes taking part during the real-time protocol were:

1. First, reading the online signals received from the amplifiers through the DAQ device (Fig. 5.4B), which were recorded from CPG neurons in the living preparation (Figure 5.4C).
2. Extracting from the signal, in real-time, the duration of the temporal intervals of the cycle-by-cycle CPG activity and sending them to the robot’s controller via Bluetooth.

3. In the communication from the robot to the computer, the robot's light-sensor data was sent through the same Bluetooth connection.
4. When the data indicated that the robot was located under a shadow a signal was sent back to the DAQ. At that moment, a current was injected into the neurons altering their behavior.

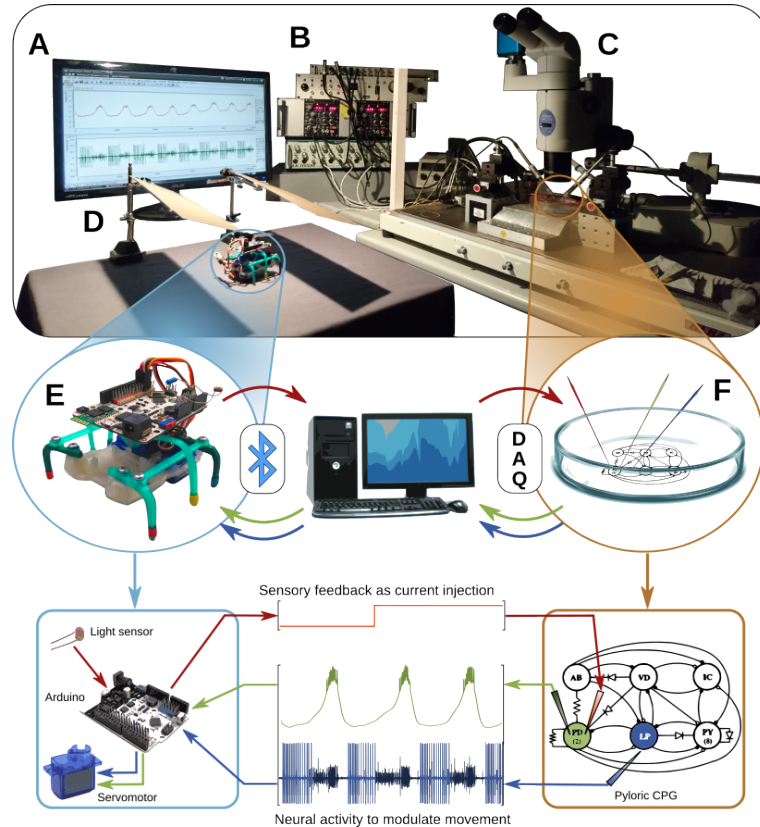


Figure 5.4: Hybot experiment design **Top panel:** illustration of the experimental setup for the FLC-Hybot implementation: A) Computer controlling the closed-loop interaction between the living CPG and the robot. B) DAQ and signal amplifiers; C) Microscope; D) Testing track with light and shadow regions. **Middle panel:** Detail of the elements of the setup: E) Hexapod robot, receives the neural information from the computer and sends back the sensory feedback through a Bluetooth connection; F) *In vitro* pyloric CPG preparation with three electrodes to: (1) record extracellular activity from the nerve which includes the activity from the LP neuron (blue) (2) to record intracellular activity from the PD neuron (green) and (3) to introduce the feedback current into a PD neuron (red). The signal recorded from the electrode is received through the DAQ device. **Bottom panel:** detail of the elements of the robot and the preparation. PD neuron (intracellular recording, green trace) and LP neuron (extracted from the extracellular recording, blue trace) the activity is analyzed online by the computer and used to modulate the movement of the robot. Meanwhile, robot's light sensor detects the presence of light or shadow over it and the Arduino board sends that information to the computer, which injects feedback current into the PD neuron (red trace) accordingly.

All these operations were repeated while the robot walked through the trial track (Figure 5.4D).

Robot's locomotion was determined by its legs oscillation, so we utilized video tracking tools to capture their movement during the experiment (Figure 5.4E). Two electrodes were used in order to measure the pyloric CPG activity. First, an extracellular electrode picked up all the surrounding neurons' activity. In this signal, the spikes and bursts of the LP neuron were clearly recognizable due to their larger amplitude. One of the PD neurons' membrane potential was recorded using an intracellular electrode. A second intracellular electrode was used to inject the feedback current into a PD neuron to implement the robotic sensory feedback (Figure 5.4F).

5.3 Sequential dynamical invariants in computational models

We start the research of the presence of cycle-by-cycle sequential restrictions found in Elices et al. (2019) by exploring them in a computational model. The detailed reproduction of the activity allows to study the mechanisms associated to the cycle-by-cycle activity of the circuit and the time-interval relations. We used the feeding CPG model description of Vavoulis et al. (2007), which even though it does not have a chaotic mode, the model is flexible enough to adapt to the variability induced in one of the neurons. Following the ramp current injection protocol defined in section 5.2.2, N1M, N3t and SO neurons in the model were stimulated for our analysis of the sequence interval variability. Using this induced variability we were able to explore the presence of sequential dynamical invariants under different scenarios. The effect on injecting a current ramp on N2v is not reported here since it leads to lower variability than the other cases. In all simulations, we could test the robustness of the rhythm while inducing the external perturbation that evoked variability in the search for dynamical invariants. The results summarized and adapted for this section were published in Garrido-Peña et al., 2021.

First we saw that the model of the feeding CPG faithfully reproduces the activity of the main neurons involved in the generation of its triphasic rhythm (Vavoulis et al., 2007). This includes their waveforms and the relationships between the cycle period and the duration of several intervals reported in (Elliott & Andrew, 1991). Note that, since there was not a description of a chaotic mode, all the rhythms explored here were analyzed from induced stimulation, not by simulating spontaneous activity. This was a restriction when exploring spontaneous activity, since the circuit needed to be altered by one of the neurons, simulating the corresponding experimental protocol, but still altering the circuit in a predefined way. Also, another phenomenon known in the pyloric CPG experimental work, the "resetting" of dynamical invariants between intervals belonging to consecutive cycles, could not be explored in this model, since the ramp value was progressive (see Appendix Fig. B.1 for a description of this resetting). All this will be illustrated in the following Section 5.4 with experimental

recordings, and a biohybrid robot to assess the functional role of sequential interval variability will be discussed in Section 5.5.

5.3.1 N1M driven variability

N1M neuron can be stimulated using ramp protocols in living preparations (Elliott & Andrew, 1991). Such current injection protocols can initiate the CPG rhythm. In our case, after applying the current injection protocol into N1M and detecting the spike and burst events for each neuron in the CPG model, all intervals represented in Fig. 5.2 were quantified. We show in Fig. 5.5 the variability and the correlation between the period and each interval in these experiments.

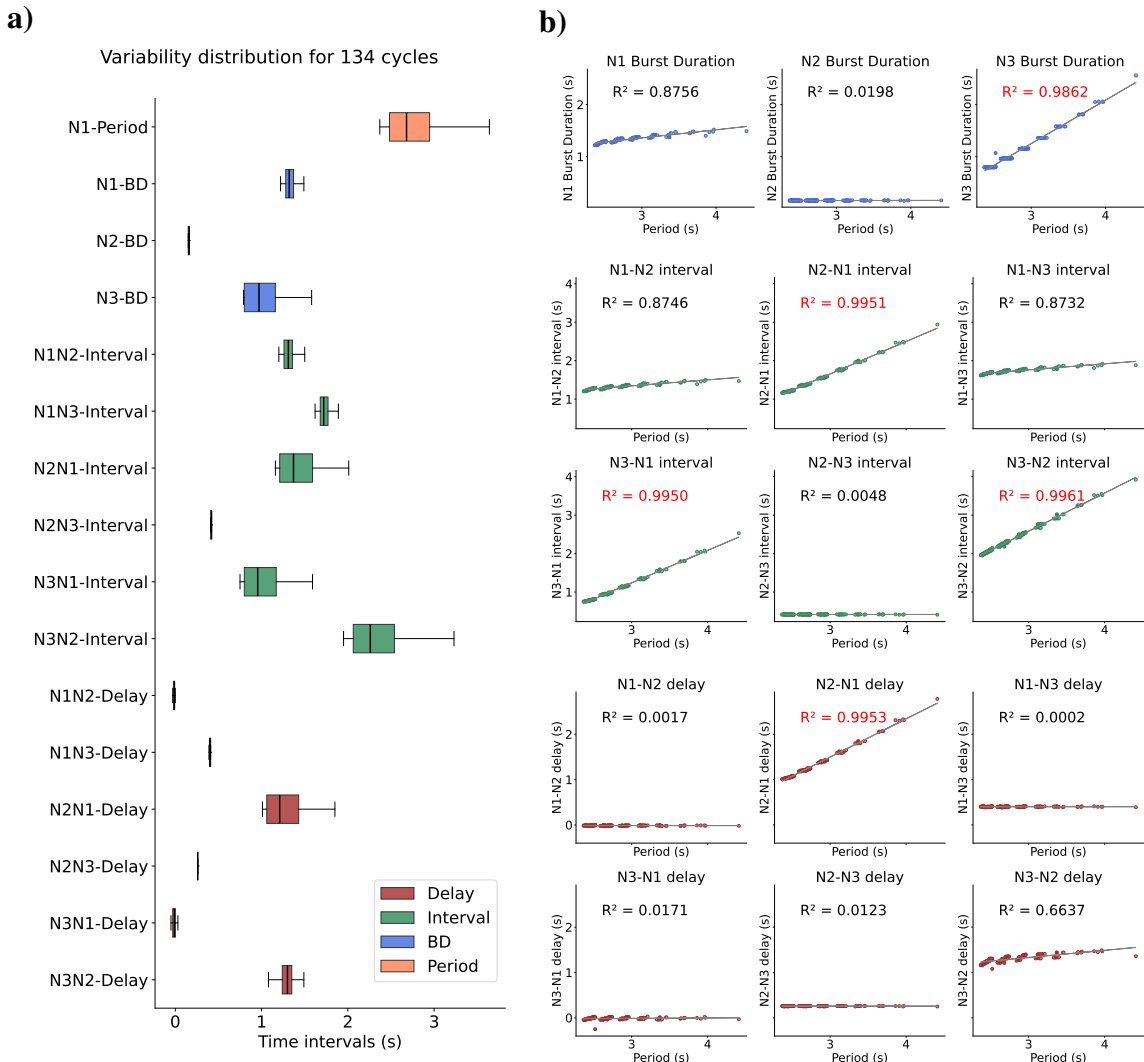


Figure 5.5: N1M stimulation: a) Box-plots of the sequence intervals under N1M neuron stimulation. b) Interval correlations to period for N1M-driven simulation. First row: Burst durations. Second and third row: Two-neuron *intervals*. Forth and fifth row: Two-neuron *delays*. Linear relationships are quantified by the R^2 values of the linear regression.

Figure 5.5.a) displays the boxplots of the duration of all sequence intervals defined above. Regarding burst duration of the neurons (N1M-BD, N2v-BD, N3t-BD), we can observe in this figure that the most variable one corresponds to N3t neuron. Furthermore, the derived intervals which cover N3 phase are also the ones presenting larger variability (i.e., N2-N1, N3-N1 and N3-N2 intervals and N2-N1 delay). On the other hand, the least variable intervals correspond to the ones related to N2v and N1M burst duration, i.e., N1-N2, N1-N3, N2-N3 intervals and N1-N2, N1-N3, N3-N1, N2-N3, N3-N2 delays. They show a nearly a constant duration during each cycle.

Figure 5.5.b) plots the cycle-by-cycle measurements of the intervals defined in Fig. 5.2 against the period. The first row displays burst duration intervals, which are the intervals analyzed in Elliott and Andrew (1991) from data obtained in electrophysiological recordings of living neurons, and in Vavoulis et al. from data obtained in model simulations (Vavoulis et al., 2007). The results shown in this row match those results, being N3t-BD the most correlated to the period, which can be noted by the R^2 value close to one in the linear regression. The other two intervals (N1M-BD and N2v-BD), which were also the least variable, are not strongly correlated to the period. For our discussion in this case and the following cases reported here, we focus on invariant relations with $R^2 > 0.9$ and notable slopes in the resulting linear regression to the data.

Likewise, the most variable intervals derived from other time references of the sequence also show a high correlation with the period, i.e., they present dynamical invariants, in this case N2-N1, N3-N1, N3-N2 intervals and N2-N1 delay. The cycle-by-cycle period variability is a consequence of the variability in these specific intervals.

On the other hand, intervals related to neuron N2v and N1M are the least variable. N2v is the one less affected by the global activity of the circuit, in terms of its burst duration. Moreover, some of the intervals are very short, or even negative, since the end of a given neuron's burst overlaps the next one's beginning (N1-N2 and N3-N1 delay). This is the case for N1-N2 and N3-N1 delay (4th row, 1st column and 5th row, 1st column, respectively in Fig. 5.5.b).

5.3.2 N3t driven variability

The stimulation protocol was also applied to N3t neuron. Although no previous analysis on injecting a current ramp into this neuron has been reported neither experimentally nor in the feeding CPG computational model, due to the connectivity in the circuit, it can be expected that the stimulation of N3t will induce variability in the rhythm. The characterization of the sequence intervals in this case are shown in Fig. 5.6.a) and the correlation analysis is displayed in Fig. 5.6.b).

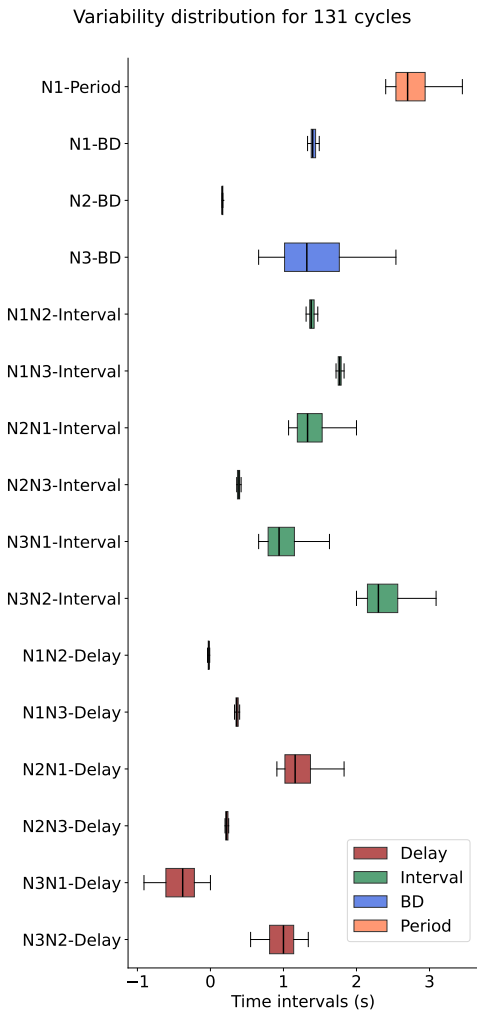
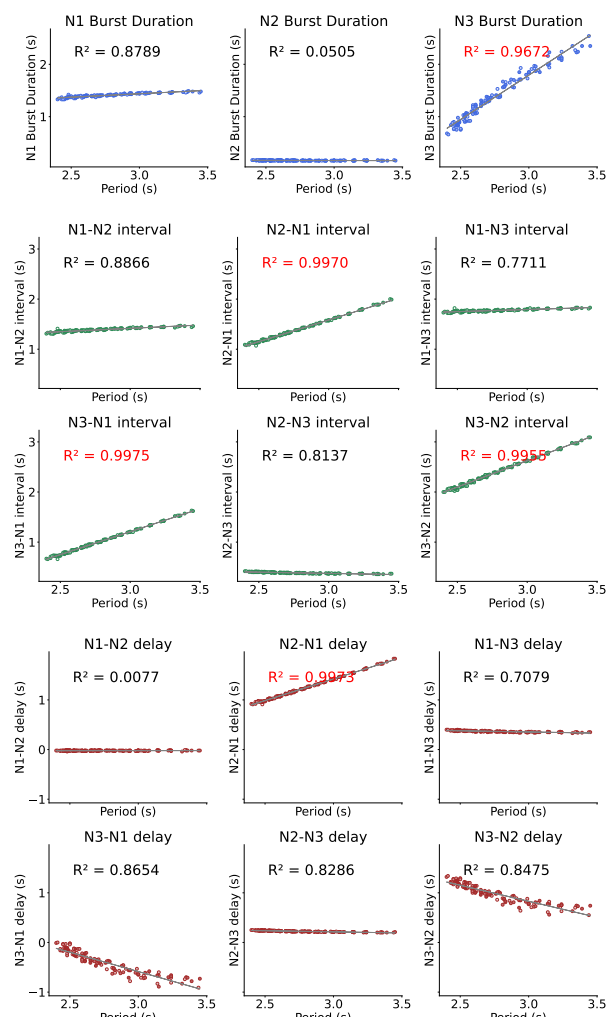
a)**b)**

Figure 5.6: N3t stimulation: a) Box-plots of the sequence intervals under N3t neuron stimulation. b) Interval correlations to Period for N3t-driven simulation. First row: Burst durations. Second and third row: Two-neuron *intervals*. Forth and fifth row: Two-neuron *delays*. Linear relationships are quantified by the R^2 values of the linear regression.

Results shown in Fig. 5.6.a) indicate that the largest variability is present in the same intervals related to N3t burst duration, as when the stimulation was delivered to N1M. However, in this simulation we observe that N1M had a lower variability while N3t had a higher variability with respect to the previous condition. In contrast, N2v-BD maintained its variability, as well as all the derived intervals containing this burst duration.

Note that N3-N1 delay, which is the interval from the end of the N3t burst to the beginning of N1M burst, shows negative values. This means that neuron N1M started earlier than the end of N3t in every cycle. Whilst this was also present in N1M-driven activity simulations, here the variability of this interval is much higher, leading to a larger overlapping.

Figure 5.6.b) plots each interval duration against the period. As in the previous condition, the dynamical invariants (i.e., intervals presenting a strong correlation to the period) show up in the intervals related to N3 phase, which were the ones presenting also the highest variability, whereas those intervals that do not participate in dynamical invariants are the ones related to N1M and mostly N2v (the least variable ones).

5.3.3 SO driven variability

The same protocol was implemented with a ramp stimulation applied to SO to induce variability, using the injected current values shown in Table 5.1 for each neuron. Events were detected and all intervals were measured (Fig. 5.2) and their variability was characterized.

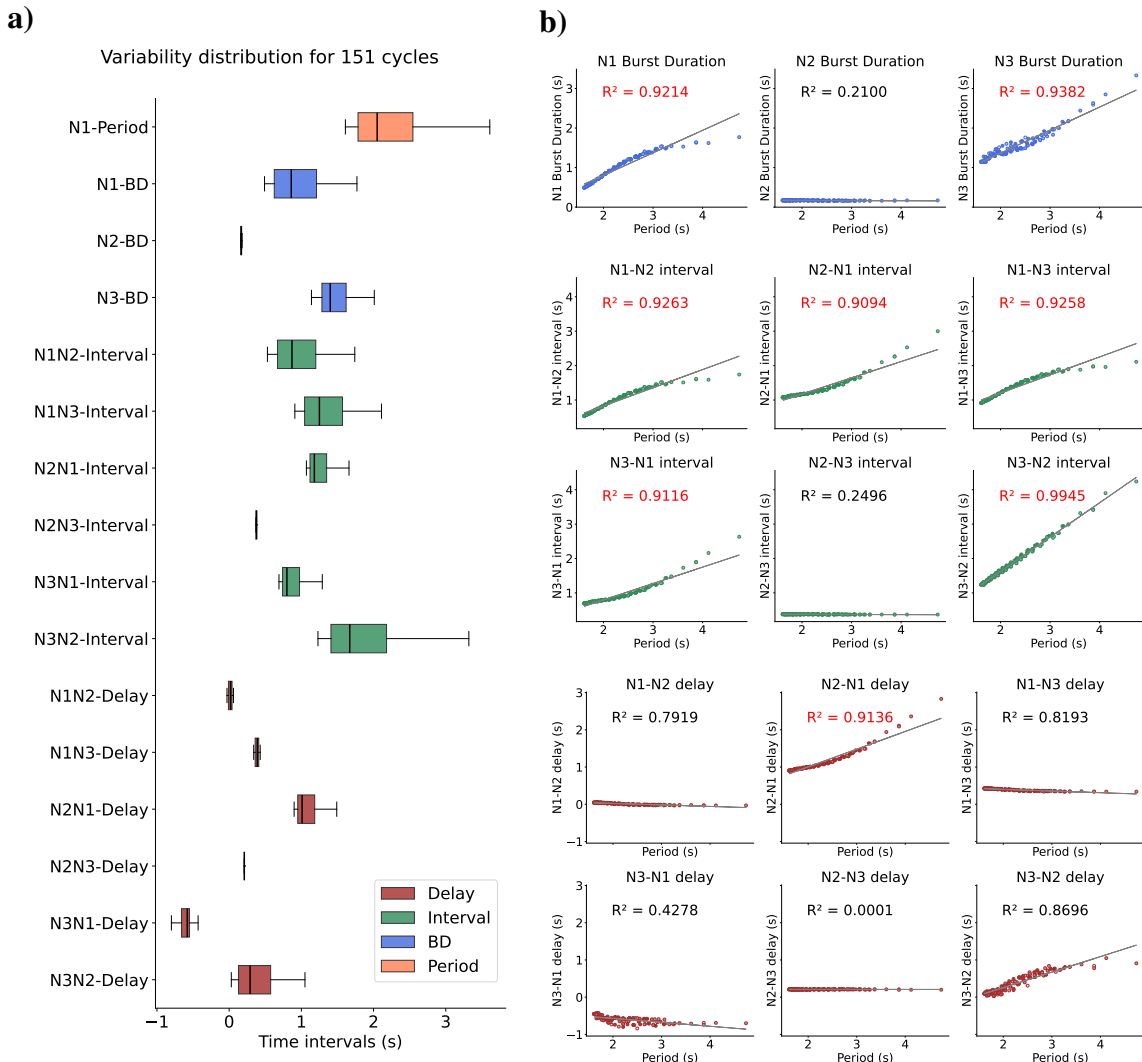


Figure 5.7: SO stimulation: a) Box-plots of the sequence intervals under SO modulatory neuron stimulation. b) Interval correlations to Period for SO-driven simulation. First row: Burst durations. Second and third row: Two-neuron intervals. Forth and fifth row: Two-neuron delays. Linear relationships are quantified by the R^2 values of the linear regression.

Figure 5.7.a) displays the box-plot representing the distinct interval variability. In this case, we found more intervals showing large variability than in the previous cases. N2v intervals, as it happened in the previous results, show low variability. N1M and N3t neurons show high variability in their burst duration intervals, being N1M even more variable than N3t, as opposed to the previous results when the stimulation was introduced in other cells. All intervals derived from these two neurons have high variability and a similar structure.

Figure 5.7.b) displays the corresponding correlation analysis between all intervals and the period. In this case, we found correlations in the same intervals as before: N2-N1, N3-N1, N3-N2 intervals and N2-N1 delay; which are the intervals related to N3t burst duration. However, under SO stimulation, N1-N2, N1-N3 intervals were also highly correlated to the period. Even the correlation for N3-N2 delay considerably increased in relation to the other stimulation conditions. These intervals are the ones related to N1M neuron activity, and were also the most variable ones. These results reproduce the experimentally analyzed effects set out in (Elliott & Andrew, 1991), when rhythm and variability was induced by injecting current into a living SO neuron.

Compared to the N1M and N3t stimulation results, there is another difference when driving the rhythm with SO: burst duration is much shorter, so the period and the rest of intervals are consequently smaller. Therefore, when driving the rhythm by SO, the period variability seems to arise from both N3t and N1M.

5.3.4 Cycle-by-cycle interval relations not only involving the period

We have discussed so far the sequential dynamical invariants in terms of strong linear relationships between the distinct intervals in a cycle and the period. However, studying the relations between all possible combinations between intervals can also show interesting information about the temporal variability distribution in the ongoing sequential activity. Figures 5.8 to 5.10 provide a representation of all these combinations of the defined intervals for the three scenarios of induced variability (current in N1M, N3t or SO) discussed in this section. In this extended representation of the cycle-by-cycle relationships, we can see that there are multiple intervals presenting strong linear relations in addition to the periods. Some of them are intervals that are contained within others, as in the case of N1-BD and N1-N2 intervals, which have similar duration, and so they are more likely to have a strong linear relation between them. However, there are other intervals that, although they share part of the time-interval, they are not correlated. This was the case of the N2 burst duration with the period, i.e., burst duration is contained in the period but it had no relation to it. We also observe this in the relation of N2-BD with N2-N1 interval. This distinction can help dissecting the source of variability

and its distribution when an interval is related to the period. A further study of linear relationships between intervals (such as N1-BD and N3-BD) that do not share any other common time-interval can show important information about the ongoing cycle-by-cycle activity. This representation can also show non-linear relations between the intervals, as we can see in some plots in the case of SO (Fig. 5.10). These nonlinear relationships have been observed in the pyloric CPG both in modeling and experimental scenarios (Berbel et al., 2024).

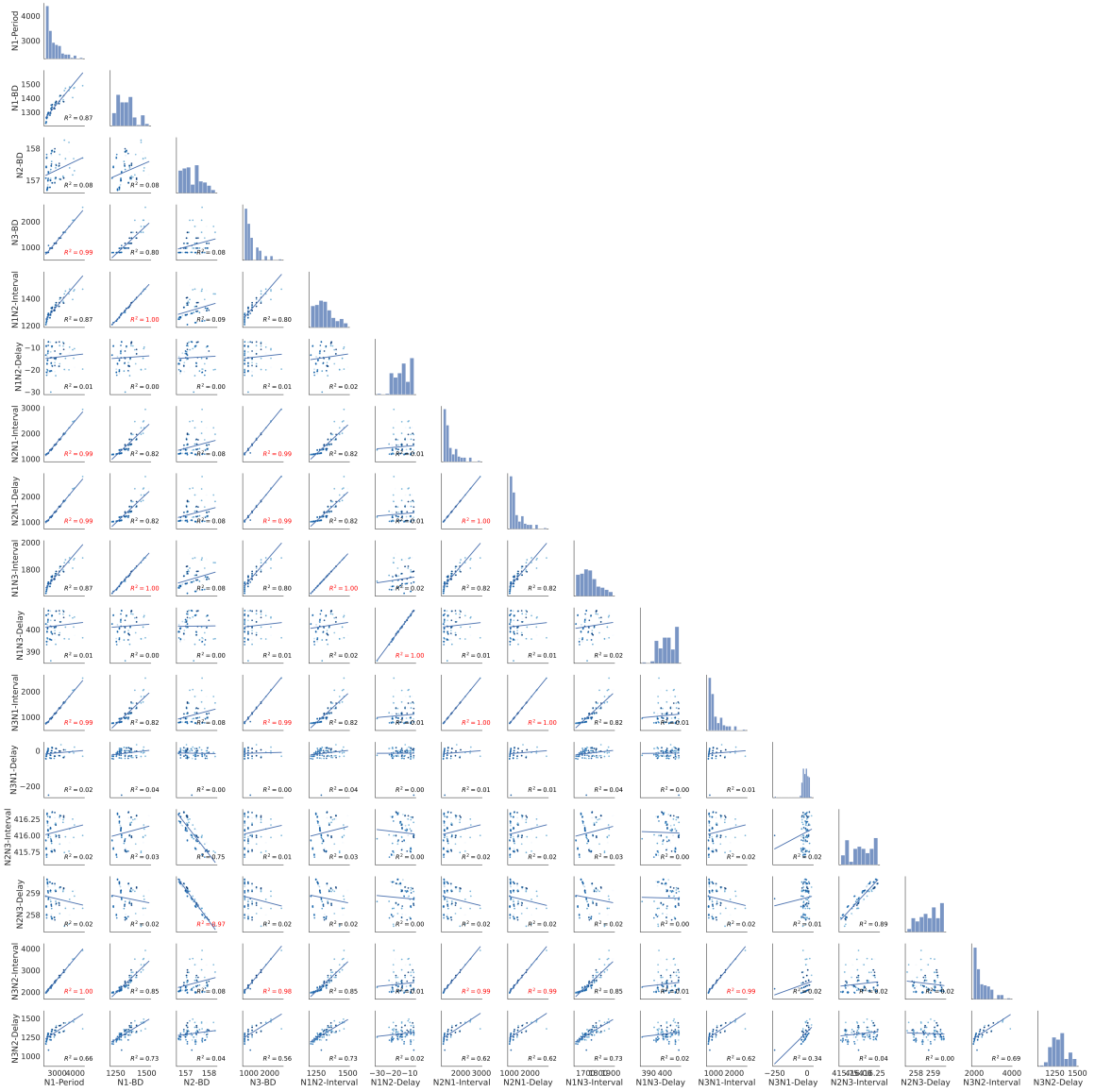


Figure 5.8: N1M stimulation: Pairplot with all possible combination between time intervals within a cycle.

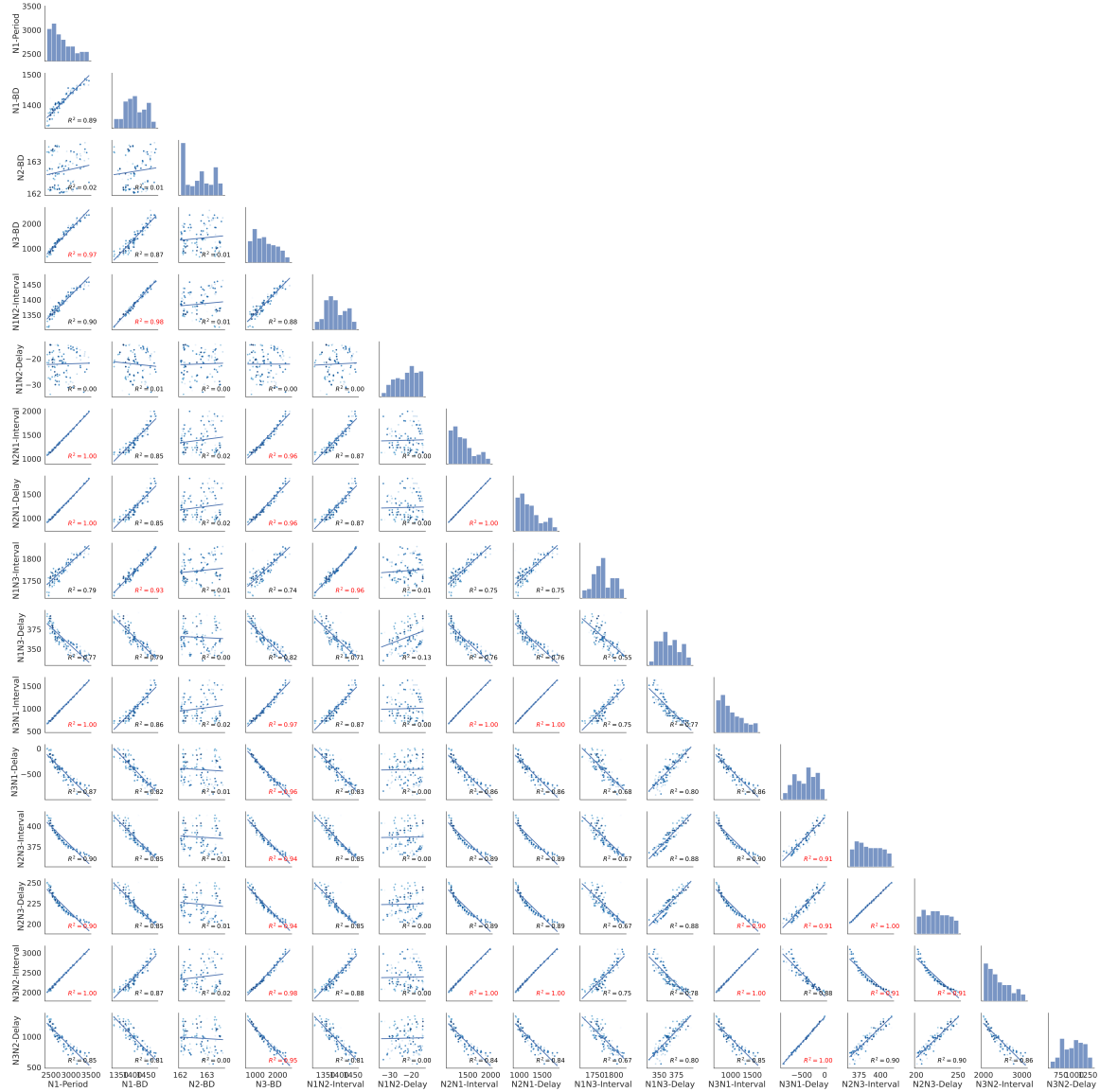


Figure 5.9: N3t stimulation: Pairplot with all possible combination between time intervals within a cycle.

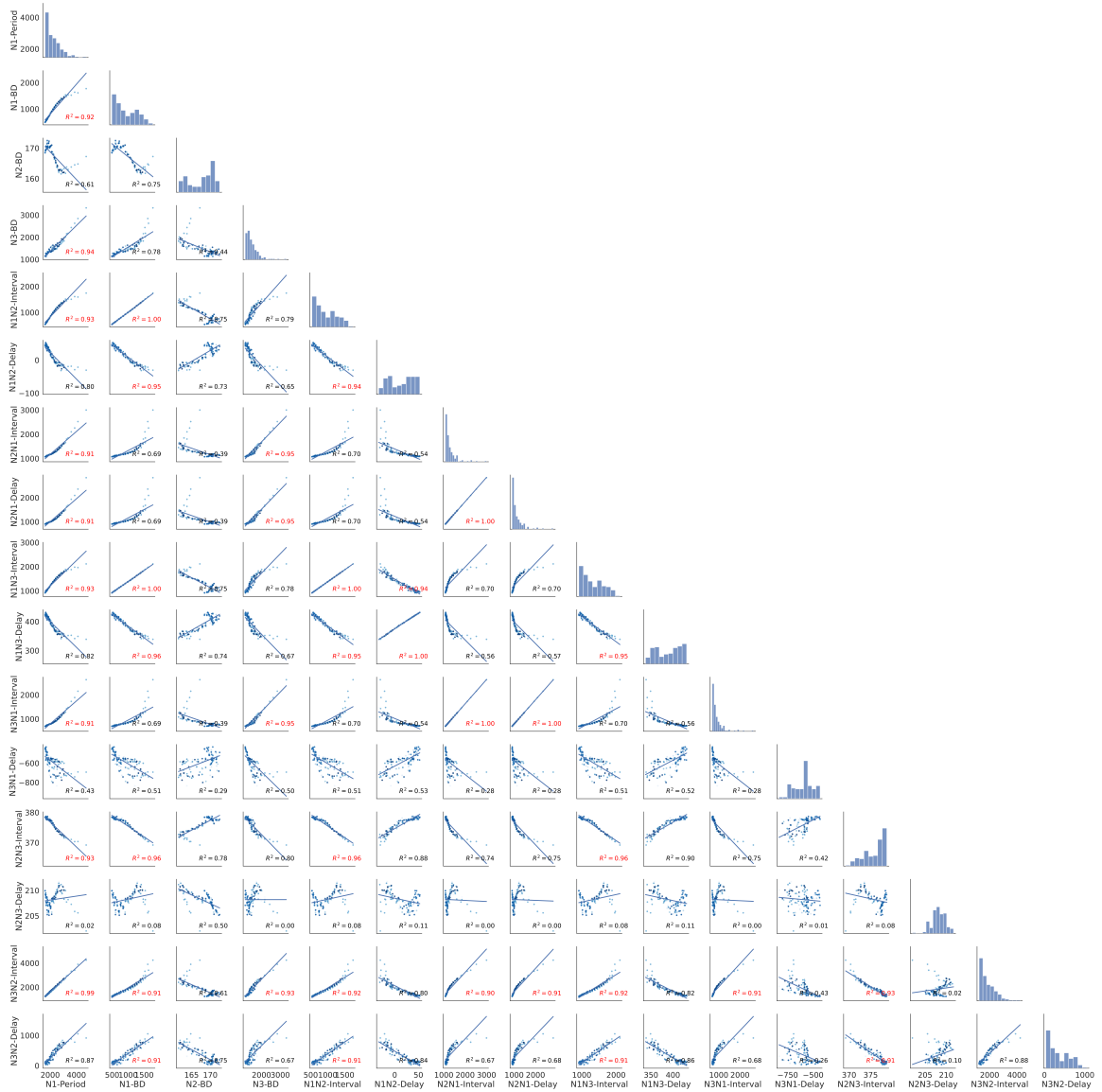


Figure 5.10: SO stimulation: Pairplot with all possible combination between time intervals within a cycle.

5.3.5 Comparison with two-phase intervals

In the previous subsections, we analyzed the sequential dynamical invariants for three phases, but we can also define two-phase intervals, taking as reference, for example, N1 and N3. This is the case discussed in the work by Elices et al. (2019), and in the following section we will also use two phases for some of the recordings were it was not possible to characterize the N2 phase out of the intracellular recordings. Figure 5.11 provides a comparison of different intervals conforming the sequence and associated relationships when the time references are set in N1, N2 and N3 (as we have shown so far) or only for N1 and N3.

When we only consider two phases, we have less possible combinations and the time-intervals that would correspond to the third neuron are contained in the resulting ones. For example, as we can see in Fig. 5.11a), N2N3 delay would be represented by N1N3 delay and N2 burst duration is included in the N2N3 interval. This result is relevant when analyzing two-phase intervals in triphasic rhythms.

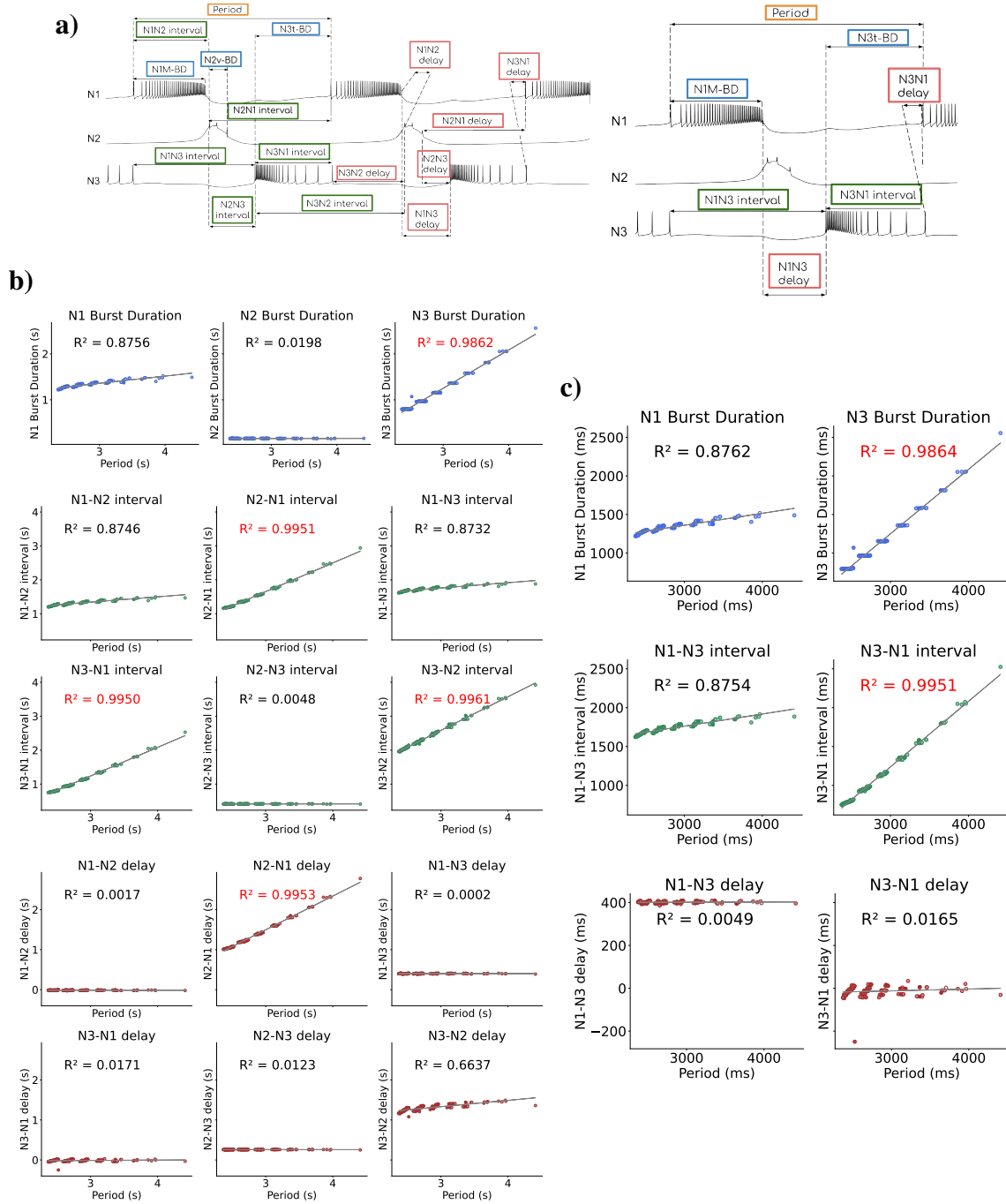


Figure 5.11: a) Representation of the intervals for each cycle when considering three or two phases (left and right, respectively). b) Interval correlations to period for SO-driven simulation for three phases. First row: Burst duration. Second and third row: Two-neuron intervals. Forth and fifth row: Two-neuron delays (data shown in Fig. 5.5). c) Interval correlations to period for N1M-driven simulation for two phases. First row: Burst duration. Second row: Two-neuron *intervals*. Third row: Two-neuron *delays*. For b) and c) the linear relationships are quantified by the R^2 values of the regression.

5.4 Experimental results in *Lymnaea Stagnalis*

In the previous section we analyzed the presence of sequential dynamical invariants in a CPG model, showing that strong correlations can be formed when stimulating certain neurons in the circuit and only when the circuit modeled has enough flexibility to adapt to the changes in the rhythm. In this section we will explore these phenomena in intracellular recordings of the living activity of the feeding CPG of *Lymnaea stagnalis*. The aim here is to search for sequential dynamical invariants as those reported in Elices et al. (2019), and also explore their functional meaning by analyzing different sources of stimulation of the rhythm. The data here characterized was kindly provided for this work by Dr. Michael Crossley, University of Sussex (see Sec. 5.2.3).

When studying temporal structures in neural dynamics, the definition of time references is a key first point. In the computational analysis described in the previous section, the time references to define cycle-by-cycle sequence intervals were the first and last spikes of each burst. In that case, as in the case of the pyloric neurons in *C. maenas*, the CPG phases are directly related to the bursting activity of these motoneurons and the burst can be consistently identified by the first and last spike. However, in the case of the feeding CPG in *Lymnaea stagnalis*, the activity is usually characterized with recordings from both interneurons and motoneurons (Elliott & Benjamin, 1985; Staras et al., 1998; Benjamin, 2012). This requires a more complex combination of burst references to characterize the phases of the CPG –protraction, rasp and swallow– based on cycle-by-cycle time intervals. Thus, for this analysis, we will consider again the three phases of the CPG which are associated mainly to the three interneurons –N1M, N2v and N3t. Since it is not always possible to record these neurons at the same time (specially N2v that is located in the ventral side), we will establish the time references for the sequence analysis by a combination of interneuron and motoneuron events following their activity at each phase.

For example, in Figure 5.12 the three phases in the CPG are marked by a colored background over the recording. Note that they can be delimited by the neurons in the circuit but some of the motoneurons cover several phases, as it is the case of B4 in panel a) or B3 in panel b). Phases can also be defined by the first and last spike, as it is the case for phase N3 and neuron B8, but in other cases as the phase N2, the relevant reference is the hyperpolarization of specific neurons, such as the strong inhibition visible in neuron B5 in panel b). Also, the depolarization of some neurons carries relevant information, since, for example in the case of B1 in Fig. 5.12.b), the visible depolarizations that did not generate action potentials represent the N1 phase through the connection between N1M and B1. Therefore, to characterize the time sequences in the feeding CPG, we needed compound references from several neural recordings, which are summarized in Table 5.2. Note that, different

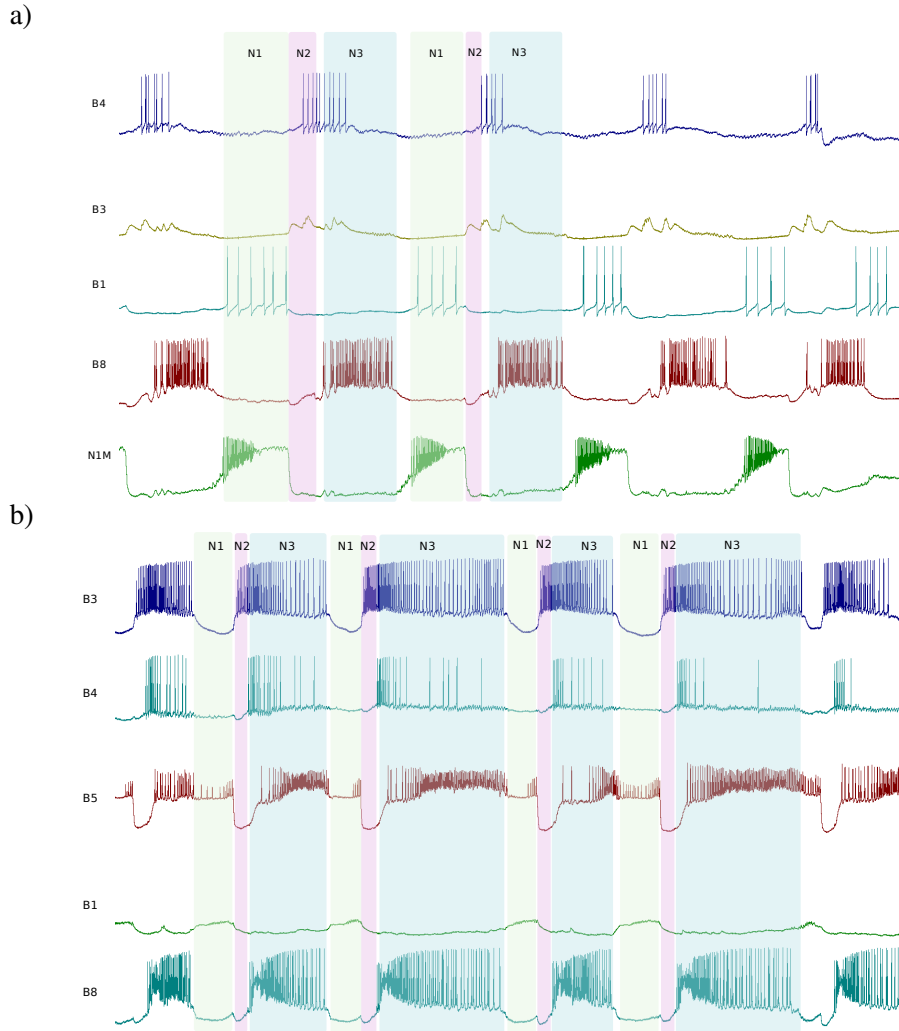


Figure 5.12: Delimitation of phases in the feeding CPG of *Lymnaea stagnalis* based on different recordings. Panel a) intracellular recordings for motoneurons B4, B3, B1 and B8 and the interneuron N1M. Phases are delimited by N1M and B1, which have the same activation time for phase N1, the inhibition of N1M and the start of the depolarization in B8 for phase N2, and the first and last spike of burst B8 for phase N3. Panel b) intracellular recordings for motoneurons B3, B4, B5, B1 and B8. Phases are delimited by B1 depolarization for phase N1, the strong inhibition of B5 for phase N2, and the first and last spike of burst B8 for phase N3.

time references must be taken into account to reach conclusions about the time-interval constraints in the cycle-by-cycle analysis. All possible intervals conforming each cycle between the neurons are taken into account in this analysis (see 5.2.1). The events and neural recordings to define each time-interval for each are described in section 5.2.3 for each experiment.

Another key point in the study of the feeding CPG of *L. stagnalis* is that the generation of the rhythm is a combined action of different cells (Benjamin, 2012), not only interneurons but also motoneurons have a role in the activation (Staras et al., 1998), and modulatory neurons in the buccal and cerebral

	N1-Protraction	N2-Rasp	N3-Swallow
Start	Last spike of N3t/B3 Depolarization or first spike in B1 First spike in B6	Inhibition of B5	First spike of B8
End	Last spike of B5 Hyperpolarization in B1 or B6	First spike of B8	Last spike of N3t/B3

Table 5.2: Time reference boundaries for the three phases in the feeding CPG.

ganglia are involved in the rhythm. Figure 5.13 shows a diagram with the distributed circuit connections in the CPG and modulatory neurons connected to it. All these factors affect the rhythm and

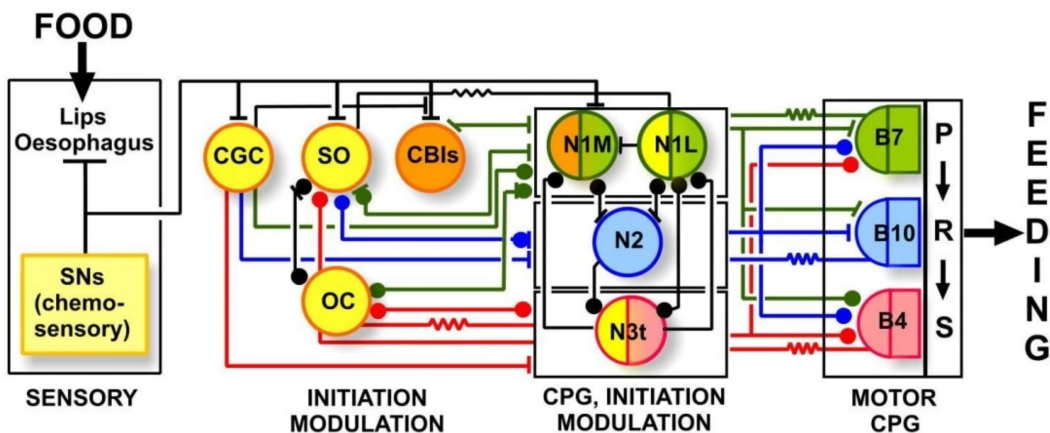


Figure 5.13: Representation of the distributed system of the feeding CPG. Dots indicate inhibitory chemical synapses, bars excitatory chemical synapses and resistor symbols electrical synapses. Colors indicate the function of the neuron classified as modulatory or initiator (yellow and orange, respectively), and the three phases: protraction, rasp and swallow (green, blue and red, respectively). From left to right: food detection represented by Lips that stimulate CGC, SO CBIs and N1M neurons initiate the rhythm. The ongoing activity is then modulated by those neurons but also by OC neurons and N1 and N3t neurons. Some examples of motoneurons are represented on the right side of the panel, associated to each feeding phase. This figure was adapted from Panel C of Fig. 1 in Benjamin (2012) (work under license [Creative Commons Attribution](#)).

thus the neuronal sequential activation and how variability is distributed among the different intervals cycle by cycle. Also, not all the neurons are involved every time the rhythm is active, and that gives also information about the different contexts in which the rhythm evolves. For example, the rhythm can be activated by the presence of food or sucrose stimulation, in which case the animal needs to initiate the activity and ingest food. Then, the rhythm is started by the stimulation of the lip nerve that also excites N1M neuron. Also, even at the absence of food, when the animal is hungry, the CPG can be activated, in this case with a strong role of N3t as modulator. The modulation of the rhythm is also a key aspect, and modulatory neurons such as SO or CV1a control the rhythm after its initiation,

and they have shown to have distinct alternative roles in the activity (Kemenes et al., 2001).

In this section we will analyze and describe different examples of experiments for the isolated ganglia with intracellular recordings under different conditions: spontaneous activity, SO-driven activity (spontaneous and by stimulation), medium lip nerve (MLN) stimulation driven activity, and CV1a-driven activity by induced stimulation.

5.4.1 Invariants in spontaneous activity

The spontaneous activity here refers to intracellular recordings of the buccal ganglia after the isolation of the CNS with no chemical or electrical induced stimulation. In that case, since the CPG is able to maintain the activity in an autonomous manner, it keeps the motor activity as if the CNS was not isolated. In this condition, although the characterization of the sequential dynamical invariants can be done, their possible functionality association is more complicated, since the context of the movement origin is lost. The study of these sequential restriction in artificial stimulation contexts can help classify this spontaneous activity, even when the rest of the system is not available.

Here we analyze three examples of spontaneous activity. We do not know what was the source or context for the feeding activation, but there are differences between the three experiments regarding their dynamical invariants. The case with the strongest linear correlation is the first example shown in Fig. 5.14, where the N3 burst duration and the associated intervals covering N3 phase (N2N1 interval, N3N1 interval, N3N2 interval and N2N1 delay) had a strong linear correlation with the period ($R^2 > 0.9$). This is also clear in the variability boxplot, where the variability distribution of the period is similar to that of N3 burst duration, N2N1 interval, N3N1 interval, N3N2 interval and N2N1 delay. The rest of the intervals do not present a similar distribution to the period. This difference in variability is also important, since while there are intervals with a strong linear correlations illustrating cycle-by-cycle dynamical restrictions, some other intervals have no relation, all have $R^2 < 0.1$, i.e., are free to display unrelated variability. Observing the recording of this example (first row in Fig. 5.14), we can see that the N3 neuron had long periods of tonic firing (which were excluded from the time-interval relations), and that the spontaneous activity was lead by N3 neuron, associated in the literature with spontaneous activity in satiated animals. The N3t was tonically firing producing long periods of silence interrupted by short rasps (Staras et al., 2003; Benjamin, 2012).

In the following examples shown in Figs. 5.15 and 5.16, the variability distribution is different. In the example shown in Fig. 5.15, we can see the distribution of the variability between N1 and N3 phases illustrated in the boxplot and also in the linear regressions, in which, although they have low R^2 values, we can observe some linear tendencies between specific time intervals and the period,

specially in combined intervals such as the N3-N2 interval. A common characteristic with the previous example is the presence of unrelated intervals to the period, since N2 burst durations and other time-intervals associated to the N2 phase (N2N3 delay, N1N2 delay) have $R^2 < 0.1$. These intervals also remain unrelated to the period in the third example, shown in Fig. 5.16, where N2 and N2N3 delay have similar R^2 values. In that last case, however, the variability is mostly in the N1 phase. Again, the linear correlations with the period are in combined intervals, usually the ones involving N1 and N3 phases: N31N1 interval, N2N1 delay, N3N1 delay; this points to the distribution of variability between those two phases. Also, the fact that the combined intervals have much stronger linear correlations is affected by the time references in these intervals.

Figure 5.17 shows the pairplots for each of these three experiments, with all possible combinations between intervals. Note that, for a better representation, there are only two phases taken here into account: N1 and N3. (Figures B.2, B.3 and B.4 in the Appendix show the pairplot for intervals from the three-phases). Most part of the time-intervals involved in the N2 phase are contained in the N1N3 delay, which goes from the end of N1 to the start of N3 (see 5.2.1). The intervals' relations with the period correspond to the first column, the rest are combinations between all possible intervals, including the period defined from N3 beginning to the beginning of the next N3 burst (analogously to N1-period). We see again that each recording has a different variability distribution: In the first panel, we can observe several robust dynamical invariants. This is also the case for the second panel, where we can observe that, in relation to N1 and N3, the N1-BD has a really strong linear relation with the N1N3 interval, which suggests that all variability in that phase comes from the burst duration, and the N2 phase remains mostly constant. In the last panel, we can appreciate this increase in the correlation between N1-BD and the period and the decrease in the correlation with the N3-BD. This is shown in the linear correlation unveiled in this pairplot by the N3N1 interval and the N3N1 delay, representing the constancy in the time duration of the burst.

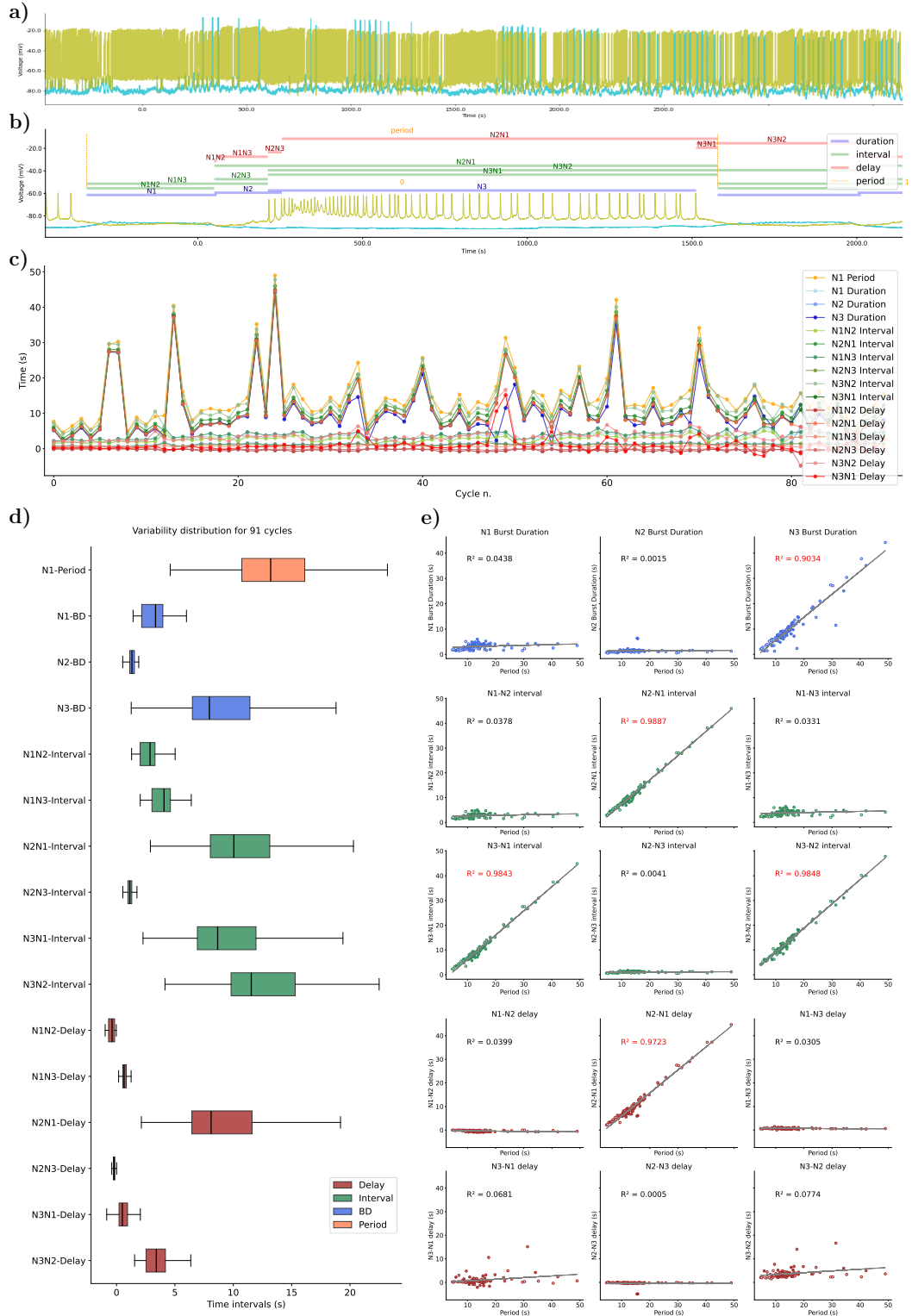


Figure 5.14: Spontaneous case 1: Panel of interval distributions and dynamical invariants for the three phases in the CPG for spontaneous activity. a) Voltage traces for the intracellular recording analyzed for this panel. b) Representation of the time-intervals described. c) Duration of each time interval (y-axis) at each cycle. d) Box-plot with the variability distribution of the duration of each time-interval. e) Time-intervals duration against the period for NX-Burst duration (blue), NXNY-Interval (green) and NXNY-Delay (red).

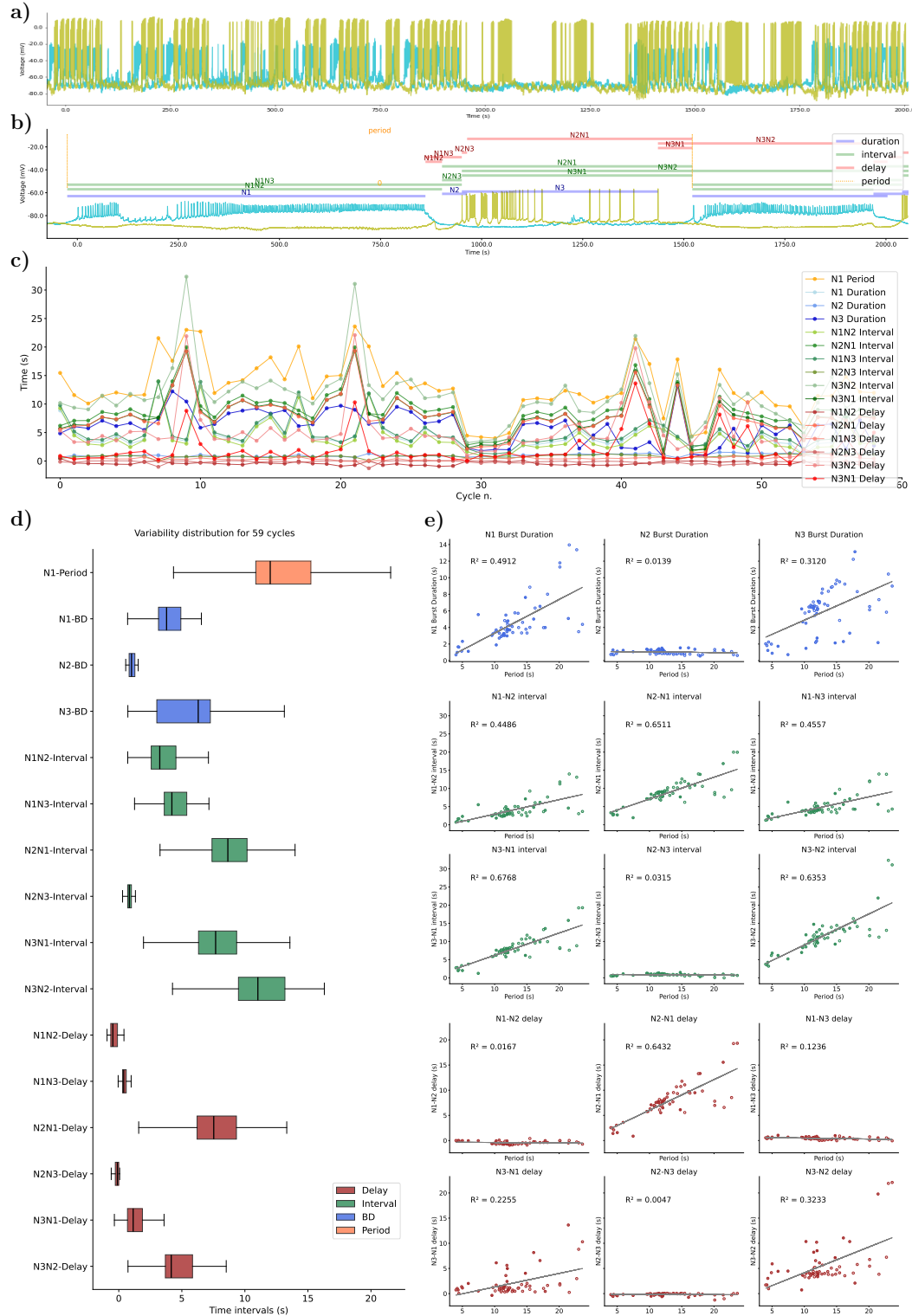


Figure 5.15: Spontaneous case 2: Panel of interval distributions and dynamical invariants for the three phases in the CPG for spontaneous activity. a) Voltage traces for the intracellular recording analyzed for this panel. b) Representation of the time-intervals described. c) Duration of each time interval (y -axis) at each cycle. d) Box-plot with the variability distribution of the duration of each time-interval. e) Time-intervals duration against the period for NX-Burst duration (blue), NXNY-Interval (green) and NXNY-Delay (red).

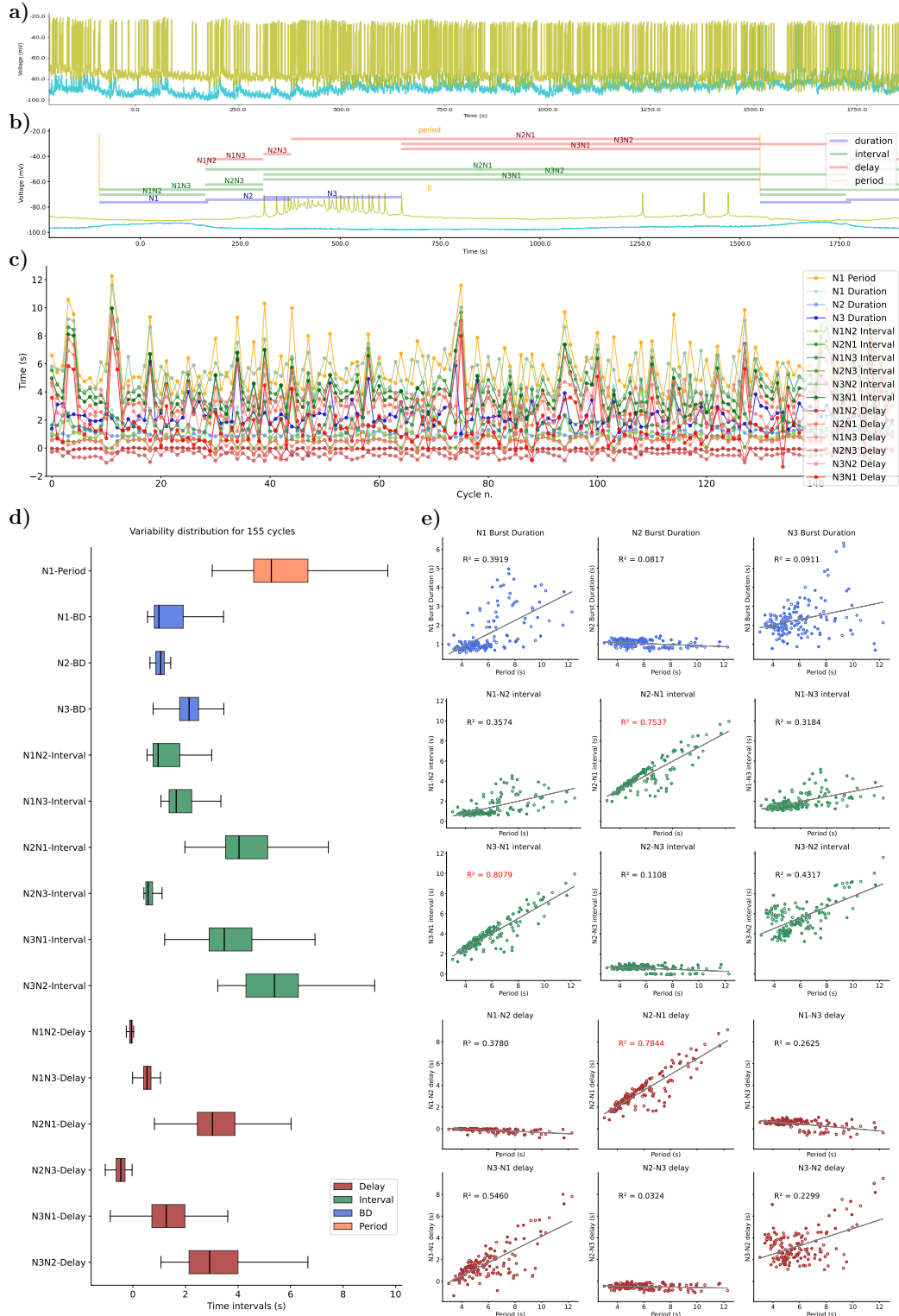


Figure 5.16: Spontaneous case 3: Panel of interval distributions and dynamical invariants for the three phases in the CPG for spontaneous activity. a) Voltage traces for the intracellular recording analyzed for this panel. b) Representation of the time-intervals described. c) Duration of each time interval (y-axis) at each cycle. d) Box-plot with the variability distribution of the duration of each time-interval. e) Time-intervals duration against the period for NX-Burst duration (blue), NXNY-Interval (green) and NXNY-Delay (red).

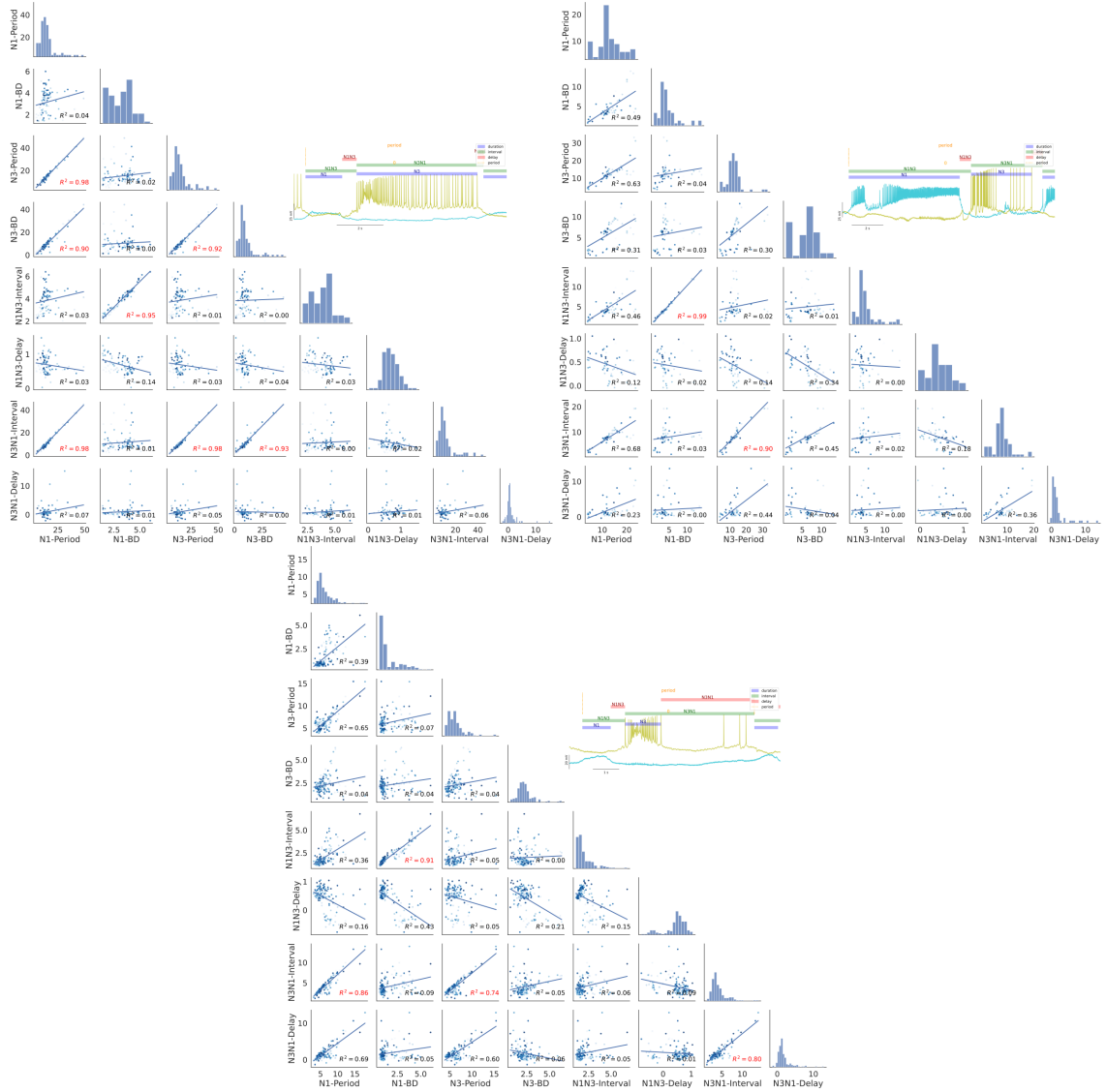


Figure 5.17: Spontaneous activity summary: Panel of the pairplots for all possible combinations between the time intervals defined for two phases (N1 and N3) in the CPG recordings for the three examples of spontaneous activity recordings.

5.4.2 Invariants in SO driven activity

As we saw before, the SO role in the feeding CPG is modulatory, which means, that it modifies the rhythm once it is activated. In the model analysis, in section 5.3.3, we showed that when the variability in the simulations was induced by adding a ramp current to the SO neuron, the time-interval variability was distributed between the N1 and N3 phases, having both a strong correlation with the period, which increased the R^2 values. Therefore, in the living recordings we can expect that the variability cycle-by-cycle is distributed during the modulation of SO, which is connected to N1M and N3t (see Fig. 5.13).

In this subsection, we will see an example from a spontaneous activity where the SO neuron was modulating for two lapses of time during the recording. This can be identified by the inhibition of B4 and the activation of B3, as illustrated in Fig. 5.18. We can also see in this figure how, during the SO modulation, the rhythm was "stabilized" with less variability in the intervals' duration. The characterization of the variability of the time intervals and their relation to the cycle period for this trace is depicted in Figs. 5.19, 5.20 and 5.21, when SO was modulating, when it ceased its modulation, and when it then restarted it, respectively. Note that in those Figures only two phases are considered to characterize the time intervals cycle-by-cycle. In this section and the following ones we will consider the references from N1 and N3.

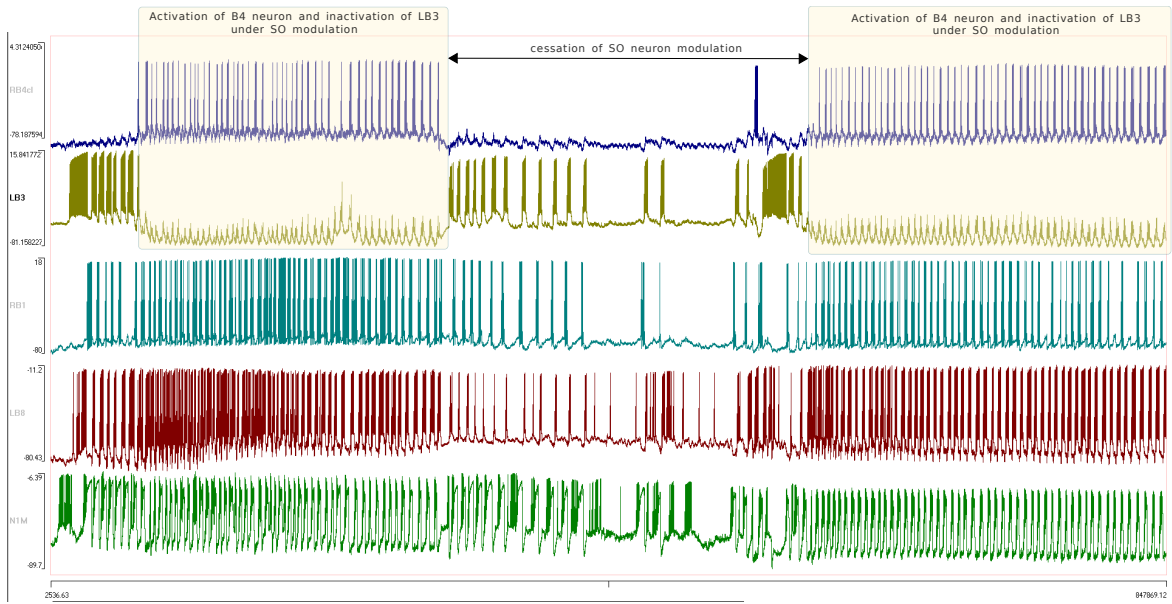


Figure 5.18: Representation of recordings of the spontaneous activity with lapses of SO modulation. The parts of the recording with yellow background highlight when the activity was modulated by the SO neuron. From top to bottom: intracellular recording of a neuron from the B4 cluster, B3 motoneuron, B1 motoneuron, B8 motoneuron, and N1M interneuron.

When the rhythm was driven by SO, we can see how the variability for N1-BD and N3-BD was limited, which is reflected in the low variability observed in the boxplots of Figs. 5.19 and 5.21, and also panels c) for both cases that show the duration of each interval per cycle and there were not large changes in the duration, as we saw for example in Fig. 5.14.c). In the correlation of the intervals with the period, shown in panel e), although R^2 value is not significantly high, N1-BD and N3-BD have around 0.7 and 0.3 in both cases, pointing to this redistribution of the variability. Figure 5.20 shows the characterization of the intervals variability when the SO stops its modulation. During that lapse of time (depicted in Fig. 5.18), the variability concentrates in the N1 phase as it can be seen in the duration of the interval in panels c) and d), and also in the high correlation to the period in panel e) only for intervals such as N1-BD ($R^2 = 0.9$). Also, while the R^2 value of N1-BD is in the order of 0.9, the N3-BD is close to 0. Although this example had only a few cycles, it suggests that the variability in that lapse of time was all carried by the N1 phase. Regarding the rest of the time-intervals in the cycle, the one with the largest variability is N3N1 interval, since it contains N1-BD. Also, when the modulation of SO ceases, the N3N1 delay variability rises, which is notable compared to the rest of the experiments and the model, and might be caused by the burst shape and how the intervals where defined (see Fig. 5.20, first panel). This result, also matches the experimental work by Elliott and Andrew (1991), which showed this distribution between N1-BD and N3-BD. In that work, the SO modulation was induced by stimulating SO neuron.

Figure 5.22 shows an example inducing the SO modulation by electrical stimulation. Again, we can see the same variability distribution between N1 and N3 phases, having N1 a strongest correlation with the period, reaching $R^2 = 0.8$ this time. It is also important to the intervals associated to N2 phase (N1N3 delay and N3N1 delay) do not have any relation with the period, and their variability is minimal. To further compare this two panels, the pairplots for one example of spontaneous activity and the SO induced modulation are shown in Fig. 5.23. In the pairplot, we see the same time-interval relations and also another strong relation between N1N3 Interval and N1-BD, which appears in both cases and exemplifies that the variability is mostly in N1-BD and N2 phase shows constant activity, since in the N1N3 interval, all the variability is associated with N1-BD.

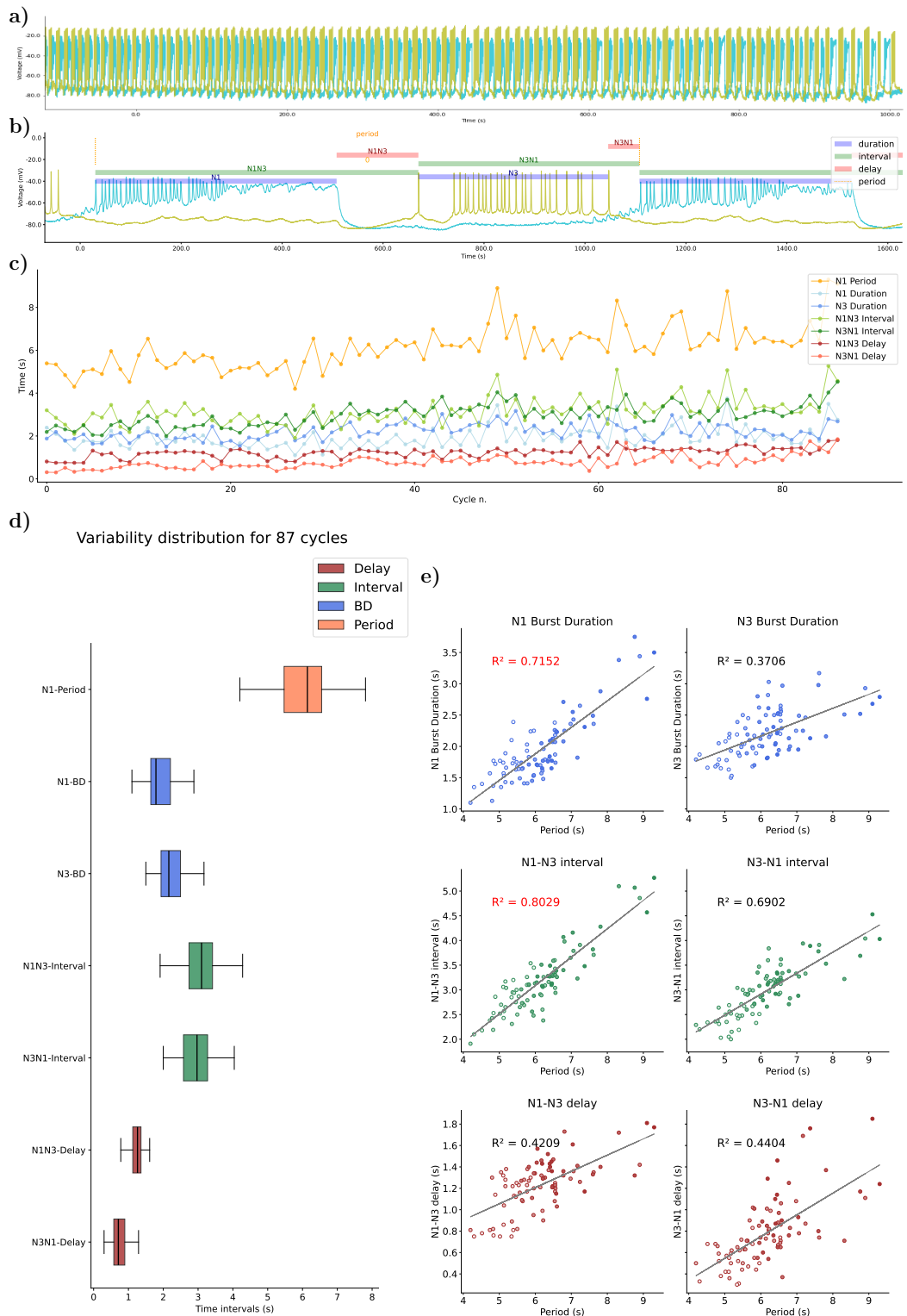


Figure 5.19: SO neuron driven spontaneous activity: Panel of interval distributions and dynamical invariants for the two phases in the CPG for spontaneous activity driven by SO neuron. a) Voltage traces for the intracellular recording analyzed for this panel. b) Representation of the time-intervals described. c) Duration of each time interval (*y* – axis) at each cycle. d) Box-plot with the variability distribution of the duration of each time-interval. e) Time-intervals duration against the period for NX-Burst duration (blue), NXNY-Interval (green) and NXNY-Delay (red).

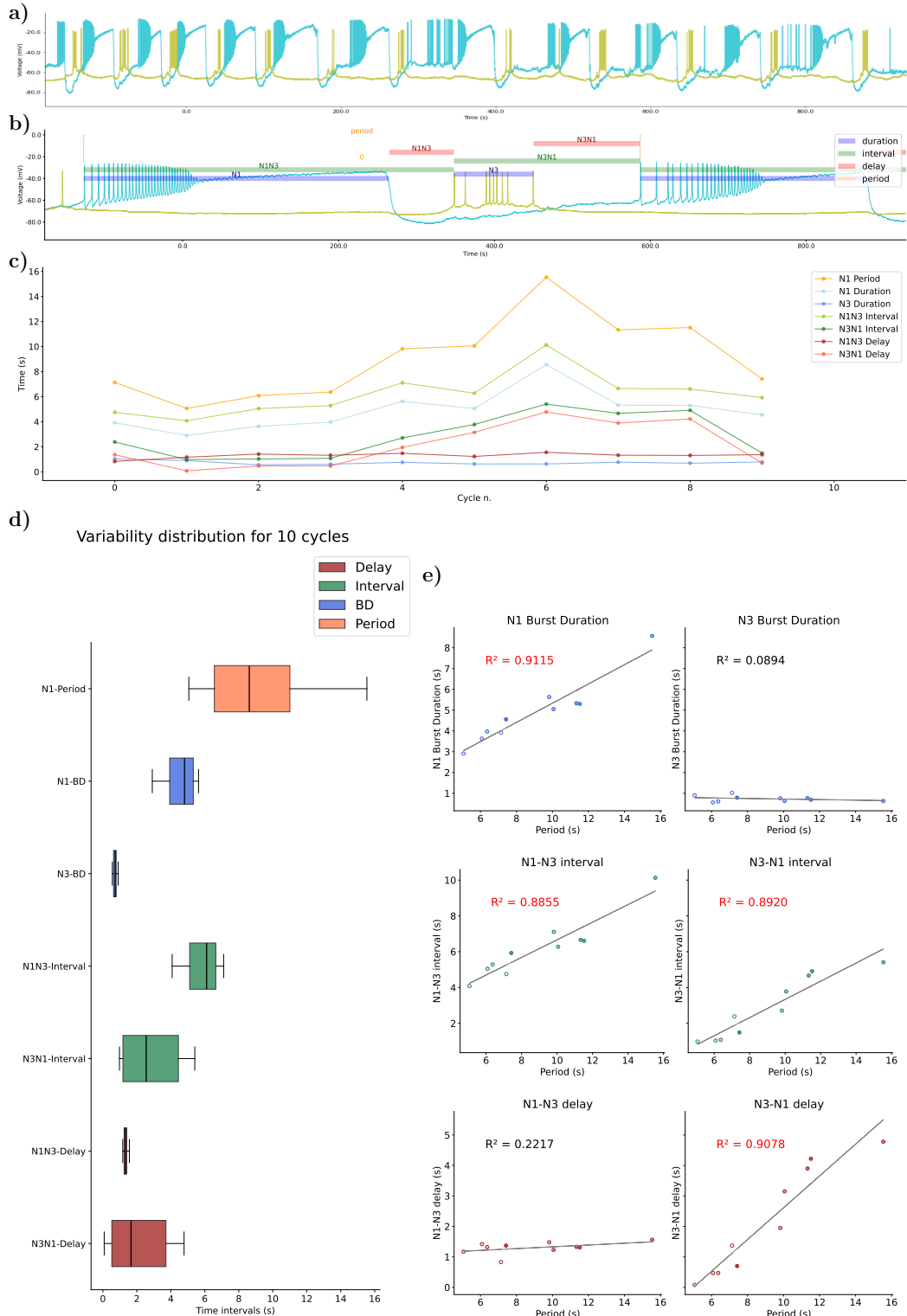


Figure 5.20: Spontaneous activity when the SO-driven modulation ceases: Panels illustrate the interval distribution and dynamical invariants for the two phases in the CPG during spontaneous activity without SO modulating the rhythm. a) Voltage traces for the intracellular recording analyzed for this panel. b) Representation of the time-intervals described. c) Duration of each time interval (*y* – axis) at each cycle. d) Box-plot with the variability distribution of the duration of each time-interval. e) Time-intervals duration against the period for NX-Burst duration (blue), NXNY-Interval (green) and NXNY-Delay (red).

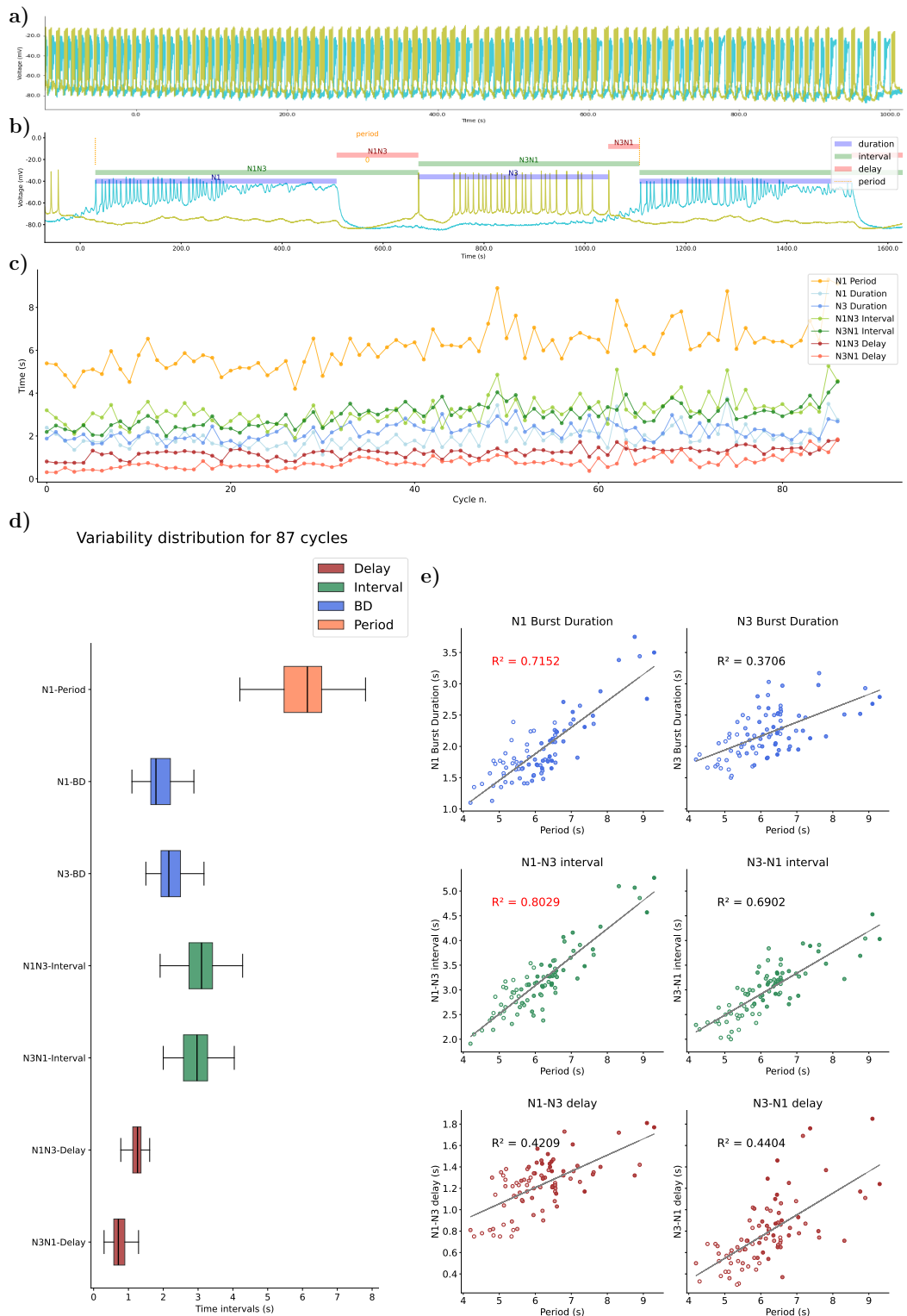


Figure 5.21: Spontaneous SO neuron modulation restarts: Panel of interval distributions and dynamical invariants for the two phases in the CPG for spontaneous activity driven by SO neuron. a) Voltage traces for the intracellular recording analyzed for this panel. b) Representation of the time-intervals described. c) Duration of each time interval (y – axis) at each cycle. d) Box-plot with the variability distribution of the duration of each time-interval. e) Time-intervals duration against the period for NX-Burst duration (blue), NXNY-Interval (green) and NXNY-Delay (red).

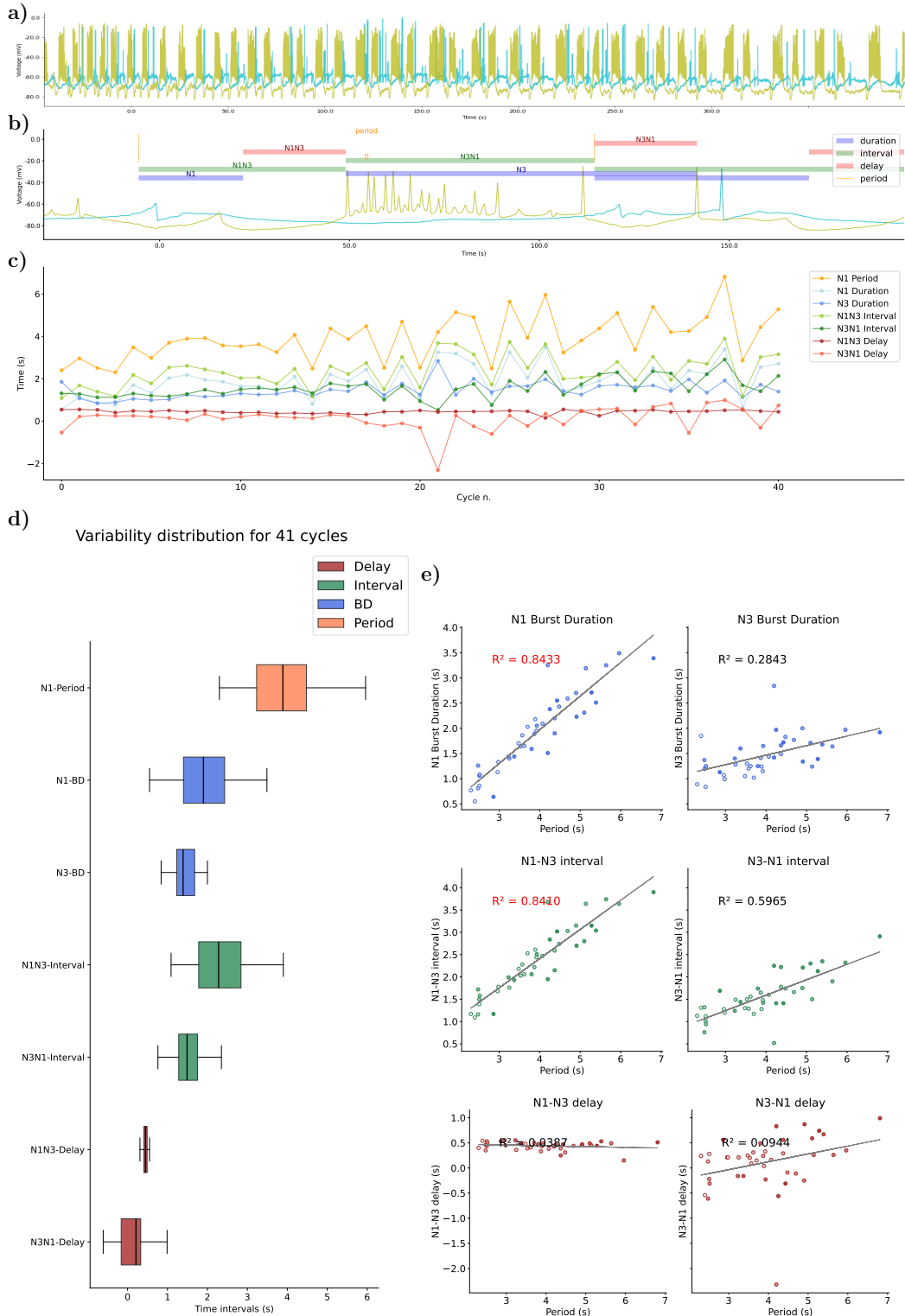


Figure 5.22: SO neuron stimulation: Panel of interval distributions and dynamical invariants for the two phases in the CPG for activity driven by SO neuron induced by its electrical stimulation. a) Voltage traces for the intracellular recording analyzed for this panel. b) Representation of the time-intervals described. c) Duration of each time interval (y – axis) at each cycle. d) Box-plot with the variability distribution of the duration of each time-interval. e) Time-intervals duration against the period for NX-Burst duration (blue), NXNY-Interval (green) and NXNY-Delay (red).

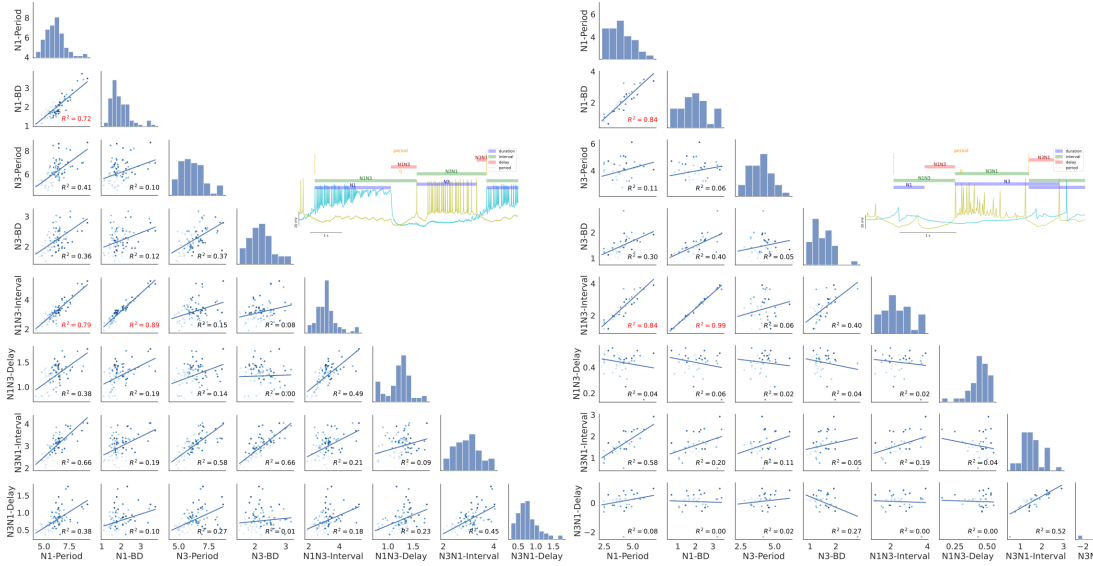


Figure 5.23: Panel of the pairplots for all possible combinations between the time intervals for two phases in the CPG recordings for (left) spontaneous SO rhythm modulation and (right) the induced SO rhythm modulation.

5.4.3 Invariants in MLN stimulation driven activity

The snail's lips are connected to the cerebral ganglia by the MLN (median lip nerves). It is possible to activate CPG activity by its stimulation, simulating the initiation of the rhythm in food presence (Staras et al., 1999). This nerve directly stimulates the N1M interneuron, in charge of the initiation of the rhythm, associated to the protraction phase. In Fig. 5.24 the variability and time-intervals correlations are characterized for a recording of this induced stimulation. We can see in that Figure that there is a strong linear correlation in the panel, leading the rhythm completely by N1 phase. This is visible in the robust dynamical invariant between N1 burst duration and the period and by N1N3 interval and the period. It is also important that no other intervals have relation with the period, so both N2 and N3 phases remain constant. Note that the N1 burst duration takes a wide range of values for its duration, even at really low ranges, shorter than N3 burst for example. This is also clearly represented in the figure in the third row, where N1 burst duration and N1N3 interval robustly follow the period. In Fig. 5.25 all possible combination of time-intervals for two phases are represented. We can see there other strongly related intervals: N1N3 interval with N1 burst duration, which again highlights the steadiness of N2 phase. These results suggest that during the MLN stimulation, the feeding rhythm variability is lead by N1 phase, activating the rhythm and stabilizing the activity.

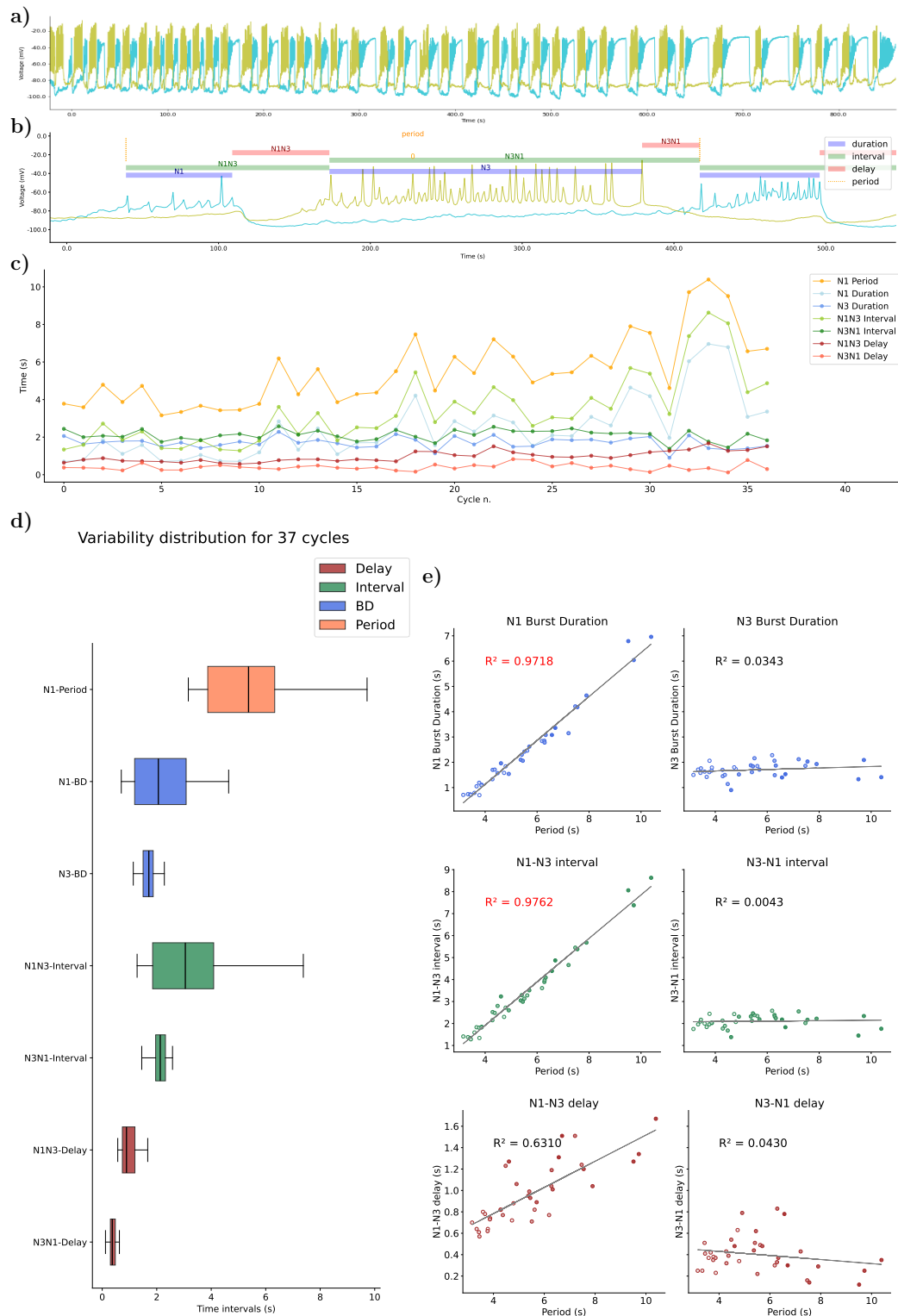


Figure 5.24: MLN stimulation: Panel of interval distributions and dynamical invariants for the three phases in the CPG under MLN Medium Lip Nerve (MLN) stimulation. a) Voltage traces for the intracellular recording analyzed for this panel. b) Representation of the time-intervals described. c) Duration of each time interval (*y – axis*) at each cycle. d) Box-plot with the variability distribution of the duration of each time-interval. e) Time-intervals duration against the period for NX-Burst duration (blue), NXNY-Interval (green) and NXNY-Delay (red).

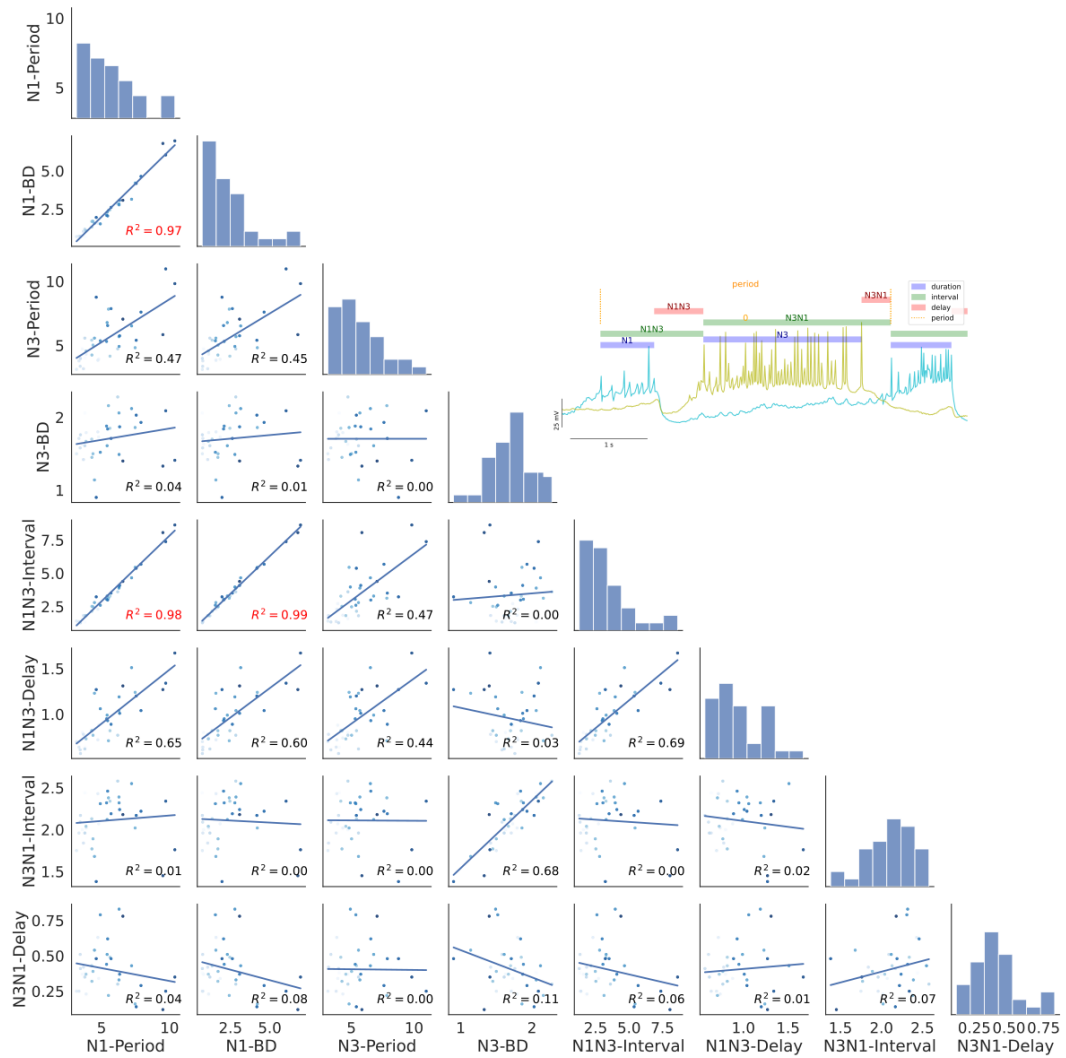


Figure 5.25: MLN stimulation: Pairplot with all possible combinations in the intervals.

5.4.4 Invariants in CVa1 driven activity induced by electrical stimulation

CV1a neuron is part of a larger population of CBIs that is influenced by sucrose, which can drive the rhythmic activity in that group of neurons. CBIs are connected by mutual excitation to the interneuron N1M, involved in the rhythm initiation (see Fig. 5.13). Therefore, it can be expected to observe in this case a stronger role of N1 phase in the variability distribution. For this case, there are four examples of different recordings, represented in figures 5.26 to 5.29. In the first three panels, we can see that the stronger relation is in N1 burst duration, specially in the first case where there is a strong sequential dynamical invariant with $R^2 > 0.9$. The rest of the intervals conforming that sequence were not strongly related, being N3 phase more variable than the N2 phase, barely presenting variability and with no linear correlation with the period. It is interesting to highlight that not in all cases where the variability was larger, the correlation to the period was also larger, as it is the case in illustrated in Figs. 5.27 and 5.28. In those examples, the variability in N3 phase is large but it is not related to the period. Seeing the third figure in each of those panels, we can explain it by the opposite direction of the changes in N3 (dark blue), N1 (light blue) and the period (orange), pointing that the N3 burst is adapting to the N1 strongest variability. This distribution is maintained for the three first cases, however, in the last case this is shifted. In the example characterized in Fig. 5.29, the N3 burst duration has a stronger linear relation with the period than N1, presenting also a larger variability. During that period the electrode stimulating CV1a slipped away and the stimulation was not as effective as it was in the rest of the examples. We can appreciate in the correlation between N1 and the period that there are some points white-colored that correspond to the beginning of the trace, which might look as outliers but present a tendency to a linear regression. Although this was not a methodic study, we decided to include this case since it represents the sensitivity of the circuit to changes in the context, redistributing the activity between the different phases in a flexible way, in this case from N1 to N3.

Finally, Fig. 5.30 depicts the plots for two phases for each panel as a summary of previous Figures. In one of the recordings, the N2 phase could be well identified, and the corresponding pairplot for three phases is in the Appendix B.5. In the pairplot, again we see a similar distribution in all figures except of the last one, where there are new correlations, present in the N3 burst duration with the N3N1 interval. Also there is a correlation of a negative slope in the first case, in case N3-BD and N3N1 delay, representing a regular overlapping of N1 and N3 phases.

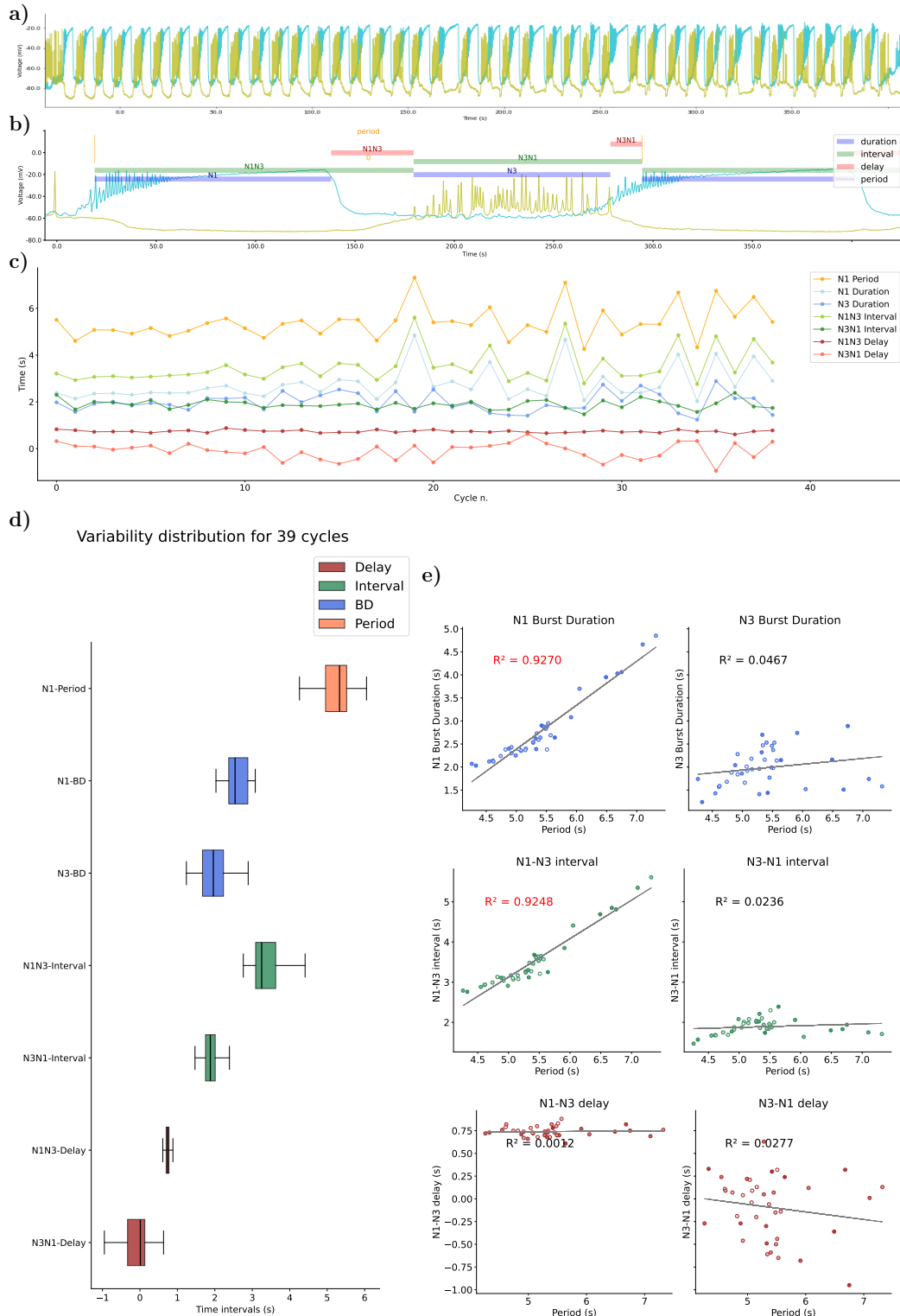


Figure 5.26: CV1a driven case 1: Panel of interval distributions and dynamical invariants for the two phases in the CPG under CV1a stimulation. a) Voltage traces for the intracellular recording analyzed for this panel. b) Representation of the time-intervals described. c) Duration of each time interval (y – axis) at each cycle. d) Box-plot with the variability distribution of the duration of each time-interval. e) Time-intervals duration against the period for NX-Burst duration (blue), NXNY-Interval (green) and NXNY-Delay (red).

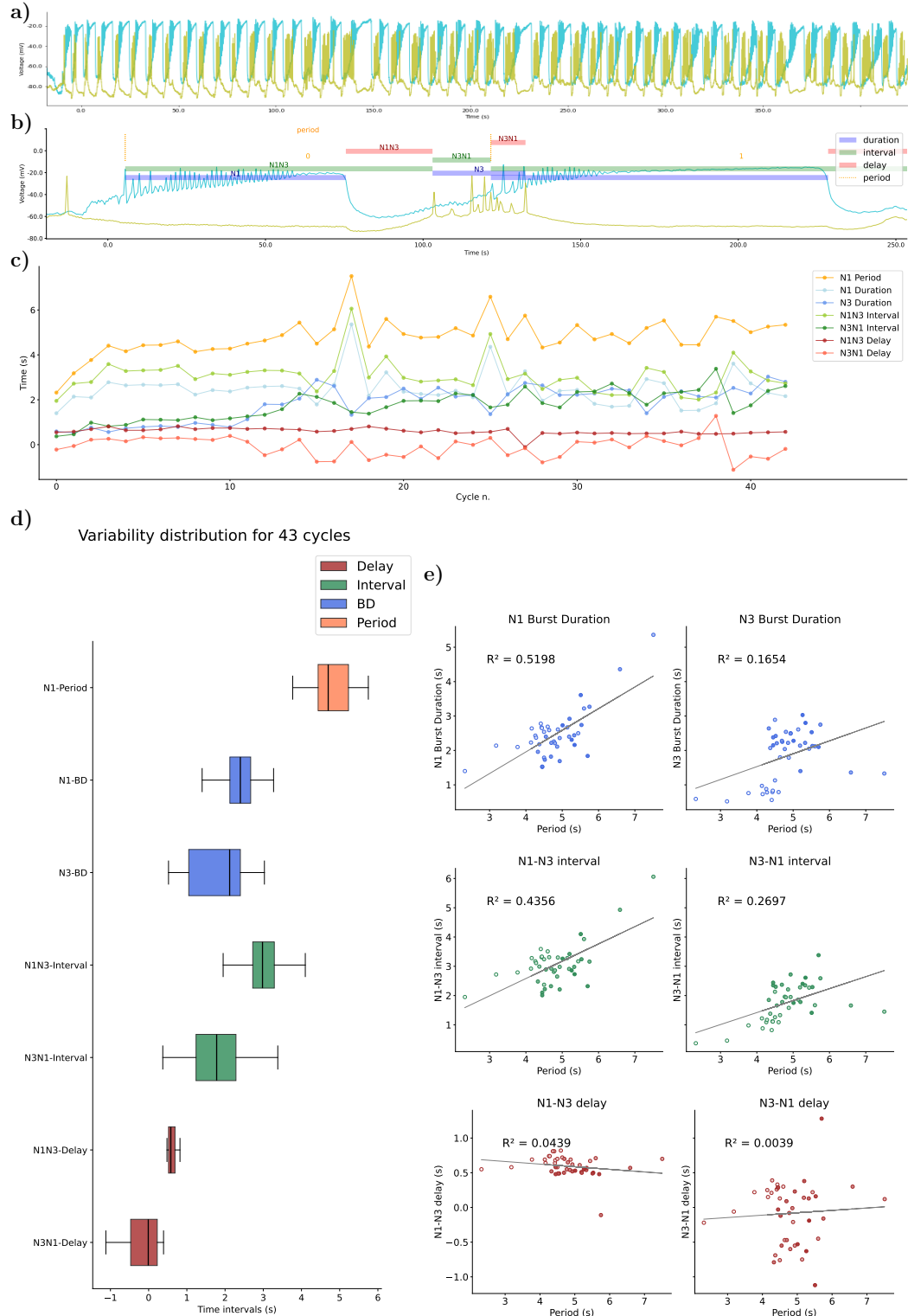


Figure 5.27: CV1a driven case 2: Panel of interval distributions and dynamical invariants for the two phases in the CPG under CV1a stimulation. a) Voltage traces for the intracellular recording analyzed for this panel. b) Representation of the time-intervals described. c) Duration of each time interval (y-axis) at each cycle. d) Box-plot with the variability distribution of the duration of each time-interval. e) Time-intervals duration against the period for NX-Burst duration (blue), NXNY-Interval (green) and NXNY-Delay (red).

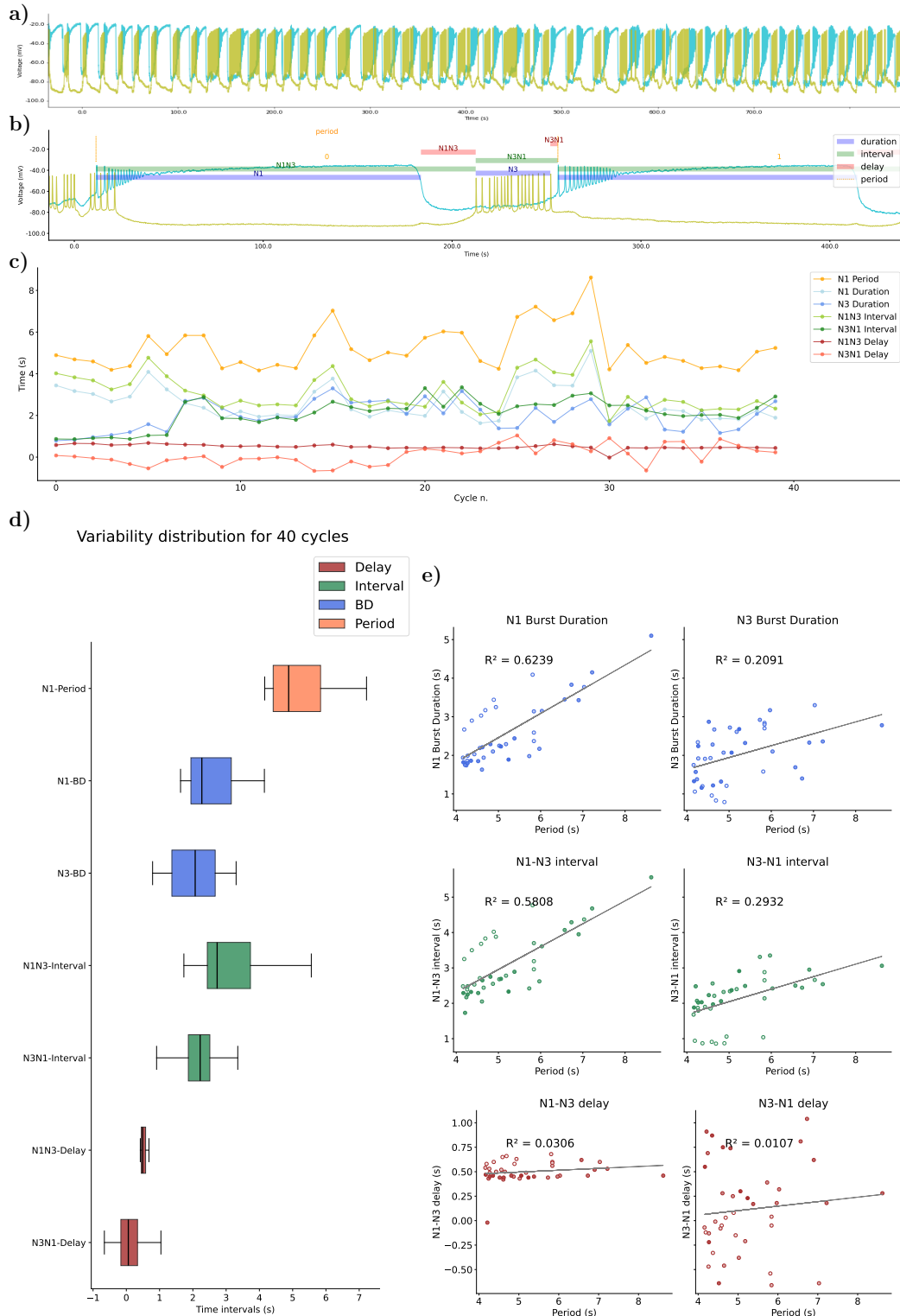


Figure 5.28: CV1a driven case 3: Panel of interval distributions and dynamical invariants for the two phases in the CPG under CV1a stimulation. a) Voltage traces for the intracellular recording analyzed for this panel. b) Representation of the time-intervals described. c) Duration of each time interval (y – axis) at each cycle. d) Box-plot with the variability distribution of the duration of each time-interval. e) Time-intervals duration against the period for NX-Burst duration (blue), NXNY-Interval (green) and NXNY-Delay (red).

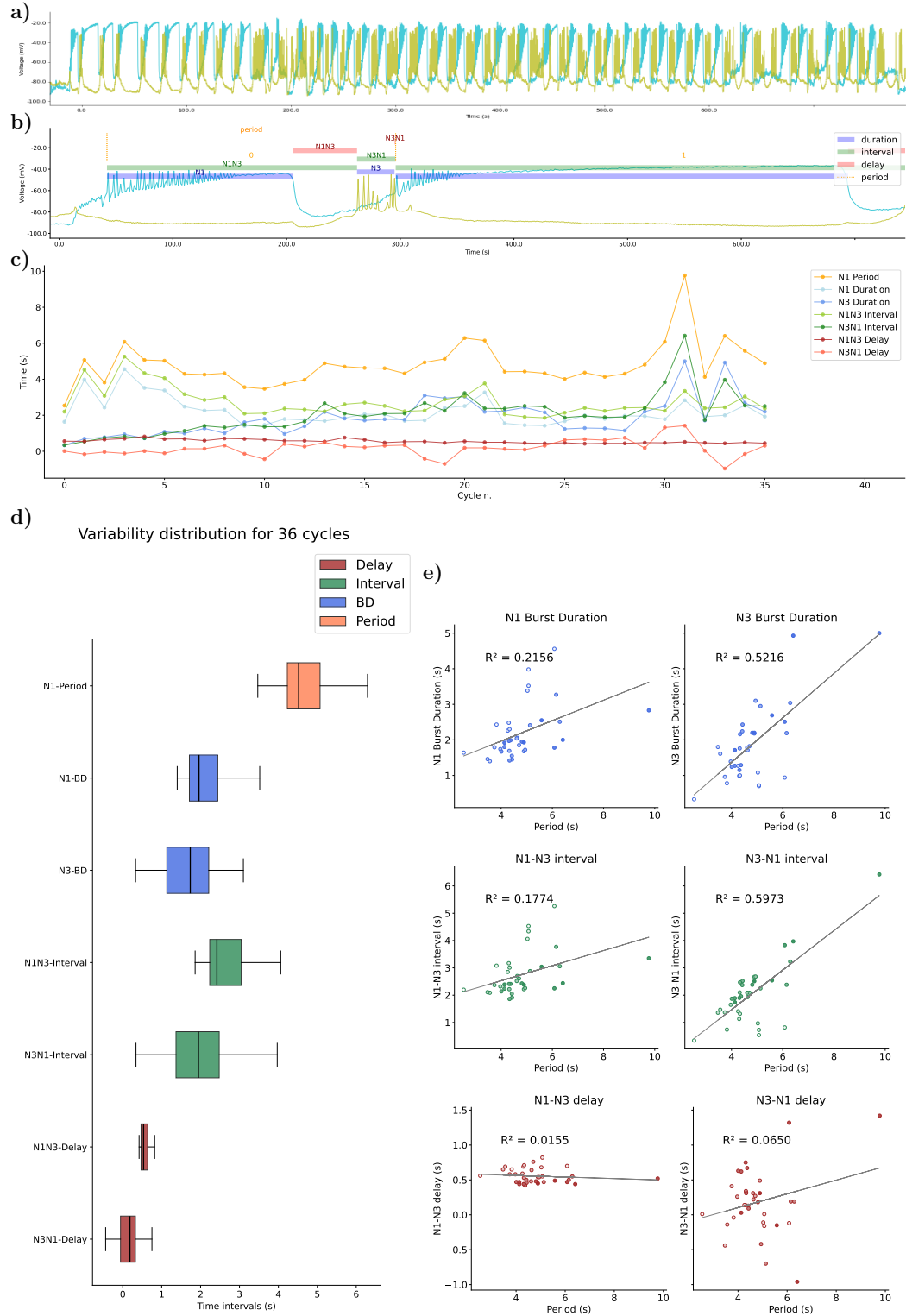


Figure 5.29: CV1a driven case 4: Panel of interval distributions and dynamical invariants for the two phases in the CPG under CV1a stimulation. a) Voltage traces for the intracellular recording analyzed for this panel. b) Representation of the time-intervals described. c) Duration of each time interval (y – axis) at each cycle. d) Box-plot with the variability distribution of the duration of each time-interval. e) Time-intervals duration against the period for NX-Burst duration (blue), NXNY-Interval (green) and NXNY-Delay (red).

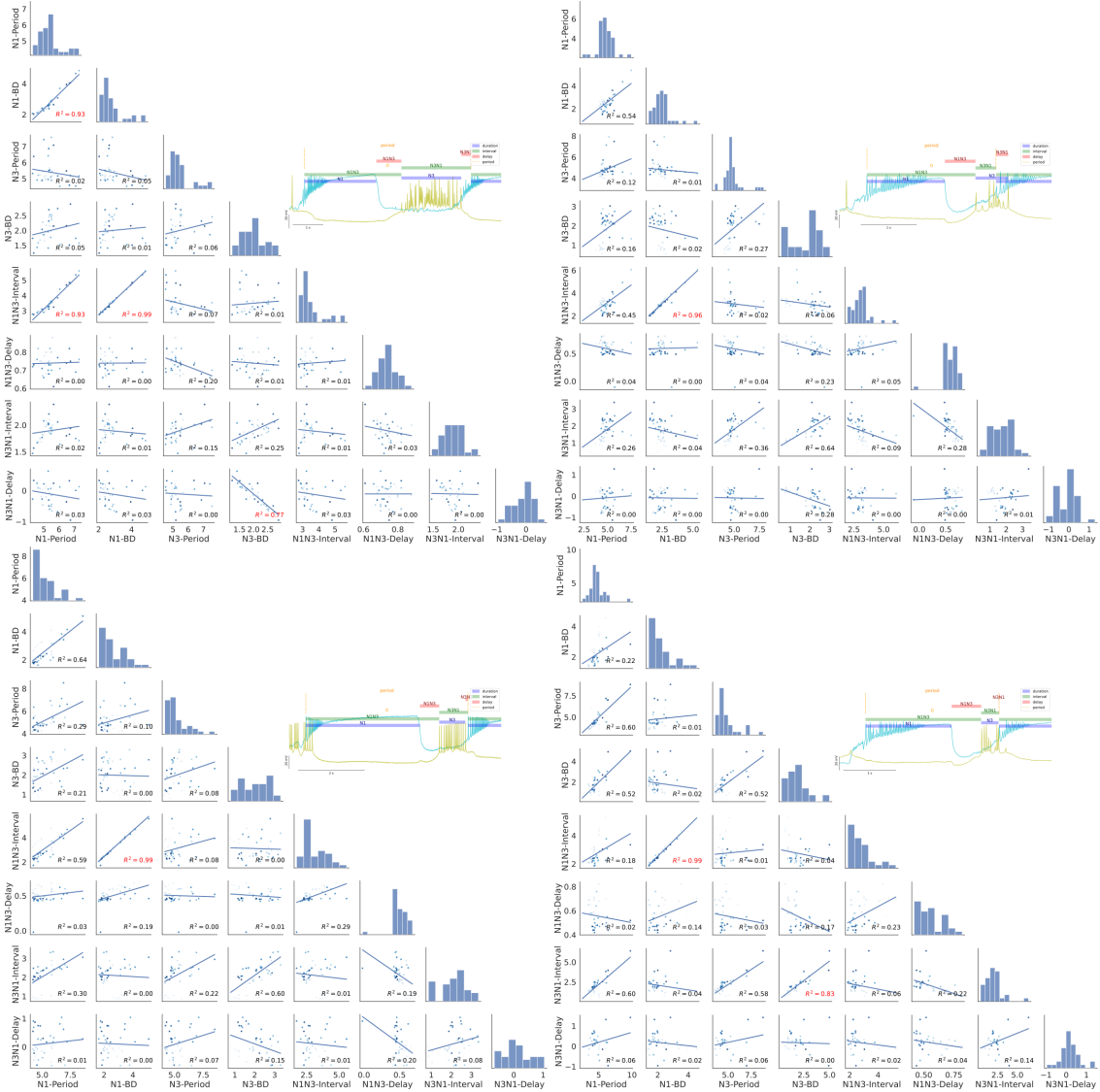


Figure 5.30: Panel of the pairplots for all possible combinations between the time intervals for two phases (N1 and N3) in the CPG recordings for the four examples of induced CV1a neuron modulation recordings.

5.4.5 Summary of changes in the invariants due to stimulation

Figure 5.31 shows the time-interval relationships for four examples in each stimulation case studied in this section. We can see that the relations between the intervals change as the source of the stimulation changes (including the case of spontaneous activity).

In the case of the spontaneous activity, there is a dynamical invariant in the N3 phase intervals, e.g., see the strong correlation between N3 burst duration and the period; while there is no relation between N1 burst duration and the period. When the stimulation is induced by SO, we can see a change in the distribution of the variability, being N1 burst duration and N1N3 interval the strongest ones related to the period, but N3 phase presenting also some tendency to a linear relation visible in the relation of N3 burst duration with specific intervals as the period, N1N3 interval and N3N1 interval. When stimulating MLN and CV1a, the strongest correlation was in N1 with no relation of N3 phase to the period (in contrast to the SO-driven results). MLN case showed a clear and strong linear relation to the period in a large range of values of the duration of the time-intervals, i.e., for low values of the intervals duration there were also low values for the period duration.

Each of these cases represent a different source of modulation or initiation in the rhythm. The spontaneous case might be during a hunger phase with no food, with longer phases of N3 activation but constant intervals for N1 (protraction) and N2 (rasp) phases. SO modulation is associated to sucrose stimulus, changing the importance of each phase, enhancing the protraction, as it is the case of MLN, when the stimulus of the lip might prioritize an effective protraction activity. Also, the CV1a modulatory neuron used for the rhythm activation presented a distribution between the protraction (N1) and swallow (N3) phases. This redistribution indicated by the changes in the sequential dynamical invariants points to the relation of the variability and the functional context of the feeding motor activity.

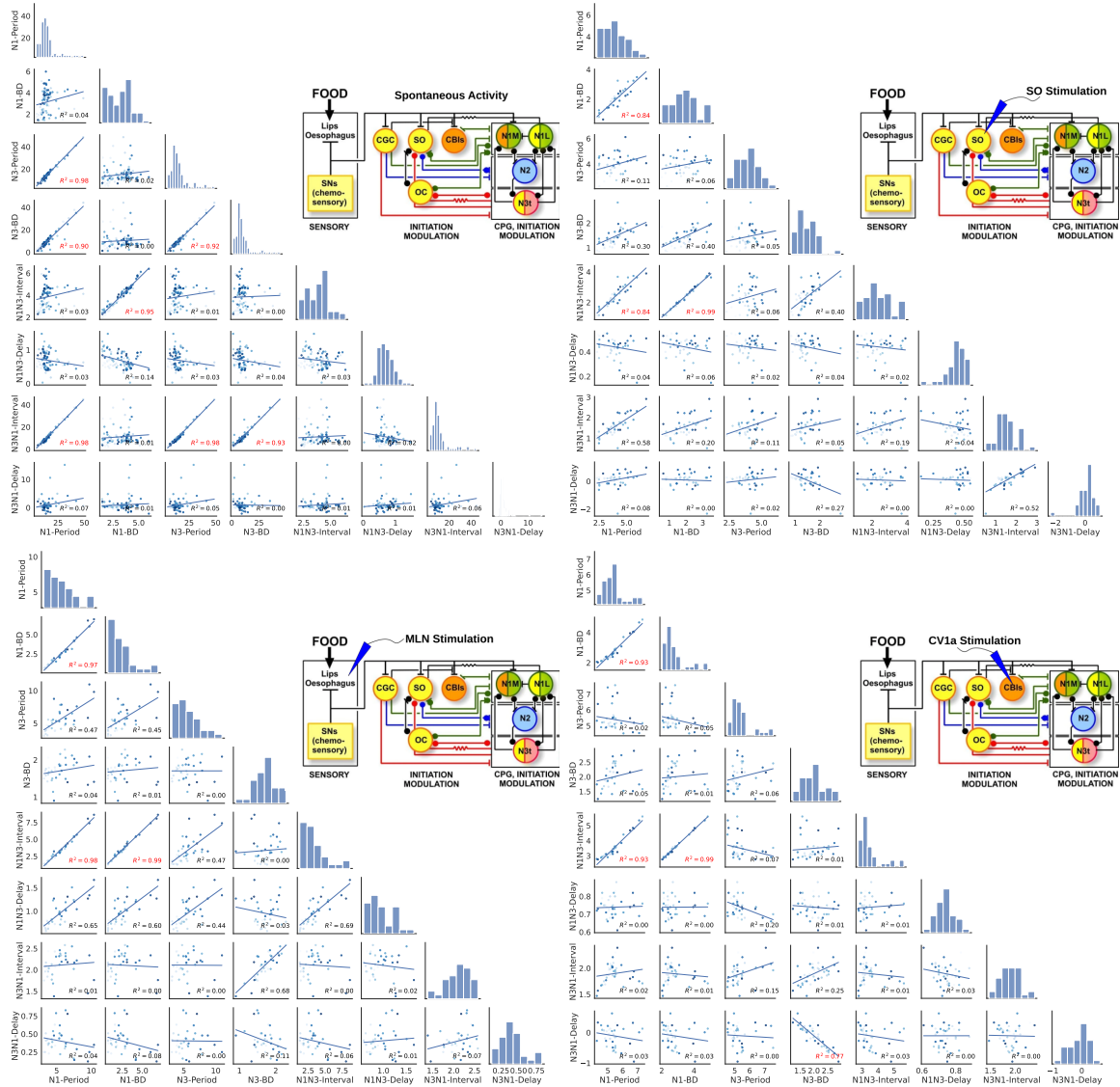


Figure 5.31: Summary of the results discussed for different rhythm modulations. Each pairplot shows all possible interval combinations, the upper right connection diagram shows the neuron stimulated for each case. The examples shown here correspond to (from left to right and top to bottom): Spontaneous activity example 1 (Fig. 5.14), SO induced modulation (Fig. 5.22), MLN stimulation (Fig. 5.24) and CVa1 stimulation example 1 (Fig. 5.26).

5.4.6 Invariant resetting

There is another important feature of the sequential dynamical invariants reported in Elices et al. (2019): there is no relation between time intervals belonging to different cycles. In the model, the study of these phenomena was not possible since the current ramp provided a gradual change of the time-intervals' duration, which forced all intervals correlated in a cycle to be also correlated in the next one (see Appendix Fig. B.1).

In this subsection, we include several experimental examples of this invariant resetting for cases presenting robust sequential dynamical invariants. We illustrate this "reset" with pairplots gathering the interval relations of a given cycle in the bottom triangle sector (below the diagonal indicated by a dashed line), and the relations of each interval with those of the next cycle represented in the upper triangle (Fig. 5.32). When comparing intervals of one cycle to those of the next one, existing robust correlations disappear, the most clear example is illustrated in the first Figure for the spontaneous activity. All strong linear interval relationships are gone when intervals between consecutive cycles are compared, with R^2 close to 0. In the two examples illustrated in the second row, i.e., MLN stimulation and CV1a stimulation recordings, what were strong linear relations are diluted and a few new strong correlations appear between intervals of consecutive cycles, but note that none of them existed between those intervals in the same cycle. For example, the robust dynamical invariant between N1 burst duration and the period is diluted when comparing the relation for consecutive cycles in both cases. Strong correlations are present between N1 and N3 periods and between N1 burst duration and N3 period. Both periods overlap between cycles, which can explain the relation that appears between intervals of consecutive cycles. Therefore, robust dynamical invariants in the form of related interval variability exist only between specific intervals of the same cycle, and they are not propagated between cycles. Time intervals that overlap between consecutive cycles can be related.

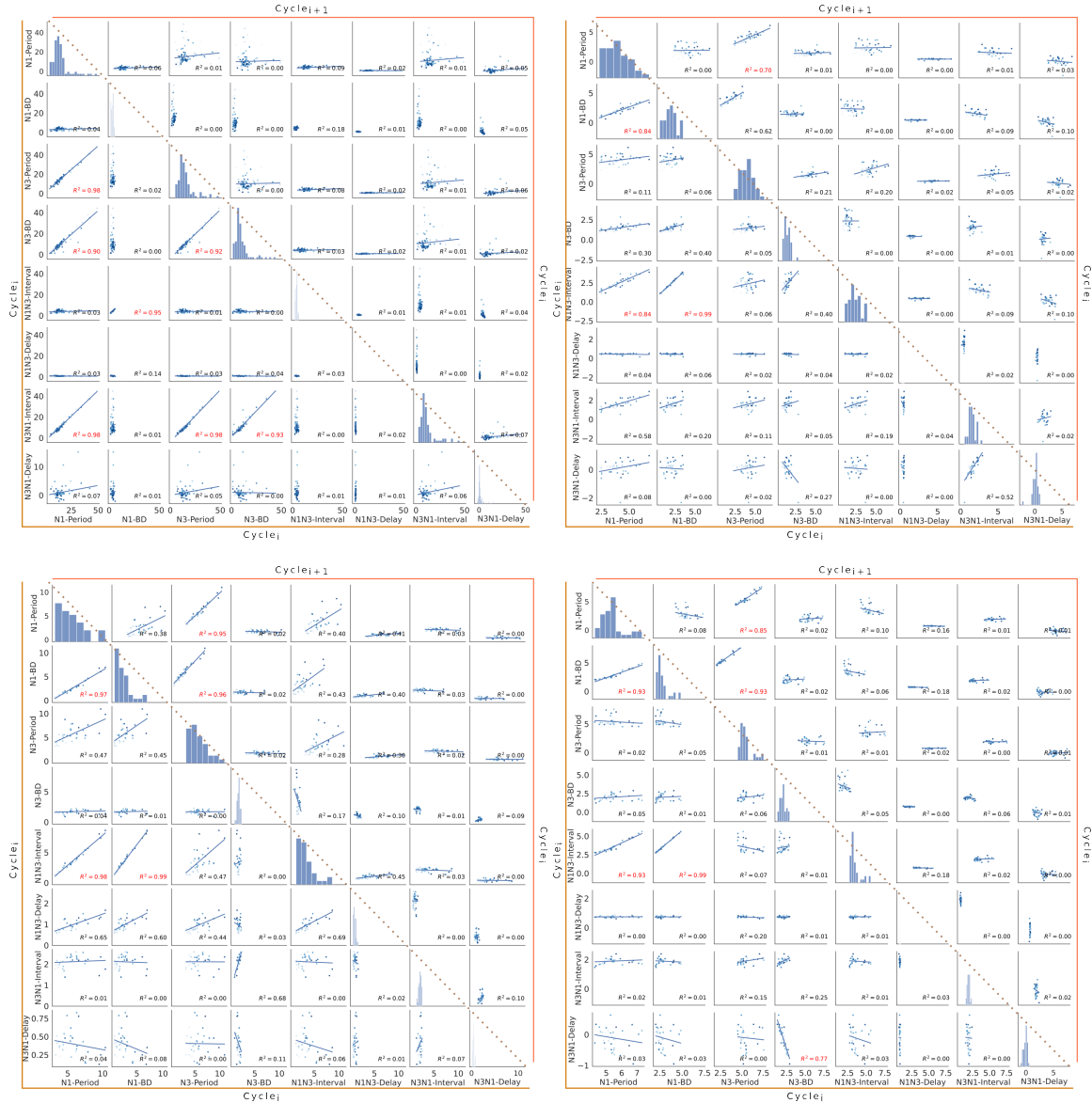


Figure 5.32: Absence of dynamical invariants between non-overlapping intervals in consecutive cycles. For each pairplot, the lower triangle represents interval relationships in the same cycle and the upper triangle represents relationships between intervals of one cycle against intervals of the next cycle. The examples shown here correspond to (from left to right and top to bottom): Spontaneous activity example 1 (Fig. 5.14), SO induced modulation (Fig. 5.22), MLN stimulation (Fig. 5.24) and CVa1 stimulation example 1 (Fig. 5.26).

5.5 Characterization of variability in bursting models and its functionality

Bursting dynamics has been extensively studied in a wide variety of neural systems and theoretical models (Coombes & Bressloff, 2005; Izhikevich, 2007; Zeldenrust et al., 2018), as it is instrumental for many brain functions, including motor coordination and cognitive performance, and can be related to both healthy and pathological states. Neuronal models in computational neuroscience often reproduce key functional features of their biological counterparts. However, they also present limitations such as their poor ability to mimic the observed intrinsic variability of living neurons, particularly in membrane potential waveforms and in collective adaptive dynamics. Biophysical models typically produce stereotyped fixed membrane potential depolarization and repolarization waveforms, and restricted dynamical flexibility as compared to those observed in experimental recordings. Variability in the activity of living neurons has been proven to play an important role in relevant information processing tasks, e.g. see (Stein et al., 2005; Renart & Machens, 2014; Waschke et al., 2021). We have seen in this chapter the importance of variability in the presence of sequential dynamical invariants in bursting activity, and the limitations of studying them in a model when the variability is induced by a current ramp stimulation. Variability in models is usually induced by Gaussian noise, but this disregards the importance of functional variability in neurons, as in several cases observed variability is not only a cause of stochasticity but of a functional dynamical outcome.

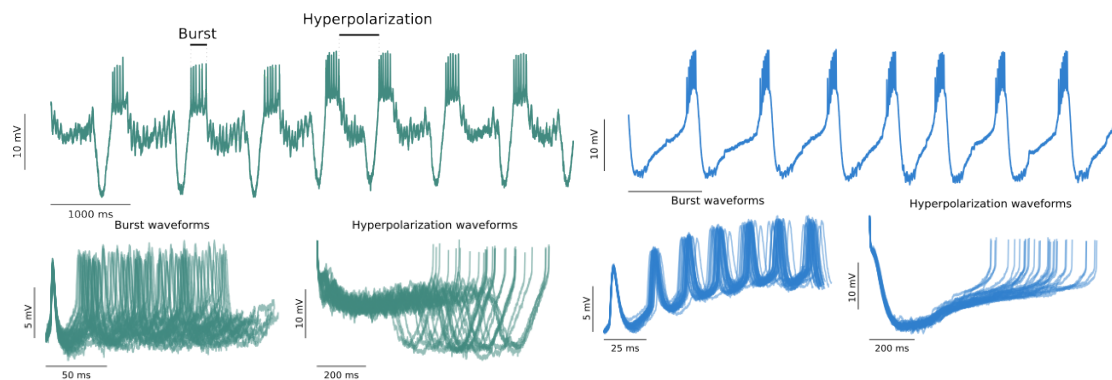


Figure 5.33: Example of variability in waveforms from intracellular recordings of the LP and PD neurons in the pyloric CPG.

In this section, we will describe bursting variability characteristics in experimental recordings, not only regarding the sequence time-intervals but also their waveforms. We will compare this variability with that of classical models and models able to produce chaotic activity. Figure 5.33 shows examples of bursting and waveform variability in intracellular recordings of LP and PD neurons in the pyloric CPG of *Carcinus maenas*. In both neurons, we can appreciate large variability in the burst shape and

duration, including variability in the hyperpolarization.

Although specific models can faithfully reproduce the overall activity and voltage waveform of living neurons, they usually fail on reproducing the intrinsic and collective variability that we observe in electrophysiological recordings. This is the case for example of Ghigliazza and Holmes (2004) or Vavoulis et al. (2007) models, represented in Fig. 5.34. Although the waveform shape is accurate for many purposes, the functional variability is hindered, and the models steady bursting activity.

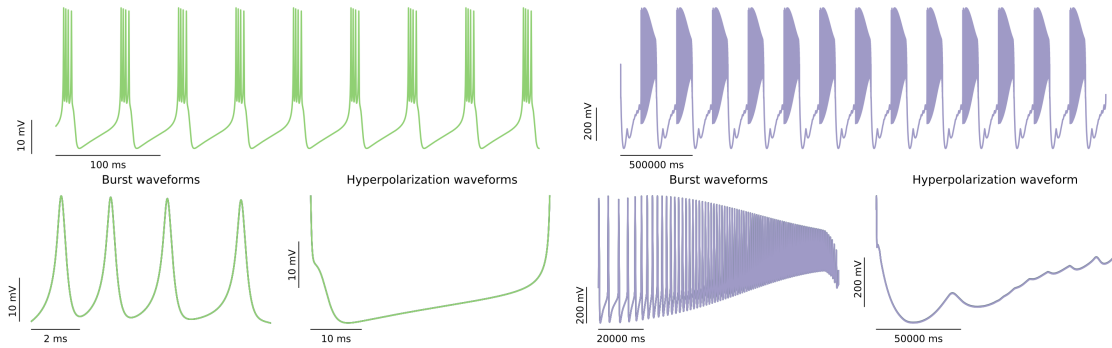


Figure 5.34: Example of bursts with no waveform variability in the Ghigliazza and Holmes (2004) model from the ODEs neurons in the insect locomotion CPG and in the N1M neuron model from Vavoulis et al. (2007) with no ramp stimulation in the CPG circuit. The equations for both models can be found in Secs. 5.2.4 and 4.4.1, respectively.

In section 4.4.1, we saw that variability can be induced by including a current ramp. Although this methodology can produce bursting variability, when studying the activity cycle-by-cycle, it hinders the functional variability of spontaneous activity. Figure 5.35.a) shows an example of a model with chaotic mode, displaying variability in the duration, the waveform shape and the hyperpolarization, in contrast to the example of N1M neuron when inducing variability by a current ramp (panel b) in that Figure), that displays a moderate variability.

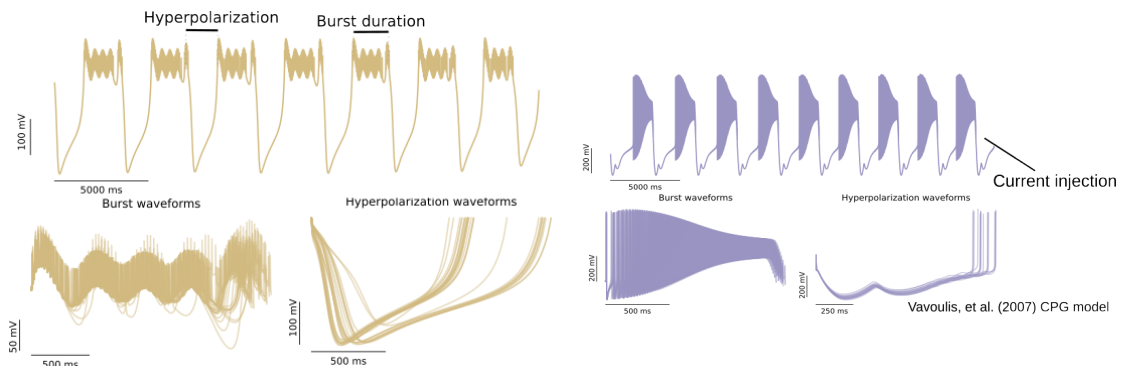


Figure 5.35: Example of variability in waveforms from model simulation of neuron from Nowotny et al. (2008) model in chaotic mode and N1M neuron from Vavoulis et al. (2007) under current stimulation in the CPG circuit. The equations for both models can be found in Secs. 5.2.4 and 4.4.1, respectively.

Modern experimental techniques involving activity-dependent electrical, optical and chemical stimulation can further unveil and explain functional variability of bursting sequences in a wide variety of nervous systems, but it is important to rely on models able to reproduce the observed intrinsic variability. Taking into account functional variability is also relevant for designing applications in the context of neurotechnology, artificial intelligence and robotics (Garrido-Peña et al., 2024).

5.6 Transformation of sequential intervals into effective robot movement

To validate the importance of the balance between robustness and flexibility in CPG circuits, as provided by the cycle-by-cycle dynamical invariants present in the dynamics discussed in this chapter, we include in this section a validation experiment for the translation of dynamical invariants into an effective motor locomotion in a Functional-Living-Circuit-Hybrot (FLC-Hybrot) (Amaducci et al., 2020, 2021; Soëtard et al., 2023). The combination of models, novel tools and experimental approaches has proven its effectiveness in revealing and exploring features of neural dynamics (Szücs et al., 2000; Chamorro et al., 2012; Reyes-Sánchez et al., 2023). In this first step into the applications in robotics of the variability time constrains found in CPGs, we built an hexapod robot whose legs performed oscillatory activity to move forward. The period and amplitude of these oscillations were determined by the sequential cycle-by-cycle activity of the CPG neurons recorded from the living preparation and sent online to the robot. At the same time, the hybrot included a light sensor and sent feedback information regarding the light conditions around it back to the neural circuit in the form of an electrical current. These stimuli modified the behavior of the cells, resulting in a change of the hybrot locomotion, preserving always the required motor coordination, and therefore forming a real-time closed-loop interaction among living and electronic components (Figure 5.36 shows a summary of these interactions). The goal of the FLC-Hybrot is to demonstrate that a dynamical principle of the functional living circuit can be used to autonomously coordinate the locomotion with sensory feedback from the robot. In our case, we used the presence of dynamical invariants in the form of robust relationships between the time intervals that build the cycle-by-cycle activity of the neurons of the pyloric CPG in *Carcinus maenas*, which are sustained under any circumstance, even when there are external inputs to the circuit, to modulate the behavior of the robot. Section 5.2.5 provided a detailed description of the experimental setup for the hybrot.

To validate the adequate locomotion of the FLC-Hybrot when driven by the pyloric CPG online behavior, as well as the living circuit real-time adaptation to the injected feedback, we performed a

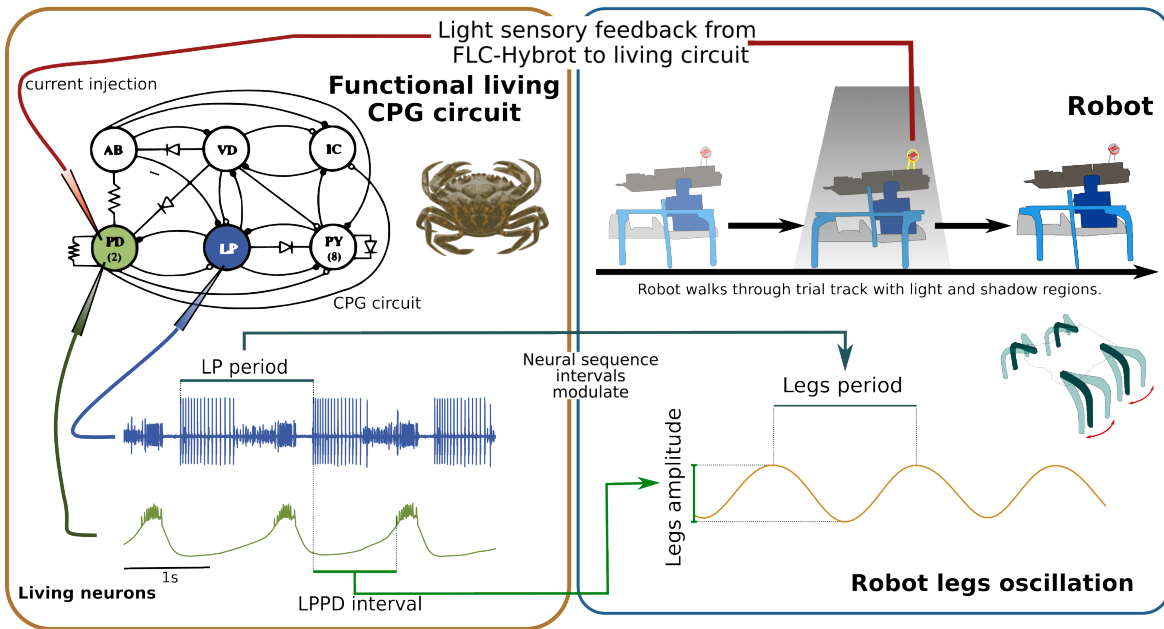


Figure 5.36: Representation of the FLC-Hybrot paradigm design. Neural dynamics from a functional living CPG circuit are recorded online and used to coordinate the robot movement in real-time. Activity from the PD neuron is recorded intracellularly (green trace), while the LP bursts are extracted from the nerve's extracellular signal (blue trace). This robot walks through a trial track with interspersed light and shadow regions. When the robot's light sensor detects that it is located under a shadow, it sends feedback current to the living circuit. CPG dynamics change as a reaction to the injected current, thus modifying the robotic locomotion. The following video shows an example of this experiment <https://youtu.be/ny2dJGbG8lo>.

set of experiments employing a 1.5 meters long trial track. Along this surface there were interspersed segments of lights and shadows. This configuration caused the FLC-Hybrot to alter its behavior several times during the experiment due to the injection of current into the PD neuron when it walked under a shadow. The current injected in the cell in a shadow section varied from one experiment to another, according to the neurons response to the stimuli. No current was injected when the robot was located on a luminous area. The following video illustrates one of such experiments <https://youtu.be/Dltec7TeGso>.

Figure 5.37 shows the results for one of these tests. We observe a change in the neural activity when -0.6nA current is inserted into the PD neuron, causing the CPG rhythm to slow down while also modifying the PD neuron membrane's potential amplitude. This change is immediately reversed as soon as the current goes back to zero, restoring its previous behavior. Concerning the robot's locomotion, a variation in the legs' oscillation is observed just after the neurons alter their activity. Despite the successive changes in the amplitude and period of its legs' oscillation, the FLC-Hybrot maintained a coordinated and effective locomotion during the whole experiment.

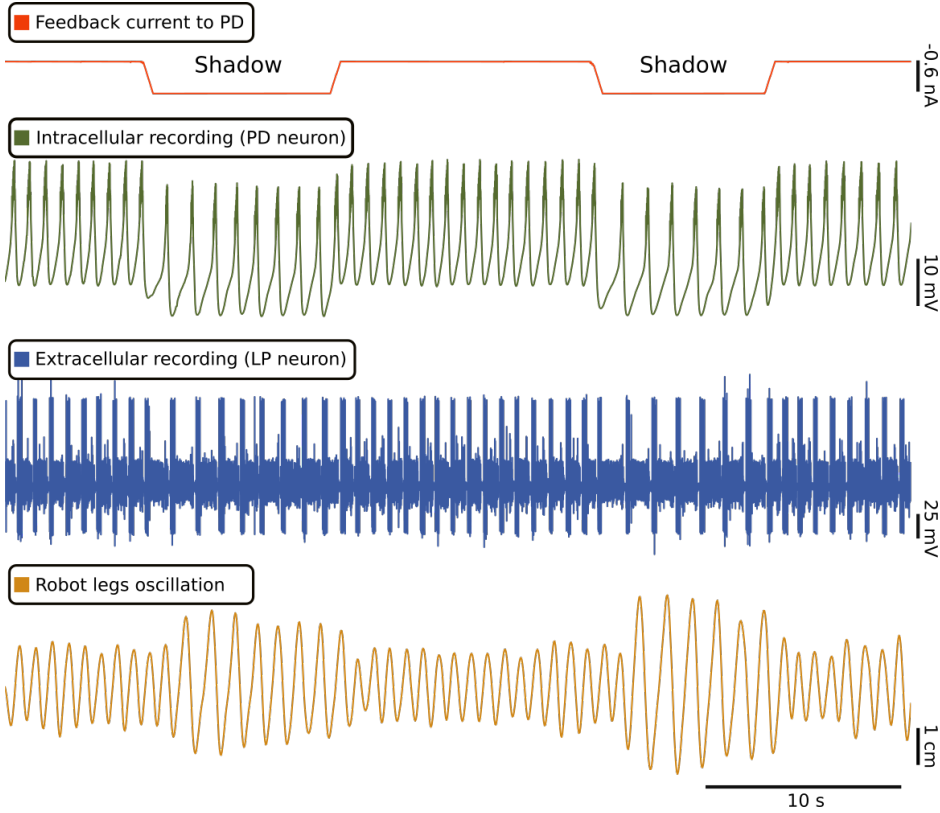


Figure 5.37: Flexible hybot adaptation to environmental changes when noticed by the robot sensors and associated coordinated locomotion. When the robot entered a shadow section, it sent sensory feedback to the living CPG in the form of positive electrical current (red trace). Blue and green traces are recordings of the extracellular and intracellular (PD neuron) activity of the circuit and display the change caused by the feedback current injection in the PD neuron, slowing down the CPG rhythm. The oscillatory movement of the robot legs is represented in the brown trace and it can be observed that a variation in the CPG rhythm leads to a change in the robotic locomotion, modifying both the period and the amplitude of the oscillation.

We know that in the pyloric CPG there is a sequential dynamical invariant, in the form of a linear relation between the LP neuron period and the LPPD interval. These are the intervals used to modulate the amplitude and period of the legs oscillation in the robot. This constrain was effectively transferred to the robot locomotion. Figure 5.38 shows a comparison between the living CPG and the robot dynamical invariant, with the later reaching an R^2 correlation of 0.87 despite the lack of precision of its servomotors. It displayed the same correlation between its legs oscillation period and amplitude, which were modulated by the two previous temporal intervals. The methodological details for the legs tracking to characterize the effective transfer of the invariants can be found in Amaducci Swarc (2023).

This hybot scenario can help simulate context change situations in which the CPG rhythm is modulated by external factors and there is a change of variability reflected in the relations between the

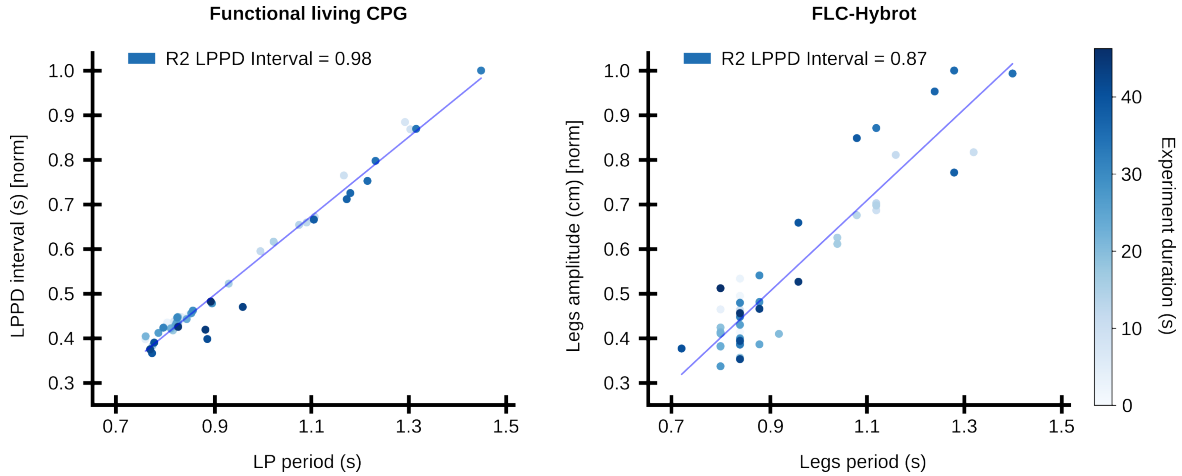


Figure 5.38: **Left:** dynamical invariant present in the living CPG activity during the validation test, represented as a cycle-by-cycle linear relation between the LP neuron bursting period and the LPPD interval. **Right:** dynamical invariant present in the FLC-Hybot locomotion during the validation test, represented as a cycle-by-cycle linear relation between its legs' oscillation period and amplitude. The dynamical invariant property is effectively translated from the living CPG to the robot locomotion, encoded as: Robot period = LP period, Robot amplitude = LPPD interval * factor.

cycle-by-cycle intervals. The reproduction of biological dynamics with preserved coordination time constraints can have strong implications in autonomous robot locomotion, and also in neurorehabilitation technologies. Under the scope of sequential dynamical invariants, coordination rules are not imposed as conditional commands but autonomously emerge from the intrinsic sequential dynamics.

5.7 Discussion

In this chapter, we studied neural sequentiality analyzing the bursting activity of the feeding CPG in *L. stagnalis*. As discussed before, CPGs are ideal circuits for this kind of study due to their ability to maintain a robust sequential activation and still present a high flexibility to adapt to changes in their functional context. Also, their rhythmic bursting activity provides clearer time references to define sequence intervals than other more complex neural circuits.

We addressed the characterization of the intervals building up the rhythmic sequence in this system with model simulations and also with experimental intracellular recordings. We identified the presence of sequential dynamical invariants in the form of linear relationships between the sequence intervals and the cycle period of the rhythm following the experimental results reported in Elices et al. (2019) for the crustacean pyloric CPG. Most common studies usually consider averaged variability, masking the information in the relations taking place at each cycle of the sequential activations.

Taking that into account, here we characterized the variability cycle-by-cycle.

In the model, we analyzed the relations reported by Elliott and Andrew (1991) in an extended characterization of each and every interval building the sequence. We also related the strong linear relationships found between specific intervals to the concept of robust sequential dynamical invariants proposed in Elices et al. (2019) for the coordination of robust yet flexible CPG rhythms. In the simulations, three main cases have been addressed for the analysis: N1M-driven, SO-driven and N3t-driven stimulation. This was based on the two different possibilities of inducing variability in the model according to the results reported in Vavoulis et al. (2007), as well as with a third neuron stimulation (N3t) which is easily addressable in the model circuit. When variability arises by the stimulation of N1M, the results are rather similar to the ones obtained by stimulating N3t: Strong linear correlations to the period, i.e., dynamical invariants, are present mainly in all intervals related to N3 phase, since these are the ones whose cycle-by-cycle variability is related to the period's variability. Note that when the current ramp was applied to N3t, N1M activity also displayed variability.

We also showed the redistribution of variability that takes place when the stimulation is applied on SO. In this scenario, more intervals are found presenting large variability than in the other stimulation protocols. This is due to the specific variability of N1M and N3t burst duration, since in this case the largest influence on the period seems to come not only from N3t but also from N1M. Hence, consequently to the variability analysis, different linear relationships are found involving all intervals related to N3 and N1 phases. The intervals unrelated to the period are the ones associated with N2 phase, which is also the least variable entity in the circuit.

These results reproduce and extend the ones discussed in Vavoulis et al. (2007) and Elliott and Andrew (1991). It is interesting to highlight the differences in the results when the period is driven by N1M/N3t or SO. When the variability is induced in N1M/N3t, N3t is still able to inhibit the N1M neuron carrying the main variability, while SO is adapting to both. However, when SO is the neuron being stimulated, since it is connected to N1M by mutual excitation, they are both boosting each other's activity, leading to the higher variability of N1M. Here, N3t must adapt to N1M, which is harder due to the SO constant excitation. For this reason, it was necessary to inject some additional current in N3t in the simulations, which might be in the living activity, an input received from the cerebral ganglia.

The flexibility of the model to adapt the induced variability into the system is not an easy feature to achieve. Note that in each case only N1M, N3t or SO were stimulated by a ramp current and still the variability was displayed in the whole circuit activity, e.g., stimulating N3t produced variability in the time intervals of that neuron but also in N1M, and the stimulation of SO modulated the activity

in N1M and N3t. Several characteristics in the description of this model, such as the gradual synapse and the separation between fast and slow dynamics for each neuron, might be key for reaching such flexibility. The realistic definition of the waveform shape and the interrelations between the neurons in the CPG model, along with the current injection, allowed the study of dynamical invariants. However, inducing the variability by a current ramp injection hinders the functional variability generated by the neurons by their spontaneous activity, being only possible to simulate a case where the variability was produced by a perturbation in the system. This limitation is manifested when comparing the model activity with the experimental intracellular recordings, where both spontaneous activity and induced modulation recordings showed large cycle-by-cycle variability in the time-interval durations in the sequential bursting activity.

Each of the three phases of the rhythm corresponds to a specific motor action: N1 protraction, N2 rasp and N3 swallow. As it was pointed out in Elliott and Andrew (1991), the motor sequence consists of a two-stroke relaxation: protraction and rasp (N1,N2), in charge of moving the radula, and swallowing (N3). In these kind of systems, it is common to find one of them fixed and the other one variable, which in our case is the swallow phase. In this context, SO stimulation can be related to sucrose stimulation (Kemenes & Elliott, 1994; Benjamin, 2012), this could be related with the increase in N1M variability, since in presence of food, protraction phase may become crucial for an effective food reaching. Thus, there might be now two phases showing more variability in their intervals duration. The discussed invariants can participate in the coordination of these mechanisms by imposing variability constraints in only specific intervals of the motor sequence. The results shown in this work also indicate that distinct constraints in the form of sequential dynamical invariants can emerge in the same network under different behavioral contexts.

In the experimental study, we could prove the model prediction that depending on the source of the activation, the distribution of variability and the intervals presenting these strong relationships changed. Also, even under scenarios of high variability, we showed that there were strong linear relationships in the form of sequential robust dynamical invariants between some of the sequence intervals. In the case of spontaneous activity, the most robust example was a strong linear correlation for N3 phase in a recording where the N3 seemed to be inducing periods of silence. In other two cases, the variability was shifted, with N1 having a larger relation to the period cycle-by-cycle and with a distribution of variability between both N1 and N3 phases. What we saw in this case, and in the rest of the experiments in that section, was the absence of relation between the N2 phase and the period, which means that the variability in each cycle is not carried by the rasp phase, which has a constant and low variable activation. In addition to the spontaneous recordings, we analyzed

three cases of CPG activity modulation: SO neuron driven, MLN stimulation and CV1a neuron driven. Each case is associated to a different source for the activity change in relation to functional processes. For each one, we observed a different distribution of the variability between the time-intervals. During the SO modulation, in spontaneous and induced scenarios we saw, as in the model, that variability was carried by N1 and N3 phases, having both relation to the period cycle-by-cycle, being stronger in the case of N1. When stimulating the middle lip nerve (MLP), directly connected to the N1M to activate the rhythm, there was a robust sequential dynamical invariant in N1, showing that during this activation (in the simulated presence of food) the role of protraction phase was key, carrying all variability. Finally, in the CV1a neuron stimulation, the N1 phase was again the one with a larger relation to the period, showing also that a small change in that stimulation altered the distribution of variability shifting to N3 phase and the related intervals.

With these results, we saw the potential of dynamical invariants as functional variability indicators, since they reflect a balance between the robustness of the sequence and the flexibility to accommodate longer or shorter intervals from the network interaction. The distinct sources of feeding activation changed the distribution of variability, readjusting it from one phase to another. Also, in the model we saw that this phenomenon is highly dependent on the intrinsic dynamics, network topology and synaptic dynamics that contribute to the generation of the dynamical invariants. Their observation in the model simulations were only possible when other neurons in the circuit adapted their activity to the neuron with the induced variability.

The study of cycle-by-cycle invariant relationships, found not only in experimental recordings but also in computational models as we report here, highlights the presence of organized variability in a motor rhythm. This points to the universality of these phenomena, and the functional associations to autonomous neural coordination mechanisms. The concept of dynamical invariants can be applied to the design of novel biomarkers, which can be key for future clinical applications, specially for novel neurotechnology tools. In this line, we showed a first approach of the extrapolation of these restrictions into an effective locomotion in the FLC-Hybrot. The hexapod robot showed that it is possible to translate the dynamical invariants into the relation between the oscillation amplitude and period, showing the possible future applications of locomotion based on dynamical CPG features. This study paves the way for further exploration of sequential dynamical invariants in more complex neural systems and their practical applications.

CHAPTER 6

CW-NIR laser as an effective neuromodulation technique

We saw in the previous chapter the importance of effective stimulation techniques to alter and explore the sequential neural dynamics in single neurons and circuits. In this chapter we will explore a novel neurotechnology to stimulate and modulate neural activity in a noninvasive manner: Continuous-wave Near-Infrared (CW-NIR) laser. We will address its effect in single neurons dynamics in sustained and activity-dependent protocols, discussing the main biophysical candidates generating the observed effect by the joint analysis of experimental and computational data. With a novel closed-loop protocol we will also assess neural dynamics in the sequential activation of ionic-channels in the action potential generation.

6.1 Introduction

Effective neural stimulation is an essential tool to study brain dynamics. Many techniques have risen since the first use of electrical, chemical and mechanical stimulation, e.g., see Refs. (Cogan, 2008; Chamorro et al., 2012; Carter & Shieh, 2015; Bickle, 2016). Optical methods are also widely spread, as they allow visualization (Lecoq et al., 2019) and stimulation in a less invasive manner. One example is optogenetics (Boyden et al., 2005; Yizhar et al., 2011; Tye & Deisseroth, 2012; Bansal et al., 2022), which is effective in modifying neural activity with high spatio-temporal resolution. Another example of non-invasive stimulation is Transcranial Magnetic Stimulation (Valero-Cabré et al., 2017), which is succeeding in clinical applications. However, they both present limitations such as the need to genetically modify the living system or restricted spatial precision, respectively. In this context, infrared laser stimulation is an optical technique that has risen in popularity in the

last decade. From its first applications (Wells et al., 2005b; Izzo et al., 2007), studies have shown its ability for modulating action potentials in different systems (Liang et al., 2009; Goyal et al., 2012; Shapiro et al., 2012; Cayce et al., 2014; Barrett et al., 2018; Brown et al., 2020; Begeng et al., 2022). Beyond its potential as a research stimulation technique, it has also been tested for clinical use, e.g., in Parkinson's disease, reversing brain age-related effects or depression treatment (Konstantinović et al., 2013; Disner et al., 2016; Wang et al., 2017; Saucedo et al., 2021; Pan et al., 2023). This neural stimulation method is so attractive because of the wide range of possibilities that can provide for non-invasive neuromodulation offering high temporal and spatial precision.

The identification of the biophysical source of infrared neuromodulation is still under discussion as it has strong implications for applications in multiple contexts. It is difficult to associate this modulation to a single specific cause, since neural systems have distinct biophysical components reactive to the irradiation. However, most of the results point to a photo-thermal effect where the excitation driven by the laser stimulation might be caused by temperature gradient (Wells et al., 2007). In addition, different candidates to explain the change in neural activity have been suggested, such as capacitance (Shapiro et al., 2012; Plaksin et al., 2018), specific modulation of channels sensitive to temperature as TRPV4 (Albert et al., 2012), acceleration of ionic channels (Liang et al., 2009), or altering the Ca^{2+} cycle possibly mediated by modulation of mitochondrial activity (Dittami et al., 2011; Lumbrales et al., 2014; Saucedo et al., 2021).

Distinct types of infrared laser and action modes, in terms of the power, duration, frequency of stimulation and wavelength have been used in previous studies, see Refs. Wells et al., 2005b; Izzo et al., 2007; Ping et al., 2023. The effect is highly dependent on the stimulation configuration. Most works have focused on pulsed lasers to induce spiking activity due to their stronger temperature gradient production. However, some clinical studies have successfully applied continuous-wave (CW) laser for brain stimulation (Saucedo et al., 2021).

The use of closed-loop techniques has a large potential in neuroscience, for both physiological and clinical research studies (Chamorro et al., 2012; Potter et al., 2014; Couto et al., 2015; Linaro et al., 2015; Lareo et al., 2016; Varona et al., 2016; Zrenner et al., 2016; Reyes-Sanchez et al., 2023), since they allow adjusting the stimulation to the context of the ongoing neural dynamics and the specific condition of the targeted system/subject. Some of these tools have been developed with open-source approaches, including optical techniques, e.g. Refs. (Siegle et al., 2015; Dagnell et al., 2017; Amaducci et al., 2019; Štih et al., 2019; Robbins et al., 2021), promoting the accessibility, reproducibility and standardization of the studies and methods. However, near-infrared (NIR) lasers have been used with fixed/periodic stimulus and, to the best of our knowledge, they have not been

exploited in activity-dependent protocols.

Here we explore the effect of CW-NIR laser on the dynamics of individual neurons in sustained and activity-dependent stimulation protocols. We employ a laser with constant optical power density on the sample for these two modalities. In the first case, the laser stimulation is sustained –the duration of the illumination is constant for more than 1 minute–, and in the second case it is driven in an activity-dependent manner implemented by the open-source RTXI (Patel et al., 2017) Linux software –the onset of the stimulation is determined by ongoing neural events and delivered transiently through software control–. We studied the effect of CW-NIR illumination focused on neurons with spontaneous tonic firing. Combining experimental results with modeling analysis allowed exploring the candidates that can explain the observed neuromodulation. We present a novel procedure for NIR laser stimulation to dissect and intervene in the waveform dynamics through activity-dependent stimulation. By interlacing results from theoretical simulations and sustained and activity-dependent stimulation, we identify the dynamical elements behind action potential dynamics under CW-NIR modulation. We discard any single candidate of the biophysical effect as the joint experimental and model analyses indicate that laser illumination affects multiple membrane factors simultaneously.

6.2 Methods

6.2.1 Sustained CW-NIR stimulation protocol

After the isolation of the *Lymnaea stagnalis* neural system, we searched for suitable neurons in the right parietal ganglion, i.e., cells with spontaneous activity preferably with fast activity and shoulder or symmetrical type in the spike waveform. Once the target neuron was identified, the laser was set-up. A lens with focal distance of $f=50\text{mm}$ was used and no polarizer was installed on the optical path. Guided with the microscope camera, the laser spot was located and then placed first over the ganglion and subsequently over the specific neuron where the electrode was recording the activity. At this point, the laser was focused with the micro-manipulator adjusting the focal distance. Finally, the laser power was increased to the above mentioned value for the experiments.

Once the laser spot was over the neuron while the membrane voltage was simultaneously recorded at the soma with the intracellular electrode, we followed the protocol described below and depicted in Fig. 6.1 to measure the effect of the CW-NIR laser on the activity of the neuron:

1. First control. The spontaneous activity in the neuron was recorded for 1-3 minutes, depending on the spiking frequency of the cell. During this control, there was no external modulation of



Figure 6.1: CW-NIR laser stimulation protocol sequence: Control, laser stimulation and recovery.

the neuron apart from the possible alteration by the intracellular procedure.

2. Laser stimulation. The laser was on during the same lapse of time than in the first control, stimulating the neuron with a constant optical power density. There was no modification in laser parameters during this time.
3. Recovery. After the illumination was off, a second control was performed, under the same conditions as the first one. During this recovery control, the activity in the neuron after the effect of the laser was recorded.

The sequence involving control, laser and recovery trials was replayed in each experiment (day and individual) for five times. Between each trial, the laser illumination was supervised to ensure that the spot was still over the neuron, guaranteeing that the procedure had as low variation as possible. Also, the laser was only turned off during the controls, it was not set aside, since that would have forced to redo the set-up for every trial altering the reproducibility between trials. The effect for each trial of a given day was very similar. For the analysis in Figure 6.6, the trial with the strongest effect in the day was selected.

6.2.2 Activity-dependent laser stimulation protocol

For stimulating the neurons depending on their ongoing activity, a closed-loop protocol was designed in the RTXI real-time software (Patel et al., 2017). This hard real-time tool allows an easy integration of new modules to read ongoing activity, process it online and send feedback in the form of analog signals. The real-time module designed for this experiment followed the scheme illustrated in Fig. 6.2. After processing the signal in RTXI, a TTL pulse was sent to the controller opening the laser shutter for the desired time, and thus stimulating the neuron during that time interval. Simultaneously, the neural activity was recorded, along with the TTL and the shutter feedback (recording the shutter delay with respect to the on signal).

The CW-NIR laser light was blocked with a mechanical shutter (Thorlabs SH05, Newton NJ). The shutter utilized in this work had a ~ 8 ms delay from the trigger signal, which might be a limitation for neural stimulation in fast spiking cells. The slow spike dynamics in the neurons used for this research

are compatible with this restriction and the protocol was developed considering this limitation.

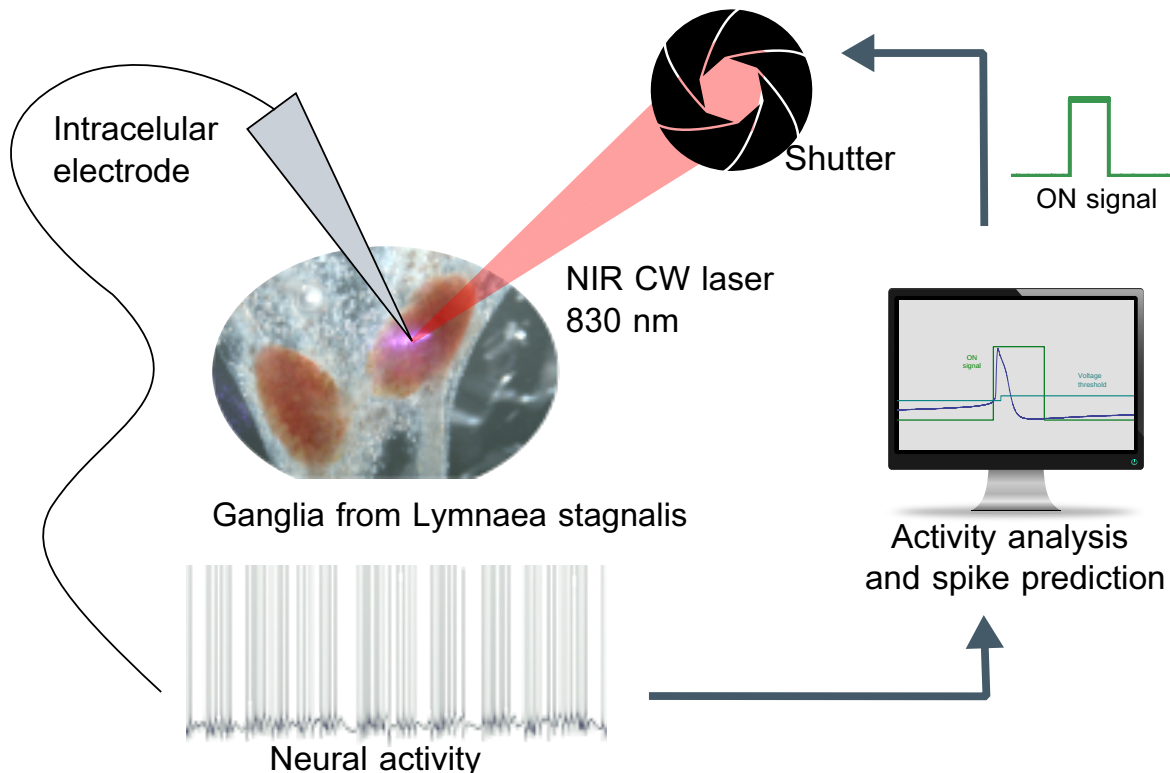


Figure 6.2: Activity-dependent protocol scheme. Neurons were recorded intracellularly and their voltage signals were processed in real-time with the RTXI software. Using the spike prediction algorithms, the shutter was triggered at the desired action potential phase illuminating the neurons.

The main challenge in this protocol is the identification of the specific phase of the spike waveform to deliver the stimulus, i.e., predicting the spike, since spontaneous neural activity has intrinsic variability that requires the online adaptation of specific thresholds instead of a hand-tuned preset value. For this purpose, the protocol relied on the reference values from the previous spike at a specific time interval from the peak. The voltage threshold was calculated based on the voltage value measured in the previous spike, and recalculated at each action potential. Thus, after each spike, the threshold for the spike prediction was updated using the following equation:

$$V_{threshold} = V[t_{spike}[i-1] - \tau], \quad (6.2.1)$$

with τ being the selected time for the prediction before the spike and t_{spike} the time instant of the spike peak.

This prediction is effective for stereotyped spikes when only low amplitude subthreshold oscillations occur, but it is limited in other scenarios. Therefore, for neurons or action modes of the same neuron when it was necessary to stimulate before the depolarization rise, another reference was used: the

area of the recorded voltage. In this other mode of the protocol defined in Eq. 6.2.2, the voltage was accumulated along the activity and the sum was reset after each spike.

$$V_{area} = \int_{V[spike_{i-1}]}^{V[spike_i]} V(t). \quad (6.2.2)$$

The stimulation was triggered when the area reached a specific threshold, which was predicted as in the voltage case, or hand-tuned. For the detection of the minimum point to reset the voltage area, we used a RTXI module based on RTHybrid, a real-time software that includes automatic adaptation algorithms to handle the ongoing variability of the recordings (Amaducci et al., 2019; Reyes-Sanchez et al., 2020, 2023), github.com/GNB-UAM/RTHybrid-For-RTXI. The use of each mode of the protocol in the experiment was decided depending on the specific requirements of the recorded activity.

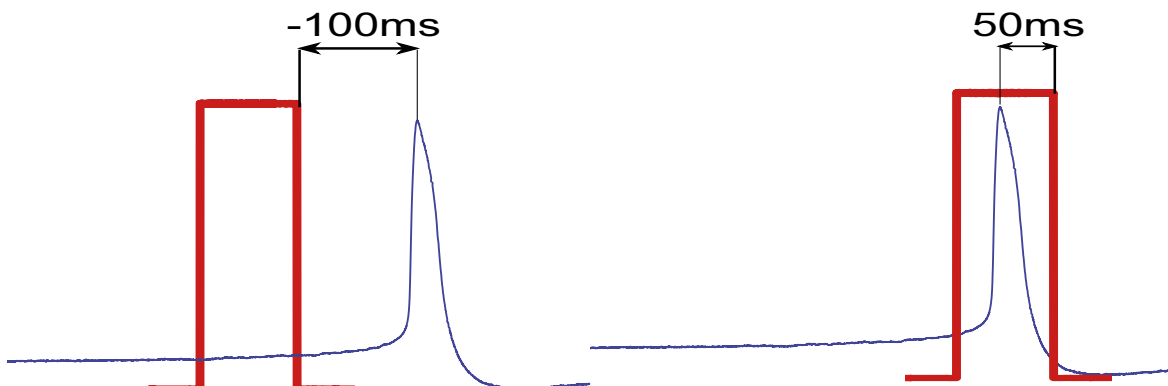


Figure 6.3: Examples of illumination offset, defined as the time interval from the end of the illumination to the peak of the spike.

Using this detection protocol, we assessed the effect of the illumination at different phases of the action potential in the range from 100 ms before the spike peak to 80 ms after the spike peak (see an example of the illumination offset in Fig. 6.3). The illumination interval was 58 ms, validated as the minimal duration for effective stimulation in the test trials. The RTXI module programmed for this study is available at github.com/GNB-UAM/spike_predictor.

6.2.3 Spike waveform characterization parameters

For both experimental recordings and model simulations, action potentials were detected as the maximum point over a threshold, and each waveform was segmented 100ms before and after the peak temporal reference. For the superposition of action potentials (Figs. 6.6, 6.13, 6.14) the waveforms were aligned in the x -axis by the peak and in the y -axis by the first point of the waveform voltage values.

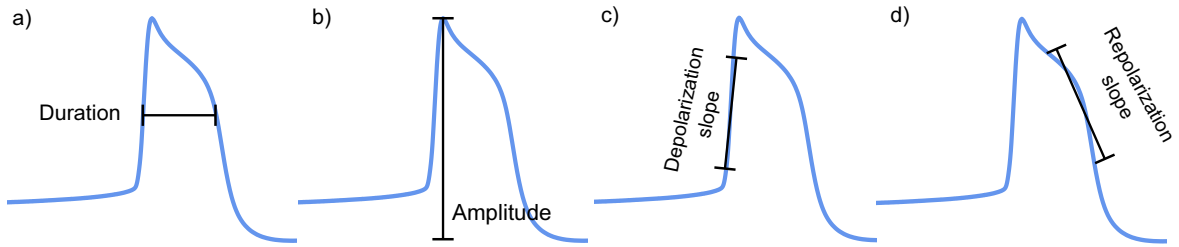


Figure 6.4: Representation of waveform shape's metrics: a) Spike duration at half width. b) Spike amplitude between the maximum and minimum voltage values. c) Depolarization slope at half width. d) Repolarization slope at half width.

For the waveform shape characterization, we used four metrics: duration, amplitude, depolarization and repolarization slopes. They are depicted in Fig. 6.4 and defined as follows:

- Duration: Time interval between the two points at half width of the action potential.
- Amplitude: Difference between minimum and maximum voltage values in the waveform in the analyzed segment.
- Depolarization slope: Slope in the depolarization phase (previous to the peak) measured 1 ms before and after the half width point reference.
- Repolarization slope: Slope in the repolarization phase (after the peak) measured 1 ms before and after the half width point reference.

These metrics were used for the quantitative analysis of the change in experimental recordings and model simulations. In Sec. 6.2.4 below we describe the quantification methodology for the waveform metric change as well as for the comparison between the experimental and model results.

6.2.4 Statistical Analysis

The statistical significance analysis in the data obtained from the sustained CW-NIR stimulation protocol in Figure 6.6 was performed applying a paired T-test to the four spike waveform metrics characterized here (see Fig. 6.4). Data from distinct experiments was gathered and paired by recordings of control-laser and control-recovery (see Fig. 6.6C). The null-hypothesis tested was that control group was equal to the laser group and that the control group was equal to the recovery group, respectively. Since we performed the test in the four waveform metrics –spike duration, depolarization slope, repolarization slope and amplitude– we applied the Bonferroni correction, thus we considered high-significance when $\rho < 0.01/4$.

To compare recordings from different neurons, we normalized the change between the laser and the control conditions for each waveform metric using the following expressions for electrophysiological data:

$$\text{metric change}_{\text{experimental}} = \frac{|\mu(\text{metric}_{\text{laser}}) - \mu(\text{metric}_{\text{control}})|}{|\mu(\text{metric}_{\text{control}})|}, \quad (6.2.3)$$

where $\mu(\text{metric}_{\text{laser}/\text{control}})$ is the mean of the corresponding metric for all waveforms in a given laser stimulation or control trial.

Analogously, to compare the change between the distinct model simulations we normalized the change in the parameter-driven simulated variability range using the following expression:

$$\text{metric change}_{\text{model}} = \frac{|\text{metric}_{\text{min}} - \text{metric}_{\text{max}}|}{|\text{metric}_{\text{max}}|}, \quad (6.2.4)$$

where $\text{metric}_{\text{min/max}}$ refers to the minimum or maximum value of the corresponding waveform metric resulting from the model simulations in the considered parameter range.

For the comparison between experimental data and model simulations in Figure 6.13, we defined an experimental reference for each metric as the general mean and standard deviation for all experiments ($N = 23$). This allowed us to define a range of change due to the laser effect to which the model values could be compared. The mean of metric experimental change (MEC) was defined as:

$$\mu_{\text{MEC}} = \frac{1}{N} \sum_{i=1}^N \frac{|\mu(\text{metric})_{\text{laser}} - \mu(\text{metric})_{\text{control}}|_i}{|\mu(\text{metric})_{\text{control}}|_i}, \quad (6.2.5)$$

Here, $\mu(\text{metric})_{\text{laser}}$ and $\mu(\text{metric})_{\text{control}}$ represent the mean values for each experiment i in laser stimulation and control trials, respectively, where the index i ranges for all experiments, with N being the number of experiments.

Thus, the percentage change in waveform from the model simulations, as described in equation 6.2.4, was mapped to this reference range: $(\mu_{\text{MEC}} \pm 2\sigma_{\text{MEC}})$, with σ_{MEC} being the standard deviation of the MEC. To visually represent this range, we utilized a color gradient with the *background_gradient* option in *DataFrame* style in Python. The formula for mapping these values is:

$$\text{Gradient value} = \frac{\text{value} - \text{Vmin}}{\text{Vmax} - \text{Vmin}}$$

Here, *value* represents the percentage change in the model simulation for a specific metric, while *Vmin* and *Vmax* represent $\mu_{\text{MEC}} - 2\sigma_{\text{MEC}}$ and $\mu_{\text{MEC}} + 2\sigma_{\text{MEC}}$ respectively, with μ_{MEC} and σ_{MEC} being the specific mean and standard deviation corresponding to the metric specified in *value*. Since all changes are in absolute value, the lower bound for *Vmin* is 0.

All data analyses were performed in Python, the scripts are available in github.com/GNB-UAM/Garrido-Pena_Modulation-neural-dynamics-by-CW-NIR-stimulation.

6.3 Temperature estimation for analyzing laser neuromodulation

To estimate the CW-NIR laser induced temperature change, we used the open-pipette method employed in previous experimental studies to measure the temperature variation during the illumination (Li et al., 2013; Rabbitt et al., 2016; Brown et al., 2020, 2021). We calibrated the resistance and temperature relation using a thermistor (EPCOS, $10k\Omega$) to measure the temperature in the preparation solution in the range from 23°C to 29°C . We used two protocols: injecting a constant current to

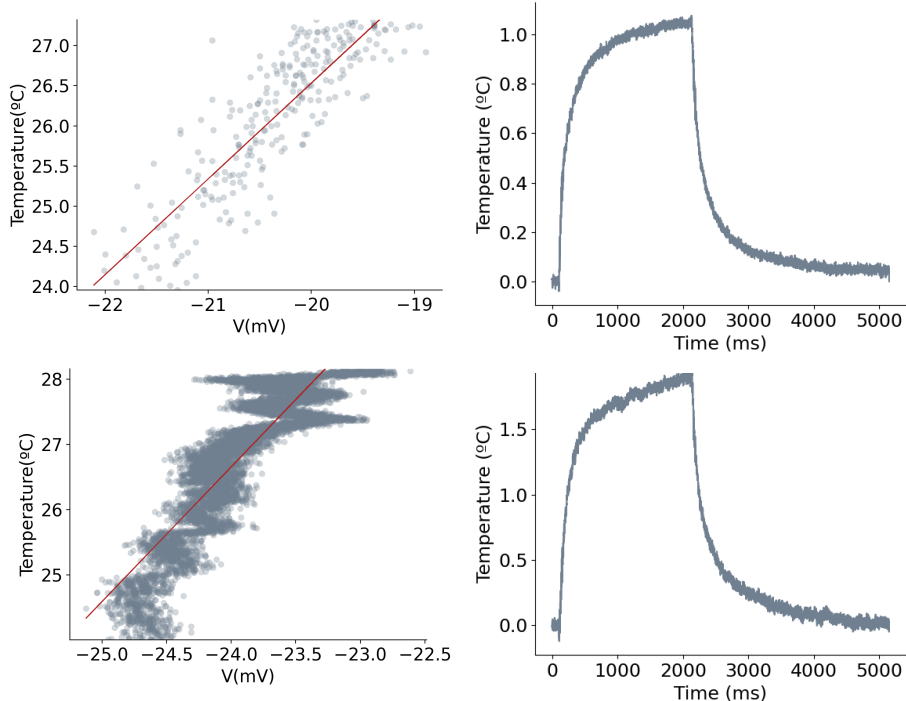


Figure 6.5: Open-pipette temperature estimation method. Each row in the panel represents pulsed and continuous current delivery for the estimation, respectively. For both examples: left column, temperature and voltage relation. Right column filtered mean of voltage recordings from short illumination intervals in the pipette.

calculate the resistance change from the voltage recording, and injecting pulses of a specific current value. From the resulting recording slope of the linear regression, we computed the conversion from voltage to temperature. For the estimation of the temperature change during the laser stimulation, we measured the voltage change during short intervals of laser illumination and the temperature value at its saturation plateau. This estimation is represented in Fig. 6.5.

6.4 Sustained CW-NIR laser stimulation effect on single neuron dynamics

6.4.1 CW-NIR laser effect on spike waveform

To study the effect of the CW-NIR laser on the spike dynamics, we performed experimental triplets of control, sustained CW-NIR laser stimulation and recovery recordings (for details see Sec. 6.2.1). This protocol provided a reference for the characterization of the laser effect. The data analyzed in this section corresponds to the spontaneous activity of neurons from the right parietal ganglion (RPG) of *Lymnaea stagnalis*, under no stimulation other than the laser illumination when specified.

Left panels in Fig. 6.6A and B illustrate the stereotyped waveform of the action potential from two experiments in two distinct neuron types present in the RPG with symmetrical and shoulder spike shapes, respectively. Note that the two neuron types differ not only in spike waveform but also in duration. In the example shown in Fig. 6.6A, the duration of the spike was \sim 20 ms whereas the one shown in Fig. 6.6B was \sim 40-50 ms. To characterize the sustained CW-NIR laser stimulation in terms of change and recovery, the three stages of the protocol –control, laser and recovery– are represented in all panels. The superimposition of the spike waveforms (\sim 40 and 110 spikes for each trial, panels A and B, respectively) for the same recording are aligned in the x axis by the spike peak and in the y axis by the voltage amplitude of the first point of the waveform, together with the trial mean spike represented with a wider line. Note how the control and recovery traces overlap for both neuron types, illustrating the resumption of the spike dynamics shortly after the laser stimulation ceases (see aligned spikes in Fig. 6.6 A and B).

Figures 6.6A and B illustrate that the variability was very small in amplitude, duration and in depolarization or repolarization slopes between the spikes within the same trial in both neuron types. However, during CW-NIR laser stimulation, the change in action potential waveform shape was notable with respect to the control and the recovery. This change was most clear in the spike duration, which was the result of changes in both depolarization and repolarization slopes.

The right panels ii) in Fig. 6.6A and B, show barcharts that quantify the change in terms of spike duration, amplitude, depolarization slope and repolarization slope. These metrics were used to characterize the action potential waveform and its possible change during the laser illumination (see also Fig. 6.4 and Sec. 6.2.3). Each one of these metrics is represented on the right panels as the absolute value of the difference of the laser stimulation to the control recording normalized by the mean control value (see Sec. 6.2.4). For both neuron types there was a change in duration and in the slopes,

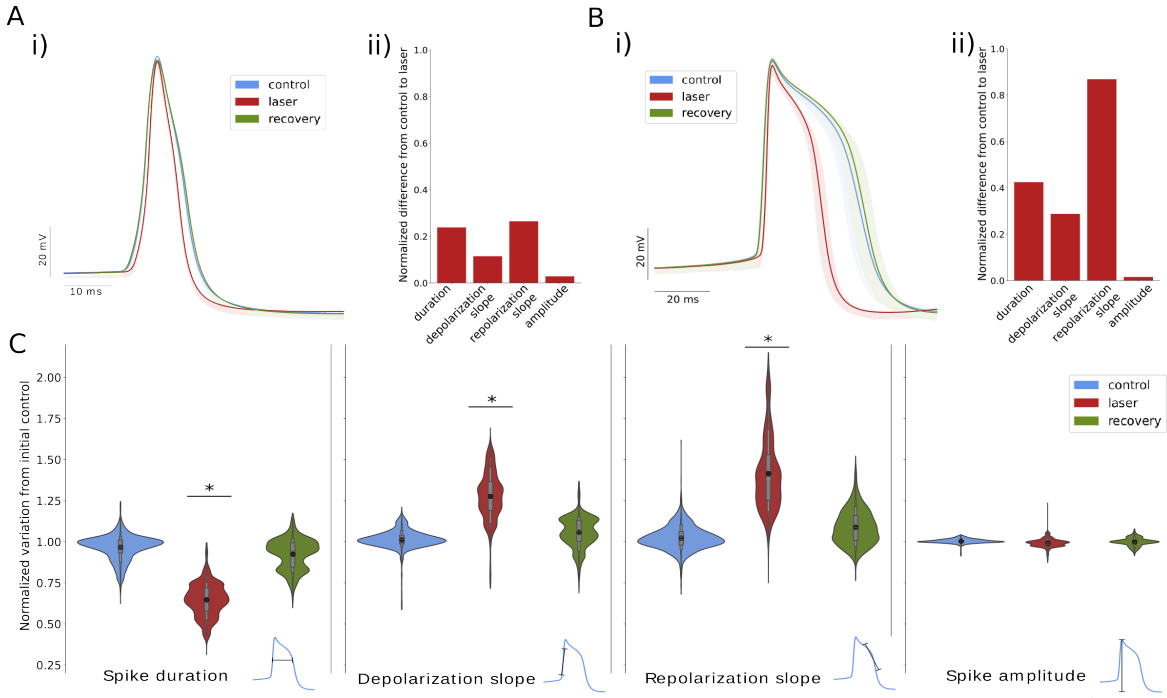


Figure 6.6: Effect of sustained CW-NIR laser stimulation on the spike waveform for two distinct neuron types. For all panels: control, laser and recovery are color coded in blue, red and green, respectively. Panel A. Characterization of no shoulder shape type neuron. Panel B. Characterization of shoulder shape type neuron. Ai) and Bi) Superimposition of spike waveforms in a single trial recording corresponding to a symmetrical and shoulder spike neuron, respectively. The spikes were aligned to the peak for the x axis and to the onset for the y axis, the mean is depicted in darker colors. Aii) and Bii) barcharts quantify the change using the difference from laser to control normalized by the mean control value for metrics: duration, depolarization and repolarization slopes, and amplitude. Panel C, violin plots representing the variation of the experiments with respect to the control ($N = 23$) for shoulder and symmetrical types together. For each metric of the waveform, the control, laser and recovery recordings are normalized to the first control. From left to right: duration, depolarization slope, repolarization slope and amplitude. Asterisks over the violins indicate that the metric change was highly significant (Bonferroni correction, $(p < 0.01/4)$, see Statistical Analysis Sec. 6.2.4 in Materials and Methods).

with the largest change being in the repolarization slope (around 26% for the symmetrical spike type neuron and 86% for the shoulder type). The alignment illustrated in the left panels shows that the change in amplitude was minimal in comparison to the rest of the metrics. Although both neuron types showed an effect of the sustained CW-NIR laser stimulation in the action potential waveform, the change in the shoulder neuron type was larger for duration and slopes. This may be due to specific channels that generate the shoulder shape of the spike, which may allow for a wider range of change in the spike dynamics, especially in terms of the repolarization slope.

Panel C in Fig. 6.6 displays the results of multiple experiments following the same protocol described

above, represented in violin plots as the normalization of each experiment with respect to the mean of the first control of the respective metric for each spike detected during control, laser and recovery. To avoid possible bias from the natural evolution of the intracellular recordings, in this figure we only included experiments where the activity was recovered within 10% change in firing rate with respect to the control. For each trial, only stereotyped waveforms were considered and large deviations (in the form of $z_{score} < -0.1$ in the normalized duration) were filtered out. The variability characterized in the control violins represents the variation within controls, which was also the most homogeneous in terms of density distribution. This is represented for each one of the selected spike waveform characterization metrics as in panels A and B –duration, depolarization slope, repolarization slope and spike amplitude (see Fig. 6.4).

The results shown in Fig. 6.6, panel C are consistent with the described change in the illustrative individual experiments shown in panels A and B in the same figure. On the one hand, the activity recovered its initial characteristics after the CW-NIR laser stimulation ceased for every metric, i.e., the recovery (green violin) returned to the same level as the control (blue violin). The differences in these distributions are mainly caused by the natural variability in the biological system. Also, as all values are normalized to the mean of the first control, it can be expected that the distributions may diverge more in laser and recovery violins than in control violins. A separate analysis for the two neuron types is available in Fig. 6.7

Regarding the change during the laser stimulation, for every waveform metric except amplitude, we can see in Fig. 6.6C how the overlapping of the distributions is minimal. The distribution for the duration was the most homogeneous, whereas the variation for depolarization and repolarization slopes had different density distributions, being the repolarization slope the one presenting a larger change in most cases. This can be explained by the variety of neurons in the collected data, the change in the slopes differed from one type of neuron to another. Thus, the distribution of variability was different. Some laser stimulation recordings presented a milder change than others. The slight change along neurons of the same type was likely due to the physical restrictions of the setup in each experiment: the angle of the laser, the laser focusing, the maximum power used and the overlaying tissue. Overall, considering these factors, we can see that stimulating with the sustained CW-NIR laser resulted in a significant change of the spike waveform. In the case of the amplitude, the change was very small.

We performed statistical tests on these data and confirmed that the changes in duration, depolarization and repolarization slopes were highly significant ($p < 0.01/4$) when comparing control and laser samples. The amplitude change was not highly significant, and so were not the changes in any metric

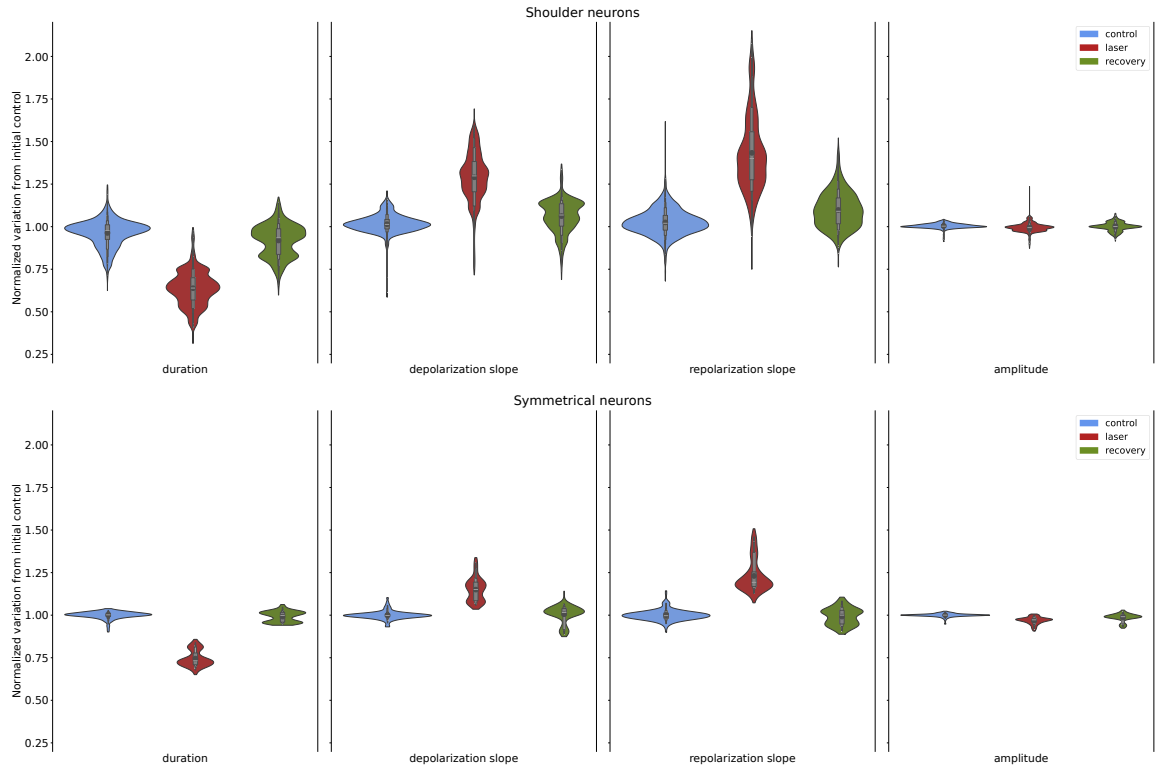


Figure 6.7: Segregation of data into shoulder and symmetrical neural types. Violin plots for the four metrics -duration, depolarization slope, repolarization slope and amplitude- grouped by control, laser and recovery trials. Spikes metrics are normalized to the first control, as in Fig. 6.6 panel C.

comparing control and recovery samples (see Statistical Analysis Sec. 6.2.4).

This combination of changes points out to different biophysical candidates that might be involved in the modulation for the global change in both slopes or specific channels involved in the CW-NIR laser effect, since the depolarization and repolarization slopes were affected differently, while the amplitude did not change, and for distinct neuron types the characterized metrics had different variations (i.e., the repolarization slope in the shoulder shape neuron type was reduced to a greater extent than in the symmetrical type). In section 6.5 we assess these possible candidates using a computational model.

6.4.2 CW-NIR laser effect on spiking rate

During the identification of the biophysical effect at different phases of the action potential dynamics on single neurons, we identified a robust acceleration of the action potential (a shorter duration of the spike waveform). This could also point to an acceleration of the tonic activity of the neurons. Pulsed NIR laser stimulation has been proven effective as a stimulation technique, mainly eliciting action potentials (APs) in silent neurons at specific combinations of pulse duration and intensity

(Wells et al., 2005b; Izzo et al., 2007; Shapiro et al., 2012; Cayce et al., 2014). Thus, we also assessed the effect during sustained CW-NIR infrared laser stimulation on the spiking frequency in long stimulation recordings (1-3 min).

To avoid possible bias originated from intrinsic properties of the neuron and the circuit in which it was integrated, we only considered recordings where the neurons effectively recovered their control activity rate after the stimulation (i.e., absolute recovery change within 10% from the initial control). The activity frequency was characterized by the absolute firing rate (AFR) for control, laser and recovery, and by a histogram of Inter Spike Intervals (ISIs), i.e., the time interval from peak to peak.

In Fig. 6.8, the mean firing rates for control, laser and recovery are represented along with their standard error of the mean. Panel A depicts the general change in frequency for the neurons, showing the neural activity trend to excitation in the mean. In panels B and C, this set of triplets is divided into two groups depending on the difference between the laser and the control, classified as no change when the difference between control and laser was less than 10% (panel B), and as excitation for the opposite case (panel C). There is no representation of inhibition in this panel, since there was not any experiment that fulfilled the criteria of a 10% negative change during the laser stimulation with respect to the control. Note how cases where the activity increases are the most consistent ones (12 out of 23) and that even in the set classified as unchanged, the mean of the AFR during laser stimulation is larger than the controls. These results support an excitatory tendency during CW-NIR sustained stimulation.

The absolute firing rate hinders some characteristics of the neural activity, such as the refractory period or the presence of bursting activity, which might also influence the firing frequency study. Thus, Fig. 6.8D displays the ISI histogram for each experiment showing again the triplets of control, laser and recovery, for each sample. Experiments showing excitation are highlighted in a red square. Note that for most cases classified as excitation, the ISIs tendency is to be reduced, which is observed in the laser histogram at the left of the control and the recovery. Note that there are some experiments where the laser ISI histogram seems to overlap with the controls and the recovery (see Fig. 6.8D, panels [2,A] [3,A] and [2,C]) but still the mean AFR of the laser recording was 10% higher than the control. In these situations, even though the activity was faster under stimulation, the time between spikes did not show a proportional change, which can be due to a modulation in the refractory period that compensated the spike acceleration. Under the laser modulation, we also found that some neurons would start firing in shorter ISIs, tuning the tonic spiking into pair spiking similar to small bursts, e.g. Fig. 6.8D, panel [2,F].

Overall, our results in this subsection show a larger tendency to a frequency increase in response

to the NIR illumination indicating that it is possible to achieve neuronal excitation under sustained CW-NIR laser stimulation. It is also important to highlight that inhibition was not found in any of these experiments with sustained CW-NIR laser stimulation during tonic firing activity.

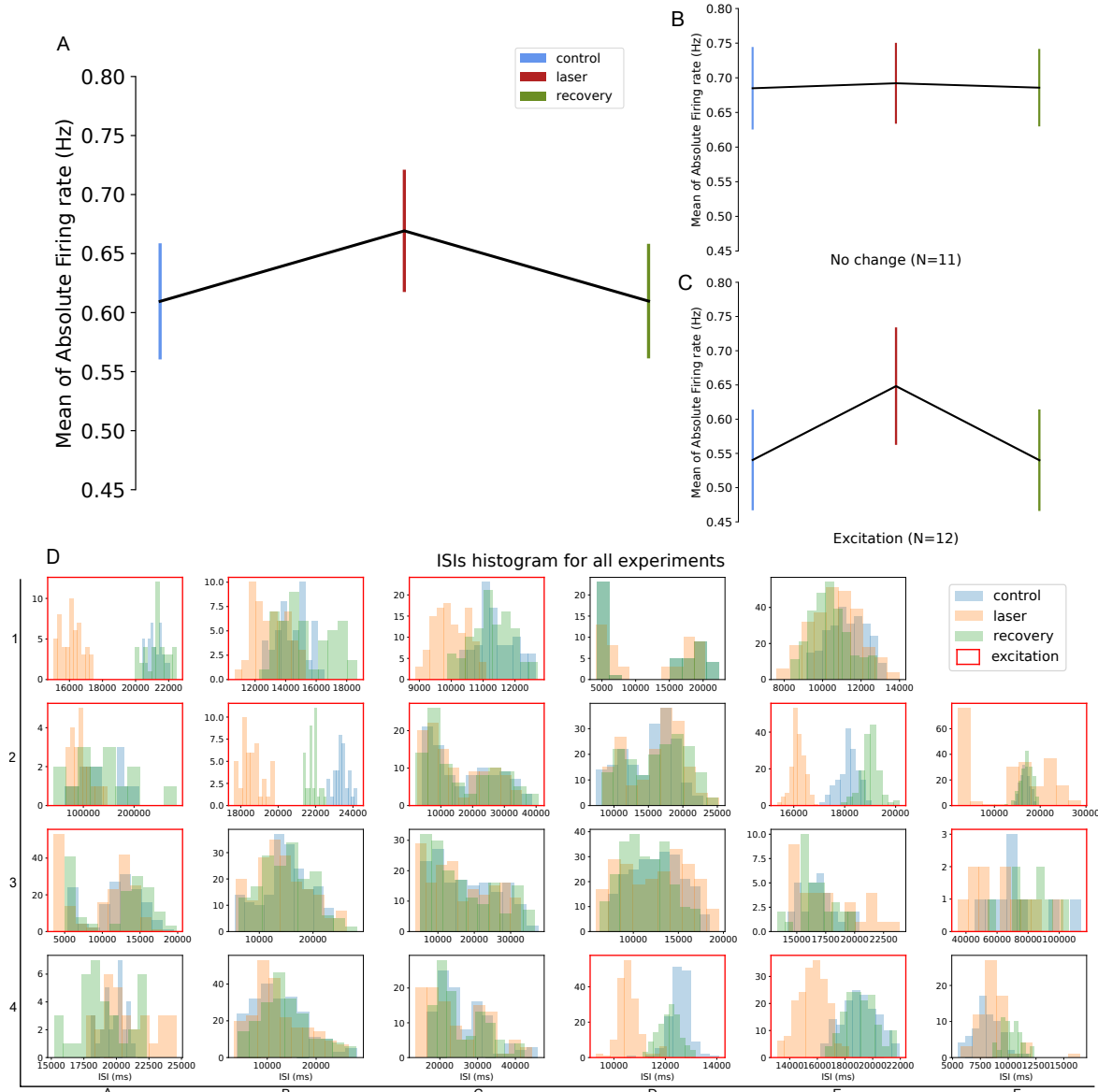


Figure 6.8: Firing rate and interspike interval (ISIs) analysis for the CW-NIR laser stimulation. A. Absolute firing rate in all experiments (N=23). B. Absolute firing rate for cases from the experiments in A with no change during laser illumination (N=11); C. Absolute firing rate for experiments from A showing an increase in the firing rate (N=12); D. ISI histograms for control, laser and recovery for each experiment. Cases showing increased excitation in their firing rate (sample in panel C) when illuminated by the CW-NIR laser are highlighted in a red square.

6.4.3 Effect of CW-NIR stimulation in a minimal circuit

In addition to the study of the direct effect on the spike waveform and the firing rate in single neurons, it is important to test the CW-NIR laser capability to modify the activity in a circuit. The aim is to show that a neuron affected by the laser illumination can also affect the circuit it is included in. As a first approach to test this, we illuminated two electrically coupled cells in *Lymnaea stagnalis*, VD1 and RPD2 in the visceral and right parietal ganglion, respectively (Benjamin & Pilkington, 1986; Beekharry et al., 2015). In this experiment, we kept the same protocol with control, laser and recovery trials for the recordings, illuminating a single neuron of the circuit at a time. In addition, we also tested the possible modulatory effect of the laser in the gap junction by illuminating areas where, based on the literature, the synapse should be located for these two neurons. Note that the location of the gap junction and the two neurons is highly dependent on the position of the ganglia in the preparation, so this approach provides just an approximation. Figure 6.9 shows an image of the ganglia during the illumination of the VD1 neuron in the visceral ganglion (left photograph), the RPD2 neuron in the right parietal ganglion (right photograph), and the gap junction at its estimated position (middle photograph). Figure 6.10 shows the results for this experimental protocol in three

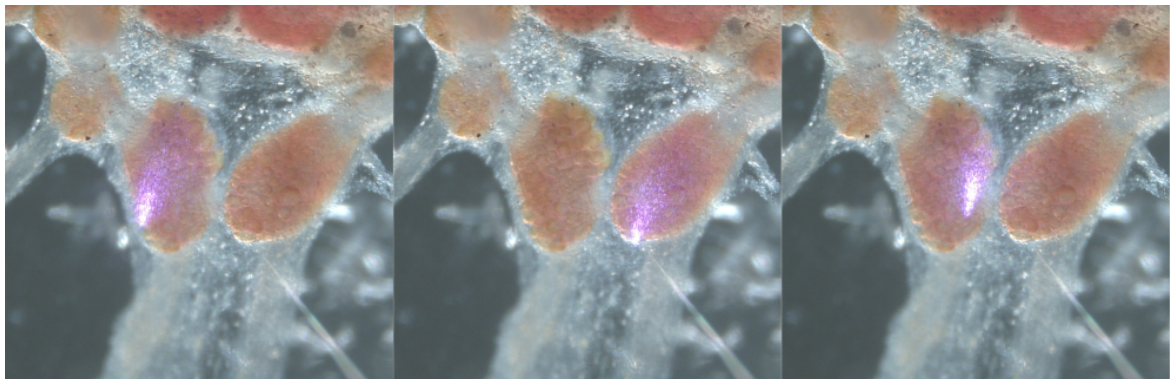


Figure 6.9: Microscope image of the three cases of illumination in electrically coupled neurons. From left to right: illumination of VD1 neuron, RPD2 neuron and the gap junction of their electrical coupling. The electrode recording each cell can be seen in these images, filaments approaching the cells from the bottom right and from the top left.

different cases. In these preliminary results, we can see that, for the recordings of the neuron being illuminated (VD1 recording during VD1 illumination and RPD2 recording during RPD2 illumination), we observe the same effect reported in section 6.4: the spike accelerates and its duration is shorter, affecting the slopes and without changing the amplitude. In the recordings of the electrically coupled neuron, for all cases we can appreciate a mild change, specially clear in the example 3, where also the change is larger in the VD1 recording when the illumination was in RPD2, with respect to the change in RPD2 when the illumination was in VD1. When illuminating the gap junction, there is

a small and equivalent effect in both neurons (more noticeable in example 3).

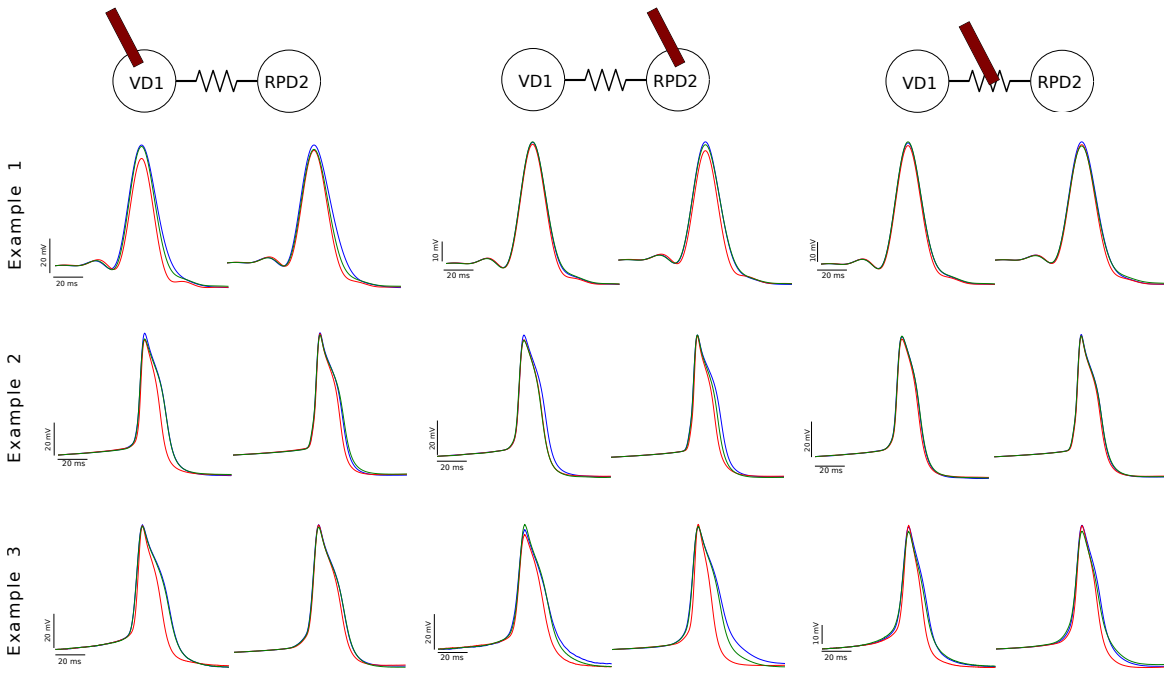


Figure 6.10: Electrically coupled neurons illumination: superposition of the averaged waveform for control, laser and recovery in the three different illumination scenarios (three examples are shown for each case): spike waveforms of VD1 and RPD2 illuminating VD1 (left column); waveforms of VD1 and RPD2 illuminating RPD2 (middle column); and finally neuronal waveforms illuminating the gap junction (right column). Each plot follows the previous color code for control, laser and recovery: blue, red and green, respectively).

A methodical reproduction of these results would provide further information about the laser action and also pave the path to boost novel applications of this stimulation method for the modulation of neural circuit dynamics.

6.4.4 Effect of CW-NIR stimulation at different wavelengths

To address one of the main questions in infrared laser stimulation, i.e., what is the source of the effect (photo-thermal, photo-electrical, metabolic), it is necessary to characterize the modulation in different configurations. It has been proven that a specific configuration of wavelength, pulse duration and frequency, and intensity, is crucial for an effective neural stimulation (Izzo et al., 2007; Wells et al., 2007). However, the details on what is each parameter tuning or affecting have not been analyzed in detail. In this subsection we analyze the data from a preliminary study in collaboration with Riccardo Marin, Liyan Ming and Daniel Jaque from the laboratory of *Nanoparticles for Biomedical Applications* in the Department of Physics of Materials at UAM. Here we employed different wavelengths in CW-NIR lasers of 808nm, 830nm, 980nm and 1450nm. Following the hypothesis of the strong role

of the temperature modification, the first difference between those wavelengths that we need to take into account is the water absorption at each one of them. Figure 6.11 shows a representation of the water absorption curve for different wavelengths. We can classify the wavelengths in this experiment regarding water absorption in three groups: 808nm and 830nm in the lowest range; 980nm in the first peak and 1450nm with a significant increase of the extinction coefficient. Therefore, the first thing to consider is the difference in the heating capacity of each laser in the surrounding water and the tissue.

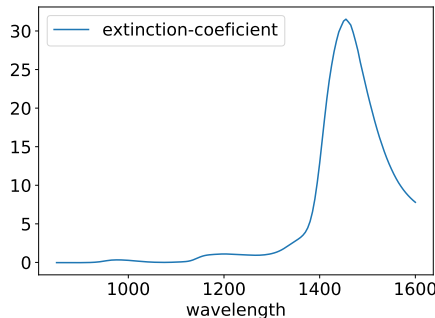


Figure 6.11: Water absorption for different wavelengths values.

As preliminary results, we present here the effect in the spike waveform for 830nm and 1450nm. We saw so far that the CW-NIR laser stimulation affects the spike waveform metrics in a reversible manner accelerating it, with a shorter duration, changing its depolarization and repolarization but with a minimal or negligible change in the amplitude. Those results, performed with a 830nm laser, correspond to the results depicted here for 830nm (see Fig 6.12 first row). In the case of 1450nm, the change is larger in every metric (specially regarding the comparison between the laser and the recovery) but particularly in the amplitude, which presents a change that was not commonly visible in the 830nm stimulation. During this experiment, there was a tendency in the recording to decrease the amplitude naturally. However, relying on the recovery metrics, we can see that although there is a tendency in the recording to change the waveform, the effect during the laser stimulation is notable. In this last case, it is remarkable that after this large change in amplitude, the recovery value was not achieved remaining far from the level of the first control.

Based on this preliminary study, we can observe a relation between the wavelength and the effect on the waveform. Again, with a methodical repetition of this experiment, this relation could be set and the role of the wavelength and other factors beside the photo-thermal effect, could be explored.

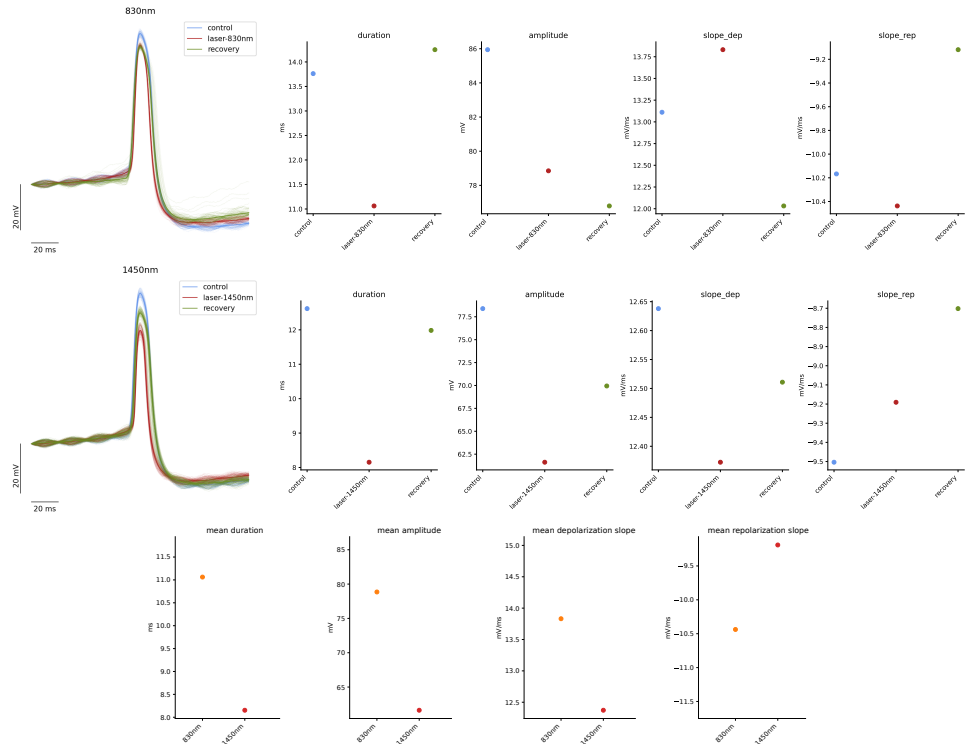


Figure 6.12: Representation of the effect of sustained laser stimulation at 830nm at 90mW and 1450nm at 120mW. In terms of power density, the corresponding values are: 194.88 W/cm² and 315.78 W/cm², respectively. The left panel in each row is the superimposition of the spike waveforms aligned to the first point, during a control recording with no stimulation, a laser recording during the illumination at the specific wavelength and a recovery control, again with no stimulation. The four panels in each row correspond to the mean value for each trial of control, laser and recovery for the spike waveform metrics: duration, amplitude, depolarization and repolarization slopes.

6.5 Model analysis for constraining candidates to explain the effect of CW-NIR laser illumination in the spike dynamics

6.5.1 Parameter range modification for the biophysical candidates in the model

Computational models are a powerful tool to assess the source of neural dynamics where all variables involved are accessible. By considering membrane potential recordings alone, it is difficult to understand the contribution of the biophysical candidates in the underlying dynamics shaping the action potential. While it is specially hard to carry out experiments using chemical and/or electrophysiological techniques to selectively block or compensate channels to mimic the observed CW-NIR laser effect, the simultaneous accessibility to all the variables in a model provides a unique tool to dissect the contribution of all biophysical candidates. Thus, to further explore the source of the experimentally observed CW-NIR effect, we analyzed the spike generation dynamics in three dif-

ferent conductance-based models assessing the change in the most likely candidates to be affected by the laser stimulation: modulation of membrane capacitance and ionic channels. More specifically, we modulated (i) the capacitance and the conductance of the active ionic channels – I_{Na} and I_K – in the standard Hodgkin-Huxley (HH) model (Hodgkin & Huxley, 1952); (ii) the conductance of ionic channels – I_{NaP} , I_{NaT} , I_D , I_A , I_{HVA} , I_{LVA} – and capacitance in a *Lymnaea stagnalis* CGC neuron model with a shoulder shape waveform (Vavoulis et al., 2010); and (iii) the capacitance in a two-compartment model –where the fast and slow dynamics are segregated– in a *Lymnaea stagnalis* buccal ganglion neuron (N3t) model (Vavoulis et al., 2007). The implementation of these models is available in the open-source model library Neun github.com/GNB-UAM/Neun and the code for the simulations can be accessed in github.com/GNB-UAM/Garrido-Pena_Modulation-neural-dynamics-by-CW-NIR-stimulation.

The model parameters were modulated to investigate and compare their effect to that of the CW-NIR laser stimulation on the neurons, and to evaluate the interrelationship between the observed changes. To identify changes in the spike dynamics similar to those observed under the CW-NIR laser illumination, in this section we covered a complete range of values in the parameter space of each biophysical candidate. The criteria for driving the parameter exploration were the preservation of tonic spiking in the activity and the assessment of a realistic range of values. As our initial hypothesis did not assume that the CW-NIR laser effects were exclusively photo-thermal, model parameter changes were applied with no temperature description. Further down in Sec. 6.5.2 we present a detailed study considering the temperature dependency of the biophysical candidates.

The results of this study are shown in Fig. 6.13. The analysis for each model is sorted by the explored biophysical candidate –capacitance, sodium channels, potassium channels and calcium channels–. Thus, panels A, B, C and D show the superposition of all spike waveforms from the simulations for the range of explored model parameter values of each candidate. The table in Panel E represents how well the different model candidates reproduce the observed experimental effect. For each metric and biophysical candidate, there is a percentage of change in the model calculated as the change from minimum to maximum normalized with the maximum value (analogously to the quantification in Fig. 6.6, see also Sec. 6.2.4). The background color in each cell represents the ability of each model parameter modulation to produce results similar to the change in the experimental results. The color gradient (represented in the color bar) takes as reference the mean of the metric experimental change (MEC) quantification, considering the range of ($\mu_{\text{MEC}} \pm 2\sigma_{\text{MEC}}$) (see Sec. 6.2.4). The mean change and its standard deviation were computed as the normalized difference between mean values for each control and laser experimental pair for all experiments. These reference values are shown

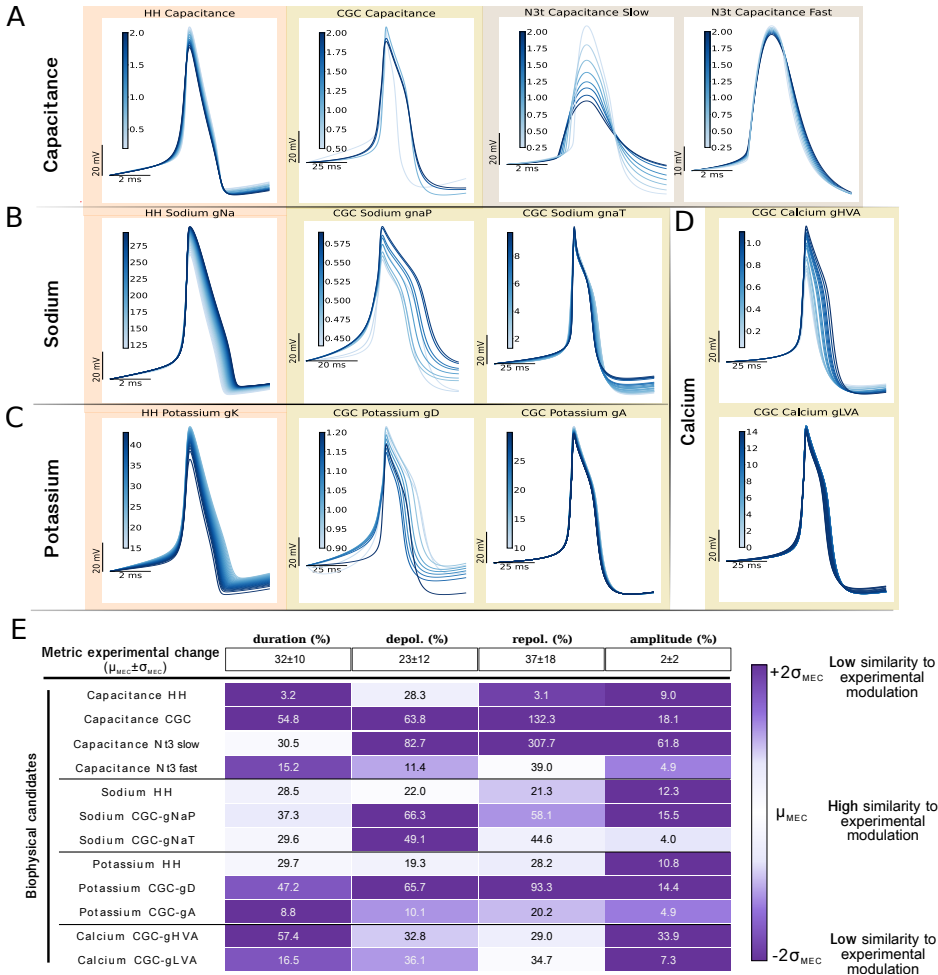


Figure 6.13: Modeling study of the CW-NIR laser stimulation effects due to isolated biophysical changes that alter the spike waveform. Panels A, B, C and D: Superposition of spike waveforms in each model by modulating a single biophysical candidate. The background colors correspond to each simulated model. In Panel A, the capacitance is changed for the HH and CGC neuron models, and in the two compartments for the N3t neuron model. Panel B shows the spike waveforms changing the conductances of I_{Na} channel currents: I_{NaP} and I_{NaT} , from the CGC-model. Panel C, displays the modulation of K conductances in ionic currents: I_K in the HH-model and I_D and I_A for the CGC-model (from left to right). Panel D shows the modification of the calcium current conductances in the CGC-model (I_{HVA} and I_{LVA}). Table in panel E represents the quantification of the changes in the spike metrics when tuning each parameter for every model. Each cell contains the waveform change normalized to the maximum. The color gradient represents similarity based on the standard deviation of the normalized experimental change. Dark purple corresponds to low similarity ($2\sigma_{MEC}$ or larger) and white to high similarity. The quantified experimental reference (MEC) is annotated in the first row of the table.

for each metric in the first row of the table in panel 6.13E to compare them with the model results. Thus, dark purple corresponds to values two times the STD of the mean over or under the mean, and white represents the mid point between those two values, i.e., high similarity to the experimental

modulation. For example, in the case of Capacitance in the HH model, the change in duration was minimal 3.2%, while the mean change in the experimental observation was 32%, this color is then represented in dark purple, since 3.2% is not in the defined range (32 ± 20). On the other hand, the change in depolarization slope for this model (28.3%) is depicted in light purple, since it is in the defined range and close to the mean metric experimental change (23 ± 12).

Change in Capacitance

Capacitance has been one of the most discussed biophysical candidates to be affected by IR laser illumination (Shapiro et al., 2012; Cayce et al., 2014; Shapiro et al., 2017; Plaksin et al., 2018). A change in capacitance has a direct effect on the spiking frequency and exerts a global modulation on all ionic currents, so many studies have discussed this change both experimentally and theoretically. Here we explored the CW-NIR modulation of capacitance in three different conductance-based models: in the Hodgkin-Huxley model, used in other studies, in the CGC-Vavoulis model, which presents a variety of channels and in the N3t-model, which is the only one with more than one compartment and, thus, has two distinct capacitance values.

Figure 6.13A displays the waveforms of each simulation. In the case of the HH-model, there was a mild change in duration, mainly caused by the depolarization modulation, and a change in amplitude larger than what was observed experimentally. The CGC-model exhibited a similar tendency to the HH-model but with an extreme case at a low value of capacitance $0.5\mu F/cm^2$, where moderated changes in depolarization and amplitude were combined with a large change in the repolarization, and consequently in the duration. This modulation made capacitance a better candidate for reproducing the experimental results in the case of the CGC neuron, preserving the metrics' change interrelations, i.e., the combination of a minimal change in amplitude and a large change in duration, together with a larger change in repolarization than in depolarization slope. In the N3t neuron, we can see contrasting results for the two different compartments. In the compartment containing slow currents, the change in amplitude was the most striking, seemingly conditioned by both slopes. In the case of the fast current compartment the main change was observed in repolarization rather than depolarization, which is more similar to the experimental outcome.

These results are quantified in the table in Fig. 6.13E. The HH-model showed a change comparable to the experimental one only for the depolarization slope. The CGC-model reached plausible values in terms of the interrelation between metrics (large change in duration generated by a larger change in repolarization than in depolarization slope), but it exceeded the experimental references. The change in amplitude was larger than seen in the experimental results for most parameters (dark

purple). It is especially clear in the case of the two-compartment model (N3t neuron), in which the modulation of capacity in the slow compartment resulted in a large change in amplitude. In contrast, the small change in amplitude in the fast compartment was the most similar value with respect to the experimental results (light purple).

By changing the capacitance, we achieved some of the expected changes, but achieving the desired results for all four metrics simultaneously was not possible. Therefore, modulating capacitance alone does not reproduce the experimentally observed effects, especially regarding the combined change, e.g., large change in repolarization and small change in amplitude, larger change in repolarization than in the depolarization. It was only when the fast compartment of N3t was modified that relations between these four metrics matched the above relationships. But note that changing the capacitance in the slow compartment is equivalent to changing several ionic currents simultaneously, not just a single current property.

Ionic channels

The other mechanism to explain the laser modulation that we assessed here was a direct effect on the ionic channels involved in the generation of action potentials. These channels are activated in a sequential manner, and each of them is directly involved at distinct stages of the action potential generation. They have been discussed in the laser stimulation literature (Liang et al., 2009; Li et al., 2013; Rabbitt et al., 2016) by a direct effect of maximal conductance, and channel opening and closing dynamics due to thermal effects, e.g., in calcium channels (Albert et al., 2012; Barrett et al., 2018). These candidates were assessed here in the two single compartment models, the HH-model due to its wide use in computational neuroscience and the Vavoulis-CGC model for its variety of channels (including calcium currents) and accurate reproduction of the observed neural waveform shape. Note that in the CGC-model analysis, all currents types are in pairs of high and low conductance as well as fast and slow dynamics, having two currents for sodium, potassium and calcium (see Fig. 4.5 in Materials and Methods).

In Fig. 6.13B the spikes from the simulations for each sodium current in the HH and CGC models – I_{Na} , and I_{NaP} and I_{NaT} , respectively– are superimposed. For the three currents, we observed modulation in both depolarization and repolarization slope, which resulted in a change in duration. Although the change in duration is close to the experimental outcome, the change in the depolarization is larger than in repolarization (see Fig. 6.13E), which is contrary to the experimental results, as it is also the change in amplitude for I_{Na} , and I_{NaP} . However, for channel I_{NaT} the change in amplitude was smaller, falling closer to the experimental range for amplitude and duration, but the change in depo-

larization exceeded the experimental range and the repolarization change was limited in the context of shoulder type neurons (the waveform type that reproduces CGC-model). Although the change of sodium channels alone generated a similar change in duration in relation to the experimental results, the rest of the metrics did not replicate those results.

Analogously, in Fig. 6.13C, simulations for potassium currents (I_K and I_D and I_A , respectively) are represented for HH and CGC models. For the three currents, the major change was in the repolarization slope followed by the depolarization (see quantification in Fig. 6.13E). This combination resulted in a modulation of the duration that lay in the range of similarity to the experimental results, with the exception of the amplitude, which does not correspond to the experimental results. It is especially applicable in the case of I_K in HH-model and in the conductance of the strong potassium current g_D of the CGC-model. Note that for the I_A current, although the combination of changes were comparable to the experimental change, their range was not, so a change in this current alone was not considered a plausible candidate. Thus, a change in potassium channels reproduced the experimental results for duration and the two slopes overall, but it was limited due to an excessive change in amplitude.

In order to inspect the CGC-model in detail, we also simulated the changes in the calcium currents – I_{HVA} and I_{LVA} – for this model. These currents have a key role in the generation of the shoulder shape in the spike (Figure 6.13D). Both created a similar change in the repolarization slopes, as well as in the depolarization, which is also close to the experimentally observed modulation. For duration, I_{HVA} better matched the change, but this modulation was also accompanied by a large change in amplitude which was not observed in the experimental results. On the other hand, I_{LVA} had one of the minimum effects on amplitude but, contrary to experimental results, its effect on the duration was also minimal, although the depolarization and repolarization slopes had a comparable change to the experimental observations. Therefore, altering each calcium channel effectively reproduced the desired change in the slopes but the modulation in duration and amplitude occurred in the same proportion, which does not match the experimental results.

The results described in this section indicate that each candidate can be modulated to bring the waveform closer to the experimentally observed results, but when changed separately they account only for a partial set of metrics matching. The desired combination of changes for duration, slopes and amplitude was not achieved by tuning only one parameter at a time. However, some of the candidates came close to this combination. Considering the ionic current candidates, the one that was closer to the *in vivo* stimulation was potassium current, which reproduced a large range of change in the repolarization, depolarization and duration, though exceeding the change in the spike amplitude.

This is relevant in terms of maintaining the observed interrelation of the metrics. Considering the range of change reached, the calcium channels where the best candidates for the reproduction of the experimental repolarization slope modulation, allowing a wide range of values and generating the shoulder shape waveform. We also saw how capacitance in single compartment models was not enough to reproduce the results. It was only when the capacitance was modified separately in two compartments, that the change reproduced the CW-NIR laser stimulation better. This points to a mechanism for explaining the CW-NIR laser effect with contribution from several candidates at the same time where specific factors might be of greater importance, such as the potassium channel in the case of shoulder shape neurons.

6.5.2 Change of spike dynamics considering temperature modulation in the model

Most studies in laser stimulation point out to a photo-thermal effect, e.g. see (Wells et al., 2007; Shapiro et al., 2012; Li et al., 2013; Ganguly et al., 2016; Rabbitt et al., 2016; Cury et al., 2021; Pan et al., 2023). Thus, in this section we include a model analysis with temperature modulation. We selected the CGC-model from Ref. (Vavoulis et al., 2010) since it is the richest model in terms of variety of channels and ability to mimic the spike waveform of shoulder type neurons. To study global temperature dependence in the model we added a Q_{10} coefficient, representing the temperature sensitivity in the model parameters. The value for this parameter is usually applied to different channel properties and kinetics in a range from 1 to 4 (Schauf, 1973; Cosens et al., 1976; Tang et al., 2010; Alonso & Marder, 2020). Thus, we choose as a common value for Q_{10} 3, as an average general value used in the literature (Hodgkin & Katz, 1949; Heitler & Edwards, 1998; Shapiro et al., 2012; Li et al., 2013; Rabbitt et al., 2016; Ganguly et al., 2019) and also proposed as a universal value for Q_{10} to characterize temperature dependency for biochemical processes (Elias et al., 2014). We estimated the temperature change under laser stimulation at maximum power following an open-pipette method, with a resulting temperature increase of 1-2°C (see Sec. 6.3 and Fig. 6.5). Note that our CW-NIR laser wavelength is at one of the lowest absorption bands of water, so the open-pipette method probably underestimates the change in temperature in the neuron, being the change in the temperature caused not only by water heating but also by heating the tissue. In addition, the reported temperature range of laser induced variation in the literature is wide, depending on the system, the estimation technique and whether it comes from a model or an *in vivo* estimation (Shapiro et al., 2012; Thompson et al., 2012; Rabbitt et al., 2016). Therefore, in our simulations we explored a wider range than our experimental estimation, considering 5°C as a reference and the quantification of the change up to 10°C.

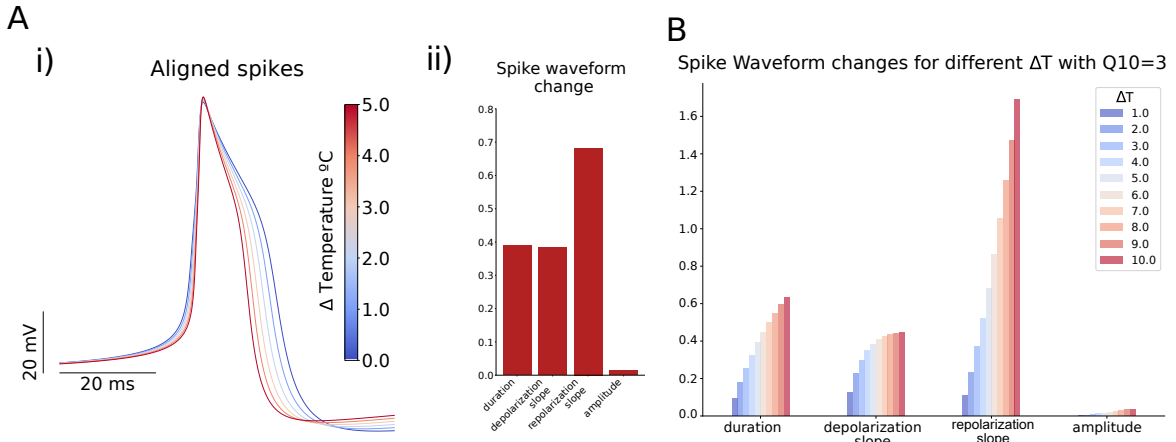


Figure 6.14: Waveform change in the CGC-model due to ΔT temperature variation. Panel Ai) shows the spike waveform superposition for distinct ΔT values. Spikes are aligned to the initial value of each waveform. In panel Aii) the normalized change in the waveform is depicted for all metrics (duration, depolarization and repolarization slopes and amplitude). Panel B shows the change in response to temperature variation from 1 to 10°C ($Q_{10} = 3$) in the normalized metrics.

Figure 6.14 shows the change in the spike waveform caused by variations in temperature. The Q_{10} factor was added to every dynamical equation in the model (i.e., conductances, activation gates and capacitance, see Sec. 4.4.2). In panel A, we show the changes in the waveform for $\Delta T = 0 - 5^\circ\text{C}$, represented as superimposed waveforms in Ai), and its quantification in Aii) normalized to the maximum, which is analogous to the previous sections (see Figs. 6.13 and 6.6): $|max - min|/|max|$. Note how both the spike waveform shape and the quantification of the changes are similar to the experimental results. We can observe changes in duration, depolarization and repolarization slopes, with a very small change in amplitude. The modulation obtained by combining these parameters was not achieved by tuning them separately. It is important to highlight that as the temperature increased (red lines), the spike got narrower by the corresponding alteration in slopes and duration, which supports the hypothesis that the observed effect in single neurons of *Lymnaea stagnalis* might be, to a large extent, caused by temperature gradient. In panel 6.14B, there is a comparison of different temperature changes for the same Q_{10} value in the model. Note that the relation of each parameter to the change in temperature is different, being the repolarization slope the one with the strongest relation, increasing much more rapidly than the duration or the repolarization slope. This points to a main role in the change from some of the channels, especially those that have more tolerance to change. This relation in the repolarization is similar to the comparison of the two neuron types analyzed in the experimental results (Figure 6.6A), where the main difference was present in the repolarization.

Analogously to the simulations in the previous sections, we characterized the variations in the wave-

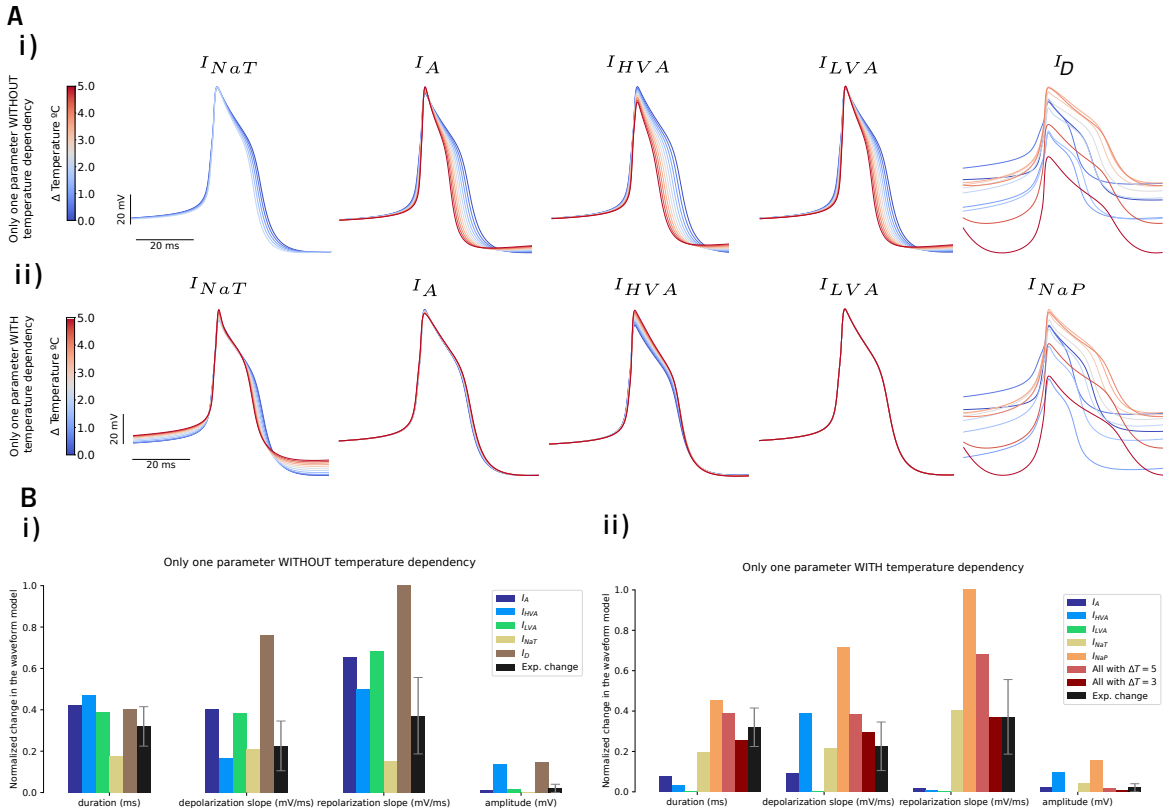


Figure 6.15: Simulation of the effect of individual channels on the spike waveform under temperature modulation. Panel A.i) Waveform modulation in the CGC-model excluding temperature dependency in one channel at a time, from left to right: I_{NaT} , I_A , I_{HVA} , I_{LVA} , I_D respectively. Panel A.ii) Waveform modulation in the CGC-model with temperature dependency only in one channel at a time, from left to right: I_{NaT} , I_A , I_{HVA} , I_{LVA} and I_{NaP} , respectively. Note that I_{NaP} is not in panel A.i) and neither is I_D in A.ii), as for these two particular simulations there was no spike generation. Panels B.i) and B.ii) show the quantification of the waveform change for $\Delta T = 5^\circ\text{C}$ in duration, depolarization slope, repolarization slope and amplitude for all channels in panel A. Both figures include, as reference, the experimental mean and STD (shown in black) and, for case B.ii) (only one channel at a time), the quantification when all channels have the same temperature dependency (all with $\Delta T = 5^\circ\text{C}/3^\circ\text{C}$, data used in Fig. 6.14) is depicted in light and dark red bars.

forms for each individual candidate, varying the temperature only for one ionic-channel at a time. To further explore these candidates and relations, we repeated the model simulation with temperature variations up to 5°C but also canceling the temperature dependency in one channel at a time. Note that overriding the temperature dependence of some of the channels at a time is only possible in a theoretical environment like this, which allows us to expose the role of each channel in relation to the temperature modulation. Figure 6.15 shows the result of these simulations. In panel A, there are depicted the waveforms of the model simulation with temperature variations up to 5°C but canceling the temperature dependency in one channel at a time (i) and describing the dependency of only one channel at a time (ii). In panel B there is a barchart with the metric characterization for each case

(with and without temperature dependency) including also the experimental change reference in the dark bars. Panel A.i) shows how the general spike waveform shape was preserved in the range of the tested temperature variations when individually excluding low potassium and calcium currents – I_A and I_{HVA} and I_{LVA} , respectively– we were able to simulate the same range as in Fig. 6.14 of $\Delta T = 0 - 5^{\circ}\text{C}$. However, when excluding the temperature dependency of I_{NaT} , the model could not generate action potentials when raising the temperature for the other channels above $\Delta T = 2^{\circ}\text{C}$, which suggests that I_{NaT} intervention during the temperature modulation is relevant for the action potential generation. This channel presented a non-linear relation between the amplitude and the temperature. It is important also to note that suppression of the temperature dependency in I_{HVA} in Fig. 6.15Ai) resulted in a large change in the amplitude (20 mV decrease). This calcium current is needed to preserve the amplitude value while the slopes and duration values change during the temperature increase. The last waveform in that row, I_D , displayed a large change in the waveform shape, modifying the duration along with the depolarization currents and thus breaking down the spike. This change corresponds to a strong role in the generation of the action potential for this channel. In the contrary case, in Figure 6.15Aii) we observe that the channels with the strongest effect in the model are I_{NaT} , I_{HVA} and I_{NaP} , since their independent change of temperature produced a notable change in the waveform. Also in opposite to the previous case with temperature dependency, now it is I_D the channel that when it is the only one with temperature dependency, there was no spiking activity, and now I_{NaP} displays a large change comparable to the one occurring before with I_D . In Panel B, we can observe for both cases that no candidate alone could reproduce the observed experimental laser modulation but some channels have a more direct relation to the temperature change such as I_{LVA} for the repolarization or I_D channel, crucial for the spike generation waveform.

Exploring the waveform change during temperature variation showed that the most similar change to the experimental laser modulation was reached in the models with the temperature dependency description in all parameters. We showed that, for most currents as the temperature increases, the experimentally observed modulation relations were maintained, changing in duration and repolarization slope, with a larger change in repolarization slope and a mild change in amplitude. This is also supported by excluding temperature dependency from isolated ion channels and proposing temperature dependency for one channel at a time. Furthermore, it is in agreement with the results of the modeling sweeping the parameter space for distinct candidates without a specific description of the temperature (see Sec. 6.5), which showed that no modulation of an individual candidate but a combination of them can explain the experimental quantification.

6.6 Activity-dependent stimulation to assess the laser effect at distinct stages of the spike dynamics

So far we have shown how sustained CW-NIR laser affects neural activity by modifying the dynamics of spike generation. In the previous section 6.5 we used a conductance-based model to theoretically assess the spike evolution and the different candidates involved in the modulation of the action potential generation (i.e., ionic channels and capacitance). To address this effect in an experimental setting is a complex task. Usually, it is accomplished using chemicals to block or open specific channels (Liang et al., 2009). This might not be a generalizable method in different systems and individuals, and it restricts the channel study to a system with a detailed description of the specific neuron being recorded. To further explore the effect from the perspective of neuronal sequential dynamics, we chose instead to assess the spike generation dynamics at different stages, which implies modifying the activity of several channels at a time in a precise timing relative to the spike generation dynamics. This task is only experimentally feasible with an activity-dependent stimulation protocol.

In infrared stimulation literature, the most spread technique has been pulsed illumination which stimulates at a fixed frequency. Although this approach has been effective in some tasks such as eliciting neural activity, it has limited possibilities in the context of precision and adaptability. Thus, with the activity-dependent protocol proposed here, we also provide an open-access alternative to the widely-used fixed-frequency pulsed laser stimulation protocols, which usually depend on a specific combination of restrictions from manufacturers, controllers, and diode laser availability. In addition, a closed-loop approach provides further means to deal with the history-dependent nature of neural dynamics and its partial observability (Varona et al., 2016).

In this section we present a new protocol for closed-loop stimulation, we first validate the hypothesis in the CGC-model, by modifying some channels conductance only during depolarization or repolarization phase, and then test the protocol in a experimental environment, controlling the laser illumination by a mechanical shutter.

6.6.1 Model simulation of activity-dependent stimulation

From the experience of the sustained CW-NIR laser stimulation experiments, a change in the waveform shape when the effect is delivered at certain phases of the action potential should be visible. We addressed this activity-dependent simulation first in a computational approach. We simulated the effect on a CGC-model neuron modulating two of the channels where the effect on the neurons was larger $-g_D$ and g_{HVA} . This way, only during a certain time interval, the conductance in those channels

was modified to the value replicating the "maximum effect" in during the laser stimulation.

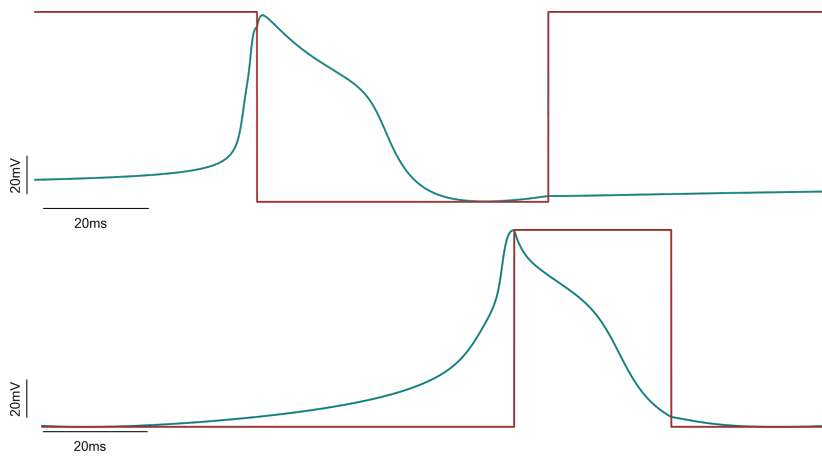


Figure 6.16: Simulation of the effect of CW-NIR laser in the CGC-model. Stimulating only during the depolarization or only during repolarization phases for first and second rows respectively.

Figure 6.17 shows the result of this simulation. We observed that the effect is larger when the stimulation is only in the repolarization slope, whereas while the effect is during the depolarization phase, the effect is only visible in the depolarization slope. Also the effect specifically during the "sustained" laser is stronger than the case of the "illumination" during the depolarization, but when the stimulus is only during the repolarization, the change in this slope is larger than in the sustained case.

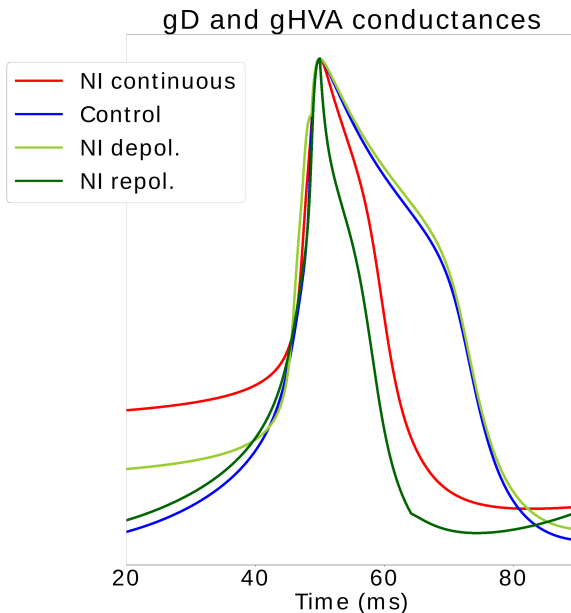


Figure 6.17: Results in the spike waveform for the simulation of the effect of CW-NIR laser in the CGC-model. Stimulating only during the depolarization (light green trace) or repolarization (dark green trace) phases and simulating a constant change value (red trace).

This suggests a localized delivery of the stimulus not only in space but also in time, affecting Note that this first simulation has limit in terms of the results we can obtain experimentally, since here,

for example, the effect was maximum from the first instant, but we saw in the previous section that the peak of the temperature takes a few seconds to be reached. This model could be benefit of more realistic laser delivery and also could be also implemented following the temperature description from CGC.

6.6.2 Experimental activity-dependent stimulation

Following our hypothesis tested in the model simulations of a possible change in the modulation, we designed the experimental protocol to stimulate in real-time the neurons in a closed-loop approach. We propose a closed-loop stimulation protocol where we can differentiate between the phases of the action potential and illuminate the neurons only at certain intervals of the spike generation dynamics. In this protocol, the laser illumination was controlled by a mechanical shutter triggered by the prediction of events in the voltage signal. A real-time software system ran the prediction algorithm and triggered the illumination for short periods of time at different phases of the spike generation when distinct channels were active (see Sec. 6.2.2 and Fig. 6.2). The prediction of the events was computed by two algorithms, one based on a voltage threshold updated at each spike peak occurrence and a second one that calculated the voltage area from the hyperpolarization (minimum) to the next hyperpolarization. Based on this prediction the illumination was triggered at the specified time before the spike occurrence (see Sec. 6.2.2 for details in these algorithms). The implementation of these algorithms is available as a module for the real-time open-source system RTXI (Patel et al., 2017) in https://github.com/GNB-UAM/spike_predictor.

Figure 6.18 shows the outcome of the application of this closed-loop protocol, with a stimulation interval lasting 58 ms. The time line in the figure represents the offset of the illumination, i.e., the time that corresponds to the end of an illumination interval to the peak of the action potential (see an illustration exemplifying the illumination offset in Fig. 6.3). The offsets were in the range from 60 ms before the action potential peak up to 80 ms after its occurrence (this wide range is required because of the natural slow dynamics of *Lymnaea stagnalis*'s neurons). Each row in the figure represents the change in relation to the mean of the respective control trials for every illumination range. The change is represented for the three metrics in which we observed modulation during sustained illumination –duration, repolarization and depolarization slopes, respectively–. The different stimulation intervals are grouped by the time offset from the illumination to the peak of the action potential. The spike shown in the figure is plotted as a reference of the phase of the action potential in which the illumination finished. Recovery and sustained laser references are also represented at the left and right of each row, in green and red, respectively. For the three metrics here displayed, we can see how as

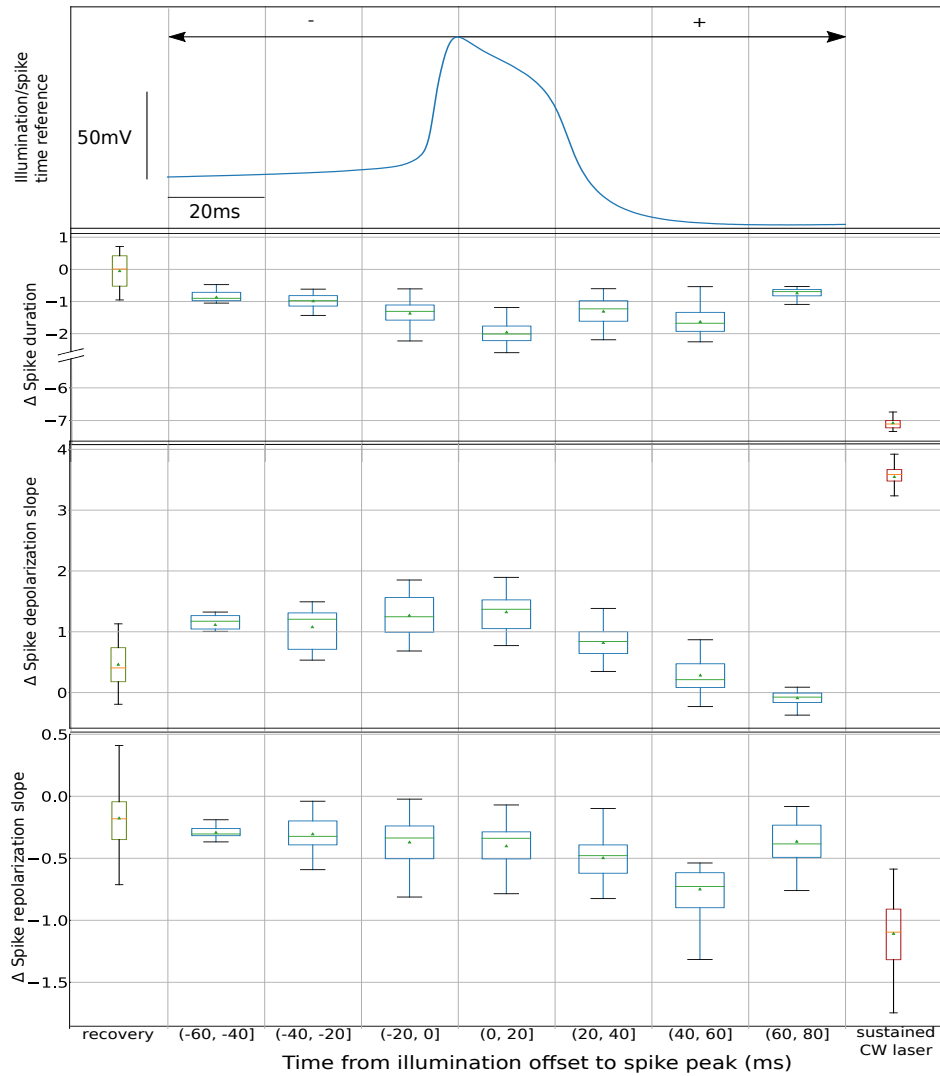


Figure 6.18: Study of the laser effect at different stages of the spike waveform with an activity-dependent stimulation protocol. The panels quantify the change induced by the laser stimulation at distinct illumination offsets, –time intervals from the end of the illumination to the peak of the spike–. Top panel shows a spike waveform from the experiment as a time reference for the offset –time 0 corresponds to the spike peak. Box-plots represent the difference of each metric with respect to the control. All illumination intervals, pictured in the blue boxes, had the same duration of 58 ms and spikes were grouped by the illumination offset. Recovery and continuous laser reference are also shown in green and red boxes at left and right in the figure, respectively. The spike metrics selected here were duration, depolarization and repolarization slopes, –second, third and fourth rows, respectively.

the illumination offset got closer to the spike, the change was larger, and then recovered as the illumination interval covered less the action potential, resulting in an arch shape trend. Although this trend is visible for the three parameters characterized, it is manifested to a different degree in each of them. Note also that there was a temporal shift of the laser effect depending on the instant of stimulation. The maximum change value and the initialization of the recovery was different for the depolarization

and for the repolarization. The effect on each of these metrics directly depended on the spike phase when the laser was illuminating the neuron. Thus, this variation of the laser effect points to a distinct modulation on each channel. The magnitude of the change under the sustained laser stimulation was larger than that observed at any of the phases addressed with the activity-dependent protocol. This may be caused by a heating delay during the stimulation, although there was no difference between the first and last spike in the sustained laser, the opening time of the laser shutter might have been smaller than the heating time necessary for the neuron to reach the maximum effect.

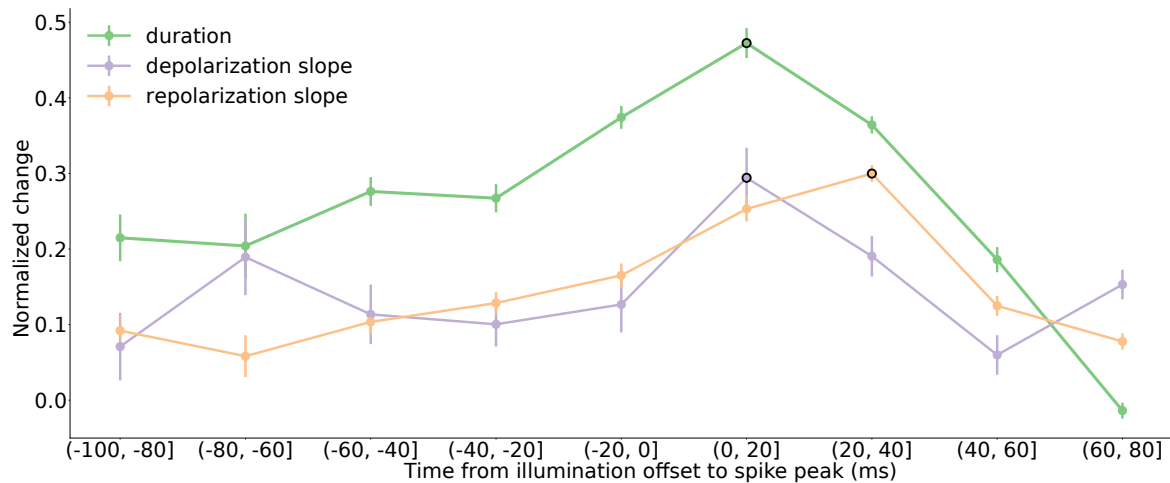


Figure 6.19: Normalized change for grouped values of spike duration, depolarization and repolarization slopes at distinct illumination offsets in the activity-dependent stimulation protocol. Each value in each group was normalized to the mean of its corresponding day controls as minimum value and the mean of the continuous laser recordings for each day as the maximum value. The maximum value for each metric is marked by a black circle.

Figure 6.19 agglutinates the results from 5 different closed-loop experiments, all of them normalized to the mean of the control and sustained laser references for each day, as minimum and maximum values, respectively. The arch trend is maintained. Again, note that the maximum effect for each spike metric occurs at a different stage. For the depolarization, the maximum change was found at the range of -20 to 0 ms, which corresponds to a stimulation during the whole depolarization. A fast rise when the illumination ceased right after the spike can be seen (i.e (0-20] range), since it corresponded to a stimulation during the depolarization and repolarization. In the repolarization, this trend was slightly delayed, reaching the maximum difference from the control at (20-40]. Such changes were also reproduced in the duration. This points to a modulatory effect of the laser depending on the stimulation instant. Previous to -20 ms, the laser was illuminating the neuron while all ionic channels were starting to activate, specially those involved in the process of the depolarization. However, those channels involved in the repolarization and hyperpolarization were also active earlier than the peak. This is why we can see a difference in all three metrics even at the early ranges of the action potential

generation (e.g. -80 ms).

Using the activity-dependent protocol we were able to assess the neural activity at different stages of its dynamics in a controlled way. The results from these experiments showed that it is possible to modify the action potential generation in a temporally precise manner and that the effect of the CW-NIR laser illumination is dependent on the instant of the stimulation. This sets the basis for assessing the biophysical sources of the effect impacting distinct channels without modifying the system condition. Also, it is a proof of concept demonstrating the possibility of developing laser stimulation protocols driven by specific neural activity events in an accessible and freely available real-time tool.

6.7 Discussion

6.7.1 Singularity of the sustained and activity-dependent CW-NIR stimulation on neural dynamics

Advantages of infrared laser neuromodulation beyond its non-invasive nature include its relative simplicity regarding stimulation protocol design, good penetration depth and the possibility to implement highly selective spatio-temporal stimulation delivery. The effectiveness of future applications will depend on a clear understanding of the mechanisms of the neural dynamics modulation.

Most previous studies used protocols involving high-frequency pulsed lasers under the assumption that continuous-wave laser stimulation paradigms do not provide significant activation or neuromodulation (Wells et al., 2005a; Wells et al., 2005b; Goyal et al., 2012; Cayce et al., 2014; Chernov & Roe, 2014; Pan et al., 2023). Their focus involved heating the neurons to elicit spiking activity. The laser wavelengths used were mostly in the range of 1800nm, close to a water absorption band. Here we explored a different approach, using a 830nm CW-NIR laser in sustained and activity-dependent triggered stimulation instead of pulsed illumination at fixed frequency. This setup has a promising future for clinical applications for long-term stimulation and patient-based treatments.

We assessed the action of sustained and activity-dependent CW-NIR stimulation to unveil the biophysical sources of the observed modulation on neuronal dynamics. We combined experimental and theoretical methods to analyze this effect. First, we quantified the change on action potential waveform dynamics and on the inter-spike intervals by comparing triplets of long intracellular recordings of control, laser stimulation and recovery. We found that sustained exposure to 830nm CW laser effectively modulated the spike waveform in a reversible manner. We showed this modulation in two

different neuron types, illustrating the generalization of the effect. We observed a stronger effect on duration and repolarization, followed by a less strong change in the depolarization slope and a minimal change on amplitude. The neuron dynamics were restored after stimulation. It is important to highlight that here we presented modulation of tonic spontaneous activity, not elicitation of spiking activity as in most previous studies (Wells et al., 2005b; Izzo et al., 2007; Shapiro et al., 2012; Rabbitt et al., 2016). We also showed a tendency to increase the spiking activity under sustained stimulation, not limited to a specific time/intensity configuration of laser pulses as it is most frequently done in the literature (Izzo et al., 2007; Goyal et al., 2012; Beier et al., 2014; Pan et al., 2023). Although there are previous studies discussing the inhibitory ability of infrared-laser illumination (Duke et al., 2013; Lothet et al., 2017; Ganguly et al., 2019; Begeng et al., 2022), we did not find evidence of any direct CW-NIR inhibitory effect. Note that the origin of tonic spiking was affected by the intrinsic properties of the cell and the synaptic inputs within the circuit, e.g., the illuminated neuron might be triggering an inhibitory or excitatory feedback from other neurons, complicating the analysis. This explains the lack of excitation in a subpopulation in Fig. 6.8. Spontaneous neural activity and the nature of the living preparation used may naturally tend to decrease the firing rate.

Our preliminary work on the action of different wavelengths on single neuron dynamics, in particular affecting the action potential amplitude, points to novel directions to study the biophysical source/s of the CW-NIR modulation. The preliminary study of the effect on circuit dynamics also opens new opportunities for multiple research goals including plasticity studies.

6.7.2 Biophysical explanation of the CW-NIR modulation through modeling and activity-dependent stimulation

The results of sustained CW-NIR illumination alone cannot discard previously suggested mechanisms such as cytochrome oxidase (Wang et al., 2017; Saucedo et al., 2021) or calcium release from internal storage (Lumbreras et al., 2014). The fact that the illumination directly affects the spike waveform but not always translates into an increased firing rate may indicate that there is more than a single mechanism involved. Moreover, our analysis of sustained laser stimulation does not point to a slow change such as the one expected with the liberation of Ca^{2+} caused by a mitochondrial modulation (Dittami et al., 2011; Lumbreras et al., 2014), since we observed a minimal delay between the illumination onset and the modulatory effect, and the illumination cessation and the recovery. The short exposure in the activity-dependent experiment with quick response time also points to a short timescale effect, such as a direct effect on the ionic channels.

Conductance-based models allowed us to identify the most compatible biophysical explanation to

the CW-NIR modulation. We evaluated the capacitance and distinct ionic channels in the parameter space of three conductance-based models, which would be highly costly experimentally. We concluded that all candidates explored contributed to partial reproduction of the waveform modulation but none was sufficient to explain the full observed effect. Capacitance is one of the most discussed candidates (Shapiro et al., 2012; Cayce et al., 2014; Thompson et al., 2015; Plaksin et al., 2018). However, in our modeling study, capacitance alone was not able to reproduce the modulation. Although the isolated modification of any channel resulted in a limited explanation of the CW-NIR change, late activation channels such as potassium –preserving the depolarization-repolarization change relation– or high-activated calcium –necessary for shoulder shape modulation– seem to play a key role reproducing the observed effect.

Temperature-dependent simulations validated that the best explanation for the sustained laser action is a combined modulation of channels, reproducing the observed change for amplitude, duration and slopes. This supports previous studies' hypothesis that the photo-thermal interaction is key in the NIR laser effect (Wells et al., 2005b; Albert et al., 2012; Li et al., 2013; Rabbitt et al., 2016; Barrett et al., 2018; Brown et al., 2020; Cury et al., 2021). We selectively excluded one channel from the temperature dependency at a time in the CGC-model, which cannot be performed experimentally. We found I_D and I_{NaP} channels to be critical for the activity modulation, radically changing the waveform when altering temperature dependency. Also, canceling the temperature dependency of I_{HVA} largely changed the amplitude, indicating its importance in preserving the observed amplitude-repolarization relation during the modulation.

Finally, a closed-loop protocol allowed altering the action potential at distinct generation phases. We presented a new open-source protocol for spike prediction to stimulate at precise times around the occurrence of the action potentials. The outcome of the CW-NIR effect at distinct time intervals in relation to the timing of the spike's peak highlighted the importance of the stimulus delivery time. By changing the illumination instant, we shifted the effect on the waveform shape, getting different maximum metric changes at different stages of the action potential generation.

These changes in the waveform open a discussion about the biophysical source of this effect. With short closed-loop illumination intervals ($< 60\text{ms}$), we observed a controlled modulation of neural activity smaller than the effect during the sustained laser illumination. In the open-pipette estimation, the maximum change for the steady state temperature value ($1\text{-}2^\circ\text{C}$) was reached after 1s and the change after 50ms was only of 0.1°C . This estimation was performed on the preparation's solution, and our laser wavelength is far from the intense water absorption bands. So temperature change could be higher in the neuronal membrane, as the specific heat capacity of the water is $\sim 30\%$ larger

than the estimated on the membrane (Thompson et al., 2012). This would result in a faster temperature increase under heat-inducing stimulation. Also, in the model, we observed a change similar to the experimental results with $\Delta T >= 5^{\circ}\text{C}$. Thus, the modulation might not be caused by simply heating the surrounding water. In the sustained stimulation, there might be additional modulation sources such as an effect on the mitochondria as it has been discussed in previous studies (Dittami et al., 2011; Lumbreiras et al., 2014; Saucedo et al., 2021), which we cannot discard as adding to the modulation of ionic channels. However, the effect observed during the activity-dependent stimulation is unlikely to have other than fast sources such as ionic-channels. A rigorous characterization of the timescale of the temperature changes induced by the CW-NIR and the associated instantaneous voltage dynamics could provide further insight on the fast and slow biophysical mechanisms underlying the waveform modulation. This is particularly relevant for the design of fast activity-dependent protocols to produce the observed effect safely with minimal biophysical perturbation. An accurate characterization of the relation between temperature and neuronal dynamics under CW-NIR stimulation requires novel highly precise protocols to measure the membrane temperature and fast non-periodic electro-optical shutters controlled by real-time software technology. This could be performed using nanothermometry by estimating the temperature change in the membrane by the emission on nanoparticles in the tissue (Hamraoui et al., 2023).

6.7.3 Applications for research and clinical use

The open-source approach described in this thesis can be generalized for any animal and preparation. In addition, our protocol leaves plenty of possibilities for other closed-loop stimulation methodologies, including clinical interventions. We provided an open-access repository with the code to reuse our protocols and the module for RTXI, which can be used with any control hardware including fast electro-optical shutters.

Regarding the non-invasive nature of the CW-NIR laser effect, we could not observe any damage to the cells linked to the stimulation in our experiments. We can hypothesize that stimulation from a laser with higher power could be tolerated by neurons. The recovery of the neural dynamics after illumination does not mean that the CW-NIR laser stimulation cannot be employed to address laser-driven plasticity in protocols designed for this goal. We have shown that sustained CW-NIR laser effectively accelerates neural dynamics in single neurons affecting a combination of biophysical mechanisms. Also, our results indicate that novel research and clinical applications of the excitability increase of laser stimulation must rely on a careful selection of the stimulus parameters and the timing of the illumination. In this context, the results of our pioneer activity-dependent infrared laser

stimulation provide a novel approach to adapt the modulation of neural dynamics to specific applications, particularly in the field of personalized treatments including stimulation-driven plasticity.

CHAPTER 7

Conclusion and Discussion

During this work, we have explored with distinct complementary experimental and computational approaches the sequentiality of neuronal dynamics: from the sequential activation of ionic channels in the generation of action potentials to the cycle-by-cycle dynamics in CPG circuits. Here is a summary of the main results presented in this thesis (see also Fig. 7.1):

- Part 1: Sequential dynamical invariants.
 - We have illustrated the importance of the study of neuronal sequential dynamics at different description levels.
 - We have hinted the universality of sequential dynamical invariants by showing their presence in the feeding CPG of *Lymnaea stagnalis* both in experimental and modeling data, i.e., in a different animal model from the one used in the work that reported their discovery.
 - We have shown that dynamical invariants can be found in models when the circuit displays enough cycle-by-cycle variability, which can be induced by an external stimulus.
 - The models that simulated the variability under the stimulation of specific neurons predicted that the dynamical invariants change depending on the neuron stimulated. This prediction was validated experimentally.
 - Dynamical invariants are indicators of the functional distribution of variability in the CPG.
 - Neural intrinsic variability in models is usually limited but crucial to study the sequential variability in neural dynamics.
 - It is possible to study the functional role of sequential dynamical invariants by using the

robust linear relations of neural sequence intervals to control the motor coordination of a hybrot.

- Part 2: CW-NIR laser illumination as an effective modulatory technique.
 - Sustained CW-NIR laser illumination asymmetrically accelerates action potential dynamics and the spiking rate on single neurons.
 - The preliminary results in electrically coupled neurons (a minimal circuit) show the potential of CW-NIR to modulate circuit dynamics.
 - Modifying the wavelengths of the CW-NIR laser can evoke different changes in action potential metrics. The results illustrate the importance of selecting wavelength, power and duration for a specific modulation goal.
 - A model study of the effect of CW-NIR showed that no biophysical candidate alone could fully reproduce the observed modulation, and that the global modulation through temperature change by the simulation was the closest approximation to explain it.
 - The closed-loop illumination protocol unveiled the CW-NIR laser effect at different phases of the neuron dynamics, showing a different modulation depending on the instant of illumination.
 - The code of this closed-loop protocol was published in open-access and can be easily generalized for other neuron types and research contexts.

In chapter 5, we analyzed the sequential dynamical invariants in a CPG circuit. The goal was to prove the hypothesis presented in Elices et al. (2019) that the strong linear relationships found between specific cycle-by-cycle intervals in the pyloric CPG of the *Carcinus maenas* were not a unique feature of that particular CPG, but a general phenomenon for effective autonomous motor coordination. Thus, the first result shown in chapter 5 was **the generalization of sequential dynamical invariants**, found also in the feeding CPG of *Lymnaea stagnalis*. We proved this by showing their presence not only in a detailed model of the circuit, but also in experimental recordings of the CPG. In the model, we quantified the variability induced by a ramp-current in specific neurons. We explored the variability and the correlations between period and the different intervals in the cycle showing the presence of sequential dynamical invariants. **The variability distribution and, consequently, the sequential dynamical invariants change as the neuron stimulated in the model simulation changes.** This highlights the importance of the balance between robustness and flexibility of the sequences for motor coordination through the relation between the neurons in the circuit dynamics. The restriction of

variability in specific intervals allows an autonomous cycle-by-cycle adaptation. Thus, the computational model configuration and the resulting dynamics must reach a minimum degree of variability in the simulations for the emergence of sequential dynamical invariants. We supported these results by analyzing different recordings from representative neurons in the buccal ganglion. We discussed in that chapter the difficulties defining the three phases of the feeding CPG in comparison with the pyloric CPG. After identifying the three phases of the circuit based on a combination of interneuron and motoneuron signals, we analyzed the variability and relations between cycle-by-cycle intervals for spontaneous activity cases and current stimulation driven activity in electrophysiological recordings. We quantified the interval variability and their relationships in examples of spontaneous activity and **found sequential dynamical invariants in this spontaneous neural activity**. We also analyzed different cases of stimulation: first SO driven stimulation, which reproduced the results observed in the model, **showing a change in the variability distribution when the rhythm is modulated by SO**. From this premise that the rhythm is different as the source varies, we analyzed cases where the rhythm was modulated by CV1a neuron stimulation and by MLN nerve stimulation. In both cases, **the interval variability was distributed between N1 and N3 phases, with N1 being highly correlated to the period**.

Based on these experimental and theoretical results, we also presented in chapter 5 a study on neural variability. In the modeling side, **we analyzed the importance of variability in the study of neuronal dynamics and the limitation of classical models to reproduce the intrinsic functional variability of neurons**. We compared different examples of neural activity in living and modeled neurons and their variability, **discussing the model limitations in reproducing the experimentally observed variability**. Regarding the experimental approach, we explored the possibility of translating the sequential intervals into effective robot movement. This is important in order to explain the functional meaning of the strong relationships that we observed in specific time-intervals, which as we discussed is related to the context and the source of the rhythm. In this first prototype, **we demonstrated that it is possible to achieve an effective autonomous coordination in the locomotion of a robot by maintaining the strong cycle-by-cycle linear relations of sequential dynamical invariants**.

In the study of the sequentiality in CPGs, we saw the importance of using effective tools to alter the spontaneous neural activity noninvasively. In chapter 6, **we explored in detail the CW-NIR laser as a stimulation technique experimentally, theoretically and in novel activity-dependent protocols**. First, we showed the effect of illuminating single cells and how **CW-NIR sustained illumination asymmetrically accelerates action potential dynamics and increases the firing rate**

on single neurons. We tested the effect of the laser stimulation in a minimal circuit by illuminating electrically coupled neurons, showing that the main modulation was in the illuminated neuron, slightly modifying the coupled neuron that did not receive the laser stimulation. We also showed preliminary results of the wavelength-effect relation, analyzing the laser effect in spike duration, amplitude and slopes with different laser wavelengths and powers, showing a modulation of the amplitude as the laser wavelength and power increases, which is not present at low-wavelengths values. The experimentally observed effect in the waveform under sustained laser stimulation (830nm) was dissected through model simulations, exploring the possible candidates to explain it: ionic channels and capacitance, in conductance-based models, with and without temperature dependence description, showing that no candidate alone could fully reproduce the observed modulation and that the global modulation through temperature change in the simulation was the closest approximation to it. Finally, we presented a closed-loop protocol to alter the action potential at specific sequential stages of its generation, which can be generalized for distinct neurons and nervous systems. With this stimulation protocol we unveiled the CW-NIR laser effect at different phases of the neuron dynamics, identifying different spike waveform changes depending on the time instant of the illumination. We also supported these results with a model simulation, tuning ionic channels only at depolarization and repolarization phases, showing the enhancement of the effect as the stimulation time changes.

The study of temporal restrictions in the sequential activation of motor circuits can have strong implications in neurorhabilitation and in the understanding of brain processing for motor activation. This can unveil the key aspects of the relation between neural variability, robust sequentiality and flexibility in motor control that is observed in living systems, such as the one performed by CPGs. For this task, it is necessary to expand the study of sequential neural variability in different animals but also to link sequential dynamical invariants to their role in motor output, relating their activation to different behavioral contexts. These restrictions can be indicators of the state of the system and can be associated to the importance of modulating each phase at the current moment, e.g., protraction phase in the presence of food is crucial to achieve the food ingestion as in the MLN stimulation example, while its role when the circuit is active in the absence of food it is not that important, so the variability can be distributed differently, as it was the case of the spontaneous activity with a high-correlation of N3 to the period. In this direction, it is important to improve intrinsic variability in model simulations by an extended description of chaotic dynamics of neural activity and its expansion to more complex circuits and systems. The study of the time-interval restrictions in living circuits that produce and ensure the presence of sequential dynamical invariants can also be translated to the design of robots with the robust motor coordination observed in CPGs. These examples will be of high interest for

applications in neurotechnology and autonomous robotics design.

CW-NIR laser stimulation can help to further explore sequential neural dynamics through its effective modulation with high temporal and spatial accuracy. The study of this novel neuromodulatory technique might have strong implications for both research and clinical applications by its noninvasive nature. Laser stimulation has been gaining ground in the field of optical stimulation, often implemented as long-wavelength pulsed laser stimulation. It is important to validate different stimulation options such as the sustained continuous-wave and activity-dependent stimulation, of high interest for personalized treatments. The protocol presented in this work might be enhanced with a larger temporal precision, down to the nanosecond scale. This will be relevant to extrapolate it to different systems, regardless of their neural activation time scale, but also to dissect precisely the ionic channel activation dynamics. Furthermore, a in-depth characterization of the laser illumination and its safety range of activation will be of great importance for disseminating future clinical applications. In this work, we showed a strong and reversible effect that did not damage the neurons illuminated, which indicates that the power used could be increased. A precise characterization of the power tolerated by the neurons would set the safety ranges of its application. A preliminary study of the wavelength-effect relation showed the importance not only of the power, but also that of the laser wavelength in terms of the effect produced, so the analysis of the roll of the wavelength might expand this range of applications and also might help distinguishing between different action mechanisms such as photo-electrical, photo-thermal, etc. A future line of study would also assess the effect of CW-NIR laser in circuits, based on the preliminary results shown here. It should be possible to modulate circuit dynamics by the stimulation of one or multiple neurons. This could be studied in CPG circuits, as in the case of the feeding CPG, by illuminating neurons that have an activation/modulatory role in the circuit, such as the CGC neuron in the cerebral ganglia, away from the buccal ganglia but connected to it. Finally, as discussed in this work and laser neurotechnology literature, a photo-thermal effect is one of the main actuators behind the neuronal laser stimulation, however with the current tools and techniques it is not possible to have a detailed description of the change of temperature in the cell. In this line, although the preliminary results were not included in this work, we have explored the possibility of a more precise estimation of the temperature change using silver nanoparticles. These particles could be directly delivered on the membrane, reducing the area of temperature change measurement, and the variation of temperature could be estimated by their irradiation. This precise measurement of the temperature could also help to improve the model simulations, and their predictive power. Also, exploring the fast change observed in the activity-dependent protocol with a small change in temperature according to the pipette estimation, can help to understand the source of the effect.

CHAPTER 7: CONCLUSION AND DISCUSSION

In this thesis, we have illustrated the potential of a multidisciplinary approach in the study of neural sequential dynamics and of effective techniques to modulate it. By combining experimental and computational approaches, we could provide an extended analysis of sequential dynamics in CPG circuits and in the action potential generation, and also explore in detail the effect of a novel neurotechnology, as the CW-NIR laser on it. The combination of experimental and computational approaches showed the wide range of possibilities that real-time closed-loop protocols provide for effective sequential modulation. The study of neural sequences at multiple spatial and temporal scales can provide novel insights to relate neural dynamics and behavior. Novel neurotechnologies can contribute to identifying and exploiting the sequential nature of neural information processing in multiple nervous systems. The results discussed in this thesis in the context of neural sequences can also have strong implications in the field of neurorhabilitation, robotics, and artificial intelligence derived from the understanding of sequential dynamical invariants.

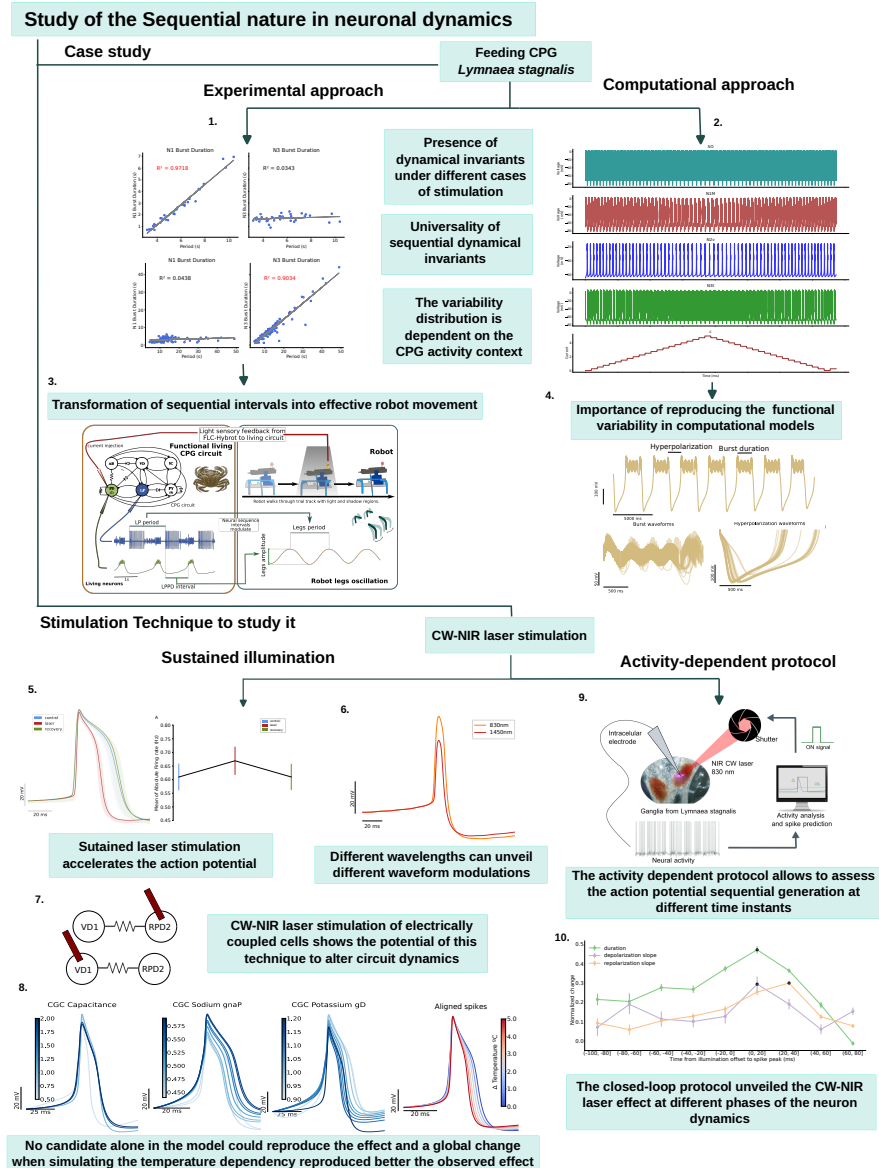


Figure 7.1: Schematic summary of the results presented in this work. In the feeding CPG of *Lymnaea stagnalis*, we explored in (1) experimental and (2) computational data the presence of dynamical invariants (Secs. 5.4 and 5.3), showing strong linear relations in sequence intervals and associating them to the possible functional role of this dynamical phenomenon. The experimental results were complemented by exploring the translation of (3) cycle-by-cycle invariant intervals into effective robot movement maintaining these strong linear relations (Sec. 5.6). We also showed the (4) importance of reproducing the functional variability in computational models (Sec. 5.5). As a way to modulate neural dynamics, we characterized the effect of the CW-NIR laser in single neurons in sustained and activity dependent illumination protocols. We showed that (5) the spike waveform is modified during the laser illumination, as well as the firing rate (Sec. 6.4), and discussed the effect at (6) different wavelengths (Sec. 6.4.4). We showed also (7) preliminary results in the stimulation of a minimal circuit (Sec. 6.4.3). The computational model analysis (8) revealed the combination of candidates to reproduce the effect and the importance of the role of temperature (Sec. 6.5). (9) The activity-dependent protocol (10) allowed to assess the laser effect at different phases of the action potential generation (Sec. 6.6).

CHAPTER 7: CONCLUSION AND DISCUSSION

CHAPTER 8

Conclusiones y Discusión

A lo largo de este trabajo, hemos explorado con distintos enfoques experimentales y computacionales complementarios la naturaleza secuencial de la dinámica neuronal: desde la activación secuencial de canales iónicos en la generación de potenciales de acción, hasta la dinámica ciclo a ciclo en circuitos CPG. A continuación, se presenta un resumen de los principales resultados de esta tesis:

- Parte 1: Invariantes dinámicos secuenciales.
 - Ilustramos la importancia de estudiar dinámicas neuronales secuenciales en diferentes niveles de descripción.
 - Sugerimos la universalidad de invariantes dinámicos secuenciales al demostrar su presencia en el CPG alimentario de *Lymnaea stagnalis* en datos experimentales y en simulaciones computacionales, en un modelo animal diferente al utilizado en el trabajo que reportó su descubrimiento.
 - Mostramos que los invariantes dinámicos pueden identificarse en modelos cuando el circuito presenta suficiente variabilidad ciclo a ciclo, aunque sea inducida por estímulos externos.
 - Los modelos que generaban variabilidad mediante la estimulación neuronal predijeron que los invariantes cambian según la neurona estimulada. Dicha predicción se comprobó experimentalmente.
 - Los invariantes dinámicos sirven como indicadores de la distribución de variabilidad funcional en el CPG.
 - La variabilidad neuronal intrínseca en los modelos comúnmente utilizados es limitada comparada con la observada experimentalmente, sin embargo, es esencial para estudiar la dinámica neuronal secuencial.

- Demostramos el papel funcional de los invariantes dinámicos secuenciales mediante el uso de relaciones lineales robustas entre intervalos temporales de la actividad neuronal para controlar la coordinación motora en un robot biohíbrido.
- Parte 2: Iluminación con láser CW-NIR como técnica de modulación neuronal efectiva.
 - La iluminación sostenida con láser CW-NIR acelera asimétricamente la dinámica de los potenciales de acción y aumenta la frecuencia de disparo en neuronas individuales.
 - Los resultados preliminares en neuronas eléctricamente acopladas (como circuito mínimo) muestran el potencial del láser CW-NIR para modular la dinámica en circuitos.
 - Mostramos que distintas longitudes de onda del láser CW-NIR pueden evocar diferentes cambios en las formas de onda de los potenciales de acción, resaltando la importancia de seleccionar la longitud de onda, la potencia y la duración para objetivos específicos de modulación neuronal.
 - El estudio computacional del efecto del láser CW-NIR reveló que ningún único candidato biofísico puede replicar completamente la modulación observada y la explicación más plausible es la modulación global a través del cambio de la temperatura.
 - Con el protocolo de ciclo cerrado, mostramos el efecto del láser CW-NIR en varias fases de la dinámica neuronal de la generación del potencial de acción, demostrando cambios en la modulación neuronal según el momento de la iluminación.
 - El protocolo de ciclo cerrado disponible en código abierto puede generalizarse fácilmente para otro tipo de neuronas y contextos de investigación.

En el capítulo 5, analizamos los invariantes dinámicos secuenciales en un circuito CPG. El objetivo fue demostrar la hipótesis presentada en Elices et al. (2019) de que las relaciones lineales robustas encontradas entre intervalos ciclo a ciclo en el CPG pilórico del *Carcinus maenas* no eran una característica específica de ese CPG en particular, sino un fenómeno general para la coordinación motora autónoma. El principal resultado del capítulo 5 fue mostrar **la generalización de la presencia de los invariantes dinámicos secuenciales**, ya que se encontraron no solo en un modelo detallado del circuito, sino también en registros experimentales del CPG alimentario de *Lymnaea stagnalis*. En el modelo, cuantificamos la variabilidad inducida por una corriente en forma de rampa en neuronas específicas. Exploramos la variabilidad y las correlaciones entre el período y los diferentes intervalos en el ciclo, mostrando la presencia de invariantes dinámicos secuenciales. Observamos que **la distribución de variabilidad y, por lo tanto, los invariantes dinámicos secuenciales cambian según la neurona estimulada en la simulación del modelo**. Esto resalta la importancia del balance

entre robustez y flexibilidad para la coordinación motora mediante la relación entre las neuronas en la dinámica del circuito, de modo que la variabilidad restringida permite una adaptación autónoma ciclo a ciclo. Por lo tanto, la configuración del modelo computacional y la dinámica resultante deben alcanzar un grado de variabilidad mínima en las simulaciones para garantizar la existencia de los invariantes dinámicos. Apoyamos estos resultados analizando diferentes registros de neuronas en el ganglio bucal. Discutimos en ese capítulo las dificultades para definir las tres fases del CPG alimentario en comparación con el CPG pilórico. Después de identificar las tres fases del circuito mediante la combinación de señales de interneuronas y motoneuronas, analizamos la variabilidad y las relaciones entre los intervalos ciclo a ciclo para casos de actividad espontánea y actividad inducida por estimulación eléctrica en neuronas individuales. Caracterizamos la variabilidad de intervalos y sus relaciones ciclo a ciclo en diferentes registros de actividad sin estímulo y **encontramos invariantes dinámicos secuenciales en la actividad neuronal espontánea**. También analizamos diferentes casos de estimulación, y reprodujimos los resultados predichos por el modelo, **mostrando un cambio en la distribución de variabilidad cuando el ritmo es modulado por SO**. A partir de la premisa de que el ritmo es diferente según varía su fuente de activación, analizamos casos donde el ritmo fue modulado por la estimulación de la neurona CV1a y por el nervio MLN. En ambos casos, **la variabilidad de los intervalos se distribuyó entre las fases N1 y N3**.

Motivados por estos resultados experimentales y teóricos, también presentamos en el capítulo 5 un estudio sobre la variabilidad neuronal. En los modelos, **analizamos la importancia de la variabilidad en la dinámica secuencial neuronal y las limitaciones de los modelos clásicos para reproducir la variabilidad funcional intrínseca de las neuronas**. Comparamos ejemplos de actividad en neuronas vivas y modeladas y su variabilidad, **analizando diferentes modelos y sus limitaciones**. En cuanto al enfoque experimental, exploramos la posibilidad de emplear los intervalos secuenciales de invariantes dinámicos para coordinar eficazmente la locomoción de un robot biohíbrido. Esto es importante para abordar el papel funcional de estas relaciones robustas que observamos en intervalos específicos de secuencias neuronales, que como discutimos, están influenciadas por el contexto y el origen del ritmo. En este primer prototipo, **demostramos que es posible lograr un movimiento efectivo del robot biohíbrido manteniendo estas relaciones lineales ciclo a ciclo**.

En el estudio de la secuencialidad en los CPGs, vimos la importancia de utilizar herramientas eficaces para alterar la actividad neuronal de forma no invasiva. En el capítulo 6, **exploramos en detalle el láser CW-NIR como técnica de estimulación de forma experimental, teórica y en protocolos dependientes de la actividad**. Primero, mostramos el efecto de iluminar células individuales y cómo la iluminación sostenida acelera asimétricamente la dinámica del potencial de acción y aumenta la

frecuencia de *spikes* en neuronas individuales. Probamos el efecto del láser en un circuito mínimo iluminando neuronas acopladas eléctricamente, mostrando que la principal modulación fue en la neurona iluminada, modificando ligeramente la neurona acoplada que no recibía la fuente de luz. También mostramos resultados preliminares de la relación efecto-longitud de onda, analizando la acción del láser en duración, amplitud y pendientes del potencial de acción con diferentes longitudes de onda y potencias, mostrando una modulación de la amplitud a medida que aumenta la longitud de onda y la potencia del láser que no se observa en valores de baja longitud de onda. El efecto observado experimentalmente en la forma de onda se disecó mediante simulaciones en modelos de conductancia, explorando los posibles candidatos para explicarlo: canales iónicos y capacitancia, con y sin descripción de dependencia de temperatura, mostrando que **ningún candidato por sí solo reproduce completamente la modulación observada y que la modulación global a través de la descripción del cambio de temperatura es la explicación más plausible**. Finalmente, presentamos un protocolo en ciclo cerrado para alterar el potencial de acción en distintas fases de su generación secuencial que puede generalizarse para distintos sujetos y neuronas. Con este protocolo de estimulación, caracterizamos el efecto del láser CW en diferentes fases de la dinámica neuronal, identificando diferentes cambios en la onda según el momento de iluminación. También respaldamos estos resultados con una simulación del modelo, ajustando algunos de los canales solo en las fases de despolarización y repolarización, mostrando el aumento del efecto a medida que cambia el tiempo de estimulación.

El estudio de las restricciones temporales en la activación secuencial de circuitos motores puede tener fuertes implicaciones en neurorrehabilitación y en la comprensión del procesamiento cerebral de la activación motora. Este análisis puede revelar aspectos clave de la relación entre la variabilidad neuronal, la secuencialidad robusta y la flexibilidad en el control motor que se observa en sistemas vivos, como en los CPG. En este contexto, es necesario ampliar el estudio de la variabilidad neuronal secuencial en diferentes animales, pero también relacionar los invariantes dinámicos secuenciales con su papel en la acción motora, asociando su activación en diferentes contextos. Estas restricciones pueden ser indicadores del estado del sistema y pueden asociarse a la importancia de modular cada fase en el momento actual, por ejemplo, la fase de protracción en presencia de alimentos es crucial para la ingesta, como en el ejemplo de estimulación MLN, mientras que su papel cuando el circuito está activo en ausencia de alimentos no es tan importante, por lo que la variabilidad puede distribuirse de manera diferente, como en el caso de la actividad espontánea con una alta correlación de N3 con el período. En esta dirección, es importante mejorar la variabilidad intrínseca del modelo con una descripción ampliada de la dinámica caótica de la actividad neuronal, y su expansión a circuitos y sistemas más complejos. El estudio de las restricciones entre intervalos de tiempo secuenciales

en circuitos vivos que producen y mantienen los invariantes dinámicos también puede trasladarse al diseño de robots que reproduzcan la robustez de la coordinación observada en los CPGs. Estos estudios son de gran interés para aplicaciones en neurotecnología y el diseño de robótica autónoma.

La estimulación láser CW-NIR puede ayudar a explorar más en detalle la dinámica neuronal secuencial mediante su modulación efectiva. El estudio de esta nueva técnica neuromoduladora puede tener fuertes implicaciones tanto para investigación como para aplicaciones clínicas debido a su naturaleza no invasiva. La estimulación láser ha ido ganando terreno en el campo de la estimulación óptica, a menudo implementada como estimulación con láseres pulsados de longitud de onda larga. Es importante validar diferentes opciones de estimulación como la estimulación sostenida del láser CW-NIR y la estimulación dependiente de la actividad, de gran interés para tratamientos personalizados. El protocolo presentado en este trabajo podría mejorarse con una mayor precisión temporal, llegando incluso a la capacidad de estimular en escala de nanosegundos. Esto permitirá extrapolarlo a diferentes sistemas, independientemente de su escala temporal de activación neuronal, y también para diseccionar con precisión la dinámica de activación de los canales iónicos. Además, una caracterización en detalle de la iluminación láser y su rango de seguridad de actuación será de gran importancia para el desarrollo de futuras aplicaciones clínicas. En este trabajo hemos mostrado un efecto notable y reversible que no dañó las neuronas iluminadas, lo que indica que la potencia utilizada podría aumentarse aún más. Una caracterización precisa de la potencia tolerada por las neuronas establecería los rangos de seguridad de su aplicación. El estudio preliminar de la relación efecto-longitud de onda mostró que no solo es importante la potencia, sino la longitud de onda del láser en términos del efecto observado, por lo que el análisis de la relación de la longitud de onda podría ampliar el rango de aplicaciones y ayudar a distinguir las causas del efecto entre otros posibles mecanismos como los fotoeléctricos o fototérmicos. Una línea de estudio futura también podría evaluar el efecto del láser CW-NIR en circuitos, según los resultados preliminares obtenidos, ya que debería ser posible modular la actividad de un circuito globalmente o mediante la estimulación de componentes individuales. Esto podría estudiarse en los circuitos CPG, como el caso del CPG alimentario de *L. stagnalis*, iluminando neuronas que tienen un papel activador/modulador en el circuito, como la neurona CGC en el ganglio cerebral, alejada del bucal pero conectada a él. Finalmente, como se discutió en este trabajo y en la literatura sobre neurotecnología láser, el efecto fototérmico es uno de los principales responsables de la modulación neuronal resultante, sin embargo, con las herramientas y técnicas actuales no es posible tener una descripción detallada del cambio de temperatura en la célula. Aunque los resultados preliminares no se han incluido en este trabajo, hemos explorado la posibilidad de una estimación más precisa del cambio de temperatura utilizando nanopartículas de plata. Estas partículas podrían alojarse directamente en la membrana, reduciendo el área de medición del cambio de tem-

peratura, y la variación de la temperatura podría estimarse a partir de su irradiación. Esta medición precisa de la temperatura también contribuiría a mejorar las simulaciones del modelo, con el dato específico del cambio de temperatura en las neuronas. También permitiría explorar el cambio rápido observado en el protocolo dependiente de la actividad que se produce con un pequeño cambio en la temperatura (según la estimación de la pipeta) y aportar información adicional para comprender la fuente del efecto.

En esta tesis hemos utilizado el potencial de una aproximación multidisciplinar en el estudio de la dinámica neuronal secuencial y de técnicas eficaces para modularla. Combinando metodologías experimentales y computacionales, hemos podido proporcionar un análisis detallado de la dinámica secuencial en circuitos CPG y explorar el efecto modulador de una nueva neurotecnología basada en láser CW-NIR en la dinámica de generación de potenciales de acción. La combinación de metodologías ha demostrado las amplias posibilidades que proporcionan los protocolos de ciclo cerrado en tiempo real para proporcionar una modulación secuencial eficaz. El estudio de secuencias neuronales en múltiples escalas espaciales y temporales puede aportar nuevas ideas para relacionar la dinámica neuronal y el comportamiento. Las nuevas neurotecnologías contribuirán a identificar y explotar la naturaleza secuencial del procesamiento de información neuronal en múltiples sistemas nerviosos. Los resultados discutidos en esta tesis en el contexto de secuencias neuronales también pueden tener fuertes implicaciones en el campo de la neurorrehabilitación, la robótica y la inteligencia artificial por las nuevas perspectivas derivadas de la comprensión de los invariantes dinámicos secuenciales.

Bibliography

- 30th Annual Computational Neuroscience Meeting: CNS*2021–Meeting Abstracts. (2021). *Journal of Computational Neuroscience*, 49(1), 3–208. <https://doi.org/10.1007/s10827-021-00801-9> (cit. on pp. 10, 30).
- Aguirre, C., Campos, D., Pascual, P., & Vázquez, L. (2007). Pattern formation and encoding rhythms analysis on a spiking/bursting neuronal network. *The European Physical Journal Special Topics*, 146(1), 169–176. <https://doi.org/10.1140/epjst/e2007-00177-8> (cit. on pp. 14, 34).
- Albert, E. S., Bec, J. M., Desmadryl, G., Chekroud, K., Travo, C., Gaboyard, S., Bardin, F., Marc, I., Dumas, M., Lenaers, G., Hamel, C., Muller, A., & Chabbert, C. (2012). TRPV4 channels mediate the infrared laser-evoked response in sensory neurons. *Journal of Neurophysiology*, 107(12), 3227–3234. <https://doi.org/10.1152/jn.00424.2011> (cit. on pp. 122, 143, 156).
- Alonso, L. M., & Marder, E. (2020). Temperature compensation in a small rhythmic circuit. *eLife*, 9, 1–24. <https://doi.org/10.7554/eLife.55470> (cit. on p. 145).
- Amaducci, R., Elices, I., Reyes-Sánchez, M., Garrido-Peña, A., Levi, R., Rodriguez, F. B., & Varona, P. (2020). Hybrid robot driven by a closed-loop interaction with a living central pattern generator with online feedback. 29th Annual Computational Neuroscience Meeting: CNS*2020. P207. [Related to Chapter 5]. *BMC Neuroscience*, 21, 54. <https://doi.org/10.1186/s12868-020-00593-1> (cit. on p. 113).
- Amaducci, R., Elices, I., Reyes-Sánchez, M., Garrido-Peña, A., Levi, R., Rodriguez, F. B., & Varona, P. (2021). Controlling robotic locomotion by a closed-loop interaction with living central pattern generators. [Related to Chapter 5]. *COSYNE*. https://www.cosyne.org/s/Cosyne2021_program_book.pdf (cit. on p. 113).
- Amaducci, R., Reyes-Sánchez, M., Elices, I., Rodriguez, F. B., & Varona, P. (2019). RThybrid: A standardized and open-source real-time software model library for experimental neuroscience. *Frontiers in Neuroinformatics*, 13, 1–14. <https://doi.org/10.3389/fninf.2019.00011> (cit. on pp. 122, 126).

BIBLIOGRAPHY

- Amaducci Swarc, R. V. (2023). *Real-time software technology and its implementation in experimental neuroscience closed-loop protocols* [UAM Doctoral Thesis]. (Cit. on p. 115).
- Amunts, K., Knoll, A., Lippert, T., Pennartz, C., Ryvlin, P., Destexhe, A., Jirsa, V., D'Angelo, E., & Bjaalie, J. (2019). The Human Brain Project—Synergy between neuroscience, computing, informatics, and brain-inspired technologies. *PLOS Biology*, 17, e3000344. <https://doi.org/10.1371/journal.pbio.3000344> (cit. on pp. 10, 30).
- Anwar, H., Martinez, D., Bucher, D., & Nadim, F. (2022). Inter-Animal Variability in Activity Phase Is Constrained by Synaptic Dynamics in an Oscillatory Network. *eNeuro*, 9(4). <https://doi.org/10.1523/ENEURO.0027-22.2022> (cit. on p. 43).
- Arichi, T., Whitehead, K., Barone, G., Pressler, R., Padorno, F., Edwards, A. D., & Fabrizi, L. (2017). Localization of spontaneous bursting neuronal activity in the preterm human brain with simultaneous EEG-fMRI. *eLife*, 6, 1–14. <https://doi.org/10.7554/eLife.27814> (cit. on p. 62).
- Bansal, A., Shikha, S., & Zhang, Y. (2022). Towards translational optogenetics. *Nature Biomedical Engineering*, 7, 1–21. <https://doi.org/10.1038/s41551-021-00829-3> (cit. on p. 121).
- Barrett, J. N., Rincon, S., Singh, J., Matthewman, C., Pasos, J., Barrett, E. F., & Rajguru, S. M. (2018). Pulsed infrared releases Ca²⁺ from the endoplasmic reticulum of cultured spiral ganglion neurons. *Journal of Neurophysiology*, 120(2), 509–524. <https://doi.org/10.1152/jn.00740.2017> (cit. on pp. 19, 40, 122, 143, 156).
- Beekharry, C. C., Zhu, G. Z., & Magoski, N. S. (2015). Role for electrical synapses in shaping the output of coupled peptidergic neurons from Lymnaea. <https://doi.org/10.1016/j.brainres.2015.01.039> (cit. on p. 136).
- Begeng, J. M., Tong, W., del Rosal, B., Ibbotson, M., Kameneva, T., & Stoddart, P. R. (2022). Activity of Retinal Neurons Can Be Modulated by Tunable Near-Infrared Nanoparticle Sensors. *ACS Nano*, 17(3), 2079–2088. https://doi.org/10.1021/ACSNANO.2C07663/ASSET/IMAGES/LARGE/NN2C07663_0006.JPG (cit. on pp. 19, 40, 122, 155).
- Beier, H. T., Tolstykh, G. P., Musick, J. D., Thomas, R. J., & Ibey, B. L. (2014). Plasma membrane nanoporation as a possible mechanism behind infrared excitation of cells. *Journal of Neural Engineering*, 11(6), 066006. <https://doi.org/10.1088/1741-2560/11/6/066006> (cit. on p. 155).
- Benjamin, P. R. (2008). Lymnaea. *Scholarpedia*, 3(1), 4124. <https://doi.org/10.4249/scholarpedia.4124> (cit. on p. 47).

BIBLIOGRAPHY

- Benjamin, P. R. (2012). Distributed network organization underlying feeding behavior in the mollusk Lymnaea. *Neural Systems & Circuits*, 2(1), 1–16. <https://doi.org/10.1186/2042-1001-2-4> (cit. on pp. 49, 83, 84, 85, 86, 118).
- Benjamin, P. R., & Elliott, C. J. H. (1989). Snail feeding oscillator: The central pattern generator and its control by modulatory interneurons. *Neuronal and Cellular Oscillators* (cit. on pp. 17, 38).
- Benjamin, P. R., & Pilkington, J. B. (1986). The electrotonic location of low-resistance intercellular junctions between a pair of giant neurones in the snail Lymnaea. *The Journal of Physiology*, 370, 111–126. <https://doi.org/10.1113/jphysiol.1986.sp015925> (cit. on pp. 17, 38, 136).
- Benjamin, P. R., & Rose, R. M. (1979). Central generation of bursting in the feeding system of the snail, Lymnaea stagnalis. *Journal of Experimental Biology*, 80, 93–118 (cit. on pp. 16, 37).
- Benjamin, P. R., Rose, R. M., Slade, C. T., & Lacy, M. G. (1979). Morphology of Identified Neurones in the Buccal Ganglia of Lymnaea Stagnalis. *Journal of Experimental Biology*, 80(1), 119–135 (cit. on pp. 17, 38).
- Berbel, B., Latorre, R., & Varona, P. (2024). Emergence of sequential dynamical invariants in central pattern generators from auto-organized constraints in their sequence time intervals. *Neurocomputing*, 127378. <https://doi.org/10.1016/j.neucom.2024.127378> (cit. on pp. 9, 30, 78).
- Bezaire, M. J., Raikov, I., Burk, K., Vyas, D., & Soltesz, I. (2016). Interneuronal mechanisms of hippocampal theta oscillations in a full-scale model of the rodent CA1 circuit. *eLife*, 5, e18566. <https://doi.org/10.7554/eLife.18566> (cit. on pp. 10, 31).
- Bickle, J. (2016). Revolutions in Neuroscience: Tool Development. *Frontiers in Systems Neuroscience*, 10. <https://doi.org/10.3389/fnsys.2016.00024> (cit. on p. 121).
- Boyden, E. S., Zhang, F., Bamberg, E., Nagel, G., & Deisseroth, K. (2005). Millisecond-timescale, genetically targeted optical control of neural activity. *Nature Neuroscience* 2005 8:9, 8(9), 1263–1268. <https://doi.org/10.1038/nn1525> (cit. on p. 121).
- Brenner, S. (1974). The genetics of Caenorhabditis elegans. *Genetics*, 77(1), 71–94. <https://doi.org/10.1093/genetics/77.1.71> (cit. on pp. 16, 37).
- Brierley, M. J., Staras, K., & Benjamin, P. R. (1997). Behavioral function of glutamatergic interneurons in the feeding system of Lymnaea: Plateauing properties and synaptic connections with motor neurons. *Journal of Neurophysiology*, 78(6), 3386–3395. <https://doi.org/10.1152/jn.1997.78.6.3386> (cit. on pp. 17, 38).
- Brown, W. G. A., Needham, K., Begeng, J. M., Thompson, A. C., Nayagam, B. A., Kameneva, T., & Stoddart, P. R. (2020). Thermal damage threshold of neurons during infrared stimulation.

BIBLIOGRAPHY

- Biomedical Optics Express*, 11(4), 2224. <https://doi.org/10.1364/boe.383165> (cit. on pp. 19, 40, 122, 129, 156).
- Brown, W. G. A., Needham, K., Begeng, J. M., Thompson, A. C., Nayagam, B. A., Kameneva, T., & Stoddart, P. R. (2021). Response of primary auditory neurons to stimulation with infrared light in vitro. *Journal of Neural Engineering*, 18(4), 046003. <https://doi.org/10.1088/1741-2552/ABE7B8> (cit. on p. 129).
- Buonomano, D. V., & Merzenich, M. M. (1995). Temporal information transformed into a spatial code by a neural network with realistic properties. *Science (New York, N.Y.)*, 267(5200), 1028–1030. <https://doi.org/10.1126/science.7863330> (cit. on pp. 7, 27).
- Burke, K. J. J., & Bender, K. J. (2019). Modulation of Ion Channels in the Axon: Mechanisms and Function. *Frontiers in Cellular Neuroscience*, 13. <https://doi.org/10.3389/fncel.2019.00221> (cit. on pp. 9, 28).
- Buzsáki, G., & Tingley, D. (2018). Space and Time: The Hippocampus as a Sequence Generator. *Trends in Cognitive Sciences*, 22(10), 853–869. <https://doi.org/10.1016/J.TICS.2018.07.006> (cit. on p. 61).
- Carelli, ., Reyes, ., Sartorelli, ., & Pinto, . (2005). Whole cell stochastic model reproduces the irregularities found in the membrane potential of bursting neurons. *Journal of neurophysiology*, 94(2), 1169–1179 (cit. on p. 16).
- Carter, M., & Shieh, J. C. (2015). *Guide to research techniques in neuroscience*. Academic Press. <https://doi.org/10.1016/C2013-0-06868-5> (cit. on p. 121).
- Castillo, A., & de la Guardia, Y. (2017). Spineless solutions. *EMBO reports*, 18(11), 1885–1888. <https://doi.org/10.15252/embr.201744113> (cit. on pp. 17, 38).
- Catterall, W. A., Raman, I. M., Robinson, H. P. C., Sejnowski, T. J., & Paulsen, O. (2012). The Hodgkin-Huxley Heritage: From Channels to Circuits. *The Journal of Neuroscience*, 32(41), 14064–14073. <https://doi.org/10.1523/JNEUROSCI.3403-12.2012> (cit. on pp. 10, 30).
- Cayce, J. M., Friedman, R. M., Chen, G., Jansen, E. D., Mahadevan-Jansen, A., & Roe, A. W. (2014). Infrared neural stimulation of primary visual cortex in non-human primates. *NeuroImage*, 84, 181. <https://doi.org/10.1016/J.NEUROIMAGE.2013.08.040> (cit. on pp. 19, 40, 122, 134, 142, 154, 156).
- Chambers, J. J., & Kramer, R. H. (2008). Light-Activated Ion Channels for Remote Control of Neural Activity. *Methods in Cell Biology*, 90, 217–232. [https://doi.org/10.1016/S0091-679X\(08\)00811-X](https://doi.org/10.1016/S0091-679X(08)00811-X) (cit. on pp. 9, 28).

BIBLIOGRAPHY

- Chamorro, P., Muñiz, C., Levi, R., Arroyo, D., Rodríguez, F. B., & Varona, P. (2012). Generalization of the dynamic clamp concept in neurophysiology and behavior. *PLoS ONE*, 7(7), e40887. <https://doi.org/10.1371/journal.pone.0040887> (cit. on pp. 19, 40, 113, 121, 122).
- Chen, W., Li, C., Liang, W., Li, Y., Zou, Z., Xie, Y., Liao, Y., Yu, L., Lin, Q., Huang, M., Li, Z., & Zhu, X. (2022). The Roles of Optogenetics and Technology in Neurobiology: A Review. *Frontiers in Aging Neuroscience*, 14. <https://doi.org/10.3389/fnagi.2022.867863> (cit. on pp. 19, 40).
- Chernov, M., & Roe, A. W. (2014). Infrared neural stimulation: A new stimulation tool for central nervous system applications. *Neurophotonics*, 1(1), 011011. <https://doi.org/10.1117/1.NPh.1.1.011011> (cit. on p. 154).
- Clarke, M., Lankappa, S., Burnett, M., Khalifa, N., & Beer, C. (2018). Patients with depression who self-refer for transcranial magnetic stimulation treatment: Exploratory qualitative study. *BJPsych Bulletin*, 42(6), 243–247. <https://doi.org/10.1192/bjb.2018.49> (cit. on pp. 19, 41).
- Cogan, S. F. (2008). Neural Stimulation and Recording Electrodes. *Annual Review of Biomedical Engineering*, 10(1), 275–309. <https://doi.org/10.1146/annurev.bioeng.10.061807.160518> (cit. on p. 121).
- Cole, K. S. (1955). Ions, potentials and the nerve impulse. In T. Shedlovsky (Ed.), *Electrochemistry in biology and medicine* (pp. 121–140). Wiley. (Cit. on pp. 18, 40).
- Coombes, S., & Bressloff, P. C. (2005). *Bursting: The genesis of rhythm in the nervous system*. World Scientific. (Cit. on p. 111).
- Cosens, B., Thacker, D., & Brimijoin, S. (1976). Temperature-dependence of rapid axonal transport in sympathetic nerves of the rabbit. *Journal of Neurobiology*, 7(4), 339–354. <https://doi.org/10.1002/neu.480070406> (cit. on p. 145).
- Couto, J., Linaro, D., De Schutter, E., & Giugliano, M. (2015). On the Firing Rate Dependency of the Phase Response Curve of Rat Purkinje Neurons In Vitro. *PLOS Computational Biology*, 11(3), 1–23. <https://doi.org/10.1371/journal.pcbi.1004112> (cit. on p. 122).
- Cury, J., Perre, L. V., Smets, H., Stumpp, L., Vespa, S., Vanhoestenberghe, A., Doguet, P., Delbeke, J., Tahry, R. E., Gorza, S. P., & Nonclercq, A. (2021). Infrared neurostimulation in ex-vivo rat sciatic nerve using 1470 nm wavelength. *Journal of Neural Engineering*, 18(5). <https://doi.org/10.1088/1741-2552/ABF28F> (cit. on pp. 145, 156).
- Dagnew, R., Lin, Y.-Y., Agatep, J., Cheng, M., Jann, A., Quach, V., Monroe, M., Singh, G., Minasyan, A., Hakimian, J., Kee, T., Cushman, J., & Walwyn, W. (2017). CerebraLux: A low-cost, open-source, wireless probe for optogenetic stimulation. *Neurophotonics*, 4(4), 045001. <https://doi.org/10.1117/1.NPh.4.4.045001> (cit. on p. 122).

BIBLIOGRAPHY

- De Carlos, J. A., & Borrell, J. (2007). A historical reflection of the contributions of Cajal and Golgi to the foundations of neuroscience. *Brain Research Reviews*, 55(1), 8–16. <https://doi.org/10.1016/j.brainresrev.2007.03.010> (cit. on pp. 1, 21).
- de Castro, F. (2019). Cajal and the Spanish Neurological School: Neuroscience Would Have Been a Different Story Without Them. *Frontiers in Cellular Neuroscience*, 13 (cit. on pp. 1, 21).
- de Castro, F., & Merchán, M. A. (2016). Editorial: The Major Discoveries of Cajal and His Disciples: Consolidated Milestones for the Neuroscience of the XXIst Century. *Frontiers in Neuroanatomy*, 10, 85. <https://doi.org/10.3389/fnana.2016.00085> (cit. on pp. 1, 21).
- Delgado-García, J. M. (2015). Cajal and the Conceptual Weakness of Neural Sciences. *Frontiers in Neuroanatomy*, 9, 128. <https://doi.org/10.3389/fnana.2015.00128> (cit. on pp. 1, 21).
- Dimitrijevic, M. R., Gerasimenko, Y., & Pinter, M. M. (1998). Evidence for a spinal central pattern generator in humans. *Annals of the New York Academy of Sciences*, 860, 360–76. <https://doi.org/10.1111/j.1749-6632.1998.tb09062.x> (cit. on p. 62).
- Dimitrov, A. G., Lazar, A. A., & Victor, J. D. (2011). Information theory in neuroscience. *Journal of Computational Neuroscience*, 30(1), 1–5. <https://doi.org/10.1007/s10827-011-0314-3> (cit. on pp. 10, 30).
- Ding, M., & Glanzman, D. (2011, January). *The Dynamic Brain*. Oxford University Press. <https://doi.org/10.1093/acprof:oso/9780195393798.001.0001> (cit. on pp. 15, 36).
- Ding, N., Patel, A. D., Chen, L., Butler, H., Luo, C., & Poeppel, D. (2017). Temporal modulations in speech and music. *Neuroscience and Biobehavioral Reviews*, 81, 181–187. <https://doi.org/10.1016/j.neubiorev.2017.02.011> (cit. on pp. 7, 27).
- Disner, S. G., Beevers, C. G., & Gonzalez-Lima, F. (2016). Transcranial Laser Stimulation as Neuroenhancement for Attention Bias Modification in Adults with Elevated Depression Symptoms. *Brain Stimulation*, 9(5), 780–787. <https://doi.org/10.1016/j.brs.2016.05.009> (cit. on p. 122).
- Dittami, G. M., Rajguru, S. M., Lasher, R. A., Hitchcock, R. W., & Rabbitt, R. D. (2011). Intracellular calcium transients evoked by pulsed infrared radiation in neonatal cardiomyocytes. *The Journal of Physiology*, 589(Pt 6), 1295–1306. <https://doi.org/10.1113/JPHYSIOL.2010.198804> (cit. on pp. 122, 155, 157).
- Dragoi, G. (2020). Cell assemblies, sequences and temporal coding in the hippocampus. *Current Opinion in Neurobiology*, 64, 111–118. <https://doi.org/10.1016/j.conb.2020.03.003> (cit. on pp. 9, 30).

BIBLIOGRAPHY

- Duke, A. R., Jenkins, M. W., Lu, H., Mcmanus, J. M., Chiel, H. J., & Jansen, E. D. (2013). Transient and selective suppression of neural activity with infrared light. *Scientific Reports*, 3, 2600. <https://doi.org/10.1038/srep02600> (cit. on p. 155).
- Eisen, J. S., & Marder, E. (1982). Mechanisms underlying pattern generation in lobster stomatogastric ganglion as determined by selective inactivation of identified neurons. III. Synaptic connections of electrically coupled pyloric neurons. *Journal of Neurophysiology*, 48(6), 1392–1415. <https://doi.org/10.1152/jn.1982.48.6.1392> (cit. on pp. 16, 37).
- Elias, M., Wieczorek, G., Rosenne, S., & Tawfik, D. S. (2014). The universality of enzymatic rate–temperature dependency. *Trends in Biochemical Sciences*, 39(1), 1–7. <https://doi.org/10.1016/j.tibs.2013.11.001> (cit. on p. 145).
- Elices, I., Levi, R., Arroyo, D., Rodriguez, F. B., & Varona, P. (2019). Robust dynamical invariants in sequential neural activity. *Scientific Reports*, 9(1). <https://doi.org/10.1038/s41598-019-44953-2> (cit. on pp. 9, 30, 43, 61, 62, 63, 70, 72, 81, 83, 109, 116, 117, 160, 168).
- Elliott, C. J., & Benjamin, P. R. (1985). Interactions of the slow oscillator interneuron with feeding pattern-generating interneurons in Lymnaea stagnalis. *Journal of Neurophysiology*, 54(6), 1412–1421. <https://doi.org/10.1152/jn.1985.54.6.1412> (cit. on p. 83).
- Elliott, C. J. H., & Andrew, T. (1991). Temporal Analysis of Snail Feeding Rhythms: A Three-Phase Relaxation Oscillator. *Journal of Experimental Biology*, 157(1), 391–408 (cit. on pp. 62, 66, 72, 73, 74, 77, 93, 117, 118).
- Fishbein, A. R., Idsardi, W. J., Ball, G. F., & Dooling, R. J. (2019). Sound sequences in birdsong: How much do birds really care? *Philosophical Transactions of the Royal Society B: Biological Sciences*, 375(1789), 20190044. <https://doi.org/10.1098/rstb.2019.0044> (cit. on pp. 6, 27).
- FitzHugh, R. (1961). Impulses and Physiological States in Theoretical Models of Nerve Membrane. *Biophysical Journal*, 1(6), 445–466. [https://doi.org/10.1016/S0006-3495\(61\)86902-6](https://doi.org/10.1016/S0006-3495(61)86902-6) (cit. on pp. 10, 31).
- Fodor, I., Hussein, A. A., Benjamin, P. R., Koene, J. M., & Pirger, Z. (2020). The unlimited potential of the great pond snail, Lymnaea stagnalis (S. R. King, P. Rodgers, I. Irisarri, E. E. Voronezhskaya, & M.-A. Coutellec, Eds.). *eLife*, 9, e56962. <https://doi.org/10.7554/eLife.56962> (cit. on pp. 18, 39).
- Friedenberger, Z., Harkin, E., Tóth, K., & Naud, R. (2023). Silences, spikes and bursts: Three-part knot of the neural code. *The Journal of Physiology*, 601(23), 5165–5193. <https://doi.org/10.1113/JP281510> (cit. on pp. 4, 25).
- Ganguly, M., Jenkins, M. W., Chiel, H. J., & Jansen, E. D. (2016, March). Modeling the effects of elevated temperatures on action potential propagation in unmyelinated axons. In S. J. Mad-

BIBLIOGRAPHY

- sen, V. X. D. Yang, E. D. Jansen, Q. Luo, S. K. Mohanty, & N. V. Thakor (Eds.), *Clinical and Translational Neurophotonics; Neural Imaging and Sensing; and Optogenetics and Optical Manipulation* (96901O, Vol. 9690). SPIE. <https://doi.org/10.1117/12.2211048> (cit. on p. 145).
- Ganguly, M., Jenkins, M. W., Jansen, E. D., & Chiel, H. J. (2019). Thermal block of action potentials is primarily due to voltage-dependent potassium currents: A modeling study. *Journal of Neural Engineering*, 16(3), 036020. <https://doi.org/10.1088/1741-2552/ab131b> (cit. on pp. 145, 155).
- Garrido-Peña, A. (2022, March). *TFM 2019/20. Máster en Investigación e Innovación en Tecnologías de la Información y las Comunicaciones*. TFM. (Cit. on p. 50).
- Garrido-Peña, A., Elices, I., & Varona, P. (2021). Characterization of interval variability in the sequential activity of a central pattern generator model. *Neurocomputing*, 461, 667–678. <https://doi.org/10.1016/j.neucom.2020.08.093> (cit. on pp. 9, 30, 72).
- Garrido-Peña, A., Sánchez-Martín, P., Elices, I., Reyes-Sánchez, M., Berbel, B., Latorre, R., Rodríguez, F. B., & Varona, P. (2024). Exploring the ability of biophysical models to reproduce the functional variability of neurons. 32nd Annual Computational Neuroscience Meeting: CNS*2023. [Related to Chapter 5]. In Press for *Journal of Computational Neuroscience* (cit. on p. 113).
- Gelperin, A. (2019). Recent trends in invertebrate neuroscience. *The Oxford Handbook of Invertebrate Neurobiology*, 1936, 3 (cit. on pp. 16, 37).
- Ghigliazza, R. M., & Holmes, P. (2004). A Minimal Model of a Central Pattern Generator and Motoneurons for Insect Locomotion. *SIAM Journal on Applied Dynamical Systems*, 3(4), 671–700. <https://doi.org/10.1137/040607563> (cit. on pp. 69, 112).
- Gleeson, P., Cantarelli, M., Marin, B., Quintana, A., Earnshaw, M., Sadeh, S., Piasini, E., Birgiolas, J., Cannon, R. C., Cayco-Gajic, N. A., Crook, S., Davison, A. P., Dura-Bernal, S., Ecker, A., Hines, M. L., Idili, G., Lanore, F., Larson, S. D., Lytton, W. W., ... Silver, R. A. (2019). Open Source Brain: A Collaborative Resource for Visualizing, Analyzing, Simulating, and Developing Standardized Models of Neurons and Circuits. *Neuron*, 103(3), 395–411.e5. <https://doi.org/10.1016/j.neuron.2019.05.019> (cit. on pp. 11, 32).
- Gonçalves, P. J., Lueckmann, J.-M., Deistler, M., Nonnenmacher, M., Öcal, K., Bassetto, G., Chintaluri, C., Podlaski, W. F., Haddad, S. A., Vogels, T. P., Greenberg, D. S., & Macke, J. H. (2020). Training deep neural density estimators to identify mechanistic models of neural dynamics (J. R. Huguenard, T. O’Leary, & M. S. Goldman, Eds.). *eLife*, 9, e56261. <https://doi.org/10.7554/eLife.56261> (cit. on pp. 10, 30).

BIBLIOGRAPHY

- Goyal, V., Rajguru, S., Matic, A. I., Stock, S. R., & Richter, C. P. (2012). Acute Damage Threshold for Infrared Neural Stimulation of the Cochlea: Functional and Histological Evaluation. *The Anatomical Record: Advances in Integrative Anatomy and Evolutionary Biology*, 295(11), 1987–1999. <https://doi.org/10.1002/AR.22583> (cit. on pp. 19, 40, 122, 154, 155).
- Grillner, S., & Kashin, S. (1976). On the Generation and Performance of Swimming in Fish BT - Neural Control of Locomotion. In R. M. Herman, S. Grillner, P. S. G. Stein, & D. G. Stuart (Eds.), *Neural Control of Locomotion* (pp. 181–201). Springer US. https://doi.org/10.1007/978-1-4757-0964-3_8 (cit. on p. 62).
- Hahnloser, R. H., Kozhevnikov, A. A., & Fee, M. S. (2002). An ultra-sparse code underlies the generation of neural sequences in a songbird. *Nature*, 419(6902), 65–70. <https://doi.org/10.1038/nature00974> (cit. on p. 61).
- Hamill, O. P., Marty, A., Neher, E., Sakmann, B., & Sigworth, F. J. (1981). Improved patch-clamp techniques for high-resolution current recording from cells and cell-free membrane patches. *Pflugers Archiv: European Journal of Physiology*, 391(2), 85–100. <https://doi.org/10.1007/BF00656997> (cit. on pp. 18, 19, 40).
- Hamraoui, K., Torres-Vera, V. A., Zabala Gutierrez, I., Casillas-Rubio, A., Alqudwa Fattouh, M., Benayas, A., Marin, R., Natile, M. M., Manso Silvan, M., Rubio-Zuazo, J., Jaque, D., Melle, S., Calderón, O. G., & Rubio-Retama, J. (2023). Exploring the Origin of the Thermal Sensitivity of Near-Infrared-II Emitting Rare Earth Nanoparticles. *ACS Applied Materials & Interfaces*, 15(27), 32667–32677. <https://doi.org/10.1021/acsami.3c04125> (cit. on p. 157).
- Hariz, M., & Blomstedt, P. (2022). Deep brain stimulation for Parkinson's disease. *Journal of Internal Medicine*, 292(5), 764–778. <https://doi.org/10.1111/joim.13541> (cit. on pp. 19, 41).
- Hartline, D. K., & Maynard, D. M. (1976). Motor patterns in the stomatogastric ganglion of the lobster Panulirus argus. *J. Exp. Biol.*, 62(2), 405–420 (cit. on p. 61).
- He, B. J. (2018). Robust, Transient Neural Dynamics during Conscious Perception. *Trends in Cognitive Sciences*, 22(7), 563–565. <https://doi.org/10.1016/j.tics.2018.04.005> (cit. on pp. 7, 27).
- Heitler, W. J. (2007). DataView: A Tutorial Tool for Data Analysis. Template-based Spike Sorting and Frequency Analysis. *Journal of undergraduate neuroscience education : JUNE : a publication of FUN, Faculty for Undergraduate Neuroscience*, 6(1), A1–7 (cit. on p. 59).
- Heitler, W. J., & Edwards, D. H. (1998). Effect of Temperature on a Voltage-Sensitive Electrical Synapse in Crayfish. *Journal of Experimental Biology*, 201(4), 503–513. <https://doi.org/10.1242/jeb.201.4.503> (cit. on p. 145).

BIBLIOGRAPHY

- Hindmarsh, J. L., & Rose, R. M. (1984). A model of neuronal bursting using three coupled first order differential equations. *Proceedings of the Royal Society of London. Series B, Containing papers of a Biological character. Royal Society (Great Britain)*, 221(1222), 87–102. <https://doi.org/10.1098/rspb.1984.0024> (cit. on pp. 10, 15, 31, 37).
- Hodgkin, A. L., & Huxley, A. F. (1952). A quantitative description of membrane current and its application to conduction and excitation in nerve. *The Journal of Physiology*, 117(4), 500–44. <https://doi.org/10.1113/jphysiol.1952.sp004764> (cit. on pp. 10, 11, 14, 16, 31, 35, 37, 50, 51, 140).
- Hodgkin, A. L., & Katz, B. (1949). The effect of temperature on the electrical activity of the giant axon of the squid. *The Journal of Physiology*, 109(1), 240–249. <https://doi.org/10.1113/jphysiol.1949.sp004388> (cit. on p. 145).
- Hooper, S. L. (1997). Phase Maintenance in the Pyloric Pattern of the Lobster (*Panulirus interruptus*) Stomatogastric Ganglion. *Journal of Computational Neuroscience*, 205(3), 191–205. <https://doi.org/10.1023/A:1008822218061> (cit. on p. 62).
- Huerta, R., Varona, P., Rabinovich, M. I., & Abarbanel, H. D. (2001). Topology selection by chaotic neurons of a pyloric central pattern generator. *Biological Cybernetics*, 84(1), L1–L8. <https://doi.org/10.1007/PL00007976> (cit. on pp. 6, 7, 14, 27, 28, 34, 62).
- Hutt, A., Rich, S., Valiante, T. A., & Lefebvre, J. (2023). Intrinsic neural diversity quenches the dynamic volatility of neural networks. *Proceedings of the National Academy of Sciences*, 120(28), e2218841120. <https://doi.org/10.1073/pnas.2218841120> (cit. on pp. 15, 36).
- Ivry, R. B. (1996). The representation of temporal information in perception and motor control. *Current Opinion in Neurobiology*, 6(6), 851–857. [https://doi.org/10.1016/s0959-4388\(96\)80037-7](https://doi.org/10.1016/s0959-4388(96)80037-7) (cit. on pp. 7, 27).
- Izhikevich, E. M. (2003). Simple model of spiking neurons. *IEEE Transactions on Neural Networks*, 14(6), 1569–1572. <https://doi.org/10.1109/TNN.2003.820440> (cit. on pp. 10, 31).
- Izhikevich, E. M. (2007). *Dynamical systems in neuroscience: The geometry of excitability and bursting*. MIT Press. (Cit. on pp. 3, 23, 111).
- Izzo, A. D., Walsh, J. T., Jansen, E. D., Bendett, M., Webb, J., Ralph, H., & Richter, C. P. (2007). Optical parameter variability in laser nerve stimulation: A study of pulse duration, repetition rate, and wavelength. *IEEE Transactions on Biomedical Engineering*, 54(6), 1108–1114. <https://doi.org/10.1109/TBME.2007.892925> (cit. on pp. 122, 134, 137, 155).
- Kandel, E. R., Schwartz, J. H., & Jessell, T. M. (2012). *Principles of Neural Science*. McGraw-Hill Education. (Cit. on pp. 2, 23).

BIBLIOGRAPHY

- Katz, P. S. (2016). Evolution of central pattern generators and rhythmic behaviours. <https://doi.org/10.1098/rstb.2015.0057> (cit. on pp. 4, 7, 25, 28).
- Kecskes, M., Peigneur, S., & Held, K. (2023). Editorial: Contribution of ion channels to neuropathologies. *Frontiers in Cell and Developmental Biology*, 11, 1179663. <https://doi.org/10.3389/fcell.2023.1179663> (cit. on pp. 9, 28).
- Kemenes, G., & Elliott, C. J. H. (1994). Analysis of the feeding motor pattern in the pond snail, *Lymnaea stagnalis*: Photoinactivation of axonally stained pattern-generating interneurons. *Journal of Neuroscience*, 14(1), 153–166. <https://doi.org/10.1523/JNEUROSCI.14-01-00153.1994> (cit. on p. 118).
- Kemenes, G., Staras, K., & Benjamin, P. R. (2001). Multiple Types of Control by Identified Interneurons in a Sensory-Activated Rhythmic Motor Pattern. *The Journal of neuroscience : the official journal of the Society for Neuroscience*, 21, 2903–11. <https://doi.org/10.1523/JNEUROSCI.21-08-02903.2001> (cit. on pp. 17, 38, 86).
- Kiebel, S. J., Daunizeau, J., & Friston, K. J. (2008). A Hierarchy of Time-Scales and the Brain. *PLOS Computational Biology*, 4(11), e1000209. <https://doi.org/10.1371/journal.pcbi.1000209> (cit. on pp. 6, 27).
- Kiebel, S. J., von Kriegstein, K., Daunizeau, J., & Friston, K. J. (2009). Recognizing sequences of sequences. (R. Kötter, Ed.). *PLoS computational biology*, 5(8), e1000464. <https://doi.org/10.1371/journal.pcbi.1000464> (cit. on pp. 6, 27).
- Koch, C. (1999). *Biophysics of computation*. Oxford University Press, New York. (Cit. on pp. 3, 23).
- Komendantov, A. O., & Kononenko, N. I. (1996). Deterministic chaos in mathematical model of pacemaker activity in bursting neurons of snail, *Helix pomatia*. *Journal of Theoretical Biology*, 183(2), 219–230. <https://doi.org/10.1006/jtbi.1996.0215> (cit. on pp. 15, 37).
- Konstantinović, L. M., Jelić, M. B., Jeremić, A., Stevanović, V. B., Milanović, S. D., & Filipović, S. R. (2013). Transcranial application of near-infrared low-level laser can modulate cortical excitability. *Lasers in Surgery and Medicine*, 45(10), 648–653. <https://doi.org/10.1002/lsm.22190> (cit. on p. 122).
- Krames, E., Peckham, P. H., & Rezai, A. R. (2009). *Neuromodulation* (1st ed). Elsevier Academic Press. (Cit. on pp. 19, 40).
- Lareo, A., Forlim, C. G., Pinto, R. D., Varona, P., & Rodriguez, F. d. B. (2016). Temporal Code-Driven Stimulation: Definition and Application to Electric Fish Signaling. *Frontiers in Neuroinformatics*, 10(OCT), 41. <https://doi.org/10.3389/fninf.2016.00041> (cit. on p. 122).

BIBLIOGRAPHY

- Latorre, R., Aguirre, C., Rabinovich, M. I., & Varona, P. (2013). Transient dynamics and rhythm coordination of inferior olive spatio-temporal patterns. *Frontiers in Neural Circuits*, 7(SEP), 138. <https://doi.org/10.3389/fncir.2013.00138> (cit. on pp. 14, 34).
- Lecoq, J., Orlova, N., & Grawe, B. F. (2019). Wide. Fast. Deep: Recent Advances in Multiphoton Microscopy of In Vivo Neuronal Activity. *Journal of Neuroscience*, 39(46), 9042–9052. <https://doi.org/10.1523/JNEUROSCI.1527-18.2019> (cit. on p. 121).
- Levitin, I. B., & Kaczmarek, L. K. (2002). *The neuron: Cell and molecular biology* (3rd ed). Oxford University Press. (Cit. on pp. 5, 26).
- Li, X., Liu, J., Liang, S., Guan, K., An, L., Wu, X., Li, S., & Sun, C. (2013). Temporal Modulation of Sodium Current Kinetics in Neuron Cells by Near-Infrared Laser. *Cell Biochemistry and Biophysics*, 67(3), 1409–1419. <https://doi.org/10.1007/s12013-013-9674-9> (cit. on pp. 129, 143, 145, 156).
- Liang, S., Yang, F., Zhou, C., Wang, Y., Li, S., Sun, C. K., Puglisi, J. L., Bers, D., Sun, C., & Zheng, J. (2009). Temperature-dependent activation of neurons by continuous near-infrared laser. *Cell Biochemistry and Biophysics*, 53(1), 33–42. <https://doi.org/10.1007/s12013-008-9035-2> (cit. on pp. 19, 40, 122, 143, 149).
- Limousin, P., & Foltyne, T. (2019). Long-term outcomes of deep brain stimulation in Parkinson disease. *Nature Reviews Neurology*, 15(4), 234–242. <https://doi.org/10.1038/s41582-019-0145-9> (cit. on pp. 19, 41).
- Linaro, D., Couto, J., & Giugliano, M. (2015). Real-time Electrophysiology: Using Closed-loop Protocols to Probe Neuronal Dynamics and Beyond. *JoVE (Journal of Visualized Experiments)*, e52320–e52320. <https://doi.org/10.3791/52320> (cit. on p. 122).
- Linaro, D., Storace, M., & Giugliano, M. (2011). Accurate and Fast Simulation of Channel Noise in Conductance-Based Model Neurons by Diffusion Approximation. *PLOS Computational Biology*, 7(3), e1001102. <https://doi.org/10.1371/journal.pcbi.1001102> (cit. on pp. 15, 36).
- Lothet, E. H., Shaw, K. M., Lu, H., Zhuo, J., Wang, Y. T., Gu, S., Stoltz, D. B., Jansen, E. D., Horn, C. C., Chiel, H. J., & Jenkins, M. W. (2017). Selective inhibition of small-diameter axons using infrared light. *Scientific Reports*, 7(1), 1–8. <https://doi.org/10.1038/s41598-017-03374-9> (cit. on p. 155).
- Lumbreras, V., Bas, E., Gupta, C., & Rajguru, S. M. (2014). Pulsed infrared radiation excites cultured neonatal spiral and vestibular ganglion neurons by modulating mitochondrial calcium cycling. *Journal of Neurophysiology*, 112(6), 1246. <https://doi.org/10.1152/JN.00253.2014> (cit. on pp. 122, 155, 157).

BIBLIOGRAPHY

- Lundqvist, M., Rose, J., Herman, P., Brincat, S. L., Buschman, T. J., & Miller, E. K. (2016). Gamma and Beta Bursts Underlie Working Memory. *Neuron*, 90(1), 152–164. <https://doi.org/10.1016/j.neuron.2016.02.028> (cit. on pp. 4, 23).
- MacKay-Lyons, M. (2002). Central Pattern Generation of Locomotion: A Review of the Evidence. *Physical Therapy*, 82(1), 69–83. <https://doi.org/10.1093/ptj/82.1.69> (cit. on pp. 7, 27).
- Marder, E., & Bucher, D. (2001). Central pattern generators and the control of rhythmic movements. *Current Biology*, 11(23), R986–R996. [https://doi.org/10.1016/S0960-9822\(01\)00581-4](https://doi.org/10.1016/S0960-9822(01)00581-4) (cit. on pp. 7, 27, 61).
- Marmont, G. (1949). Studies on the axon membrane. I. A new method. *Journal of cellular and comparative physiology*, 34(3), 351–382 (cit. on pp. 18, 40).
- Martinez, D., Anwar, H., Bose, A., Bucher, D. M., & Nadim, F. (2019). Short-term synaptic dynamics control the activity phase of neurons in an oscillatory network. *eLife*, 8. <https://doi.org/10.7554/ELIFE.46911> (cit. on p. 62).
- Masquelier, T. (2013). Neural variability, or lack thereof. *Frontiers in Computational Neuroscience*, 7. <https://doi.org/10.3389/fncom.2013.00007> (cit. on pp. 15, 36).
- Mauk, M. D., & Buonomano, D. V. (2004). THE NEURAL BASIS OF TEMPORAL PROCESSING. *Annual Review of Neuroscience*, 27(Volume 27, 2004), 307–340. <https://doi.org/10.1146/annurev.neuro.27.070203.144247> (cit. on pp. 7, 28).
- McCrohan, C. R., & Benjamin, P. R. (1980). Patterns of activity and axonal projections of the cerebral giant cells of the snail, *Lymnaea stagnalis*. *Journal of Experimental Biology*, 85, 149–168 (cit. on pp. 17, 38).
- Minassian, K., Hofstoetter, U. S., Dzeladini, F., Guertin, P. A., & Ijspeert, A. (2017). The Human Central Pattern Generator for Locomotion: Does It Exist and Contribute to Walking? *The Neuroscientist: A Review Journal Bringing Neurobiology, Neurology and Psychiatry*, 23(6), 649–663. <https://doi.org/10.1177/1073858417699790> (cit. on pp. 7, 27).
- Moulins, M., & Selverston, A. I. (1987). Introduction. In A. I. Selverston & M. Moulins (Eds.), *The Crustacean Stomatogastric System: A Model for the Study of Central Nervous Systems* (pp. 1–8). Springer. https://doi.org/10.1007/978-3-642-71516-7_1 (cit. on pp. 7, 28).
- Neher, E., & Sakmann, B. (1976). Single-channel currents recorded from membrane of denervated frog muscle fibres. *Nature*, 260(5554), 799–802. <https://doi.org/10.1038/260799a0> (cit. on pp. 18, 40).
- Noland, L. E., & Carricker, M. R. (1946). Observations on the Biology of the Snail *Lymnaea stagnalis appressa* During Twenty Generations in Laboratory Culture. *The American Midland Naturalist*, 36(2), 467–493. <https://doi.org/10.2307/2421516> (cit. on pp. 17, 38).

BIBLIOGRAPHY

- Nowotny, T., Levi, R., & Selverston, A. I. (2008). Probing the Dynamics of Identified Neurons with a Data-Driven Modeling Approach (K. J. Friston, Ed.). *PLoS ONE*, 3(7), e2627. <https://doi.org/10.1371/journal.pone.0002627> (cit. on pp. 68, 112).
- Nowotny, T., & Varona, P. (2022). Dynamic Clamp Technique. In D. Jaeger & R. Jung (Eds.), *Encyclopedia of Computational Neuroscience* (pp. 1240–1243). Springer. https://doi.org/10.1007/978-1-0716-1006-0_126 (cit. on pp. 19, 40).
- Nüsslein-Volhard, C., & Wieschaus, E. (1980). Mutations affecting segment number and polarity in Drosophila. *Nature*, 287(5785), 795–801. <https://doi.org/10.1038/287795a0> (cit. on pp. 16, 37).
- Palmu, K., Wikström, S., Hippeläinen, E., Boylan, G., Hellström-Westas, L., & Vanhatalo, S. (2010). Detection of 'EEG bursts' in the early preterm EEG: Visual vs. automated detection. *Clinical Neurophysiology: Official Journal of the International Federation of Clinical Neurophysiology*, 121(7), 1015–1022. <https://doi.org/10.1016/j.clinph.2010.02.010> (cit. on pp. 4, 23).
- Pan, L., Ping, A., Schriver, K. E., Roe, A. W., Zhu, J., & Xu, K. (2023). Infrared neural stimulation in human cerebral cortex. *Brain Stimulation*, 16(2), 418–430. <https://doi.org/10.1016/J.BRS.2023.01.1678> (cit. on pp. 122, 145, 154, 155).
- Patel, Y. A., George, A., Dorval, A. D., White, J. A., Christini, D. J., & Butera, R. J. (2017). Hard real-time closed-loop electrophysiology with the Real-Time eXperiment Interface (RTXI) (T. Poisot, Ed.). *PLOS Computational Biology*, 13(5), e1005430. <https://doi.org/10.1371/journal.pcbi.1005430> (cit. on pp. 123, 124, 151).
- Paton, J. J., & Buonomano, D. V. (2018). The Neural Basis of Timing: Distributed Mechanisms for Diverse Functions. *Neuron*, 98(4), 687–705. <https://doi.org/10.1016/j.neuron.2018.03.045> (cit. on p. 61).
- Pavlidis, E., Cantalupo, G., Cattani, L., Tassinari, C. A., & Pisani, F. (2016). Neonatal seizure automatism and human inborn pattern of quadrupedal locomotion. *Gait and Posture*, 49, 232–234. <https://doi.org/10.1016/j.gaitpost.2016.07.015> (cit. on p. 62).
- Pearson, K. G. (1972). *Central Programming and Reflex Control of Walking in the Cockroach* (tech. rep. No. 1). (Cit. on pp. 7, 27).
- Pezo, D., Soudry, D., & Orio, P. (2014). Diffusion approximation-based simulation of stochastic ion channels: Which method to use? *Frontiers in Computational Neuroscience*, 8. <https://doi.org/10.3389/fncom.2014.00139> (cit. on pp. 15, 36).

BIBLIOGRAPHY

- Ping, A., Pan, L., Zhang, J., Xu, K., Schriver, K. E., Zhu, J., & Roe, A. W. (2023). Targeted Optical Neural Stimulation: A New Era for Personalized Medicine. *The Neuroscientist*, 29(2), 202–220. <https://doi.org/10.1177/10738584211057047> (cit. on p. 122).
- Plaksin, M., Shapira, E., Kimmel, E., & Shoham, S. (2018). Thermal Transients Excite Neurons through Universal Intramembrane Mechanoelectrical Effects. *Physical Review X*, 8(1), 011043. <https://doi.org/10.1103/PHYSREVIEWX.8.011043/FIGURES/4/MEDIUM> (cit. on pp. 122, 142, 156).
- Potjans, T. C., & Diesmann, M. (2014). The cell-type specific cortical microcircuit: Relating structure and activity in a full-scale spiking network model. *Cerebral Cortex (New York, N.Y.: 1991)*, 24(3), 785–806. <https://doi.org/10.1093/cercor/bhs358> (cit. on pp. 10, 31).
- Potter, S. M., El Hady, A., & Fetz, E. E. (2014). Closed-Loop Neuroscience and Neuroengineering. *Frontiers in Neural Circuits*, 8(115). <https://doi.org/10.3389/fncir.2014.00115> (cit. on p. 122).
- Prather, J. F., Okanoya, K., & Bolhuis, J. J. (2017). Brains for birds and babies: Neural parallels between birdsong and speech acquisition. *Neuroscience and Biobehavioral Reviews*, 81, 225–237. <https://doi.org/10.1016/j.neubiorev.2016.12.035> (cit. on pp. 6, 27).
- Preuss, T. M. (2000). Taking the Measure of Diversity: Comparative Alternatives to the Model-Animal Paradigm in Cortical Neuroscience. *Brain Behavior and Evolution*, 55(6), 287–299. <https://doi.org/10.1159/000006664> (cit. on pp. 16, 37).
- Rabbitt, R. D., Brichta, A. M., Tabatabaee, H., Boutros, P. J., Ahn, J., Santina, C. C. D., Poppi, L. A., & Lim, R. (2016). Heat pulse excitability of vestibular hair cells and afferent neurons. *Journal of Neurophysiology*, 116(2), 825–843. <https://doi.org/10.1152/jn.00110.2016> (cit. on pp. 129, 143, 145, 155, 156).
- Rabinovich, M. I., Bick, C., & Varona, P. (2023). Beyond neurons and spikes: Cognon, the hierarchical dynamical unit of thought. *Cognitive Neurodynamics*. <https://doi.org/10.1007/s11571-023-09987-3> (cit. on pp. 6, 27).
- Rabinovich, M. I., & Varona, P. (2018). Discrete sequential information coding: Heteroclinic cognitive dynamics. *Frontiers in Computational Neuroscience*, 12. <https://doi.org/10.3389/fncom.2018.00073> (cit. on pp. 6, 27, 61).
- Rabinovich, M. I., Zaks, M. A., & Varona, P. (2020). Sequential dynamics of complex networks in mind: Consciousness and creativity. *Physics Reports*, 883, 1–32. <https://doi.org/10.1016/j.physrep.2020.08.003> (cit. on pp. 5, 7, 26, 27).
- Ramón y Cajal, S., & Sánchez, D. (1915). Sobre la estructura de los centros ópticos de los insectos. *Revista Chilena de Historia Natural*, 25, 1–18 (cit. on pp. 2, 22).

BIBLIOGRAPHY

- Ramón y Cajal, S. (1899). *Textura del sistema nervioso del hombre y de los vertebrados*. Imprenta y Libería de Nicolás Moya. (Cit. on pp. 1, 21).
- Renart, A., & Machens, C. K. (2014). Variability in neural activity and behavior. *Current Opinion in Neurobiology*, 25, 211–220. <https://doi.org/10.1016/j.conb.2014.02.013> (cit. on pp. 15, 36, 111).
- Reyes, M. B., Huerta, R., Rabinovich, M. I., & Selverston, A. I. (2008). Artificial synaptic modification reveals a dynamical invariant in the pyloric CPG. *European Journal of Applied Physiology*, 102(6), 667–675. <https://doi.org/10.1007/s00421-007-0635-0> (cit. on pp. 9, 30, 62).
- Reyes-Sanchez, M., Amaducci, R., Elices, I., Rodriguez, F. B., & Varona, P. (2020). Automatic adaptation of model neurons and connections to build hybrid circuits with living networks. *Neuroinformatics*, 18(3), 377–393. <https://doi.org/10.1007/s12021-019-09440-z> (cit. on p. 126).
- Reyes-Sanchez, M., Amaducci, R., Sanchez-Martin, P., Elices, I., Rodriguez, F. B., & Varona, P. (2023). Automatized offline and online exploration to achieve a target dynamics in biohybrid neural circuits built with living and model neurons. *Neural Networks*, 164, 464–475. <https://doi.org/10.1016/j.neunet.2023.04.034> (cit. on pp. 113, 122, 126).
- Ribeiro, T. L., Jendrichovsky, P., Yu, S., Martin, D. A., Kanold, P. O., Chialvo, D. R., & Plenz, D. (2024). Trial-by-trial variability in cortical responses exhibits scaling of spatial correlations predicted from critical dynamics. *Cell Reports*, 43(2). <https://doi.org/10.1016/j.celrep.2024.113762> (cit. on pp. 15, 36).
- Robbins, M., Siddiqui, O., Fuchsberger, T., Goodfellow, G., Paulsen, O., Kaminski, C. F., Euser, T., & Schierle, G. S. K. (2021). OptoGenie: An open-source device for the optogenetic stimulation of cells. *Journal of Open Hardware*, 5(1), 2. <https://doi.org/10.5334/joh.32> (cit. on p. 122).
- Romanova, E. V., & Sweedler, J. V. (2018). Animal Model Systems in Neuroscience. *ACS Chemical Neuroscience*, 9(8), 1869–1870. <https://doi.org/10.1021/acschemneuro.8b00380> (cit. on pp. 16, 37).
- Rose, R. M., & Benjamin, P. R. (1979). The Relationship of the Central Motor Pattern to the Feeding Cycle of *Lymnaea Stagnalis*. *Journal of Experimental Biology*, 80(1), 137–163. <https://doi.org/10.1242/jeb.80.1.137> (cit. on pp. 17, 38).
- Rose, R. M., & Benjamin, P. R. (1981). Interneuronal Control of Feeding in the Pond Snail *Lymnaea Stagnalis*: I. Initiation of Feeding Cycles by a Single Buccal Interneurone. *Journal of*

BIBLIOGRAPHY

- Experimental Biology*, 92(1), 187–201. <https://doi.org/10.1242/jeb.92.1.187> (cit. on pp. 17, 38).
- Russell, D. F., & Hartline, D. K. (1978). Bursting Neural Networks: A Reexamination. *Science*, 200(4340), 453–456. <https://doi.org/10.1126/science.644309> (cit. on pp. 4, 23).
- Saucedo, C. L., Courtois, E. C., Wade, Z. S., Kelley, M. N., Kheradbin, N., Barrett, D. W., & Gonzalez-Lima, F. (2021). Transcranial laser stimulation: Mitochondrial and cerebrovascular effects in younger and older healthy adults. *Brain Stimulation*, 14(2), 440–449. <https://doi.org/10.1016/j.brs.2021.02.011> (cit. on pp. 122, 155, 157).
- Schauf, C. L. (1973). Temperature dependence of the ionic current kinetics of Myxicola giant axons. *The Journal of Physiology*, 235(1), 197–205 (cit. on p. 145).
- Schwiening, C. J. (2012). A brief historical perspective: Hodgkin and Huxley. *The Journal of Physiology*, 590(Pt 11), 2571–2575. <https://doi.org/10.1113/jphysiol.2012.230458> (cit. on pp. 10, 30).
- Silverston, A. I., Rabinovich, M. I., Abarbanel, H. D. I., Elson, R., Szücs, A., Pinto, R. D., Huerta, R., & Varona, P. (2000). Reliable circuits from irregular neurons: A dynamical approach to understanding central pattern generators. *Journal of Physiology-Paris*, 94(5-6), 357–374. [https://doi.org/10.1016/S0928-4257\(00\)01101-3](https://doi.org/10.1016/S0928-4257(00)01101-3) (cit. on pp. 7, 15, 27, 36, 61, 62).
- Silverston, A. I., & Ayers, J. (2006). Oscillations and oscillatory behavior in small neural circuits. *Biological Cybernetics*, 95(6), 537–554. <https://doi.org/10.1007/s00422-006-0125-1> (cit. on pp. 7, 28).
- Silverston, A. I., Russell, D. F., Miller, J. P., & King, D. G. (1976). The stomatogastric nervous system: Structure and function of a small neural network. *Progress in Neurobiology*, 7, 215–289. [https://doi.org/10.1016/0301-0082\(76\)90008-3](https://doi.org/10.1016/0301-0082(76)90008-3) (cit. on pp. 16, 37).
- Shannon, C. E. (1948). A mathematical theory of communication. *The Bell System Technical Journal*, 27(3), 379–423. <https://doi.org/10.1002/j.1538-7305.1948.tb01338.x> (cit. on pp. 10, 30).
- Shapiro, M. G., Homma, K., Villarreal, S., Richter, C. P., & Bezanilla, F. (2012). Infrared light excites cells by changing their electrical capacitance. *Nature Communications*, 3(1), 1–11. <https://doi.org/10.1038/ncomms1742> (cit. on pp. 19, 40, 122, 134, 142, 145, 155, 156).
- Shapiro, M. G., Homma, K., Villarreal, S., Richter, C.-P., & Bezanilla, F. (2017). Correction: Corrigendum: Infrared light excites cells by changing their electrical capacitance. *Nature Communications*, 8(1), 16148. <https://doi.org/10.1038/ncomms16148> (cit. on p. 142).
- Siegle, J. H., Hale, G. J., Newman, J. P., & Voigts, J. (2015). Neural ensemble communities: Open-source approaches to hardware for large-scale electrophysiology. *Current Opinion in Neurobiology*, 32, 53–59. <https://doi.org/10.1016/j.conb.2014.11.004> (cit. on p. 122).

BIBLIOGRAPHY

- Smith, S. L., Smith, I. T., Branco, T., & Häusser, M. (2013). Dendritic spikes enhance stimulus selectivity in cortical neurons *in vivo*. *Nature*, 503(7474), 115–120. <https://doi.org/10.1038/nature12600> (cit. on pp. 10, 31).
- Soëtard, P., Amaducci, R., Sánchez-Martín, P., Reyes-Sánchez, M., Garrido-Peña, A., Levi, R., Rodriguez, F. B., & Varona, P. (2023). Dynamical principles of functional neural sequences validated in hybrid robots built with living central pattern generators. 31st Annual Computational Neuroscience Meeting: CNS*2022. P110 [Related to Chapter 5]. *Journal of Computational Neuroscience*, 51, 3–101. <https://doi.org/10.1007/s10827-022-00841-9> (cit. on pp. 70, 113).
- Staras, K., Kemenes, G., & Benjamin, P. R. (1998). Pattern-generating role for motoneurons in a rhythmically active neuronal network. *Journal of Neuroscience*, 18(10), 3669–3688 (cit. on pp. 48, 83, 84).
- Staras, K., Kemenes, G., & Benjamin, P. R. (1999). Electrophysiological and Behavioral Analysis of Lip Touch as a Component of the Food Stimulus in the Snail *Lymnaea*. *Journal of Neurophysiology*, 81(3), 1261–1273. <https://doi.org/10.1152/jn.1999.81.3.1261> (cit. on p. 98).
- Staras, K., Kemenes, I., Benjamin, P. R., & Kemenes, G. (2003). Loss of self-inhibition is a cellular mechanism for episodic rhythmic behavior. *Current biology: CB*, 13(2), 116–124. [https://doi.org/10.1016/s0960-9822\(02\)01435-5](https://doi.org/10.1016/s0960-9822(02)01435-5) (cit. on p. 86).
- Stein, R. B., Gossen, E. R., & Jones, K. E. (2005). Neuronal variability: noise or part of the signal? *Nature Reviews Neuroscience*, 6(5), 389–397. <https://doi.org/10.1038/nrn1668> (cit. on p. 111).
- Stephan, P. (2015, September). How Economics Shapes Science. (Cit. on pp. 17, 38).
- Steuer, I., & Guertin, P. A. (2018). Central pattern generators in the brainstem and spinal cord: An overview of basic principles, similarities and differences. *Reviews in the Neurosciences*. <https://doi.org/10.1515/revneuro-2017-0102> (cit. on pp. 4, 25).
- Štih, V., Petrucco, L., Kist, A. M., & Portugues, R. (2019). Stytra: An open-source, integrated system for stimulation, tracking and closed-loop behavioral experiments. *PLOS Computational Biology*, 15(4), e1006699. <https://doi.org/10.1371/journal.pcbi.1006699> (cit. on p. 122).
- Straub, V. A., Staras, K., Kemenes, G., & Benjamin, P. R. (2002). Endogenous and network properties of *Lymnaea* feeding central pattern generator interneurons. *Journal of Neurophysiology*, 88(4), 1569–1583. <https://doi.org/10.1152/jn.00872.2001> (cit. on p. 49).
- Streisinger, G., Walker, C., Dower, N., Knauber, D., & Singer, F. (1981). Production of clones of homozygous diploid zebra fish (*Brachydanio rerio*). *Nature*, 291(5813), 293–296. <https://doi.org/10.1038/291293a0> (cit. on pp. 16, 37).

BIBLIOGRAPHY

- Szücs, A., Varona, P., Volkovskii, A. R., Abarbanel, H. D. I., Rabinovich, M. I., & Selverston, A. I. (2000). Interacting Biological and Electronic Neurons Generate Realistic Oscillatory Rhythms. *Neuroreport*, 11(3), 563–569 (cit. on p. 113).
- Tang, L. S., Goeritz, M. L., Caplan, J. S., Taylor, A. L., Fisek, M., & Marder, E. (2010). Precise Temperature Compensation of Phase in a Rhythmic Motor Pattern. *PLOS Biology*, 8(8), e1000469. <https://doi.org/10.1371/journal.pbio.1000469> (cit. on p. 145).
- Tatsuno, M. (Ed.). (2015). *Analysis and Modeling of Coordinated Multi-neuronal Activity* (Vol. 12). Springer. <https://doi.org/10.1007/978-1-4939-1969-7> (cit. on pp. 9, 30).
- Thompson, A. C., Fallon, J. B., Wise, A. K., Wade, S. A., Shepherd, R. K., & Stoddart, P. R. (2015). Infrared neural stimulation fails to evoke neural activity in the deaf guinea pig cochlea. *Hearing Research*, 324, 46–53. <https://doi.org/10.1016/j.heares.2015.03.005> (cit. on p. 156).
- Thompson, A. C., Wade, S. A., Brown, W. G. A., & Stoddart, P. R. (2012). Modeling of light absorption in tissue during infrared neural stimulation. *Journal of Biomedical Optics*, 17(7), 0750021. <https://doi.org/10.1117/1.jbo.17.7.075002> (cit. on pp. 145, 157).
- Torres, J. J., & Varona, P. (2012). Modeling Biological Neural Networks. In *Handbook of Natural Computing* (pp. 533–564, Vol. 1–4). Springer. https://doi.org/10.1007/978-3-540-92910-9_17 (cit. on pp. 11, 14, 31, 35).
- Tsodyks, M., & Markram, H. (1997). The neural code between neocortical pyramidal neurons depends on neurotransmitter release probability. *P. Natl. Acad. Sci. USA*, 94, 719–723 (cit. on pp. 15, 36).
- Tye, K. M., & Deisseroth, K. (2012). Optogenetic investigation of neural circuits underlying brain disease in animal models. *Nature Reviews Neuroscience* 2012 13:4, 13(4), 251–266. <https://doi.org/10.1038/nrn3171> (cit. on p. 121).
- Ullén, F., Forssberg, H., & Ehrsson, H. H. (2003). Neural networks for the coordination of the hands in time. *Journal of Neurophysiology*, 89(2), 1126–1135. <https://doi.org/10.1152/jn.00775.2002> (cit. on pp. 9, 30).
- Valero-Cabré, A., Amengual, J. L., Stengel, C., Pascual-Leone, A., & Coubard, O. A. (2017). Transcranial magnetic stimulation in basic and clinical neuroscience: A comprehensive review of fundamental principles and novel insights. *Neuroscience & Biobehavioral Reviews*, 83, 381–404. <https://doi.org/10.1016/j.neubiorev.2017.10.006> (cit. on pp. 19, 41, 121).
- Varona, P., Arroyo, D., Rodríguez, F. B., & Nowotny, T. (2016). Online event detection requirements in closed-loop neuroscience. In A. El Hady (Ed.), *Closed-Loop Neuroscience* (pp. 81–91). Academic Press. <https://doi.org/10.1016/B978-0-12-802452-2.00006-8> (cit. on pp. 122, 149).

BIBLIOGRAPHY

- Varona, P., & Rabinovich, M. I. (2016). Hierarchical dynamics of informational patterns and decision-making. *Proceedings of the Royal Society B*, 283(1832), 20160475. <https://doi.org/10.1098/rspb.2016.0475> (cit. on pp. 7, 27).
- Vavoulis, D. V., Nikitin, E. S., Kemenes, I., Marra, V., Feng, J., Benjamin, P. R., & Kemenes, G. (2010). Balanced plasticity and stability of the electrical properties of a molluscan modulatory interneuron after classical conditioning: A computational study. *Frontiers in Behavioral Neuroscience*, 4, 19. <https://doi.org/10.3389/fnbeh.2010.00019> (cit. on pp. 14, 35, 50, 54, 140, 145).
- Vavoulis, D. V., Straub, V. A., Kemenes, I., Kemenes, G., Feng, J., & Benjamin, P. R. (2007). Dynamic control of a central pattern generator circuit: A computational model of the snail feeding network. *European Journal of Neuroscience*, 25(9), 2805–2818. <https://doi.org/10.1111/j.1460-9568.2007.05517.x> (cit. on pp. 15, 36, 49, 50, 51, 52, 53, 62, 66, 67, 72, 74, 112, 117, 140).
- Vehovszky, Á., Szabó, H., & Elliott, C. J. (2004). Octopamine-containing (OC) interneurons enhance central pattern generator activity in sucrose-induced feeding in the snail Lymnaea. *Journal of Comparative Physiology A: Neuroethology, Sensory, Neural, and Behavioral Physiology*, 190(10), 837–846. <https://doi.org/10.1007/s00359-004-0539-y> (cit. on p. 49).
- Venaille, A., Varona, P., & Rabinovich, M. I. (2005). Synchronization and coordination of sequences in two neural ensembles. *Physical Review E*, 71(6 Pt 1), 61909. <https://doi.org/10.1103/PhysRevE.71.061909> (cit. on p. 61).
- Wachtel, H., & Kandel, E. R. (1967). A Direct Synaptic Connection Mediating Both Excitation and Inhibition. *Science*, 158(3805), 1206–1208. <https://doi.org/10.1126/science.158.3805.1206> (cit. on pp. 16, 37).
- Wang, X., Reddy, D. D., Nalawade, S. S., Pal, S., Gonzalez-Lima, F., & Liu, H. (2017). Impact of heat on metabolic and hemodynamic changes in transcranial infrared laser stimulation measured by broadband near-infrared spectroscopy. *Neurophotonics*, 5(01), 1. <https://doi.org/10.1111/1.NPh.5.1.011004> (cit. on pp. 122, 155).
- Waschke, L., Kloosterman, N. A., Obleser, J., & Garrett, D. D. (2021). Behavior needs neural variability. *Neuron*, 109(5), 751–766. <https://doi.org/10.1016/j.neuron.2021.01.023> (cit. on p. 111).
- Wells, J., Kao, C., Konrad, P., Milner, T., Kim, J., Mahadevan-Jansen, A., & Jansen, E. D. (2007). Biophysical mechanisms of transient optical stimulation of peripheral nerve. *Biophysical Journal*, 93(7), 2567–2580. <https://doi.org/10.1529/biophysj.107.104786> (cit. on pp. 122, 137, 145).

BIBLIOGRAPHY

- Wells, J., Kao, C., Mariappan, K., Albea, J., Jansen, E. D., Konrad, P., & Mahadevan-Jansen, A. (2005a). Optical stimulation of neural tissue in vivo. *Optics Letters*, 30(5), 504. <https://doi.org/10.1364/ol.30.000504> (cit. on p. 154).
- Wells, J. D., M.D, C. K., Jansen, E. D., M.D, P. E. K., & Mahadevan-Jansen, A. (2005b). Application of infrared light for in vivo neural stimulation. <https://doi.org/10.1111/1.2121772>, 10(6), 064003. <https://doi.org/10.1117/1.2121772> (cit. on pp. 122, 134, 154, 155, 156).
- Winlow, W., Haydon, P., & Benjamin, P. R. (1981). Multiple Postsynaptic Actions of the Giant Dopamine-Containing Neurone R.Pe.D.I of Lymnaea Stagnalis. *Journal of Experimental Biology*, 94. <https://doi.org/10.1242/jeb.94.1.137> (cit. on pp. 17, 38).
- Woźniak, S., Pantazi, A., Bohnstingl, T., & Eleftheriou, E. (2020). Deep learning incorporating biologically inspired neural dynamics and in-memory computing. *Nature Machine Intelligence*, 2(6), 325–336. <https://doi.org/10.1038/s42256-020-0187-0> (cit. on pp. 10, 30).
- Yizhar, O., Fieni, L. E., Davidson, T. J., Mogri, M., & Deisseroth, K. (2011). Optogenetics in Neural Systems. *Neuron*, 71(1), 9–34. <https://doi.org/10.1016/J.NEURON.2011.06.004> (cit. on p. 121).
- Yuste, R., MacLean, J. N., Smith, J., & Lansner, A. (2005). The cortex as a central pattern generator. *Nat Rev Neurosci*, 6(6), 477–483. <https://doi.org/10.1038/nrn1686> (cit. on pp. 6, 27).
- Zeldenrust, F., Wadman, W. J., & Englitz, B. (2018). Neural coding with bursts—current state and future perspectives. *Frontiers in Computational Neuroscience*, 12. <https://doi.org/10.3389/fncom.2018.00048> (cit. on p. 111).
- Zheng, Q., Shen, J., & Xu, Y. (2020). Spontaneous Activity Induced by Gaussian Noise in the Network-Organized FitzHugh-Nagumo Model. *Neural Plasticity*, 2020, 6651441. <https://doi.org/10.1155/2020/6651441> (cit. on pp. 15, 36).
- Zhou, S., Masmanidis, S. C., & Buonomano, D. V. (2020). Neural Sequences as an Optimal Dynamical Regime for the Readout of Time. *Neuron*, 108(4), 651–658.e5. <https://doi.org/10.1016/j.neuron.2020.08.020> (cit. on pp. 9, 30).
- Zimnik, A. J., & Churchland, M. M. (2021). Independent generation of sequence elements by motor cortex. *Nature Neuroscience*, 24(3), 412–424. <https://doi.org/10.1038/s41593-021-00798-5> (cit. on pp. 9, 30).
- Zrenner, C., Belardinelli, P., Müller-Dahlhaus, F., & Ziemann, U. (2016). Closed-loop neuroscience and non-invasive brain stimulation: A tale of two loops. *Frontiers in Cellular Neuroscience*, 10, 92. <https://doi.org/10.3389/fncel.2016.00092> (cit. on p. 122).

BIBLIOGRAPHY

APPENDIX A

Publications

Journal Publications

Garrido-Peña, A., Elices, I., & Varona, P. (2021b). Characterization of interval variability in the sequential activity of a central pattern generator model [JCR Q2. Related to Chapter 5]. *Neurocomputing*, 461, 667–678. <https://doi.org/10.1016/j.neucom.2020.08.093>

Garrido-Peña, A., Sanchez-Martin, P., Reyes-Sanchez, M., Levi, R., Rodriguez, F. B., Castilla, J., Tornero, J., & Varona, P. (2024b). Modulation of neuronal dynamics by sustained and activity-dependent continuous-wave near-infrared laser stimulation [JCR Q1. Related to Chapter 6.]. *Neurophotonics*, 11(2), 024308. <https://doi.org/10.11117/1.NPh.11.2.024308>

International Conference Contributions

Amaducci, R., Elices, I., Reyes-Sanchez, M., Garrido-Peña, A., Levi, R., Rodriguez, F. B., & Varona, P. (2020). Hybrid robot driven by a closed-loop interaction with a living central pattern generator with online feedback. 29th Annual Computational Neuroscience Meeting: CNS*2020. P207. [Related to Chapter 5]. *BMC Neuroscience*, 21, 54. <https://doi.org/10.1186/s12868-020-00593-1>

Garrido-Peña, A., Elices, I., Levi, R., Rodriguez, F. B., & Varona, P. (2020). Experimental and computational characterization of interval variability in the sequential activity of the Lymnaea feeding CPG. 29th Annual Computational Neuroscience Meeting: CNS*2020. O11. ORAL PRESENTATION [Related to Chapter 5.]. *BMC Neuroscience*, 21, 54. <https://doi.org/10.1186/s12868-020-00593-1>

APPENDIX A: PUBLICATIONS

- Amaducci, R., Elices, I., Reyes-Sanchez, M., Garrido-Peña, A., Levi, R., Rodriguez, F. B., & Varona, P. (2021). Controlling robotic locomotion by a closed-loop interaction with living central pattern generators. [Related to Chapter 5]. *COSYNE*. https://www.cosyne.org/s/Cosyne2021_program_book.pdf
- Berbel, B., Garrido-Peña, A., Elices, I., Latorre, R., & Varona, P. (2021a). Effect of Electrical Synapses in the Cycle-by-Cycle Period and Burst Duration of Central Pattern Generators [Related to Chapter 5.]. In I. Rojas, G. Joya, & A. Català (Eds.), *Advances in Computational Intelligence* (pp. 81–92). Springer International Publishing. https://doi.org/10.1007/978-3-030-85099-9_7
- Berbel, B., Garrido-Peña, A., Elices, I., Latorre, R., & Varona, P. (2021b). Gap junctions shape the intervals that build robust sequences in a central pattern generator model. 30th Annual Computational Neuroscience Meeting: CNS*2021—Meeting Abstracts. P194. [Related to Chapter 5.]. *Journal of Computational Neuroscience*, 49, 3–208. <https://doi.org/10.1007/s10827-021-00801-9>
- Garrido-Peña, A., Elices, I., Levi, R., Rodriguez, F. B., & Varona, P. (2021a). Universality of interval variability constraints in the sequential activity of motor circuits. [Related to Chapter 5.]. *COSYNE*. https://www.cosyne.org/s/Cosyne2021_program_book.pdf
- Garrido-Peña, A., Sanchez-Martin, P., Levi, R., Castilla, J., Tornero, J., & Varona, P. (2021c). Effect of infrared laser stimulation in single neurons: Experimental and modeling study. 30th Annual Computational Neuroscience Meeting: CNS*2021—Meeting Abstracts. P193. [Related to Chapter 6]. *Journal of Computational Neuroscience*, 49, 3–208. <https://doi.org/10.1007/s10827-021-00801-9>
- Sanchez-Martin, P., Elices, I., Garrido-Peña, A., Levi, R., Rodriguez, F. B., & Varona, P. (2021). Dynamic synchronization between electrically coupled cells of central pattern generators. 30th Annual Computational Neuroscience Meeting: CNS*2021—Meeting Abstracts. P195. [Related to Chapter 5]. *Journal of Computational Neuroscience*, 49, 3–208. <https://doi.org/10.1007/s10827-021-00801-9>
- Garrido-Peña, A., Sanchez-Martin, P., Levi, R., Castilla, J., Tornero, J., & Varona, P. (2022). Activity-dependent stimulation to assess the effect of infrared-laser stimulation in single neurons. Poster Presentation [Related to Chapter 6]. *FENS*, S02–556. <https://kenesvm.azureedge.net/public/general/FENS2022.pdf>
- Garrido-Peña, A., Sánchez-Martín, P., Reyes-Sánchez, M., Castilla, J., Tornero, J., Levi, R., Rodriguez, F. B., & Varona, P. (2023). Activity-dependent infrared laser stimulation to assess its biophysical effects on single neurons. 31st Annual Computational Neuroscience Meeting:

APPENDIX A: PUBLICATIONS

- CNS*2022. F3. ORAL PRESENTATION. [Related to Chapter 6]. *Journal of Computational Neuroscience*, 51, 3–101. <https://doi.org/10.1007/s10827-022-00841-9>
- Sánchez-Martín, P., Garrido-Peña, A., Berbel, B., Rodriguez, F. B., Levi, R., & Varona, P. (2023). Influence of electrical coupling in shaping time intervals and dynamical invariants of central pattern generator sequences. 31st Annual Computational Neuroscience Meeting: CNS*2022. P109. [Related to Chapter 5]. *Journal of Computational Neuroscience*, 51, 3–101. <https://doi.org/10.1007/s10827-022-00841-9>
- Soëtard, P., Amaducci, R., Sánchez-Martín, P., Reyes-Sánchez, M., Garrido-Peña, A., Levi, R., Rodriguez, F. B., & Varona, P. (2023). Dynamical principles of functional neural sequences validated in hybrid robots built with living central pattern generators. 31st Annual Computational Neuroscience Meeting: CNS*2022. P110 [Related to Chapter 5]. *Journal of Computational Neuroscience*, 51, 3–101. <https://doi.org/10.1007/s10827-022-00841-9>
- Garrido-Peña, A., Sanchez-Martin, P., Reyes-Sánchez, M., Levi, R., Rodriguez, F. B., Castilla, J., Tornero, J., & Varona, P. (2024a). Effective noninvasive neuronal waveform modulation with sustained and activity-dependent continuous-wave near-infrared laser stimulation [Related to Chapter 6]. *FENS*. <https://doi.org/10.57736/6F07-365F>
- Garrido-Peña, A., Sánchez-Martín, P., Elices, I., Reyes-Sánchez, M., Berbel, B., Latorre, R., Rodriguez, F. B., & Varona, P. (2024c). Exploring the ability of biophysical models to reproduce the functional variability of neurons. 32nd Annual Computational Neuroscience Meeting: CNS*2023. [Related to Chapter 5]. *In Press for Journal of Computational Neuroscience*.

APPENDIX A: PUBLICATIONS

APPENDIX B

Supplementary figures for chapter 4

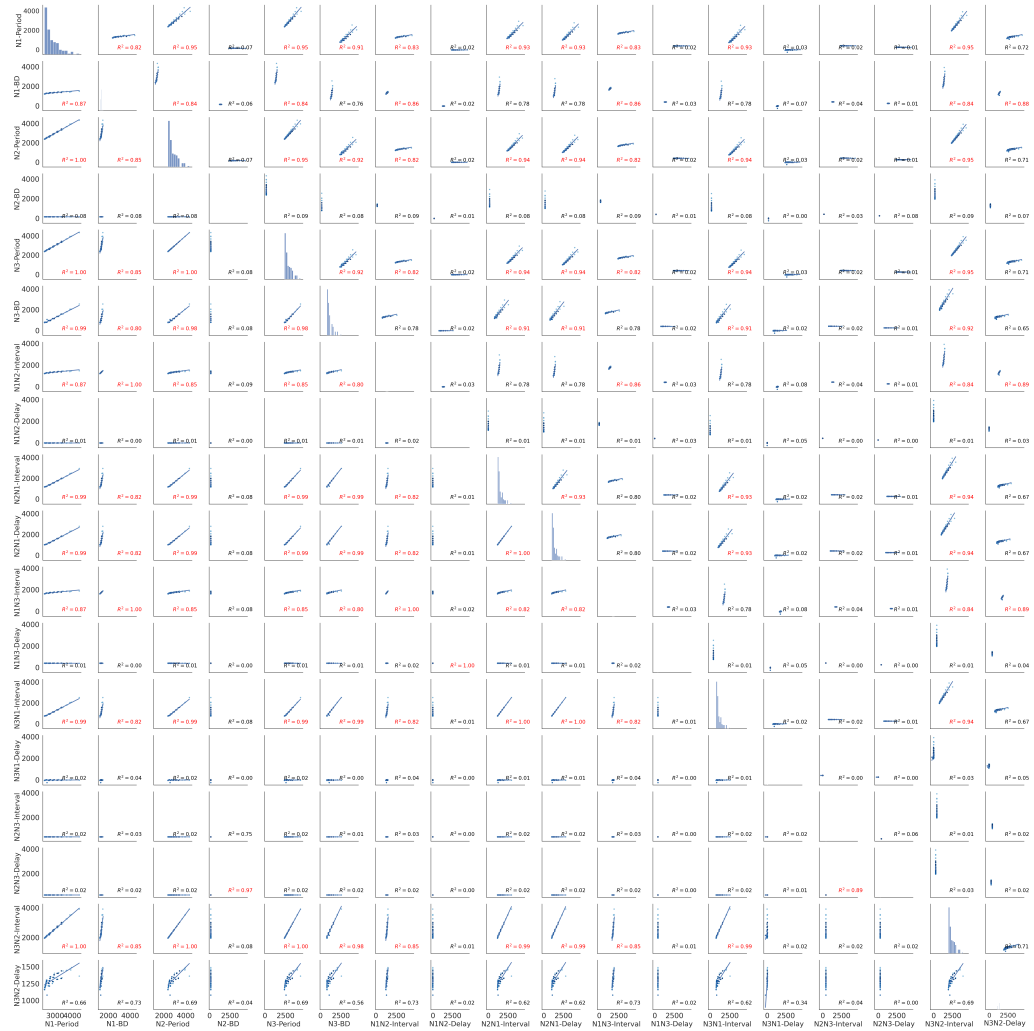


Figure B.1: N1M stimulation: Pairplot illustrating the invariant relation resetting within consecutive cycles.

Lower triangle represents the relationships between intervals within the same cycle. Upper triangle represents the relations between intervals of one cycle and those in the next one.

APPENDIX B: SUPPLEMENTARY FIGURES FOR CHAPTER 4

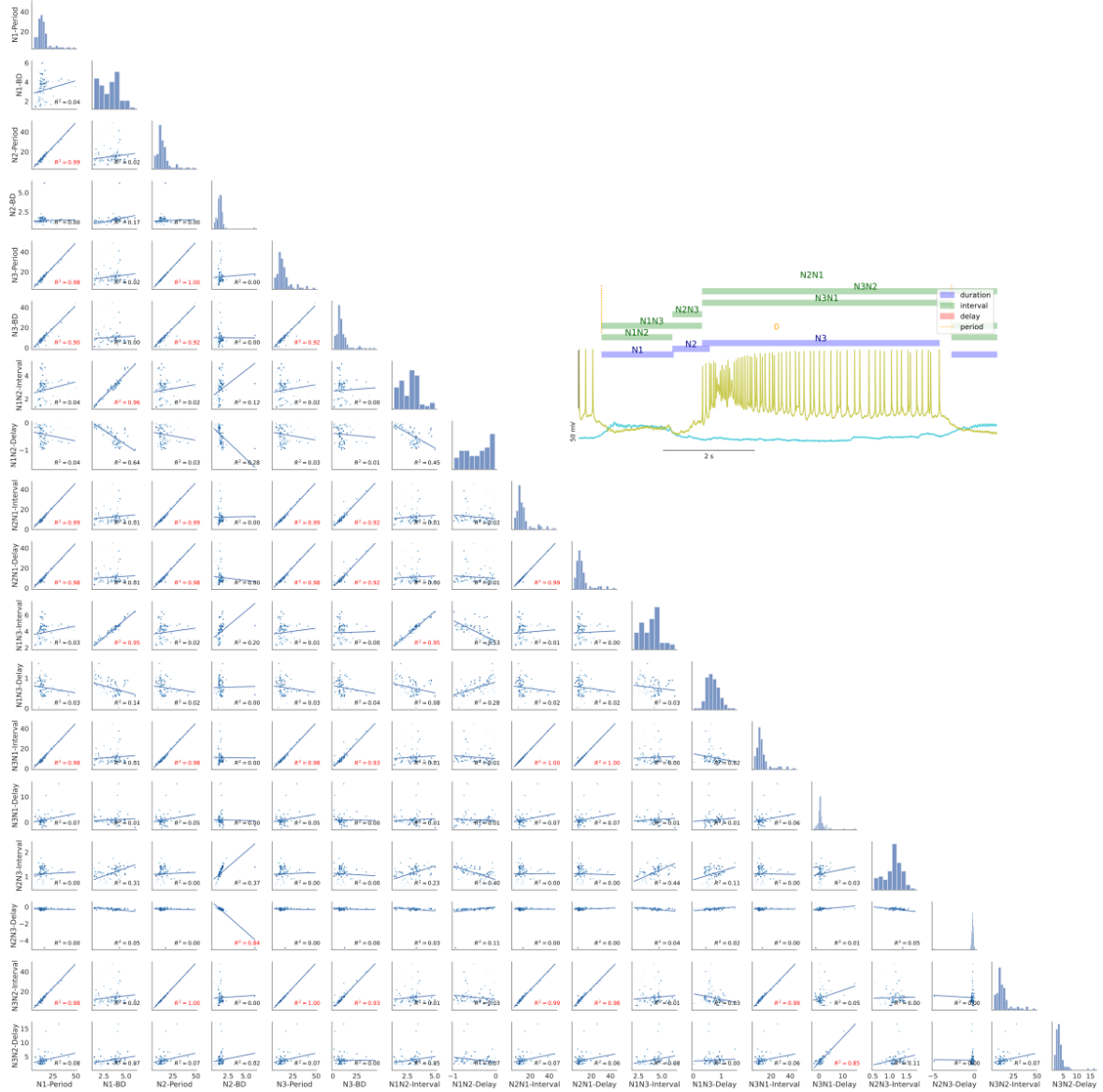


Figure B.2: Spontaneous case 1: Panel of interval distribution and dynamical invariants for the three phases in the CPG for spontaneous activity.

APPENDIX B: SUPPLEMENTARY FIGURES FOR CHAPTER 4

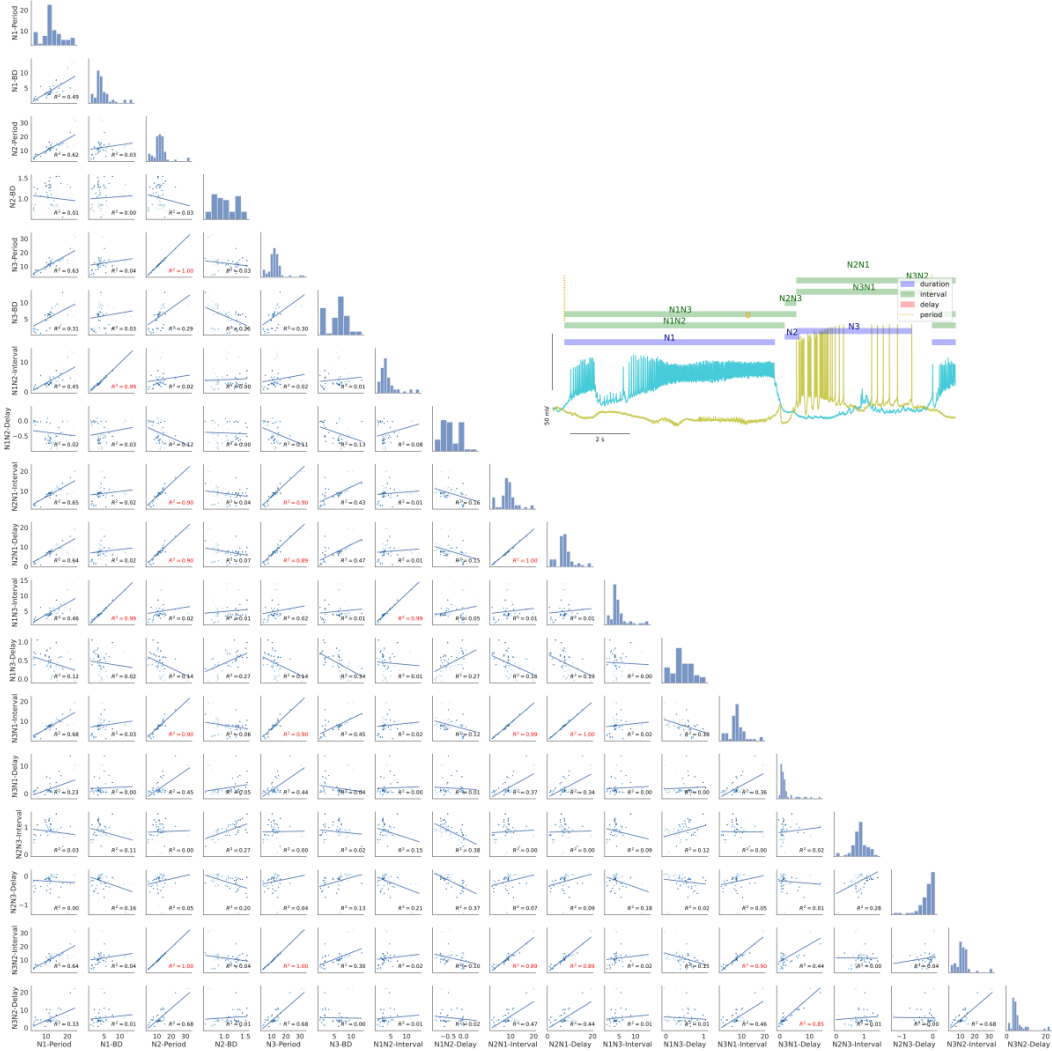


Figure B.3: Spontaneous case 2: Panel of interval distribution and dynamical invariants for the three phases in the CPG for spontaneous activity.

APPENDIX B: SUPPLEMENTARY FIGURES FOR CHAPTER 4

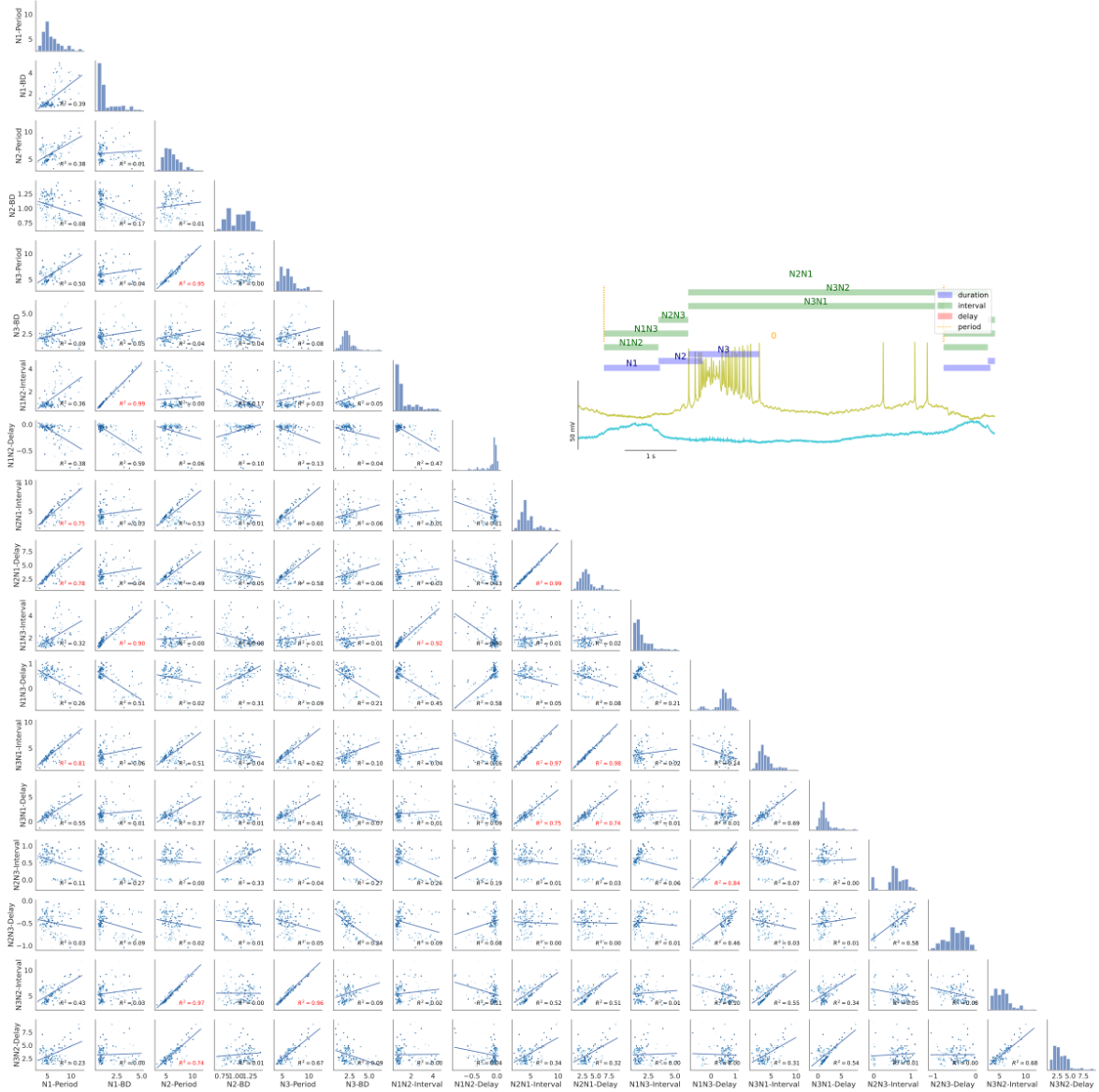


Figure B.4: Spontaneous case 3: Panel of interval distribution and dynamical invariants for the three phases in the CPG for spontaneous activity.

APPENDIX B: SUPPLEMENTARY FIGURES FOR CHAPTER 4

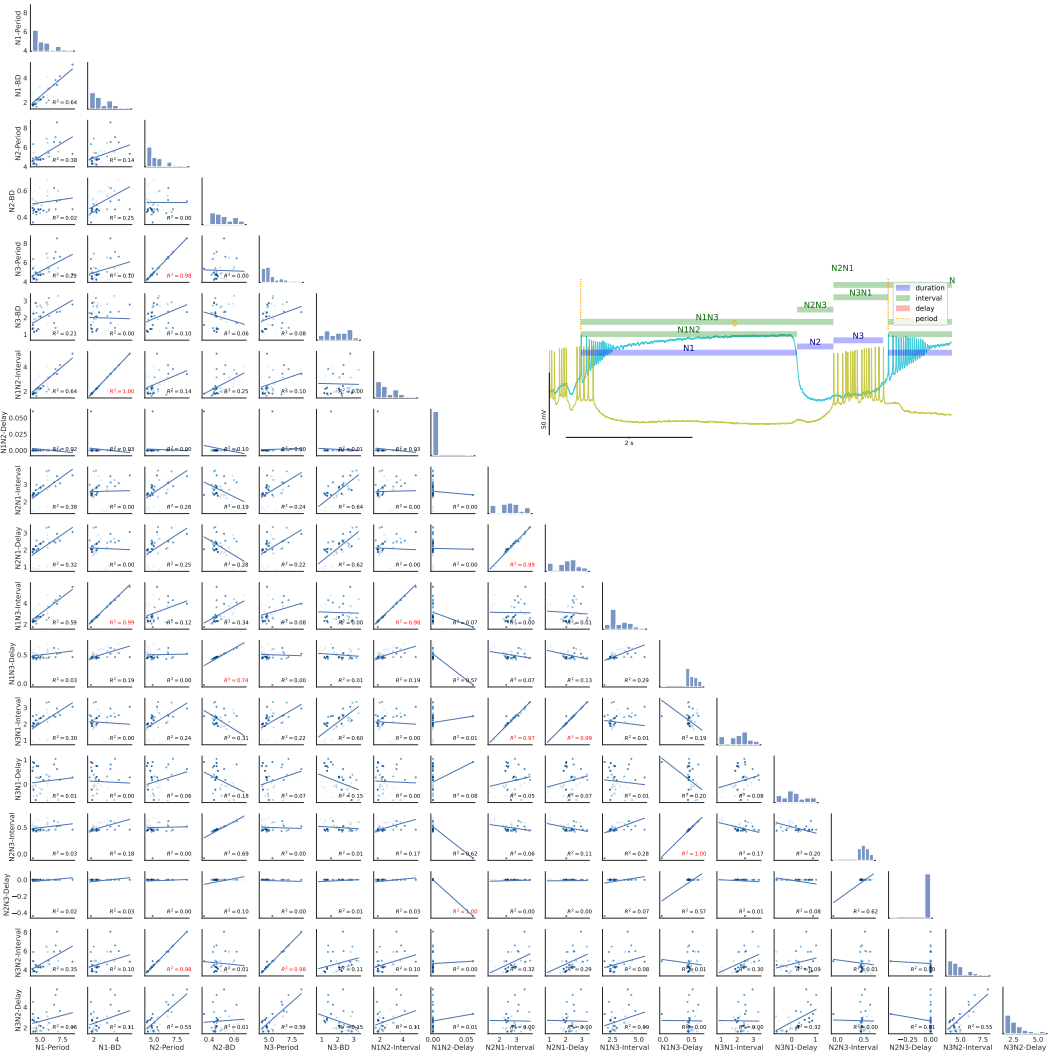


Figure B.5: CV1a driven case 4: Panel of interval distribution and dynamical invariants for the three phases in the CPG under CV1a stimulation.

Interval	Num_Cycles	N1-BD	N2-BD	N3-BD	N1N2-Interval	N2N1-Interval	N1N3-Interval	N3N1-Interval	N2N3-Interval	N3N2-Interval	N1N1-Delay	N2N1-Delay	N1N3-Delay	N3N1-Delay	N2N3-Delay	N3N2-Delay
Spont. 2; 2phases	158.00	0.39	nan	0.04	nan	nan	0.36	0.86	nan	nan	nan	0.16	0.69	nan	nan	nan
Spont. 2; 3phases	158.00	0.39	0.05	0.04	0.37	0.82	0.36	0.86	0.05	0.59	0.28	0.84	0.16	0.69	0.01	0.44
Spont. 1; 2phases	91.00	0.04	nan	0.90	nan	nan	0.03	0.98	nan	nan	nan	0.03	0.07	nan	nan	nan
Spont. 1; 3phases	91.00	0.04	0.00	0.90	0.04	0.99	0.03	0.98	0.00	0.98	0.04	0.97	0.03	0.07	0.00	0.08
Spont. 3; 3phases	59.00	0.49	nan	0.31	nan	nan	0.46	0.68	nan	nan	nan	0.12	0.23	nan	nan	nan
Spont. 3; 3phases	59.00	0.49	0.01	0.31	0.45	0.65	0.46	0.68	0.03	0.64	0.02	0.64	0.12	0.23	0.00	0.32
SO-driven Spont.	89.00	0.73	nan	0.21	nan	nan	0.82	0.72	nan	nan	nan	0.47	0.48	nan	nan	nan
SO-driven Stimulated	41.00	0.84	nan	0.28	nan	nan	0.84	0.60	nan	nan	nan	0.04	0.09	nan	nan	nan
STOP SO-driven Spont.	10.00	0.91	nan	0.09	nan	nan	0.89	0.89	nan	nan	nan	0.22	0.91	nan	nan	nan
CV1a-driven Stim. (1) 2 phases	39.00	0.93	nan	0.05	nan	nan	0.92	0.02	nan	nan	nan	0.00	0.03	nan	nan	nan
CV1a-driven Stim. (1) 3 phases	39.00	0.93	0.00	0.05	0.93	0.03	0.92	0.02	0.00	0.02	0.00	0.00	0.03	0.00	0.07	nan
CV1a-driven Stim. (2) 3 phases	43.00	0.52	nan	0.17	nan	nan	0.44	0.27	nan	nan	nan	0.04	0.00	nan	nan	nan
CV1a-driven Stim. (2) 2 phases	36.00	0.22	nan	0.52	nan	nan	0.18	0.60	nan	nan	nan	0.02	0.06	nan	nan	nan
CV1a-driven Stim. (3) 3 phases	40.00	0.62	nan	0.21	nan	nan	0.58	0.29	nan	nan	nan	0.03	0.01	nan	nan	nan
CV1a-driven Stim. (3) 2 phases	40.00	0.62	0.02	0.21	0.62	0.37	0.58	0.29	0.03	0.35	0.02	0.31	0.03	0.01	0.02	0.06
MLN-driven Stim. 2 phases	37.00	0.97	nan	0.03	nan	nan	0.98	0.00	nan	nan	nan	0.63	0.04	nan	nan	nan

Figure B.6: Table of R^2 values for the linear regression between the period and each interval for all experimental recordings discussed in this section.